NUMERICAL INVESTIGATION OF NASAL AIRFLOW: COMPARATIVE ANALYSIS OF BEFORE AND AFTER SURGERY STATES FOR AN OBSTRUCTED NASAL CAVITY

A THESIS SUBMITTED TO
THE GRADUATE SCHOOL OF NATURAL AND APPLIED SCIENCES
OF
MIDDLE EAST TECHNICAL UNIVERSITY

BY

GÖKBERK GÜNEŞ

IN PARTIAL FULFILLMENT OF THE REQUIREMENTS
FOR
THE DEGREE OF MASTER OF SCIENCE
IN
CIVIL ENGINEERING

JANUARY 2024

Approval of the thesis:

NUMERICAL INVESTIGATION OF NASAL AIRFLOW: COMPARATIVE ANALYSIS OF BEFORE AND AFTER SURGERY STATES FOR AN OBSTRUCTED NASAL CAVITY

submitted by **GÖKBERK GÜNEŞ** in partial fulfillment of the requirements for the degree of **Master of Science in Civil Engineering Department, Middle East Technical University** by,

Prof. Dr. Halil Kalıpçılar
Dean, Graduate School of **Natural and Applied Sciences** _____

Prof. Dr. Erdem Canbay
Head of Department, **Civil Engineering** _____

Prof. Dr. Mete Köken
Supervisor, **Civil Engineering, METU** _____

Examining Committee Members:

Prof. Dr. Kerem Taştan
Civil Engineering, Gazi University _____

Prof. Dr. Mete Köken
Civil Engineering, METU _____

Assoc. Prof. Dr. Elif Oğuz
Civil Engineering, METU _____

Assoc. Prof. Dr. Ali Ercan
Civil Engineering, METU _____

Assist. Prof. Dr. Cüneyt Baykal
Civil Engineering, METU _____

Date:15.01.2024

I hereby declare that all information in this document has been obtained and presented in accordance with academic rules and ethical conduct. I also declare that, as required by these rules and conduct, I have fully cited and referenced all material and results that are not original to this work.

Name, Surname: Gökberk Güneş

Signature :

ABSTRACT

NUMERICAL INVESTIGATION OF NASAL AIRFLOW: COMPARATIVE ANALYSIS OF BEFORE AND AFTER SURGERY STATES FOR AN OBSTRUCTED NASAL CAVITY

Güneş, Gökberk
M.S., Department of Civil Engineering
Supervisor: Prof. Dr. Mete Köken

January 2024, 220 pages

The nasal cavity is a multi-functional but convoluted, diverse, and dynamic structure located within the body. These chaotic characteristics make conducting the traditional research methods challenging. Consequently, the paradigm in breathing-related research shifts towards computer-centric numerical methods. In this thesis, numerical simulations are conducted on a nasal cavity both before and after surgery for an individual with nasal obstruction. The investigation is conducted using identical discharge levels for both geometries, corresponding to restful and quick breathing rates. Furthermore, only free and open-source software are used to enhance availability and reproducibility. The most noteworthy one, OpenFOAM, is employed to solve numerical simulations and generate volumetric meshes. The turbulence in the airflow is simulated by resolving the large eddies and modeling the small ones with the WALE model. Multiple parameters are controlled to interpret the results: pressure drops, discharge rates, nasal resistance values, turbulent kinetic energy levels, localized discharge rates, localized wall shear stress values. The results show that even though the nasal surgery increases cross-sectional areas, stimulation on the mechano- and thermo-receptors does not decrease; instead, it evolves into a homogeneous state throughout

the cavity. This result suggests better overall stimulation of receptors; hence, a lesser nasal obstruction feeling. The verification of grid resolution for the LES is performed using Celik indices. Similarly, time resolution is verified by comparing Kolmogorov time scale to the selected time steps. Lastly, the results are partially validated through a comparison of nasal resistance values with the existing literature.

Keywords: Breathing, Nasal cavity, LES, WALE, OpenFOAM

ÖZ

NAZAL HAVA AKIŞININ SAYISAL YÖNTEMLERLE İNCELEMESİ: TIKALI BİR BURUN BOŞLUĞUNUN AMELİYAT ÖNCESİ VE SONRASI DURUMUNDAKİ KARŞILAŞTIRMALI ANALİZİ

Güneş, Gökberk
Yüksek Lisans, İnşaat Mühendisliği Bölümü
Tez Yöneticisi: Prof. Dr. Mete Köken

Ocak 2024, 220 sayfa

İnsan nasal boşluğu vücudün içinde bulunan çok fonksiyonlu ancak karmaşık, türlü ve dinamik bir yapıdır. Bu kaotik nitelikler geleneksel araştırma yöntemlerinin uygulanmasını çetin kılmaktadırlar. Dolayısıyla, solumayla ilgili araştırmalardaki paradigma bilgisayar odaklı nümerik yöntemlere doğru kaymaktadır. Bu tezde, burun tıkanıklığı olan bir kimsenin ameliyat öncesi ve sonrası burun boşluğunda nümerik simulasyonlar gerçekleştirilmektedir. Araştırmada her iki geometri için de aynı debi miktarları kullanılmaktadır: dinlenme anındaki ve çabuk solunum anındaki debi. Dahası, ulaşılabilirliği ve tekrarlanabilirliği artırmak için bu tezde sadece özgür ve açık kaynaklı yazılımlar kullanılmaktadır. Bu yazılımların en önemlisi nümerik denklemleri çözen ve hacimsel ağ oluşturan OpenFOAM'dır. Hava akışındaki türbülans büyük girdaplar çözülerek ve küçük girdaplar WALE metoduyla modellenerek yapılmaktadır. Simülasyon sonuçlarının anlamlandırılması için birçok parametre kontrol edilmektedir: basınç düşüş miktarları, debi miktarları, türbülans kinetik enerji seviyeleri, yerel debi miktarları, lokal duvar kesme gerilim miktarları. Sonuçlara göre, ameliyat sonrası

kesit alanları artmasına rağmen, mekanik- ve termo-reseptörlerdeki uyarım azalmayıp daha homojen bir yapıya evrilmektedir. Bu sonuç reseptörlerin daha iyi uyarıldığına ve tıkanıklık hissinin azaldığına işaret etmektedir. Büyük girdap simülasyonundaki ağ yapısının çözünürlüğünün doğrulaması Celik indisleri kullanılarak yapılmaktadır. Benzer bir şekilde, zamanın çözünürlüğü Kolmogorov zaman skalasının ve seçilen zaman adımlarının karşılaştırılmasıyla yapılmaktır. Son olarak, sonuçların kısmi bir validasyonu literatürdeki diğer nazal direnç değerleriyle karşılaştırılak yapılmaktadır.

Anahtar Kelimeler: Solunum, Nazal kavite, BGS, WALE, OpenFOAM

Dedicated to open science.

ACKNOWLEDGMENTS

First and foremost, I am sincerely grateful to my supervisor, Prof. Dr. Mete Köken, for guiding, helping, and trusting me throughout my thesis. I am deeply appreciative of his approal to work on and supervise my work on this exciting thesis.

I specifically thank Op. Dr. M. Ozan Altuntaş for providing me with guidance and knowledge. Also, I appreciate all the patience and support given by the thesis committee, Prof. Dr. Kerem Taştan, Assoc. Prof. Dr. Elif Oğuz, Assoc. Prof. Dr. Ali Ercan, and Assist. Prof. Dr. Cüneyt Baykal.

I would like to acknowledge the support and company of my fellows Ahmet Dolma, Alper Tunga Bayrak, Asu Efe, Doğa Derman Çiçek, Emre Yılmaz, Gökalp Doğukan Demirbaş, Hasan Hüseyin Yıldırım, İsmet Karakan, Mert Gökgöz, Oğuz Çubuk, Thien Ha Cong Truong, and Vedat Fatih Yaman.

Moreover, I am deeply grateful for the endless support and love from my mother, Yeşim İkizünal, and from my father, Mustafa Güneş. Their assistance was critical in bringing this thesis to completion.

Last but not least, I acknowledge the encouragement, trust, and aid of my beloved wife, Jelizaveta Güneş. Her presence not only eased the completion of this thesis, but also made an otherwise challenging endeavor manageable.

TABLE OF CONTENTS

ABSTRACT v

ÖZ vii

ACKNOWLEDGMENTS x

TABLE OF CONTENTS xi

LIST OF TABLES xix

LIST OF FIGURES xxi

LIST OF ABBREVIATIONS xxv

CHAPTERS

1 INTRODUCTION 1

1.1 Background 1

1.2 Motivation 2

1.3 The Outline of the Thesis 3

2 BIOLOGICAL BACKGROUND 5

2.1 Biological Overview 5

2.2 Respiratory Tract 6

2.3 Nasal Cavity 6

2.4 Nasal Sicknesses and Surgeries 9

2.4.1 Septal Deviation 11

2.4.1.1 Septal Deviation Remedies 13
2.4.2 Sinusitis 14
2.4.2.1 Sinusitis Remedies 14
2.4.3 Nasal Polyps 16
2.4.3.1 Nasal Polyps Remedies 17
2.5 Methods to Investigate Nasal Cavity 18
2.5.1 Rhinomanometry 18
2.5.2 Acoustic Rhinometry 20
2.5.3 Nasal Endoscopy 23
2.5.4 Computed Tomography Scan 23
2.5.5 Magnetic Resonance Imaging 26
3 LITERATURE REVIEW 29
3.1 Healthy Airflow 29
3.2 Empty Nose Syndrome 31
3.3 Septal Deviation 34
3.4 Satisfaction After Nasal Surgeries 36
3.5 Numerical Simulations of Nasal Airflow 38
3.5.1 Pioneering Numerical Works on Nasal Airflow 39
3.5.2 Recent CFD Simulations on Nasal Airflow 40
3.5.3 Geometry Generation for Nasal Flow Simulations 42
3.5.4 Steady Assumption of Nasal Flow Simulations 44
3.5.5 Interpreting The Nasal Airflow Results 49
3.5.6 Numerical Simulations Against Other Methods 50

3.5.7 Virtual Surgeries Using CFD Simulations 52

4 FLUID MECHANICS BACKGROUND 55

4.1 Large Eddy Simulations 55

4.1.1 Filtering Incompressible Conservation of Mass Equation . . 58

4.1.2 Filtering Incompressible Navier-Stokes Equations 58

4.1.3 Incompressible Smagorinsky Model 61

4.1.4 Alternative Way to Derive Incompressible Smagorinsky Model 63

4.1.5 Calculation of Sub-Grid Scale Kinetic Energy 65

4.1.6 Shortcomings of Smagorinsky Model 67

4.1.7 Wall-Adapting Local Eddy-Viscosity Model 68

5 METHODS 73

5.1 Surface Mesh Generation From CT Scans 73

5.1.1 Steps to Create Surface Mesh in *3D Slicer* 74

5.2 Manual Modifications on the Surface Mesh 77

5.2.1 Removal of the Extra Walls 78

5.2.2 Removal of the Face Wall 79

5.2.3 Inlet and Outlet Creation 80

5.3 Volumetric Mesh Generation From the Surface Mesh 81

5.3.1 Background Mesh Generation 82

5.3.2 Surface Conforming Volumetric Mesh Generation 83

5.3.2.1 Castellation Step 83

5.3.2.2 Snapping Step 85

5.3.2.3 Boundary Layer Addition Step 87

5.3.3 Details of the Generated Mesh 89
5.3.3.1 Pre-Surgery Volumetric Mesh 90
5.3.3.2 Post-Surgery Volumetric Mesh 93
5.4 General Solution Strategy 94
5.5 Turbulence Modeling 95
5.5.1 Precursor Simulation's Turbulence Model 95
5.5.2 Large Eddy Simulation's Turbulence Model 97
5.6 Boundary Conditions 98
5.6.1 Pressure Boundary Conditions 99
5.6.2 Velocity Boundary Conditions 100
5.6.3 Turbulent Kinetic Energy Boundary Conditions 101
5.6.4 Boundary Condition for Specific Dissipation of Turbulent Kinetic Energy 102
5.6.5 Boundary Conditions for Turbulent Viscosity 102
5.7 Settings of Simulations 103
5.7.1 Settings of Precursor Simulations 104
5.7.1.1 Numerical Schemes 104
5.7.1.2 Solver Settings 105
5.7.1.3 Pre-processing Settings 106
5.7.2 Settings of the Transient Simulations 107
5.7.2.1 Numerical Schemes 108
5.7.2.2 Solver Settings 108
5.7.2.3 Pre-processing Settings 110

5.7.2.4 Post-processing Settings 110
5.8 Verification of Eddy Resolving Simulations 112
6 RESULTS AND DISCUSSIONS 115
6.1 Results Obtained From Nasal Geometry 116
6.1.1 Surface Area Through the Nasal Geometry 116
6.1.2 Cross-Sectional Area Through the Nasal Geometry 118
6.1.3 Volume of The Nasal Geometry 121
6.2 Results Obtained From Numerical Simulations 121
6.2.1 Pressure Results 124
6.2.1.1 Restful Inhalation's Pressure Results 124
6.2.1.2 Quick Inhalation's Pressure Results 127
6.2.2 Discharge Rates 129
6.2.2.1 Restful Inhalation's Discharge Results 131
6.2.2.2 Quick Inhalation's Discharge Results 132
6.2.3 Wall Shear Stresses 133
6.2.3.1 Restful Inhalation's Wall Shear Stresses 134
6.2.3.2 Quick Inhalation's Wall Shear Stresses 135
6.2.4 Nasal Resistances 136
6.2.4.1 Restful Inhalation's Nasal Resistance Results 137
6.2.4.2 Quick Inhalation's Nasal Resistance Results 137
6.2.5 Turbulent Kinetic Energy 138
6.2.5.1 Restful Inhalation's Turbulent Kinetic Energy Results 138
6.2.5.2 Quick Inhalation's Turbulent Kinetic Energy Results . 140

6.2.6 Localized Discharge Rates 141
6.2.6.1 Restful Inhalation's Localized Discharge Results . . . 142
6.2.6.2 Quick Inhalation's Localized Discharge Results 143
6.2.7 Investigation of Localized Wall Shear Stresses 144
6.2.7.1 Restful Inhalation's Local Shear Stresses 144
6.2.7.2 Quick Inhalation's Local Wall Shear Stresses 146
6.2.8 Energy Spectral of Numerical Simulations 148
6.2.8.1 Restful Inhalation's Energy Spectral Density 150
6.2.8.2 Quick Inhalation's Energy Spectral Density 150
6.3 Verification of Numerical Simulations 152
6.3.1 Verification of Grid Resolution 153
6.3.1.1 Restful Inhalation's Grid Resolution 153
6.3.1.2 Quick Inhalation's Grid Resolution 154
6.3.2 Verification of Time Resolution 155
6.3.2.1 Restful Inhalation's Time Resolution 155
6.3.2.2 Quick Inhalation's Time Resolution 156
6.4 Validation of Numerical Simulations 156
7 CONCLUSIONS 159
7.1 Future Work 161
BIBLIOGRAPHY 163
APPENDICES
A MISCELLANEOUS FLUID MECHANICS BACKGROUND 181

A.1 Fluid Mechanics Preliminaries 181

A.1.1 Descriptions of Motion 181

A.1.2 Mappings Between Lagrangian and Eulerian Settings 181

A.1.3 Derivative of the Determinant of a Second Order Tensor by Itself 183

A.1.4 Leibniz Integral Rule 185

A.1.5 Material Derivative of Determinant of the Deformation Gradient Tensor 185

A.2 Fundamental Principles and Governing Equations for Fluid Mechanics 187

A.2.1 Conservation of Mass 187

A.2.2 Incompressible Conservation of Mass Equation 189

A.2.3 Newton's Second Law of Motion 190

A.2.4 Cauchy Momentum Equations 193

A.3 Generalization of Newtonian Law of Viscosity 197

A.3.1 Incompressible Generalized Law of Viscosity 201

A.3.2 Compressible Generalized Law of Viscosity 201

A.3.3 Navier-Stokes Equations 204

A.3.4 Incompressible Navier-Stokes Equations 205

A.3.5 Compressible Navier-Stokes Equations 206

A.4 Turbulence Modeling 207

A.4.1 Reynolds Decomposition and Reynolds Averaging 207

A.4.2 Reynolds Averaged Incompressible Conservation of Mass Equation 210

A.4.3 Incompressible Reynolds Averaged Navier-Stokes Equations 212

A.4.4 Incompressible Unsteady Reynolds Averaged Navier-Stokes Equations 216

A.4.5 Generalization of Eddy Viscosity Approximation 217

LIST OF TABLES

TABLES

Table 2.1 Prevalence of Septal Deviation in Humans per Ethnic Group . . . 13

Table 2.2 Cost of Endoscopic Nasal Polyps Surgeries 17

Table 5.1 Cell Type Distribution in Pre-Surgery Mesh 91

Table 5.2 Pre-Surgery Mesh Quality Parameters 92

Table 5.3 Distribution of the Cell Types in Post-Surgery Mesh 93

Table 5.4 Post-Surgery Mesh Quality Parameters 94

Table 5.5 Turbulence Intensities for Restful Inhalation 97

Table 5.6 Boundary Conditions For All the Patches 99

Table 5.7 Numbers of Flow Through Time for Numerical Simulations of Pre-Surgery State 112

Table 5.8 Numbers of Flow Through Time for Numerical Simulations of Post-Surgery State 112

Table 6.1 Pressure Values: Both Cavity Averaged 126

Table 6.2 Pressures for Singular Cavities 127

Table 6.3 Pressures for Quick Inhalation 128

Table 6.4 Discharge Values in Nasal Passageways: Restful Breathing 131

Table 6.5 Discharge Values in Nasal Passageways: Quick Breathing 132

Table 6.6 Nasal Resistance Values of Restful Inhalation 137

Table 6.7 Nasal Resistance Values of Quick Inhalation 138

Table 6.8 Normal Inhalation's Localized Flow Parameters in the 11^{th} Slice . 142

Table 6.9 Quick Inhalation's Localized Flow Parameters in the 11^{th} Slice . . 143

Table 6.10 Restful Inhalation's Localized Wall Shear Stress Values 146

Table 6.11 Quick Inhalation's Localized Wall Shear Stress Values 148

Table 6.12 Pressure Values for Averaged Cavities Against Literature 157

LIST OF FIGURES

FIGURES

Figure 2.1 Anatomical Planes Depicted on a Human Body 5

Figure 2.2 Sagittal View of Human Respiratory System 7

Figure 2.3 Sagital Anatomical View of Human Nasal Cavity 8

Figure 2.4 Computed Tomography Scan of an Individual with Septal Deviation 12

Figure 2.5 Drawing of Sinus Infection or Sinusitis 15

Figure 2.6 Sketches of Anterior and Posterior Rhinomanometry 19

Figure 2.7 Hypothetical Result of a Anterior Rhinomanometry 20

Figure 2.8 Hypothetical Result of Acoustic Rhinometry 21

Figure 2.9 Computed Tomography Scan of a Human Head 24

Figure 2.10 Spectrum of Hounsfield Scale 25

Figure 2.11 Magnetic Resonance Image of a Human Head 27

Figure 4.1 Top-Hat or Box Function on a 2D Plane 57

Figure 5.1 Demonstration of *3D Slicer*'s Volume Rendering Module . . . 75

Figure 5.2 Radiodensity Threshold for Air in *3D Slicer* 76

Figure 5.3 *3D Slicer*'s Export Menu After All Steps Completed 77

Figure 5.4 The Surface Mesh After Trimming Extra Walls 78

Figure 5.5 The End Result After Adding Inlet and Outlet 81

Figure 5.6 Refinement Process for a 2D Mesh 83

Figure 5.7 Castellation Example for a 2D Mesh 84

Figure 5.8 Pre- and Post-Surgery Mesh Result After Castellation Step . . 85

Figure 5.9 Snapping of the Refined Surface in 2D 86

Figure 5.10 Pre- and Post-Surgery Mesh After Snapping Step 87

Figure 5.11 Addition of a Single Layer to the Snapped Surface in 2D . . . 88

Figure 5.12 Pre- and Post-Surgery Meshes After Adding Boundary Layers 89

Figure 5.13 Frontal View of Sliced Pre-Surgery Mesh 90

Figure 5.14 Side View of Sliced Pre-Surgery Mesh 90

Figure 5.15 View of Complete Pre-Surgery Volumetric Mesh 91

Figure 6.1 15 Slices Used Throughout the Results for Pre-Surgery (Left) and Post-Surgery (Right) 115

Figure 6.2 Total Surface Area Through the Cavities 117

Figure 6.3 Total Surface Area Profile of Both Cavities 118

Figure 6.4 Left Passageway's Surface Area Profiles 118

Figure 6.5 Right Passageway's Surface Area Profiles 119

Figure 6.6 Cross-Sectional Area Profiles of Nasal Geometries 120

Figure 6.7 Cross-Sectional Area Profiles of Right Passageway Geometries 120

Figure 6.8 Cross-Sectional Area Profiles of Left Passageway Geometries . 121

Figure 6.9 Total Volume of Nasal Cavity 122

Figure 6.10 Streamlines for Pre-Surgery (Left) and Post-Surgery (Right): Slow Inhalation 122

Figure 6.11 Streamlines for Pre-Surgery (Left) and Post-Surgery (Right): Quick Inhalation 123

Figure 6.12 Vorticity of the 11th Slice for Pre-Surgery (Left) and Post-Surgery (Right): Restful State 123

Figure 6.13 Vorticity of the 11th Slice for Pre-Surgery (Left) and Post-Surgery (Right): Quick State 124

Figure 6.14 Restful Inhalation's Pressure Drop Profile Nostril to Throat: Both Cavities Averaged 125

Figure 6.15 Pressures of the 11th Slice for Pre-Surgery (Left) and Post-Surgery (Right): Restful State 128

Figure 6.16 Quick Inhalation's Pressure Drop Profile Nostril to Throat: Both Cavities Averaged 129

Figure 6.17 Pressures of the 11th Slice for Pre-Surgery (Left) and Post-Surgery (Right): Quick State 130

Figure 6.18 Restful Inhalation's Velocity Magnitudes in All Slices for Pre-Surgery (Left) and Post-Surgery (Right) 130

Figure 6.19 Quick Inhalation's Velocity Magnitudes in All Slices for Pre-Surgery (Left) and Post-Surgery (Right) 131

Figure 6.20 Velocity Magnitudes of the 11th Slice for Pre-Surgery (Left) and Post-Surgery (Right): Restful State 132

Figure 6.21 Velocity Magnitudes of the 11th Slice for Pre-Surgery (Left) and Post-Surgery (Right): Quick State 133

Figure 6.22 Wall Shear Stress Profiles: Restful Inhalation 134

Figure 6.23 Wall Shear Force Profiles: Restful Inhalation 135

Figure 6.24 Wall Shear Stress Profiles: Quick Inhalation 136

Figure 6.25 Wall Shear Force Profiles: Quick Inhalation 136

Figure 6.26 Turbulent Kinetic Energy Profile: Restful Inhalation 139

Figure 6.27 Turbulent Kinetic Energy Profile: Quick Inhalation 140

Figure 6.28 Sectioned Pre- and Post-Surgery Shape of the 11^{th} Slice 141

Figure 6.29 Wall Shear Stress Values for Pre-Surgery (Left) and Post-Surgery (Right): Restful Inhalation 145

Figure 6.30 Wall Shear Stress Values for Pre-Surgery (Left) and Post-Surgery (Right): Quick Inhalation 147

Figure 6.31 Locations of the Tracked Fluctuations in the 11^{th} Slice 149

Figure 6.32 ESD Profile of the 11^{th} Slice's Left Middle: Restful State . . . 150

Figure 6.33 ESD Profile of the 11^{th} Slice's Right Bottom: Restful State . . 151

Figure 6.34 ESD Profile of the 11^{th} Slice's Left Middle: Quick State 152

Figure 6.35 ESD Profile of the 11^{th} Slice's Right Bottom: Quick State . . . 152

Figure 6.36 Kolmogorov Length Based Celik Index of the 11^{th} Slice for Pre-Surgery (Left) and Post-Surgery (Right): Restful State 154

Figure 6.37 Kolmogorov Length Based Celik Index of the 11^{th} Slice for Pre-Surgery (Left) and Post-Surgery (Right): Quick State 155

Figure A.1 Cauchy Stress Tensor on a Differential Element 194

Figure A.2 Cauchy Stress Tensor on a Differential Element 195

Figure A.3 A Stationary Time Series of Velocity Evolution 208

Figure A.4 A Non-Stationary Time Series of Velocity Evolution 216

LIST OF ABBREVIATIONS

ABBREVIATIONS

2D	2 Dimensional
3D	3 Dimensional
CFD	Computational Fluid Dynamics
CFL	Courant-Friedrichs-Lewy
CPU	Central Processing Unit
CSA	Cross-Sectional Area
CT	Computed Tomography
DES	Detached Eddy Simulation
DILU	Diagonal-Based Incomplete Lower Upper
DNS	Direct Numerical Simulation
ENS	Empty Nose Syndrome
ESD	Energy Spectral Density
FOSS	Free and Open-Source Software
GAMG	Geometric-Agglomerated Algebraic Multi-Grid
GPU	Graphics Processing Unit
LES	Large Eddy Simulation
MCA	Minimum Cross-Sectional Area
MRI	Magnetic Resonance Imaging
PBiCGStab	Preconditioned Bi-Conjugate Gradient Stabilized
PDE	Partial Differential Equation
PISO	Pressure-Implicit with Splitting of Operators

RANS	Reynolds-Averaged Navier-Stokes
SGS	Sub-Grid Scale
SIMPLEC	Semi-Implicit Method for Pressure Linked Equations-Consistent
SIMPLE	Semi-Implicit Method for Pressure Linked Equations
SA	Surface Area
SST	Shear Stress Transport
TKE	Turbulent Kinetic Energy
URANS	Unsteady Reynolds-Averaged Navier-Stokes
WALE	Wall-Adapting Local Eddy-Viscosity
WMLES	Wall-Modeled Large Eddy Simulation
WSS	Wall Shear Stress

CHAPTER 1

INTRODUCTION

1.1 Background

The human nasal airway is a convoluted piping system that evolved in order to perform a magnitude of functions beyond simple air transportation efficiently. These maze-like passages are separated by the nasal septum, starting from the nostrils. Later on, the surface area of the nasal cavity is greatly increased by the presence of the turbinates. While the turbinates enhance the effectiveness of the functions of the nasal cavity, e.g., filtering, cleaning, warming, and smelling of nasal airways, the turbinates also magnify the intricacy of the nasal passages.

In addition to the complexity of the geometric structure, the structure of a nasal cavity varies based on factors like time, individual state, and intra-individual differences. This variety suggests that not only do anatomical variations exist between individuals, but the geometry of nasal passages also undergo changes depending on time and body position. Furthermore, the minuscule size and internal placement within the body extend the sophistication of the nasal cavity. These reasons bring extreme challenges to the studies and experiments on the nasal airways, making the reliable and accurate investigation of the nasal airways a problematic process.

With the rise of computers, newer research techniques become popular, and they are also preferred over traditional methods for nasal airflow academic work. The reasons are multitudinous. Initially, the generation of nasal airway images became readily obtainable. Researchers may generate replicas using magnetic resonance imaging and computer-assisted tomography scans. These imaging techniques revolutionize the

research process by allowing researchers to shift conducting to in vitro [1] experiments, avoiding the in vivo [2] and ex vivo [3] experiments, which are limiting by their nature. Later, the processing power up-shift allows scientists to perform in silico[4] experiments such as numerical simulations. This way, the detail in results soared, and newer techniques like virtual surgery appeared, easing the hardship from the complexities of the nasal passageways.

Computational fluid dynamics is a branch of fluid mechanics that generally refers to computerized numerical simulations. This technique exploits computers to solve enormous matrices that describe fluid flow equations in a bounded geometry. To obtain the description of flow, various mathematical models, algorithms, and computer programs have been developed throughout history. Since numerical simulations heavily rely on computers to solve the system of equations, hardware improvements expand the limits for the most extensive and complicated simulations. Additionally, this advancement eliminates the direct dependency on supercomputers. Therefore, nowadays, CFD gets a broader range of usage in research and development.

1.2 Motivation

The first notion behind conducting this thesis to obtain detailed results to explain nasal airflow characteristics. To do this, numerical simulations are used, since the numerical simulations reveal a great deal of detailed information about physical phenomena. Numerical simulations have further advantages for fluid mechanics, such as cheaper, faster, and more convenient results than traditional methods, though verification of the results is needed. Some characteristics obtained by a numerical simulation are airflow patterns, velocity distributions, pressure drops, and wall shear stresses. For the nasal airflow, this kind of information reveals various unknowns: the natural functionality of the nasal cavity, reasoning of the sicknesses, possible reliefs, and remedies to the sicknesses. Numerical methods may also simulate external actors such as drug delivery, particle transportation, and disease spread through breathing.

[1] In glass experiments conducted outside living bodies.
[2] The kind of experimentation done within the living bodies.
[3] The type of biological experimentation conducted in or on tissue outside of the organisms.
[4] Computerized experiments or computer simulations.

Furthermore, the current behavior of the nasal airflow is misrepresented or ignored in the literature. The misrepresentation of nasal airflow primarily arises during traditional research, mainly due to the tiny size and internal location of the airways. Such hardships render traditional measurement devices to fail to extract data. Secondly, ignorance during the nasal airflow research appear during numerical simulations. For example, the localized and transitional turbulence in the nasal cavity are generally ignored. Commonly, the local turbulence is represented by using a fully turbulent model; whereas, others ignore turbulence's effects due to belief in its mild levels and unimportant effects. Nonetheless, one may claim that the turbulence exists at in a transitional or local state in the nasal cavity. Neither fully turbulent nor laminar flow can represent this state. Thus, this research aims to address misrepresentations and gaps through the application of appropriate methods.

Lastly, despite the extensive research and simulation, most of these studies are limited by the usage of proprietary software and the need for detailed explanations of steps. These two factors restrict the application of the CFD in a clinic or hospital environment to diagnosing and treating sicknesses. Following this approach, this work solely uses free and open-source software; These software applications are namely, *OpenFOAM*, *Blender*, *Paraview*, and *cfMesh*. Using such software promotes one of the critical aspects of academic work: reproducibility.

All in all, the motivation behind this study comes from the clinical and research importance of nasal airflow, the exciting physics that arises during the nasal airflow, and the requirement of detailed information regarding nasal airflow simulation in literature.

1.3 The Outline of the Thesis

This thesis deals with nasal airflow simulations of two geometries generated from the same male patient. These geometries represent the ill and the after-surgery states. The patient appears to have a visible nasal deviation; therefore, the surgery has to solve the deviation. Moreover, sinus entrances are enlarged, and the turbinates of the patient are downsized. The two further operations are required and decided by the doctor.

Ultimately, the patient underwent three different surgeries: septoplasty, turbinoplasty, and endoscopic sinus surgery.

Two different airflow speeds, restful and quick breathing, are selected for the numerical airflow simulations. This thesis simulates the inhalation part of the breathing process because the nasal obstruction during inhalation is the more prominent than exhalation. Moreover, the inhalation state assumes a quasi-steady behavior and uses the PISO algorithm to solve the system of equations. The turbulence is modeled by resolving the large eddies and modeling the small eddies. To generate the geometry, the extraction of the air-related parts is achieved using CT scans. A further modification is done by removing the sinuses and error-prone areas from the surface mesh. Then, this surface is extended in the outlet and inlet so that the imposed boundaries do not affect the internal airflow characteristics. A volumetric mesh is generated with high-quality parameters using the surface mesh. Ultimately, a steady simulation is conducted to generate the initial solution for quasi-steady simulation, and then the quasi-steady simulation is done.

The results obtained in this thesis are investigated in various ways in order to provide great insight into nasal airflow changes. First, the geometrical characteristics, such as surface area, cross-sectional area, and total volume, are given. Later, the numerical simulation's results are represented: pressure drop results, discharge and velocity profiles, nasal resistance values, turbulent kinetic energy development, localized discharge and wall shear stress investigations, and energy spectral profiles of turbulence fluctuations. Then, verifications of the LES for grid resolution and time resolution are shown. Lastly, validation of the simulations are done by comparing results with literature.

CHAPTER 2

BIOLOGICAL BACKGROUND

2.1 Biological Overview

In the thesis, some specific terms are used to describe some parts of the body. The hypothetical planes, called anatomical planes, are defined in order to describe locations within the body. As one may visualize in Figure 2.1, there are three commonly referred planes: sagittal, coronal, and transverse.

Moreover, in this thesis the terms anterior, posterior, superior, and inferior and middle are used. The word anterior refers to a structure near the frontal side of the body. The word posterior refers to a structure closer to the rear side of the body. The words superior, middle, and inferior are used to refer to positions that are located above, at the midline, and below, respectively.

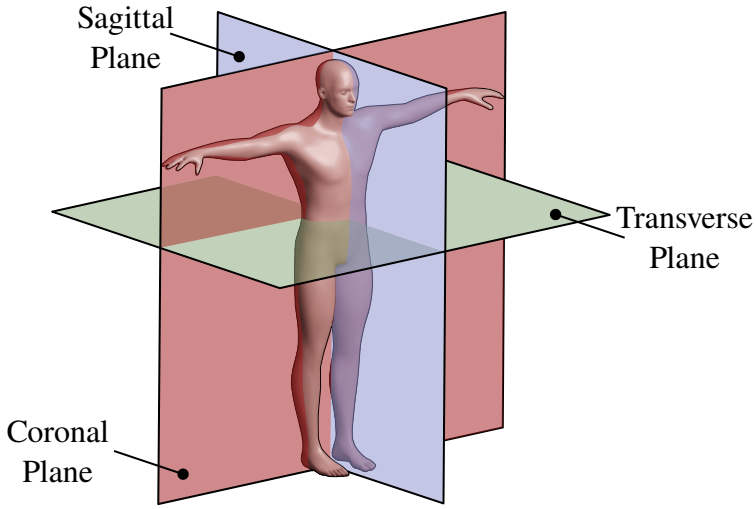

Figure 2.1. Anatomical Planes Depicted on a Human Body

2.2 Respiratory Tract

The human respiratory system is vital for a human since it enables the rhythmical breathing process. Even though this system is remarkably complex, it is a series of two connected pipes. This system allows the air to travel to the air pockets called alveoli in the lungs. During the transportation, the air undergoes warming, humidification, and cleansing to reach the lungs safely. At the lungs, through the interaction between the capillary blood vessels and the alveolar sacs, oxygen is absorbed into the blood, and carbon dioxide is released into the inhaled air.

As demonstrated in Figure 2.2, the respiratory tract is typically fragmented into two main sections about their respective functionalities: the upper and lower respiratory tract. The upper respiratory tract is divided into smaller components: nasal cavity, pharynx, and larynx. The nasal cavity is the initial air passageway where the air gets heated, mixed, warmed, and humidified; additionally, the smelling process happens here. The pharynx serves as a junction point between nasal and oral passageways. This subdivision has a switch-like role: it selectively allows food and liquids or air to continue down. The larynx, also known as the voice box, is the last section of the upper respiratory system. Its prominent role is to produce sound; hence, it enables the ability to speak.

On the other hand, the lower respiratory tract envelops the trachea, bronchi, and lungs. The trachea is a conduit connecting the upper respiratory to the bronchi. The bronchi within the lungs are the branching pathways distributing inhaled air to every part of the lungs. The terminal structures within the respiratory system, the lungs, are responsible for absorbing oxygen into the bloodstream and releasing carbon dioxide into the air through the alveolar clusters.

2.3 Nasal Cavity

The primary role of the nasal cavity is to carry the air to the lower parts of the respiratory tract. It is lined with blood vessels and a mucous fluid layer with hairlike units to provide numerous minor functions. These minor functions are listed and

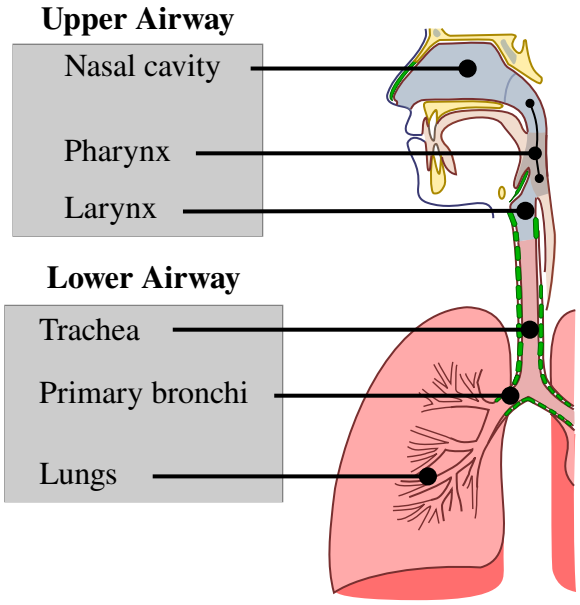

Figure 2.2. Sagittal View of Human Respiratory System

Note. Reprinted from "Conducting passages of the human respiratory system", Akryl, Lord and Jmarchn, 2010, Public Domain.

explained as follows:

- The heating of the inhaled air before it reaches the visceral organs. This functionality prevents change in the human body's internal temperature. The lack of the heating function may cause several complications in the respiratory system. If cold air is breathed into the lower respiratory system, for a healthy individual, spasms in the bronchi would appear. Moreover, inhalation of cold air may trigger asthma and other chronic obstructive pulmonary diseases in people with pre-existing health issues (D'Amato et al., 2018).

- Filtration of the air happens during the transportation process in the nasal cavity. This functionality traps inhaled particles such as dust and pollen in the mucosal layer. Additionally, filtration provides a defense mechanism to sicknesses and harmful actors. Darquenne and Prisk (2004) notes that most of the particles larger than 5 µm are filtered in the nasal cavity. Furthermore, higher flow rates amplify the amount of turbulence in the flow, thus the filtering rate for particles

smaller than 5 µm gets increased through turbulent mixing.

- The inhaled air is humidified by the nasal cavity before continuing to lower respiratory system. This functionality prevents damaging and drying the internal organs by introducing dry air.

- The sensory nerves are exposed to inhaled air to provide a smelling sensation in the olfactory region of the nasal cavity. Hahn et al. (1993)'s experiments demonstrated that only a fraction of the inhaled air, around 14 %, passes by the olfactory region during low, medium, and high breathing rates. Despite this, the nasal cavity's geometry introduces turbulence and recirculation of air in this region, which heavily augments the degree of stimulation of the olfactory nerves (Li, Jiang, et al., 2017; Quadrio et al., 2016).

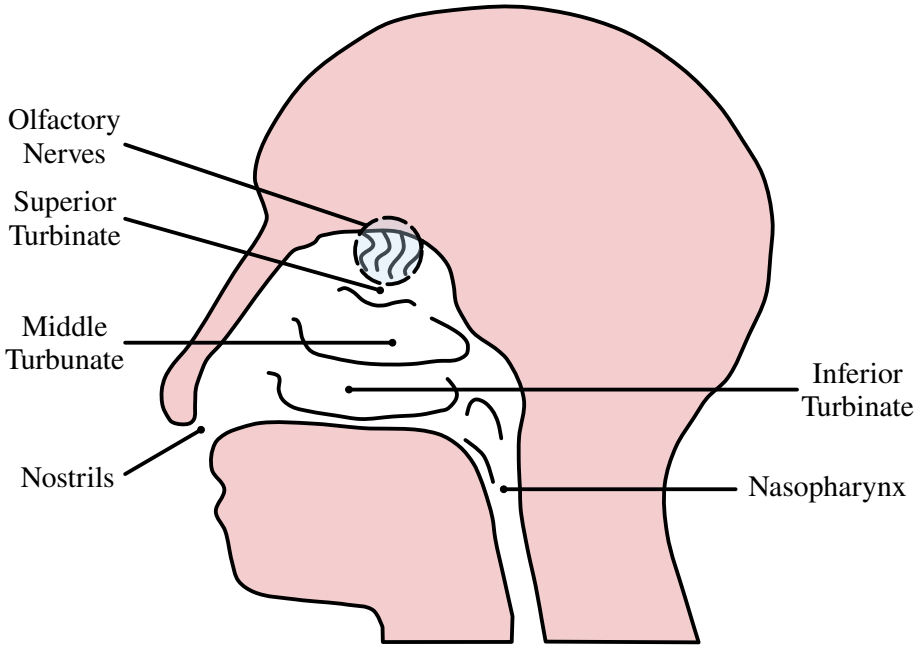

Figure 2.3. Sagital Anatomical View of Human Nasal Cavity

Note. Adapted from "Tailoring Formulations for Intranasal Nose-to-Brain Delivery: A Review on Architecture, Physico-Chemical Characteristics and Mucociliary Clearance of the Nasal Olfactory Mucosa", Gänger, Stella and Schindowski, Katharina, 2018, *Pharmaceutics*, *10* (3), p. 2. CC BY.

In order to provide the critical functionalities, the nasal cavity has evolved in a specific way: The surface area of the nasal cavity is enormous compared to its volume, and the cross-section normal to airflow is highly non-uniform. The large surface area provides an efficient heating, humidification, and filtration ratio. The non-uniformity exists to incentivize mixing to fortify the aforementioned minor functionalities. These characteristics mainly appear due to three turbinates or conchae in the nasal cavity: superior, middle, and inferior. Figure 2.3 represents the turbinates and other essential structures.

2.4 Nasal Sicknesses and Surgeries

Out of the six respiratory system components, the nasal cavity is especially vulnerable to a wide range of external and internal complications and dysfunctions. The potential reasons for the variety of sicknesses and proneness of the nasal cavity are:

- Direct exposure to cold, dry, pathogenic, and allergenic air creates a dangerous environment.
- Proximity to the surrounding environment coupled with the lack of adequate protection are critical weaknesses.
- Numerous disease-causing genetic variations exists in the human genes.
- Convoluted geometric structure allows pathogens to easily accumulate and reproduce.

In addition to the above vulnerabilities, even minor nasal cavity disruptions might cause various persistent symptoms and disturbances for individuals. The symptoms related to nasal cavity sicknesses could be listed as:

- nasal congestion
- nasal discharge
- sneezing

- snoring
- trouble falling asleep
- facial pain and pressure
- headache

The presence of the symptoms, as mentioned above, drastically diminishes an individual's life satisfaction. Furthermore, infections caused by pathological illnesses are airborne, so their spread rate is very high. As an example, according to the data set published by National Center for Health Statistics (2015–2018), 12 % of the United States population was affected by sinusitis. These statistical findings place sinusitis, which is only one of the nasal sicknesses, among the most common health issues globally (National Center for Health Statistics, 2015–2018). The widespread of nasal sicknesses is bound to grow when other nasal congestion complexities are counted. Noting that most of these nasal complications tend to lead to more critical illnesses if left untreated, thus they are sought to be remedied swiftly by patients and doctors.

The variety of malignant actors causes numerous sicknesses in the nasal cavity. Among them, the most reported symptoms among all the patients include reduced airflow (Naclerio et al., 2010). The reduced airflow symptom is also named nasal congestion or nasal obstruction. There are many possible reasons causing nasal congestion; nonetheless, the reasons are mainly divided into anatomical deformations and inflammation-related problems. Although standard medications may treat congestion, the obstruction may often be chronic or prove unresponsive to pharmaceutical treatments. For example, according to DeConde et al. (2014)'s survey, treating chronic rhino-sinusitis through surgery is 2 to 3 times more effective than medical treatments. Such a result means that doctors and ex-patients may also suggest surgical operations due to the definitive resolution over treatments with medication. Therefore, these results boost the interest and popularity of surgical interceptions for congestion-related sicknesses.

Generally, the severity of the nasal obstruction dictates the surgery requirement to relieve patients. Even though there is not an established way to treat obstruction, surgical operations statistically show promising results with a small percentage of

negative results (Datta et al., 2018; Mathai, 2004; Santosh & Rao, 2013). Critically, various surgical procedures exist, and surgeons must exercise sound judgment, possess sufficient experience, and utilize appropriate equipment to ensure satisfactory outcomes (Chhabra & Houser, 2011). The surgeries' outcomes are difficult to predict, as nasal congestion is only occasionally directly linked to low flow rates or high-pressure drops in the system. The human body perceives the obstruction by stimulating nasal receptors in the nasal tissues, i.e., wall shear stresses and heat transfers.

2.4.1 Septal Deviation

Septal deviation is the structural crookedness of the nasal septum; Figure 2.4, a computed tomography scan of this complexity, represents septal deviation. Individuals with this deformity have an unsymmetrical or offset division between the left and right airways. This complication disrupts the airflow patterns, rendering one nasal airway smaller. When combined with the nasal cycle's effect, septal deformity disallows individuals to breathe through their noses (Metson, 2005). The symptoms of a nasal septum deviation are nasal congestion, snoring, sleep apnea, nose bleeding, facial pain, headache, preference to sleep on a specific side, and awareness of the nasal cycle.

The septal deviation is a prevalent sickness: It has been seen in 79 % of adult humans and 58 % of infants, and even in some primates by 37 % (L. P. Gray, 1978). However, despite the high prevalence of septal deviation, often, it does not reduce life quality if the degree of deviation is small (Metson, 2005).

The exact reason for the septal deviation is uncertain. However, research suggests reasons generally include pressures on baby during pregnancy (L. P. Gray, 1978; L. P. Gray, 1980), forces exerted on newborn as it is delivered (L. P. Gray, 1978; L. P. Gray, 1980; Harugop et al., 2012), developmental causes (L. P. Gray, 1978; L. P. Gray, 1980), and trauma on individual's faces (L. P. Gray, 1978; L. P. Gray, 1980; Sooknundun et al., 1986). Furthermore, the infant's weight during birth and the number of births given by the mother affect deviation chances (Harugop et al., 2012).

L. P. Gray (1978) conducted data analyses to gain insight into nasal septum abnormalities. They collected data from adult human skulls, infants, and mammals in

Figure 2.4. Computed Tomography Scan of an Individual with Septal Deviation

Note. This image shows the computed tomography scan of an individual in two planes. On the left, the transverse plane is given, similar to the top view; on the right, the coronal plane is given, which appears like a view from the front.

their research work. 79 % of adults, 58 % of infants, 37 % of great apes[1], and none of non-primate mammals[2] had deviated septum. Among the adults, the deviation rates differed by the ethical groups, as shown in Table 2.1. It is shown that the Aboriginal Australian skulls had the least deformed nasal septum, followed by the African skulls.

Additionally, the Aboriginal and African skulls were thicker than the others. It is critical to note that Aboriginal Australian skulls were from the uncontacted peoples[3]. This note suggests that nasal septum deviation may not only differ due to genetic differences but also due to lifestyle choices. Besides, the high prevalence among infants proposes that septal deviation happens before childhood. Thus, individuals may require medical attention soon after the birth.

[1] Refers to non-human hominids: gorillas, orangutans, chimpanzees, and bonobos.
[2] Animals like kangaroos, wild dogs, foxes, lions, cats, dogs, antelopes.
[3] Isolated communities separated from the outside world.

Table 2.1. Prevalence of Septal Deviation in Humans per Ethnic Group

Ethnicity	Skull count	Straight (%)	Deviated (%)	Kinked (%)
Aboriginal Australian	1009	27	38	35
African	227	20	30	50
Chinese	212	15	40	45
European	395	17	34	49
Indian	269	13	38	49
All combined	2112	21	37	42

Note. Adapted from "Deviated Nasal Septum Incidence and Etiology", Gray, Lindsay P., 1978, *Annals of Otology, Rhinology & Laryngology*, *87*(3), p. 6. Copyright 1978 by the SAGE Publications.

2.4.1.1 Septal Deviation Remedies

Nasal deviation is diagnosed and treated differently based on the age group of the individuals. Commonly, practitioners seek immediate diagnosis and correction of septal deviation in infancy. The seek of quick diagnosis and remedy is due to three reasons: more accessible remediation, lack of healing process if left alone, and prevention of worsening of conditions (Sooknundun et al., 1986).

In order to diagnose nasal deviation in infants, two marked struts are gently pushed from the nostrils. If marks can not reach deep enough and the struts are not located in a parallel neat manner, a septal deviation exists. If deviation is found, quick and easy procedures without anesthesia are done, for example, the one shown by L. Gray (1965).

On the other hand, some people get septal deviation in the later stages of their lives or grow up with it. Notably, connective tissue gets loose, and deviation gets more severe with age (Metson, 2005). Therefore, individuals seek remedies for their deviated septa. Diagnosis is commonly made through a visual examination using tools; further CT scans might be used for a detailed analysis, especially if surgeries are a

topic of discussion. Initially, treatment is done through drugs such as decongestants, antihistamines, and steroid sprays; if drugs fail to solve surgeries, such as septoplasty, follows (Mayo Clinic, 2021).

2.4.2 Sinusitis

One of the most widespread illnesses related to the upper airways is sinusitis. It generally results in swelling and fluid deposition in the sinuses due to a pathogen. The resulting outlook is given in Figure 2.5 where left sinuses are filled up with nasal fluid. The sickness often causes nasal congestion, facial pain, runny nose, and headache. Commonly, treatment is firstly sought to be treated by drugs. Before surgery, the patients undergo extensive medical treatment to avoid misdiagnoses and due to medical treatment's ease of application (Bhattacharyya, 2003). The medical remedies against sinusitis include medical pills, nasal sprays, nasal nebulizers, and nasal irrigation techniques. These remedies aim to help fight the pathogen and try to ease the symptoms of the sickness. Ultimately, if the medication can not provide enough relief, surgeries are done. These surgeries aim to either help the drainage of the sinusoidal infection or increase drug delivery rates to the sinuses. These can be done by manually draining the liquid, enlarging the sinus openings, or increasing air conditioning levels.

Sinusitis has a devastating blow on the economic standings of the patients. As in one of the highly developed countries, the United States, more than 10 % of the population gets sinusitis every year (National Center for Health Statistics, 2015–2018). Furthermore, according to Bhattacharyya (2003)'s findings, the cost for chronic sinusitis per patient in 2003 was $1539. These numbers would end up that, roughly, the cost in the United States of America would be $95.6 billion to provide medical attention to fight sinusitis in 2024.

2.4.2.1 Sinusitis Remedies

At this point, the advantage of computational fluid dynamics in remedying sinus-related illnesses is not apparent. Expectedly, one may question how the airflow simulation could help with sinusoidal drainage. After a second thought, one would realize that

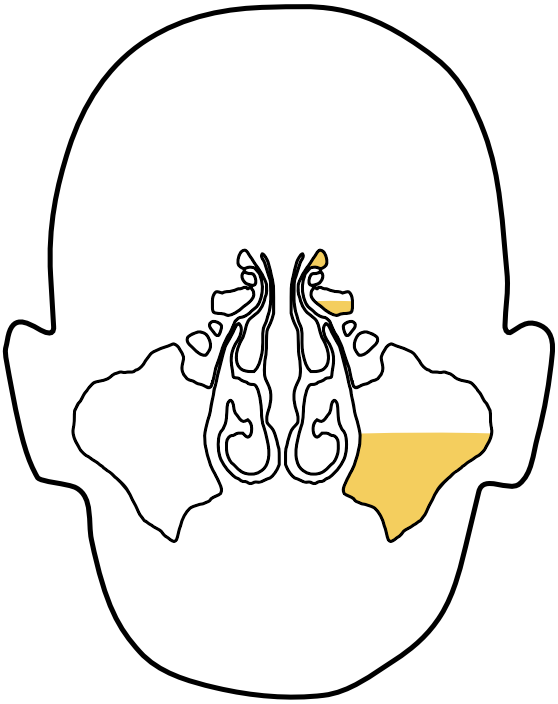

Figure 2.5. Drawing of Sinus Infection or Sinusitis

Note. The coronal cross-section of the nasal cavity is given together with the outline of the human head. The yellow-colored fluid puddles correspond to the deposition of nasal fluid in the nasal sinuses due to sinus infection.

CFD simulations could improve all the mentioned solution techniques. With the help of numerical simulations, optimizing topical medication delivery methods, nasal irrigation techniques, and surgical operations outcomes is possible.

The first topic is the simulation of drug delivery methods through CFD. These simulations easily yield detailed information on where the inhaled drug is transported. Furthermore, unlike other techniques, these simulations allow optimization of various variables such as particle size, particle velocity, spray nozzle size, and spray insertion angle (Singh & Inthavong, 2021). Therefore, drug delivery systems can be engineered to minimize undesirable effects and maximize the desirable ones.

Similar to drug delivery simulations, nasal irrigation methods can be improved to provide better coverage during sinus rinsing. Since CFD simulations yield very detailed

results, researchers are able to obtain a greater insight into the working mechanism. Also, they can perform heuristic variable analyses for nasal rinses to find out:

- the optimal body position
- the best amount of saline solutions
- the correct way of application of the saline liquids

Lastly, the researchers may exploit CFD simulations by doing geometrical alterations to foresee the outcomes of sinusoidal surgeries. These surgeries aim to increase the natural opening of one or more of the maxillary, ethmoid, frontal, and sphenoid sinuses (Pynnonen & Davis, 2014). Through preliminary CFD-based surgery, it is possible to decipher the most effective ways to increase:

- the amount of air transportation to the sinuses (increase in sinus air-conditioning)
- the amount of sinusoidal fluid drainage to the nasal cavity (reduction of fluid deposition in sinuses)
- post-operative drug delivery rates (improvement in the effectiveness of the drugs)

2.4.3 Nasal Polyps

Nasal polyps are the overgrown tissues appearing on nasal and paranasal structures. These droplet-like tissues are commonly seen in adults but found in any age group (Mayo Clinic, 2023). The polyps are considered tumors and categorized under benign nasal tumors. Additionally, nasal polyps are the most frequently found nasal and sinusoidal neoplasms; Belli et al. (2018)'s research findings support this by showing that among all the abnormally grown tissues, 81 % of them are nasal polyps.

If the polyps are few and small, they do not cause any reduction in life quality. Nevertheless, the symptoms arise if the number of polyps or their sizes are big enough. The symptoms of nasal polyps are headaches, face pain, nasal congestion, excessive nasal discharge, loss of smell or taste, and nosebleeds (Cleveland Clinic, 2021; Mayo Clinic, 2023). Further on, with the increased sizes of the nasal polyps, more severe

Table 2.2. Cost of Endoscopic Nasal Polyps Surgeries

	Without Complications (N=6011)	With Complications (N=102)
Cost of Only Surgery		
Mean	$14 604	$19 762
Median	$11 655	$16 380
Total Costs: Surgery and Medication		
Mean	$16 186	$27 406
Median	$13 101	$20 892

Note. Adapted from "Real-World Cost of Nasal Polyps Surgery and Risk of Major Complications in the United States: A Descriptive Retrospective Database Analysis", Ge, Wenzhen et al., 2022, *ClinicoEconomics and Outcomes Research*, *14*. p. 695. CC BY-NC.

symptoms are seen: increased asthma attack rate, frequent sinus infections, reduced sleep quality, and breathing problems (Cleveland Clinic, 2021).

2.4.3.1 Nasal Polyps Remedies

Commonly, the best way to scale down nasal polyps is steroids, which may be in either spray or pill form (Metson, 2005). A minimally invasive procedure called endoscopic nasal polyp surgery also exists if pharmaceutical treatments give no results. These surgeries have meager complication rates and appear safe and efficient. However, the economical cost of polyp surgeries could get very high: In Table 2.2, one may find the costs of endoscopic nasal polyp surgery by the work of Ge et al. (2022).

2.5 Methods to Investigate Nasal Cavity

The practitioners commonly use five main methods: rhinomanometry, acoustic rhinometry, nasal endoscopy, computed tomography scan, and magnetic resonance imaging technique. Multiple of these techniques may be used at the same time in order to determine the underlying issue in the patient; however, generally, they yield abundant enough information to be enough for the diagnosis.

2.5.1 Rhinomanometry

Rhinomanometry is an objective test that measures airflow and pressure drop throughout the nasal cavity during inspiration. Rhinomanometry is extensively utilized in research-oriented work (Jones et al., 1989; Juliá et al., 2011). However, this test finds lesser usage in clinical environments because of the relatively long time requirement and hardship of usage (Jones et al., 1989). Rhinomanometry is done before and after decongestion of nasal mucosa (Karbowski et al., 2023). If the results diverge from each other by a significant degree, the nasal obstruction could be attributed to swelling of the nasal tissues; hence, the possibility of having nasal structural anomalies eliminated.

There are two commonly performed types of rhinomanometry: anterior and posterior rhinomanometry, as their sketches in Figure 2.6. The anterior rhinomanometry generates a high-pressure zone in one of the nostrils, allowing the flow to exit from the other nostril. On the other hand, posterior rhinomanometry aims to detect the amount of airflow through both nostrils while recording the nasopharynx's pressure through the patient's mouth. Moreover, rhinomanometry either requires the patient to generate the flow, which is known as active rhinomanometry, or requires the patient to hold their breath to apply a pressure difference to generate the flow, which is called passive rhinomanometry (Juliá et al., 2011).

Passive rhinomanometry's measurements are considered unrealistic due to extreme flow rates (Naito et al., 2023). The unrealistic results of passive rhinomanometry leave only active rhinomanometry as a valid physiological measurement. Regardless, active rhinomanometry measurements heavily rely on patient collaboration. Patient's assistance further increases during posterior rhinomanometer measurements because

the pressure of the nasopharynx needs to be measured through the mouth (Friedman & Schalch, 2009). Therefore, it is clear that both of the rhinomanometry methods are unreliable or non-physiological.

Some researchers claim that even though rhinomanometry is widely used for research purposes, its cumbersomeness leads doctors to prefer to verbally ask patients about their symptoms or to prefer other tools (Jones et al., 1989). Also, there are mentions of a poor correlation between nasal obstruction feeling and rhinomanometry results (Jones et al., 1989). On the other hand, rhinomanometry is the closest technique to reproducing both inhalation and exhalation processes. Moreover, unlike zero flow-induced tests like acoustic rhinometry, reconstruction of shrinkage of the interior nasal passageways is possible due to pressure drop induced by the airflow. Therefore, compared to other in vivo methods, the objectivity and reality of rhinomanometry appear superior.

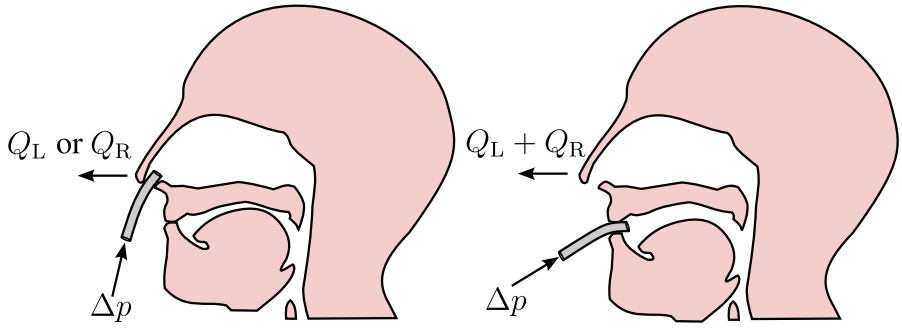

Figure 2.6. Sketches of Anterior and Posterior Rhinomanometry

Note. Left to right: anterior rhinomanometry and posterior rhinomanometry. On the left figure, pressure difference Δp applied to one nostril and either Q_{L} or Q_{R} flow obtained from the other nostril. On the right sketch, pressure difference, Δp measured when $Q_{\mathrm{L}} + Q_{\mathrm{R}}$ flow applied by the patient. Adapted from "Research Active Posterior Rhinomanometry Tomography Method for Nasal Breathing Determining Violations", Avrunin, Oleg G. et al., 2021, *Sensors*, *21* (24), p. 3. CC BY.

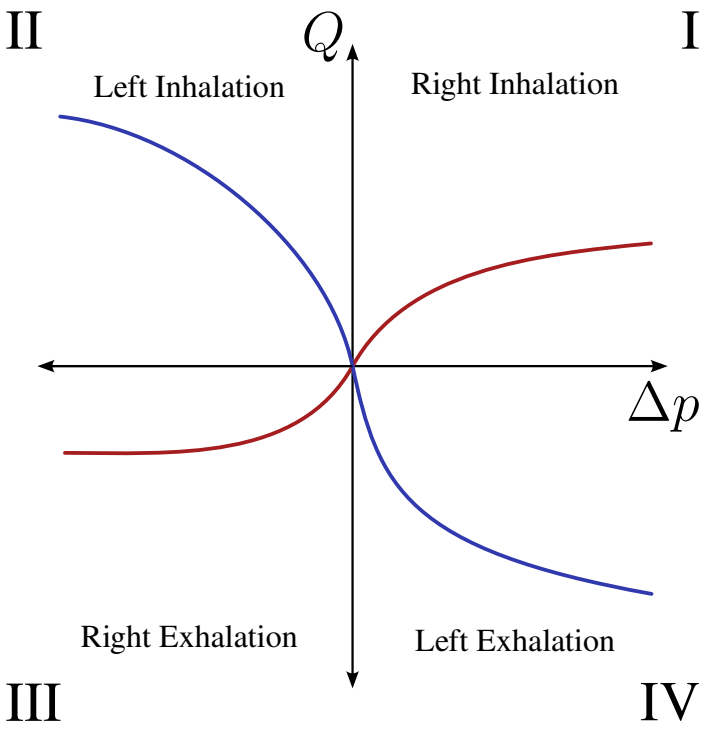

Figure 2.7. Hypothetical Result of a Anterior Rhinomanometry

Note. Quadrants I and III represent the right cavity during inhalation and exhalation. Similarly, quadrants II and IV represent the left cavity. From this hypothetical figure, one may argue that the right cavity is clogged due to a low flow rate, even if given high-pressure differences.

2.5.2 Acoustic Rhinometry

Acoustic rhinometry is a procedure used to measure the cross-sectional area of the nasal cavity. This method's working mechanism is based on generating sound waves and then measuring their reflections. These measurements are analyzed based on factors like reflection time, intensity, and pattern to estimate cross-sectional areas against distance (Nathan et al., 2005). Specifically, this method calculates the area separately for each nostril (Nathan et al., 2005) and as a function of distance through the center of the nasal cavity (Cakmak et al., 2005). These measurements are plotted as a graph, and three specific valleys appear as shown in Figure 2.8. These valleys are

traditionally named CSA1 to CSA3, corresponding to their respective cross-sectional areas. The first valley represents the nasal valve area, the second valley represents the start of the interior turbinate, and the last represents the start of the middle turbinate.

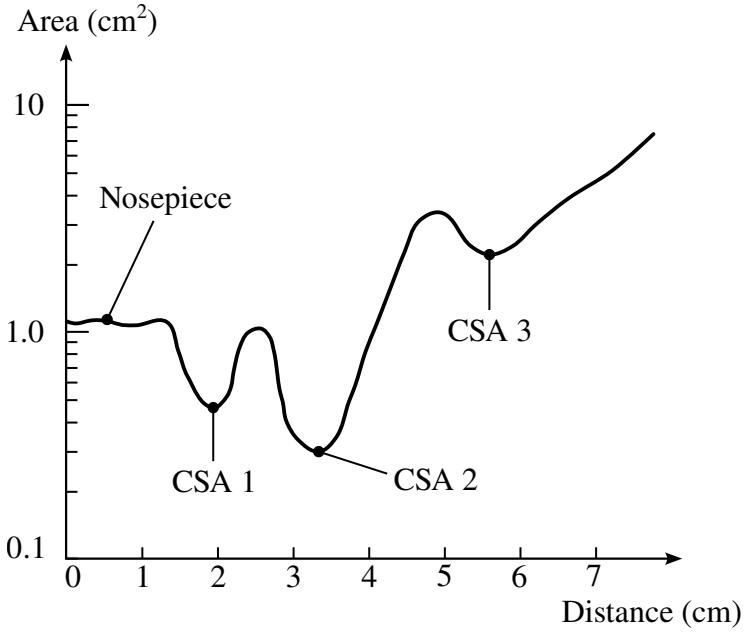

Figure 2.8. Hypothetical Result of Acoustic Rhinometry

Note. In this figure, three valleys appear. These valleys are the local minimum cross-sectional areas, from CSA1 to CSA3, respectively: the nasal valve, the anterior part of the inferior turbinate, and the anterior section of the middle turbinate.

This method has plenty of advantages:

- Acoustic rhinometry can locate the depth of nasal congestion (Fisher et al., 1994).
- It is very quick; it can be done within a few minutes (Cakmak et al., 2005; Fisher et al., 1994).
- This test is reproducible; it has a low coefficient of variation (Fisher et al., 1994; Friedman & Schalch, 2009).
- This method is a non-invasive procedure (Cakmak et al., 2005; Fisher et al.,

1994; Friedman & Schalch, 2009).

- The method only requires small patient cooperation; can be done on young children (Fisher et al., 1994; Friedman & Schalch, 2009).

- This procedure is a painless (Cakmak et al., 2005).

- Area estimations correlate well with both CT (Cakmak et al., 2005) and MRI (Corey et al., 1997) scan measurements.

Given these advantages, it is widely accepted and swiftly adopted by researchers and medical professionals (Cakmak et al., 2005). Anyhow, this tool is not perfect, and it has some serious limitations:

- There is a need for more guidelines and consistency in the literature (Cakmak et al., 2005; Tomkinson & Eccles, 1995).

- Obstructions along the nasal passageways reduce the precision of the measured cross-sectional area (Cakmak et al., 2005; Fisher et al., 1994).

- Measured areas of the deeper parts of the nasal cavity are overestimated; some work reports that at deeper areas, rhinometry measures the cross-sectional areas as almost double realistic values (Cakmak et al., 2005).

Even though acoustic rhinometry yields consistent and meaningful data to researchers, measurements should be done during a cessation of breathing. This method is found to be required to eliminate potential errors while boosting the consistency of the results by Tomkinson and Eccles (1995). Conversely, this practice is unrealistic, and patients do not experience obstructive problems in such a condition. In the light of Tomkinson and Eccles (1995)'s research, it becomes evident that momentarily pause of breathing leads to a higher mean of the minimum cross-sectional area than during inspiration but lower than during expiration. Thus, the suggested method of acoustic rhinometry may be confused when its results are compared to other procedures like rhinomanometry.

2.5.3 Nasal Endoscopy

Nasal endoscopy or rhinoscopy is the visual examination of the nasal cavity and other organs around it with an endoscope tool. This tool is a tube with a light and camera at the end. During this process, the practitioner may apply local anesthesia to avoid discomfort. Then, the endoscope is inserted through one of the nostrils. A thorough investigation of the desired areas, such as the nasal septum, turbinates, and sinusoidal openings, follows insertion. The reasons and location of the current symptoms are assessed during the examination.

Moreover, sometimes, it is required to collect tissue samples to gain further knowledge about ongoing issues. The removal and collection of tissues are done at the same time using the same endoscope. If found to be required, the removal of some localized complexities, such as nasal polyps and tumors, is done simultaneously.

In contrast to the advantages of nasal endoscopy, it does not generate objective results, limiting its usage in research endeavors. Nonetheless, in a clinical setting, the visual inspection lets doctors grasp the situation adequately and enables them to act accordingly. Moreover, nasal endoscopy allows practitioners to apply local surgeries, but it is also a quick and minimally invasive procedure, and it has only minor side effects such as nosebleeds and nasal pain. All in all, nasal endoscopy is a robust and multi-functional procedure preferred to evaluate and treat nasal sicknesses on the fly.

2.5.4 Computed Tomography Scan

Computed tomography scan or computed axial tomography scan is an imaging technique used to generate images. This method is commonly used to generate images of internal body parts; other objects may also be scanned. This technique uses X-rays to generate the imaging, and in order to do that, the number of blocked X-rays by different parts of the object is classified. X-ray usage distinguishes itself from magnetic resonance-based scans. Even though it has a mechanism similar to plain X-ray scans, CT images are very detailed and can be used to construct volume-based 3D structures.

The constructed images appear in black and white; also, the images are contrasted

based on their radiodensity, which equates to the number of X-rays a target allows passing through. Accordingly, while dense materials, such as solids, tend to have higher radiodensity levels, less dense materials, like gases, appear to have low levels of radiodensity. In CT scans, the contrast levels are put into the Hounsfield scale. The radiodensity levels are quantified by using Hounsfield units. The Hounsfield units are calculated based on radiodensity levels of water and air, as given in Equation 2.1.

$$\text{HU} = 1000\left(\frac{\mu_{\text{target}} - \mu_{\text{water}}}{\mu_{\text{water}} - \mu_{\text{air}}}\right) \tag{2.1}$$

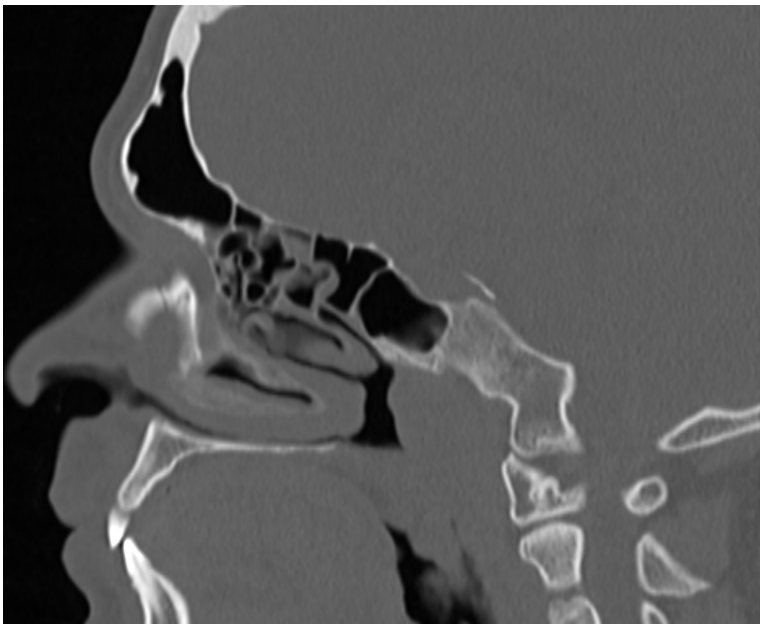

Figure 2.9. Computed Tomography Scan of a Human Head

Note. The image depicts the sagittal anatomical plane. The white parts represent the bones, the gray areas illustrate the tissues, and the black areas denote the air.

Note that if μ_{water} and μ_{air} are plugged for μ_{target} in Equation 2.1, Hounsfield unit representations for water and air would be found 0 and -1000, respectively. Commonly, in CT scans, maximum and minimum levels correspond to air and bones; these are shown by black for air and white for bones. Moreover, an example is provided in Figure 2.9; here, different tissues may be observed in the shades of gray. A more

detailed Hounsfield unit representation of biological body parts may be found in Figure 2.10. In contrast, if there are non-physical objects such as metal prosthetics, they are located at the end of the brightest spectrum due to their high radiodensity.

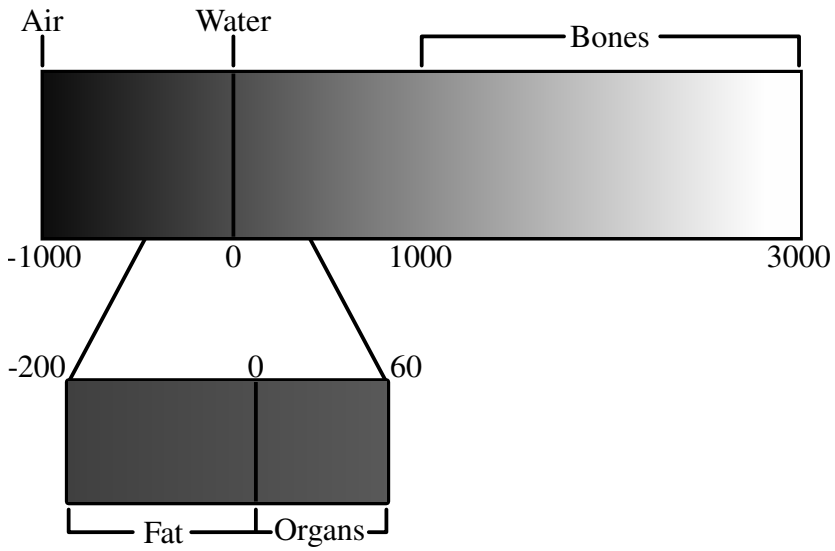

Figure 2.10. Spectrum of Hounsfield Scale

Note. The data used in this figure is obtained from the work of Jung (2021).

Medical doctors prefer CT scans since they produce the most detailed image of the upper airways (Metson, 2005). These images enable practitioners to determine the complexity's underlying cause and location accurately. Afterward, medical doctors may generate a plan of action to have an optimal resolution. Furthermore, the generated image can be used in various other settings, such as a model for 3D printers or numerical simulations. The preference for CT scans is because of their excellence in generating detailed scans in distinguishing air from other bodily tissues (Branstetter & Weissman, 2005). Thus, the image quality is considerably higher than that of other counterparts, for example, MRI scans. These reasons make CT scans the best fit for generating upper airway images.

Tomography scans do not cause any pain and are done as soon as 30 minutes.

Additionally, these scans can be used even if a ferromagnetic material is inside the body, such as an implant. However, according to the research done by Song et al. (2019), such objects inside the body spoil the scan's quality and increase radiation exposure. On the other hand, radiation is introduced to a patient's body by the CT scans. Indeed, if the radiation levels are low, there is no requirement for a warning. However, since CT scans are X-ray scanners capturing multiple images, the risks are much higher than regular X-ray scans (Mayo Clinic, 2022).

The ionizing X-rays generated cause the danger, and CT scans use them to generate the images. Thus, the patients get exposed to severe amounts of radiation by the X-rays. These ionizing radiations not only may cause damage to the tissues and organs but also may cause further complications such as cancer. Furthermore, the exposed levels of radiation are not insignificant; for example, according to United Nations Scientific Committee on the Effects of Atomic Radiation (2022), CT scans of the head, chest, abdomen, dental 1.5, 8, 11 and 0.7 mSv. Whereas, on average, a human gets exposed to radiation every year 0.57 mSv according to 2022 data of United Nations Scientific Committee on the Effects of Atomic Radiation (2022). Moreover, the limits for radiation exposure for professionals in all European countries are limited to 20 mSv per annum (Bundersamt für Strahlenschutz, 2022). Therefore, a single CT scan can cause up to 20 years of cosmic background radiation exposure. In other words, this level of radiation is equal to a year's worth of yearly limit for radiation workers.

2.5.5 Magnetic Resonance Imaging

MRI is a non-destructive image-generation technique based on nuclear magnetic resonance. MRI is exclusively designed for imaging purposes rather than its predecessor technique, which reports the tested object's molecular structure and chemical characteristics. MRI finds its usage mostly in medical endeavors to visualize inner body parts. For example, the image of a human head obtained by MRI is seen in Figure 2.11.

This imaging process is akin to CT scans regarding both application style and resulting images. In spite of this, MRI does not use ionizing waves to generate its images; it uses magnetic fields and low-frequency waves, such as radio waves, to draw the images.

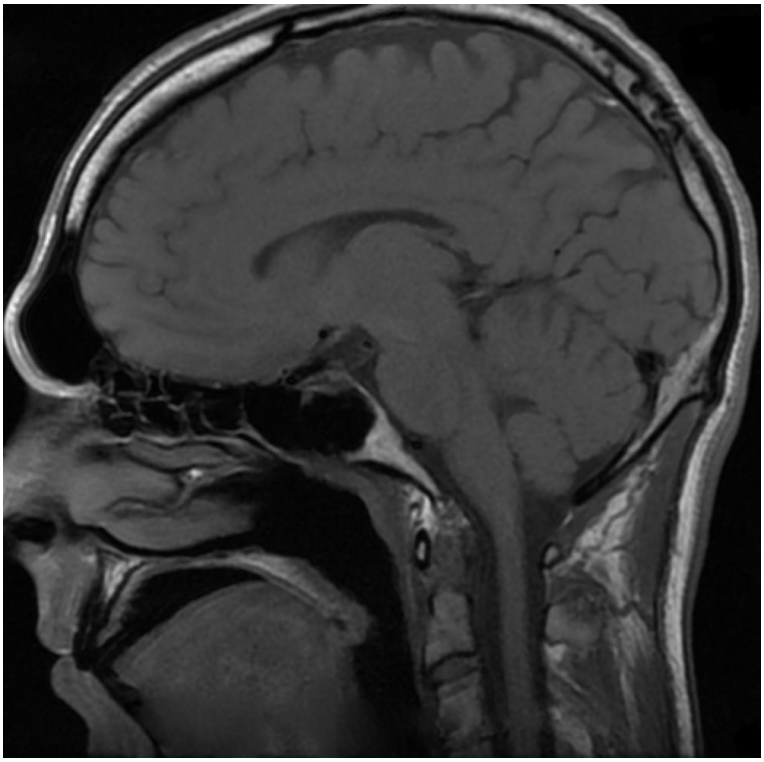

Figure 2.11. Magnetic Resonance Image of a Human Head

Note. This image is shown from the sagittal anatomical plane. An abnormal bulge on the forehead of the patient may be seen in this image. Also, nasal paths with sinuses are slightly visible. Modified from "MRI", Kiechle, Bryan, 2007, CC BY-NC.

Using non-ionizing radiation means that the MRI does not cause radiation concerns and is a danger-free technique. However, since MRI depends on strong magnetic fields to capture the snapshot of the body, it may not be applied if ferromagnetic objects exist in the human body. Expectedly, one may question why the iron atoms in the human body are unaffected by a magnetic resonance machine's magnetic field. The answer to this question is simply that human bodies have a minuscule amount of iron spread throughout the whole body.

As stated by National Institute of Biomedical Imaging and Bioengineering (2022), the working mechanism of MRI may be roughly explained in 3 steps as given below:

1) Protons inside the body are aligned by the strong magnetic field's effect.

2) Pulsing sequences are applied so that the alignment of protons is disturbed differently given their structural differences.

3) Pulsing is turned off, and protons emit energy within specific times while returning to their aligned state. The sensors record both energy amount and time to relax to generate images.

As stated by Branstetter and Weissman (2005), MRI better distinguishes objects, e.g., tissues, from one another compared to the other imaging types. This excellence means that if there are different kinds of tissues, MRI should be able to distinguish these tissues very successfully. In contrast, CT scans may fail to capture some of these tissues if they have similar radiodensity levels. The reasoning for this behavior is that MRI sequences applied during the scan can capture characteristics of tissues in great detail (Branstetter & Weissman, 2005).

CHAPTER 3

LITERATURE REVIEW

3.1 Healthy Airflow

Most commonly, the feeling of nasal obstruction, unlike common belief, is not caused by an actual obstruction in the nasal cavity. Numerous differences in nasal cavity geometries exist due to factors such as genetic diversity and dissimilar individual histories. These variations give rise to unique airflow patterns, which complicate understanding what a healthy nasal airflow is (Borojeni et al., 2020; Zhao & Jiang, 2014). Moreover, the placement and size of the nasal cavity complicate the investigation of the nasal cavity. Therefore, the truth behind the congested feeling has yet to be entirely understood, causing many theories and a lack of joint agreement on the nasal congestion issue.

For a long time, researchers have strived to explain the reasons behind why some people have high patency feelings while others suffer from congestion issues. Such interest does not solely arise from curiosity but to enhance the outcomes of surgical operations, primarily through virtual surgeries (Borojeni et al., 2020). Moreover, given that most surgeries fail to enhance patients' symptoms, better planning and strategies are needed (Jessen et al., 1989). Therefore, by gathering knowledge on healthy nasal airflow, surgical planning can be done beforehand, avoiding unsatisfactory results and potential future complications.

In the literature, conceptualization and quantification of healthy nasal airflow have been done in various ways:

- Airflow simulations of healthy individuals' nasal geometries compared against

these healthy individuals' questionnaires (Borojeni et al., 2020; Zhao & Jiang, 2014; Zhao et al., 2011).

- Simulations of unhealthy individuals' nasal geometries against these individuals' questionnaires (Radulesco, Meister, Bouchet, Giordano, et al., 2019).

- Comparison of healthy and unhealthy nasal geometries through numerical simulations (Casey et al., 2017; Li, Jiang, et al., 2017; Malik et al., 2019, 2022; Sanmiguel-Rojas et al., 2018).

- Airflow comparison of pre- and post-operative nasal geometries of those with nasal patency problems (Li, Jiang, et al., 2017; Sullivan et al., 2014; Wiesmiller et al., 2006).

Some thought minimum cross-sectional areas in the cavity could be the culprit, and they relied on acoustic rhinometry measurements. Others assumed the nasal obstruction could be explained by nasal resistance, i.e., pressure drop given flow rate, and the use of rhinomanometry preferred. Some research claims that MCA and nasal resistance are correlated (Radulesco, Meister, Bouchet, Varoquaux, et al., 2019; Zhao et al., 2011), and this correlation becomes more evident when MCA is below some threshold value (Garcia et al., 2016). Therefore, if one can explain nasal congestion, the other should be able to too. Nevertheless, others report that these predictive tools can not represent the congested feelings (Casey et al., 2017; Jones et al., 1989; Zhao et al., 2011).

On the other hand, explanations related to heat loss around the nasal cavity suggest a sound explanation of nasal patency. The reasons for this hypothesis are many: Inhalation of either cool or dry air (causing higher heat loss by the evaporation of water) seems to relieve nasal congestion (Zhao et al., 2011). Similarly, menthol appears to induce a cold sensation and aids in reducing the congested feeling (Burrow et al., 1983; Eccles, 2003). Moreover, applying anesthesia to the nasal tissue generates a false sense of congestion sense (Jones et al., 1987). Accordingly, McKemy et al. (2002) have found that receptors in the nasal cavity are sensitive to menthol and heat loss. Later research by Meusel et al. (2010) showed that cold receptors are located all around the nasal cavity, and these receptors get similar amplitudes of responses when stimulated. Therefore, it may be hypothesized that nasal patency is connected with stimulation of

the cold receptors on the nasal mucosa. Still, even though cold receptors appear to be the primary factor in the sensation of patency, it is unknown how much stimulation is needed to perceive patency and where this stimulation should be located.

Many studies find promising results examining the heat transfer phenomenon to explain subjective patency rates (Borojeni et al., 2020; Hazeri et al., 2020; Malik et al., 2022; Sullivan et al., 2014; Zhao et al., 2011, 2014). For example, some CFD simulations with heat transfer show that patency ratings of successfully treated patients are correlated with total area that has heat flux values over 50 W/m^2 (Sullivan et al., 2014). Similarly, under different air characteristics (dry, warm, humid, and similar), total heat loss in the nasal mucosa may be related to nasal patency ratings (Zhao et al., 2011). Other research suggests that peak heat flux values at specific locations of nasal passageways are a better way to describe nasal patency (Malik et al., 2022; Zhao & Jiang, 2014; Zhao et al., 2014).

On the other hand, some studies found that regional airflow distribution and wall shear stresses appear to have a relationship with patency scores (Casey et al., 2017; Li et al., 2018; Radulesco, Meister, Bouchet, Varoquaux, et al., 2019; Zhao & Jiang, 2014). The connection between patency and wall shear stress suggests that the frictional forces stimulate the mechano-receptors in the nasal cavity. This stimulation sends signals to the brain, causing the feeling of a patent nose (Di et al., 2013). In addition to stimulation of mechanical receptors, the wall shear stress values also represent heat convection rates, hence representing the amount of stimulation on cold receptors (Elad et al., 2006; Zhao et al., 2011). The airflow rate around the middle region appears to be a good indicator of having a few nasal problems (Casey et al., 2017; Zhao & Jiang, 2014). Moreover, low airflow and poor wall shear stress levels at inferior regions may cause a signal of congestive feeling (Li et al., 2018).

3.2 Empty Nose Syndrome

Empty nose syndrome is a strange phenomenon that appears after some nasal surgeries. This syndrome's main symptom is the feeling of nasal obstruction, though there is no physical obstruction. Other symptoms include nasal dryness, crusting, and pain.

Unfortunately, this syndrome goes so far that it may be the root of problems such as anxiety disorders and depression (T.-J. Lee et al., 2016).

People with ENS appear to have a jet forming in the middle of the nasal cavity. This behavior means that most of the flow passes through the middle region. As found by Zhao and Jiang (2014), in healthy individuals, airflow at the middle section is positively correlated with patency ratings, yet behavior does not hold for unhealthy people. Because of the dominant jet-like flow in the mid-region, Li, Farag, et al. (2017) speculated that nasal dryness and crusting are seen in the patients. On the other hand, Di et al. (2013) asserted that the dryness and crusting are due to vortices appearing near inferior turbinate. Furthermore, since flow is dominant in middle region flow, airflow reduces in the inferior region; this reduction causes small wall shear stresses around the inferior turbinate (Li, Jiang, et al., 2017; Li et al., 2018; Malik et al., 2019). Given that the wall shear stresses in the inferior region are small, stimulation of receptors is low; thus, individuals feel their noses congested (Li, Jiang, et al., 2017; Li et al., 2018; Malik et al., 2019).

Paradoxically, both Li et al. (2018) and Malik et al. (2019) found for people with ENS that cross-sectional area increase in the inferior nasal cavity does not channel the airflow towards the inferior region. Nevertheless, Malik et al. (2019) showed that people with inferior turbinate reduction without ENS have significant airflow in the inferior regions, exceeding the flow rates of healthy geometries. Moreover, according to the virtual turbinoplasty results of Dayal et al. (2016) and Di et al. (2013), an increase in the inferior area showed an increase in inferior flow. Although making comments directly based on area increase may be naive, this paradox could be explained by realizing that ENS patients exhibit extensive areas in the middle region, according to Li et al. (2018) and Malik et al. (2019)'s data.

Contrary to the popular belief that aggressive reduction in turbinates causes ENS, Li et al. (2018)'s dataset of people with ENS only had 15 % of the patients go through turbinectomies. Furthermore, as demonstrated by Malik et al. (2019), some people undergo aggressive turbinate reductions without experiencing any symptoms; however, these people must have middle passageway areas similar to healthy individuals.

ENS is shown to be only a feeling of congestion; in reality, individuals with shrunk

turbinates have less nasal resistance compared to healthy individuals (Malik et al., 2019). Expectedly, the nasal resistance does not correlate with questionnaires on symptom scores (Li et al., 2018). More appropriate metrics to quantify symptom scores with results could be the low wall shear stresses around the inferior region and flow rate distribution.

Consequent to knowledge of menthol's effect, some scientists enrolled in the conduction of menthol sensitivity experiments on ENS patients. The sensitivity to detect menthol is very low in those with empty nose syndrome compared to their healthy counterparts (Li, Jiang, et al., 2017; Li et al., 2018; Malik et al., 2019). Surprisingly, according to Malik et al. (2019), people whose inferior turbinates radically shrank without ENS had the highest sensitivity to menthol, noting that these people also had the highest airflow in their inferior nasal regions. Since the low menthol sensitivity appears only in those with false congestion due to ENS, menthol sensitivity appears to be a valid metric to quantify the symptom.

It appears challenging to pinpoint the main reason for ENS by using CT scans of patients because most surgeries incorporate different operations (Li et al., 2018). The existence of many operations means that numerous areas of the nasal cavity are disrupted in a single surgery. Due to this limitation, the root cause of the ENS can not be specifically found. Accordingly, the best approach to revealing the reasoning behind ENS is by applying singular operations. The singular operations are easily done by virtual surgeries; thus, virtual surgery is the strongest contender to determine the reasons behind ENS. Furthermore, these virtual surgeries are essential since they could be used to find the best geometry that optimizes flow and heat transfer rates, improving subjective nasal patency.

Total resection of either the middle or inferior turbinate increases the total airflow rates and the airflow rate in the vicinity of the removed area; also, the nasal resistance decreases in either total resections (Dayal et al., 2016; Di et al., 2013). Additionally, post-turbinectomy velocities and wall shear stresses get milder along with more disorderly flow (Di et al., 2013). However, airflow around other parts of the nose reduces compared to the pre-surgery values (Dayal et al., 2016). Given the extreme tissue removal, such a result suggests that the air starts acting like a jet. This result is

in accordance with the ENS; however, when tissue removal is milder, a more relative shift is observed (K. B. Lee et al., 2016).

Moreover, Dayal et al. (2016) found that after the turbinectomy, surface area, heating capacity, and humidification capacity of the cavity decreased; accordingly, there was less stimulation of the receptors. Similarly, Di et al. (2013)'s work reports that the excitement of mechanical receptors decreases due to reduced wall shear stresses. Additionally, this work claims that lower wall shear stresses equate to less stimulus on cold receptors. Therefore, at first glance, total removal of turbinates appears to have positive effects, yet this operation breaks the healthy function of the nasal cavity. Lastly, the effects appear to be more pronounced for inferior turbinate removals due to the larger size of inferior turbinate (Dayal et al., 2016; Di et al., 2013).

3.3 Septal Deviation

The main reason behind nasal obstruction is commonly known as septal deviation. Additionally, the septal deviation is a prevalent disorder among humans (L. P. Gray, 1978). However, there are many individuals with a septal deviation who do not exhibit any symptoms. The mystery of such an occurrence of symptomatic and asymptomatic deviated septum is not well understood. For example, some individuals have a high degree of septal deviation but do not have symptoms (Malik et al., 2022). Furthermore, such paradoxical problems often lead physicians to misidentify the underlying reason for nasal obstruction (Malik et al., 2022). These errors may lead to erroneous surgeries, wasting resources, and causing patient distress.

CFD and heat transfer research have been conducted to unravel the mystery under the septal deviation (X. B. Chen et al., 2009; Corda et al., 2022; Liu et al., 2011; Malik et al., 2022). Since this sickness brings an obstruction feeling to the patients, menthol sensitivity tests are also leveraged to investigate this sickness (Malik et al., 2022). Septal deviation CFD simulation results indicate that primary airflow rates deviate from middle regions towards inferior regions (Liu et al., 2011). Most of the flow appears to pass from the non-deviated side (Liu et al., 2011; Malik et al., 2022). Moreover, the peak velocity region appears to shift from the usual nasal valve area

(Corda et al., 2022). Nevertheless, the highest velocity values do not always appear on the non-deviated side, given the nasal cycle's effect on the areas (Liu et al., 2011).

Some metrics that fail to explain nasal patency feelings may help to distinguish symptomatic deviated septum symptoms. For healthy individuals, nasal resistance was irrelevant to nasal patency. Despite the assertion by Malik et al. (2022) that this metric fails to explain symptomatic deviated septum, their results indicate a significant increase in non-deviated nasal resistances. Moreover, nasal resistance values have the second-highest correlation with respect to visual analog score readings. Specifically, 30 % increase compared to asymptomatic and healthy individuals. Such higher nasal resistances are also observed by Corda et al. (2022): symptomatic patients tend to have up to 55 % more total nasal resistances.

On the other hand, other metrics that are used to explain nasal obstruction for healthy passageways may not be used to explain the reasoning behind the obstruction caused by the septal deviation. For example, for healthy individuals, MCA is used by Zhao and Jiang (2014), and heat flux greater than 50 W/m^2 is used by Sullivan et al. (2014) to describe healthy airflow. However, for those with a deviated septum, Malik et al. (2022)'s results indicate that heat flux and MCA poorly correlate to nasal patency ratings.

Similarly, flow rate distribution (Li, Farag, et al., 2017; Li et al., 2018; Zhao & Jiang, 2014) and wall shear stress locations (Li, Farag, et al., 2017; Li et al., 2018) are good estimators for healthy individuals. Malik et al. (2022) report that these values have no relationship with a sensation of patency. However, the assertion made by Malik et al. (2022) does not hold with the given data in the article. The data show that local investigations of shear stress and flow rate distribution have a relationship with patency ratings. There are minimal flow rates in deviated middle regions and extremely high flow rates in non-deviated middle regions. Moreover, local shear stresses that elucidate the congested feeling are also ignored by Malik et al. (2022).

Lastly, (Malik et al., 2022)'s work showed that one of the best indicators for symptomatic septal deviation appears to be menthol sensitivity results along with peak heat flux rates, especially in the inferior parts. Together with the claims of Di et al. (2013) and Zhao et al. (2011) on the correlation between heat flux and shear

stresses, this result suggests that peak wall shear stresses could also be one of the best indicators of the symptomatic septal deviation.

3.4 Satisfaction After Nasal Surgeries

The success rate of nasal cavity surgeries often depends on many factors, including the correct diagnosis, the medical experience of the surgeons, and patient aftercare. Above, it is mentioned that one has to apply relatively complex state-of-the-art techniques, i.e., CFD and heat transfer, in order to properly decide if airflow through the nasal geometry is healthy or not. Such an endeavor is challenging even on an academic level, requiring vast knowledge of engineering and biology topics. Therefore, decisions made by physicians are often heavily based on shared academic knowledge, their experiences, and their intuitive judgments.

Building academic knowledge for nasal surgeries requires recording the good and bad outcomes. However, feedback from humans is required because the experiments and surgeries are applied to patients. In order to correctly measure the success rates of such operations, researchers generated many different surveys and questionnaires.

A typical questionnaire is the nasal obstruction symptom evaluation scale. This scale aims to score nasal obstruction-related issues in just five questions with good reliability (Stewart et al., 2004). Another common way to evaluate nasal congestion-related problems is the visual analog scale. This scale is just a continuous line starting from 0 and ending at 10. On this scale, the numbers may represent any value, but for nasal congestion-related work, 0 represents no obstruction, and 10 is marked as severe obstruction.

Accordingly, given that relief from nasal obstructive issues relies on patients, the most analytical way to decide upon the success of nasal surgeries is aforesaid surveys. Even though there are many factors determining success, acknowledgment of the existence of subpar surgical operations is critical. For this reason, surgical techniques are researched by many people aiming to expand their knowledge on techniques, (Bugten et al., 2016; Jessen et al., 1989; Mondina et al., 2012; Nilsen et al., 2018; L. A. Pedersen et al., 2021).

The questionnaires are applied before and after the surgeries. Since time is required for healing and long-term results are considered more critical, post-surgery questionnaires must be late enough to represent the success rate. Most post-operation surveys are done after 6 months (Bugten et al., 2016; Mondina et al., 2012; Nilsen et al., 2018). Also, some surveys get carried over 3- to 6-month time-frames (L. A. Pedersen et al., 2021). Critically, among two similar surgeries, one could be better in the short term, and the other is superior in the long term (Datta et al., 2018). Moreover, short-term results are bound to change when questionnaires are applied over very long time frames (Jessen et al., 1989). According to Jessen et al. (1989), survey at 9^{th} month 50 % of the people reported having no nasal obstruction, the number reduced to 25 % at the second survey at 9^{th} year. Surprisingly, the objective rhinomanometry results suggest further reduction in the nasal resistance at the end of 9^{th} year. Jessen et al. (1989) speculated that patients' reports were spurious, since they could not remember the obstruction level before the surgery. Therefore, an intermediate wait period is needed for post-operative surveys to determine the success rates of medical surgeries. Both short-term and long-term questionnaire results are misguiding the success rates of nasal obstruction remedies.

In the literature, there are surveys to measure the life qualities of patients against healthy individuals. For example, the study of Bugten et al. (2016) indicates that most post-operative septoplasty patients are satisfied with the surgery, yet their symptoms and quality of life levels are still lower than their healthy counterparts. Interestingly, the satisfaction rates get considerably worse for those who undergo a follow-up septoplasty (Bugten et al., 2016; Nilsen et al., 2018). This result suggests that patients who get revision surgery have other complications or the current surgical techniques can not resolve their issues completely. Thus, such unsatisfactory results indicate that there is a room for improvement in diagnostic systems, surgical planning, and surgical techniques.

Since multiple nasal operations can be done concurrently in a surgery, physicians alter multiple locations in a single surgery to get the most efficient results. Therefore, many studies are concerned with a combination of medical operations and their effectiveness (Nilsen et al., 2018; L. A. Pedersen et al., 2021). For example, Nilsen et al. (2018) statistically investigated the effects of a radiofrequency therapy on turbinates in addition

to a septoplasty. Accordingly, those who get additional radiofrequency therapy appear to have fewer symptoms; however, they do not get a life quality increment compared to those who only get a septoplasty (Nilsen et al., 2018). In contrast, a similar work by L. A. Pedersen et al. (2021) reported that adding a turbinoplasty to a septoplasty surgery substantially boosts the quality of life results.

Nevertheless, the turbinoplasty addition does not lead to any remarkable reduction in the symptoms, e.g., nasal obstruction. Indeed, the secondary surgeries in both works are related to turbinate reduction, but the outcomes are not similar. Nevertheless, neither turbinoplasty nor radiofrequency therapy satisfy similar results in both the reduction of symptoms and the increase in quality of life compared to septoplasty alone. On the contrary, turbinate reductive surgeries without septoplasty are associated with a higher chance of post-operative complications, such as empty nose syndrome (L. A. Pedersen et al., 2021). The understanding behind the turbinate reduction surgeries is still unclear, though they are promising auxiliary surgeries to septoplasty.

Even though septoplasty surgeries appear to solve nasal obstruction-related symptoms and improve life satisfaction, their success rate is directly proportional to nasal congestion levels (L. Pedersen et al., 2019). In other words, if a patient has mild symptoms, septoplasty can not provide similar results to those with more prominent symptoms. For example, allergic rhinitis, which worsens the obstruction, enhances the positive outcomes of septoplasty (Mondina et al., 2012). Moreover, agreement on obstruction feeling and deviation side correlates to better septoplasty results (L. Pedersen et al., 2019). Notably, gender, age, body weight, and cigarette usage can not predict success rates (Mondina et al., 2012). Therefore, before subscribing to a life-altering surgery, vigorous planning must be done to provide satisfactory patient results.

3.5 Numerical Simulations of Nasal Airflow

Applications of numerical techniques in biomedical settings are finding interest due to the rich results and relatively lower costs to conduct, along with hardship to conduct other objective and descriptive research on nasal cavity (Balatinec et al.,

2021; Inthavong et al., 2014; Karbowski et al., 2023; Pynnonen & Davis, 2014). However, given the size and complexity of the nasal cavity, advancements of numerical simulations in the literature appear slowly (Keyhani et al., 1995).

3.5.1 Pioneering Numerical Works on Nasal Airflow

This part of the literature review focuses on the precursor work on the numerical simulations. These works undoubtedly informed others and shaped later research with their ideas and findings. Moreover, these studies show that numerical simulations can yield parallel, but more comprehensive insights compared to experimental work (Elad et al., 1993; Keyhani et al., 1995; Kimbell et al., 1993).

Initially, computational resources hindered the simulation of numerical simulations. Some had to use linear versions or Navier-Stokes equations because their computers lacked enough memory and CPU power (Elad et al., 1993). Most, if not all, of the research assumed nasal flow was laminar and steady (Elad et al., 1993; Keyhani et al., 1995; Kimbell et al., 1993; Tarabichi & Fanous, 1993). Expectedly, the first numerical simulations were applied to simplified geometries (Elad et al., 1993) or partial geometries (Tarabichi & Fanous, 1993) of nasal cavities. Moreover, since nasal airways are symmetric, the precursor researchers took advantage of this by simulating only a single side of the nasal cavity (Keyhani et al., 1995; Kimbell et al., 1993). Even more extreme, some pioneering research opted for 2D simulations to understand nasal airflow (Tarabichi & Fanous, 1993). Unlike the current trend of finite-volume methods, pioneering research used finite element methods (Elad et al., 1993; Keyhani et al., 1995; Kimbell et al., 1993; Tarabichi & Fanous, 1993).

The first attempt to simulate 3D airflow in the human nasal cavity was made by Elad et al. (1993). However, the geometries generated by Elad et al. (1993) were highly simplified, yet these geometries had the outline of realistic nasal cavities and turbinates. The first numerical simulation of anatomically correct geometry, specifically a rat's, has been done by Kimbell et al. (1993). Later, Keyhani et al. (1995) did the first airflow numerical simulation on a realistic human airway geometry. Keyhani et al. (1995) showed that their simulation is in perfect agreement with its experimental counterpart, Hahn et al. (1993).

3.5.2 Recent CFD Simulations on Nasal Airflow

The boom in computational power and software availability allowed many researchers to conduct numerical airflow simulations. Also, the details of the simulations have gotten higher. One of the first nasal airflow simulations, Elad et al. (1993), used 10 thousand grid elements for a nasal flow; nowadays, usage of 350 million elements has been seen (Calmet et al., 2016), which is perhaps the highest number of elements used in a CPU-based nasal airflow simulation as of 2024. Moreover, rather than using CPUs, some methods exploit GPUs, which are perfect for parallel workloads due to the abundance of processor cores. One of these methods, the lattice Boltzmann method, was recently used on a grid with 1 billion elements (Hebbink et al., 2023). However, the popular option in numerical simulations still appears to be CPUs; these simulations use up to a few million mesh elements to simulate breathing phenomena (Balatinec et al., 2021; Calmet et al., 2021).

Nowadays, most of the research considers effects of the turbulence in their simulations. As mentioned earlier, pioneering researchers have assumed the flow to be laminar. The turbulence modeling approaches observed throughout the literature uses turbulence models such as:

- $k - \varepsilon$ (Li, Jiang, et al., 2017)
- $k - \omega$ (Y. Chen et al., 2023; Cherobin et al., 2021; Li, Jiang, et al., 2017)
- $k - \omega$ SST (Balatinec et al., 2021; Y. Chen et al., 2023; Li, Jiang, et al., 2017; Schillaci & Quadrio, 2022)
- Reynolds stress modeling (Li, Jiang, et al., 2017)
- DES[1], resolving large eddies far away from walls and RANS models on the boundary layer (Strien et al., 2021)
- LES, resolving large eddies modeling small ones (Berger et al., 2020, 2021; Calmet et al., 2021; Calmet et al., 2016; Y. Chen et al., 2023; Hebbink et al., 2023; Li, Jiang, et al., 2017; Schillaci & Quadrio, 2022; Vecchietti, 2021)

[1] This approach appears unfit for wall-bounded flows since most of the flow happens near walls. However, there are some techniques exist that activate RANS modeling only very close to a wall, e.g., IDDES.

- DNS, resolving all eddies (Li, Jiang, et al., 2017; Vecchietti, 2021)

Strangely, much of the research uses models that assume fully turbulent behavior, such as $k-\varepsilon$ and $k-\omega$ SST. The usage of such turbulent models is questionable since, at best, nasal flow is thought to be transitional, locally turbulent, and disturbed at low discharge levels (Doorly et al., 2008). Y. Chen et al. (2023) demonstrated that eddy simulating flows is the closest to experimental results and that low Reynolds number alternatives to standard RANS models are superior to traditional RANS models.

Moreover, Li, Jiang, et al. (2017) have extensively worked on turbulent modeling in nasal airflow. Similar to Keyhani et al. (1995), Li, Jiang, et al. (2017) have simulated the same geometry experimented by Hahn et al. (1993). Devastatingly, the laminar model outperformed all the RANS models for the restful flow rates. Expectedly, the laminar flow failed to model faster flow rates correctly, where turbulence plays a more significant role. On another note, if DNS results are considered the ground truth, the $k-\varepsilon$ model reports considerably deviated results for nasal resistance values. Interestingly, $k-\omega$ appears to outperform its SST-included variation and all other RANS models. Also, Li, Jiang, et al. (2017) signaled that turbulence intensity reaches up to 5 % at some locations in the nasal cavity during restful inhalation, yet the laminar simulations perform as well as DNS and LES.

More detailed research has been done on comparing laminar simulation to LES by Calmet et al. (2021). This work simulated a transient restful breathing cycle and compared the prediction of turbulence-related variables. For the sub-grid scale turbulence modeling, WALE is used. Importantly, this model can reproduce the transition to turbulence, since sub-grid scale eddy viscosity vanishes in pure shear (Nicoud & Ducros, 1999). According to Calmet et al. (2021), turbulence properties were considerably high; for example, turbulence intensity peaked at 30 % within the cavity. Interestingly, the laminar model did not only capture the overall characteristics of the flow but was also 10 times faster than LES. However, it erroneously reported the fluctuations in flow parameters and turbulence characteristics.

Recently, Strien et al. (2021) conducted a nasal cavity flow simulation using a hybrid RANS-LES turbulence model, stress-blended eddy simulations, one of the first DES in the nasal cavity flow. They verified the simulations with in vitro experiments using the

same geometry. Their work used a 15 L/min discharge rate, and they reported that the laminar assumption is acceptable. Whereas at 30 L/min, the anterior part of the cavity appeared as a disturbed though laminar flow, and the flow in the posterior region was fully turbulent.

Even though there are improvements in the nasal cavity flow compared to earlier works, there are still many issues. Zubair et al. (2012) compiled most of the wrong practices regarding nasal airflow numerical simulations in the literature. Firstly, the authors recognized that body position significantly affects the nasal cavity. They detected that most, if not all, of the CT scans used in the literature were taken while patients were lying down. Since lying down is the most restrictive position for the nasal passages, the results obtained from these geometries misrepresented the realistic conditions. As a solution, cone-beam CT scans taken while standing were suggested. The next issue was the obscurity behind the gender of the nasal geometry used in the simulations. Zubair et al. (2012) argued that most of the research appeared to be done on male geometries, yet some research skipped reporting the gender of patients. The 3rd problem was the mucous layer's negligence and the geometrical model's simplification. The 4th issue was given as the plug-flow boundary condition, which is the usage of the velocity profile at the inlet. Zubair et al. (2012) reasoned that natural mechanisms are contrary to this boundary condition; hence, employing the pull-flow boundary condition was suggested. Lastly, a critique of the employed turbulence models was given. They suggested using the eddy-resolving approaches because the flow features appeared to be better predicted. However, among the Reynolds-averaged models, they recommended the employment of $k-\omega$ SST model.

3.5.3 Geometry Generation for Nasal Flow Simulations

Since nasal geometry is highly volatile, some researchers have tried to obtain an averaged nasal geometry that can represent any person. Two interesting research pieces provide these geometries: Gambaruto et al. (2012) and Brüning et al. (2020). However, both research studies fail to satisfy some critical factors.

Gambaruto et al. (2012) generated two averaged right nasal passageway geometries using two different techniques. 3 healthy individual tomography scans were used to

the seed geometries. The resulting geometries were compared using CFD simulations against each other and the seed geometries. Unfortunately, using the two candidate algorithms resulted in the loss of intricacies in the original geometries; most critically, the nasal valve region faded away. Compared to individually averaged results, both of the averaged geometries underpredicted pressure drop values and wall shear stresses.

Later, Brüning et al. (2020) fabricated an improved averaged nasal cavity geometry using tomography scans of 25 healthy individuals. Unlike Gambaruto et al. (2012), the generated representative model preserved vital anatomical features of the seed geometries; however, it was symmetric between passageways. The averaged nasal cavity again appeared more ordered than the original seed geometries. Further on, they conducted and compared the numerical simulations of average and seed geometries. The numerical results obtained from the averaged geometry underestimated three crucial factors: wall shear stresses, nasal resistances, and maximum velocity values. As expected, they were in reasonable ranges; moreover, the average geometry maintained the overall trend for pressure distributions and wall shear stresses.

On another note, Cherobin et al. (2018) worked on generating the optimal surface mesh through CT scans. Since radiodensity thresholds heavily affect the resultant nasal surface geometry, differences in three different thresholds are investigated. In order to test the outcomes, the authors simulated steady-state airflow at three radiodensity threshold levels for the upper bound. Cherobin et al. (2018) found that this threshold level does not alter surface area or general shape notoriously. Nevertheless, slice cross-sectional areas, total volume, nasal resistance, and airflow distribution were reported to be highly dependent on the threshold values.

Moreover, Inthavong et al. (2018) were interested in generating volume meshes and their quality. Thus, they thoroughly investigated mesh quality and the number of grid elements used. Given the complex structure of the nasal cavity, the researchers suggested that to test grid independence, a plane or volume difference between models may be preferred over line velocity profile comparisons. Moreover, they advised that if near-wall resolution is good enough, crude meshes may also provide good results on general flow features.

3.5.4 Steady Assumption of Nasal Flow Simulations

Breathing is a cyclic, oscillatory, hence a transient action: an inhalation of the surrounding air is followed by an exhalation of this air. Expectedly, if a pulsating action is happening very frequently, the previous action may disrupt the next one. In order to determine if the breathing pulsations require a transient simulation to be correctly represented, more information about the breathing phenomenon is required. Most critically, to further speculate on the steadiness of breathing, three variables about breathing must be known: total lung volume or tidal volume, inhalation time, and exhalation time. These variables may be obtained by directly recording the breathing cycles of individuals. Then, the breathing recording may be averaged to represent a general profile.

Such recordings have been done and reported in the literature; for example, Benchetrit et al. (1989) investigated 16 individuals twice within a 4-year time frame. 32 different breathing patterns, along with the inhalation time, exhalation time, and tidal volumes, are reported. Moreover, Benchetrit et al. (1989) reported that even though these people have had critical changes in their lives, such as smoking habits, respiratory diseases, and weight changes, their breathing patterns have not changed much. However, the variation between the tested individuals was evident. Similarly, more recent research by Tsega et al. (2019) reported not only the three aforementioned breathing variables but also sinusoidal breathing profiles. These profiles were given distinctively for inhalation and exhalation.

In both simulation-related and experimental work on breathing, the assumption of a perfect sinusoidal wave is common, assuming that the same amount of time passes for inhaling and exhaling the air. However, the correct breathing behavior shows that exhalation takes longer than inhalation (Benchetrit et al., 1989; Tsega et al., 2019). Accordingly, for a transient simulation of nasal breathing, a better description of the breathing profile is needed.

In the literature, some scholars did unsteady simulations of nasal airflow (Balatinec et al., 2021; Calmet et al., 2021; Calmet et al., 2016; Y. Chen et al., 2023; Elad et al., 2006; Hebbink et al., 2023). On the other hand, most commonly, the breathing was

assumed as a quasi-steady or a steady flow (Borojeni et al., 2020; Casey et al., 2017; Corda et al., 2022; Dayal et al., 2016; Di et al., 2013; Inthavong et al., 2014; Karbowski et al., 2023; Keyhani et al., 1995; Zhao & Jiang, 2014; Zhao et al., 2014). Nonetheless, the steady assumption was seldom explained, and the focus was on the feeling of patency against outcomes of numerical simulations.

The interference of oscillations is discussed and analytically investigated for blood circulation in arteries by Womersley (1955). Womersley (1955) introduced a dimensionless variable, the Womersley number or α. This parameter predicts transient effects in an oscillatory, laminar, and fully-developed pipe flow. The reason behind this idea is that in near-wall regions, pressure fluctuations do not affect the velocity profile because of the strong presence of no-slip conditions; moreover, if the boundary layer is at least as thick as the radius, pressure fluctuations do not affect any of the velocity profile (Pedley et al., 1977). Essentially, if α is equal to or less than unity, viscosity's effect due to a wall reaches at least up to the radius of the pipe; thus, if the boundary layer is thick enough to cover the whole flow profile, then the quasi-steady assumption is justified.

$$\alpha = \frac{D}{2}\sqrt{\frac{\omega}{\nu}} = \frac{D}{2}\sqrt{\frac{2\pi f}{\nu}}, \tag{3.1}$$

D, ω, f, and ν are the diameter of the pipe, angular frequency, ordinary frequency, and kinematic viscosity of the fluid, respectively.

Later on, Womersley (1955)'s idea was generalized to be applied to other kinds of flow by Schroter and Sudlow (1969). As said, this version replaced the laminar flow thickness, which is the radius of the pipe, with an arbitrary boundary layer thickness. The generalized Womersley number is,

$$\alpha' = \delta\sqrt{\frac{\omega}{\nu}}, \tag{3.2}$$

where δ is the steady-state boundary layer thickness. Furthermore, Pedley et al. (1977) expanded the generalized version of the Womersley number on dimensional grounds. However, this improvement does not appear to build on the generalization given by

Schroter and Sudlow (1969). The improvement puts the dimensional equivalent of the boundary layer on flat plates. Basically, the Womersley number reduces to a ratio between oscillatory boundary layer thickness and steady boundary layer thickness. The modified Womersley number is called the frequency parameter and is represented with the letter ϵ. Then, the frequency parameter is,

$$\epsilon = \frac{\omega L}{U(t)}, \tag{3.3}$$

where L is the selected location's distance to the entrance of the flow, and $U(t)$ is the mean velocity at a selected time. Similar to the Womersley number, if ϵ less than or equal to unity[2], flow can be considered quasi-steady.

Unfortunately, none of the above improvements include effect of turbulence into steady assumption's correctness. Turbulence's effect is included in the topic by Pedley et al. (1977). Pedley et al. (1977) adapted Boussinesq's turbulent, or eddy, viscosity assumption to a fully-developed Womersley number for 3 % turbulence intensity. The adaptation is made by crudely approximating turbulent viscosity and discarding kinematic viscosity[3]. In this thesis, the rough estimation is further derived for any given turbulence intensity value as follows:

$$\alpha_{\mathrm{t}} = \sqrt{\frac{\omega D}{2I^2 U}}, \tag{3.4}$$

where I is the turbulence intensity. Unfortunately, this turbulent version assumes a fully-developed boundary layer, just like the original Womersley number.

Isabey and Chang (1981) conducted experimental work on the lower respiratory system to study steadiness. The researchers used three different gases on three oscillatory levels and one steady flow. According to these results, they calculated the versions of Womersley numbers as mentioned earlier. Unfortunately, none of the indicators could

[2] Even though ϵ is derived from the square of the Womersley number, the same boundaries for the quasi-steady assumption hold.

[3] It is critical to note that in the original work Pedley et al. (1977) appears to miscalculate the approximation of turbulent viscosity in two respects. First, they divide by an extra 2 while approximating the derivative of the velocity. Secondly, while they exchange the velocity fluctuations with the mean velocity, the square of turbulence intensity is not included. Noting that the first issue was fixed in their later research, Pedley (1977).

predict at which frequency the quasi-steady assumption is valid; hence, the resistance is the same as steady state flows. They showed that even for a whopping $\alpha = 12.1$, flow can be assumed to be a quasi-steady when some conditions are met. Moreover, it was observed that precise prediction of quasi-steady behavior was impossible for both turbulent and boundary layer versions of Womersley numbers. Nevertheless, under some discharge levels, in comparison to the wild $\alpha = 12.1$ value, the turbulent Womersley number at worst approached 1. Even though this number suggests a superior prediction of quasi-steady behavior, the value of 1 is still considered very high for a flow that can be assumed to be steady.

Isabey and Chang (1981) were not satisfied by the results, even the results obtained using the turbulent Womersley number, which suggested that the quasi-steady assumption is valid. For this reason, they tried to get better predictors for their calculations. The authors ended up using the modified frequency parameter, which was suggested by Pedley (1976). This parameter ended up being the most successful quasi-steadiness predictor. This variable is,

$$\epsilon^* = \frac{L\dot{U}(t)}{(U(t))^2} == \frac{\omega L}{U(t)} \cot \omega t, \tag{3.5}$$

the right-most equation is obtained using $U(t) = U \sin(\omega t)$. Accordingly, Isabey and Chang (1981) suggested that when $\epsilon^* \leq 0.1$, flow essentially has similar resistance levels to a steady flow. It is critical to note that ϵ^* varies greatly with time: At the start of the breathing cycle and during the reversal of inhalation and exhalation, ϵ^* diverges to infinity, and near the peak flow, ϵ^* converges to 0. Therefore, the partition of the oscillatory flow must be specified, yet Isabey and Chang (1981) and the later work (Chang & Masry, 1982; Isabey et al., 1986) does not mention this.

Even though different conclusions were reported in Isabey and Chang (1981), the generalized Womersley number, α', also be used to predict quasi-steadiness very well. The authors expanded the boundary layer as $\delta = (8\nu L/U(t))^{0.5}$ which reduces the

generalized Womersley number to,

$$\alpha' = \sqrt{\frac{2\omega L}{U(t)}}. \tag{3.6}$$

According to the given figures in the research paper, when $\alpha' < 0.6$ quasi-steady assumption seems valid for most cases. Notably, the calculation of α' is straightforward, definite, and static, unlike the suggested ϵ^*.

Moreover, the generalized Womersley number, α', may be converted to the frequency parameter, ϵ. This conversation should allow an approximation of quasi-steadiness for other types of flow. Basic arithmetic yields: $\frac{\alpha'^2}{2} = \epsilon$. Therefore, the valid quasi-steady limits should be found as $\epsilon < 0.18$.

In the literature, this frequency parameter, ϵ, is seldom reported for upper airways. Keyhani et al. (1995) and Shi et al. (2006) found $\epsilon < 0.2$, Doorly et al. (2008) reported $\epsilon < 0.25$.

In the aforementioned frequency parameter results, the regular frequency, f, is selected as 15 breaths per minute. However, concrete data for this variable exist in the literature. Specifically, Tsega et al. (2019) have reported breathing-related variables in various states. For the restful, breathing frequency is reported to be around 13 rather than 15, which roughly equates to $f = 0.22/\mathrm{s}$. The total length of the nasal cavity is selected as the distance between entrance and exit, which is the worst-case scenario since L increases the frequency parameter. The length could get as long as 10 to 15 centimeters. The last variable to calculate is the average velocity in the nasal cavity. For a single nasal passageway, Hahn et al. (1993) report average velocity is equal to $5.4\,\mathrm{m/s}$ for $Q = 33.6\,\mathrm{L/s}$. A human breathes around $Q = 15\,\mathrm{L/s}$ in a sitting state, which is also referred to as eupnea, quiet breathing, or resting breathing. By interpolation, the average velocity during restful breathing is found to be $U = 2.4\,\mathrm{m/s}$. By using these values, the highest, or worst, case scenario of the frequency parameter is,

$$\epsilon = \frac{\omega L}{U} = \frac{(2\pi 0.22)0.15}{2.4} = 0.09, \tag{3.7}$$

which suggests that the quasi-steady assumption is valid when the data given by Isabey and Chang (1981) are used. Moreover, it should be noted that this value would have been lower for higher breathing frequencies or breathing speeds[4]. Therefore, one may claim that the most transient is the slow breathing state.

On the other hand, some researchers reported the Strouhal number, $\mathrm{St} = fL/U$, where L is the characteristic length, without a detailed explanation or reasoning. The reason behind the usage of this dimensionless number could be twofold. The first reason is that the modified Womersley number, ϵ, analogous to the Strouhal number. Secondly, authors might have assumed that, given small Strouhal numbers, nasal airflow should also be assumed to be quasi-steady, similar to other research areas. Accordingly, some reported Strouhal numbers were 0.01 (Hahn et al., 1993; Wen et al., 2008), 0.057 (Malik et al., 2022), 0.33 to 0.54 (Jiang & Zhao, 2010).

One particular work on the steady assumption of nasal flow, Hörschler et al. (2010), defined the Strouhal number as $\mathrm{St} = L/(TU)$, where T represents the one breathing cycle duration and L represents the total length of the nasal cavity. The number was reported as $\mathrm{St} = 0.79$, which suggests that unsteady effects are in play. Conclusively, they observed that the steady-state assumption fails near the transition between inhalation and exhalation in a sinusoidal flow. However, at other times, transient and quasi-steady results are similar. Additionally, steady results have been found to be in precise agreement with the average of transient results.

3.5.5 Interpreting The Nasal Airflow Results

Due to the geometrical complexity of the human passageways, the research and making sense of the results are challenging. Additionally, since numerical simulations generate vast amounts of data, a wide range of interpretations are possible. Accordingly, this interpretive freedom may lead to decision-making paralysis during the analysis of results. Therefore, in the literature, different methods are used to interpret and comprehend nasal simulations. Some works prefer to analyze traditional metrics, such as:

[4] During faster breathing states, the frequency decreases, and velocity increases even further; thus, reducing ϵ.

- nasal resistances (Berger et al., 2021; Borojeni et al., 2020; Inthavong et al., 2017)
- MCA along the normal to the flow direction (Borojeni et al., 2020)

While others have taken advantage of rich data from numerical simulations by investigating more sophisticated results:

- flow distributions
- WSS distributions (Inthavong et al., 2017)
- behavior of streamlines (Inthavong et al., 2014)

On the other hand, some scholarly work has coupled more advanced physical phenomena such as heat and gas transfer. These researchers examined the outcomes similar to:

- heat flux rates (Borojeni et al., 2020)
- total heating capacities (Borojeni et al., 2020)
- heating around specified regions (Zhao & Jiang, 2014; Zhao et al., 2014)
- temperature changes (Inthavong et al., 2017)
- gas transfer rates (Inthavong et al., 2017)

3.5.6 Numerical Simulations Against Other Methods

The results obtained from various techniques are inconsistent with each other. The reasoning behind this was researched by Cherobin et al. (2021). They tried to explain the discrepancy behind the low correlation between rhinomanometry and CFD results. In order to obtain results, they have done rhinomanometry measurements, CFD simulations, and in vitro experimental measurements. For nasal resistance ratings, the results of the CFD simulations and experiments showed a promising correlation between them. Nevertheless, with rhinomanometry, results were inferior to those of

their in vitro and in silico counterparts. The numerical simulation results were found to underpredict the nasal resistance values by half. On the other hand, a notable correlation was found to exist between CFD simulations and rhinomanometry tests for nasal resistance ratings. The authors speculated that the discordance is likely caused by two factors: rigid nasal wall assumptions and segmentation errors from CT scans. Cherobin et al. (2021) dismisses the potential errors arising from posture, nasal cycle, and measurement to scan time differences due to the usage of decongestants.

Recently, a similar work to Cherobin et al. (2021) had been conducted by Karbowski et al. (2023). Unlike Cherobin et al. (2021), rhinomanometry measurements were done before and after anemization[5]. This research revealed several interesting findings regarding nasal cavity flow and pressure measurements. The most noteworthy ones are listed below:

- Both CFD simulation and 3D printed in vivo experiments failed to predict the dominant flow side and flow rate compared to rhinomanometry results. Thus, in vitro and in silico results were reported as unfit to be validated through rhinomanometry.
- Numerical simulation and in vivo experiment results matched better to the results of rhinomanometry after anemization. This result has suggested that nasal mucosa could not be properly reproduced in CT scans.
- The exclusion of sinuses during the CFD simulations resulted in 2 % difference in flow prediction given constant pressure boundaries.
- During model generation, automatic threshold algorithms, e.g., Otsu's method, provided closer results to rhinomanometry results.
- Offsetting the generated geometry even by a half CT scan's pixel results in up to 46 % difference in flow rates. This result has indicated that the resolution of a CT scan is vitally important.

Critically, there were some odd choices in Karbowski et al. (2023)'s work. The authors opted to use a human subject behind the 3D-printed nasal cavity rather than using

[5] A procedure aimed to reduce nasal mucous swelling, also known as adrenalization of the nasal mucosa.

constant pressure, a breathing curve, or a constant flow rate. For example, a comparison between CFD simulations and laboratory rhinomanometry measurements was made by Cherobin et al. (2021) and Pawade (2021), demonstrating a close match between CFD simulations and rhinomanometry measurements.

On another note, a study by Inthavong et al. (2014) have done 2D mapping of simulation results along with validation of the results with the experimental results. This work suggested that by 2D mapping the numerical simulation results, numerical simulations can be enhanced in understanding the nasal cavity flows. Moreover, the best line fit to their pressure-drop versus discharge levels is obtained as $\Delta p = 0.059Q^2$. This result was found to be similar to other simulations, with slight deviations. Controversially, in vitro experimental results of Garcia et al. (2009) suggested that the exponent of the discharge, Q, was between 1.76 and 1.85.

3.5.7 Virtual Surgeries Using CFD Simulations

Since the results of some numerical simulations are well correlated to nasal patency ratings, Sanmiguel-Rojas et al. (2018) generated a way to assign healthy and unhealthy nasal flows by statistically analyzing healthy and unhealthy nasal numerical simulations. The assignment is done through two estimator variables: airflow variation and total nasal resistance. The first variable is obtained by considering degrees of asymmetric airflow and nasal obstruction. The second one is obtained by representing nasal resistance value in some dimensionless form. Plotting these two variables for all the individuals, Sanmiguel-Rojas et al. (2018) realized that healthy individuals densely reside in an area in this graph. Later on, the same group of scientists applied the two estimator-based method to unhealthy nasal geometries in on computer-based environment: A surgeon altered the nasal geometry to get the estimators into the healthy airflow range (Sanmiguel-Rojas et al., 2018). It is critical to note that, as shown by other works of Li, Jiang, et al. (2017), Malik et al. (2022), and Zhao and Jiang (2014), local airflow rates in the cavity, heat transfer rates, and localized wall shear stress rates appear to be powerful indicators of nasal obstruction. However, Sanmiguel-Rojas et al. (2018)'s method does not consider such variables but only flow balances between passageways and the nasal resistances. Therefore, further reports and research

are needed to prove that the two-estimator-based method is promising.

CHAPTER 4

FLUID MECHANICS BACKGROUND

In this chapter, only LES-related information is given to the reader. The fundamental fluid mechanics-related topics are preferred to be given in Appendix A to avoid presenting irrelevant information to the reader.

4.1 Large Eddy Simulations

LES is a turbulence modeling approach that lies between RANS and DNS approaches. Unlike RANS, LES does not try to model large turbulent structures, which are dependent on geometries that are non-universal, i.e., hard to model. Unlike DNS, LES does not try to solve small-scale turbulent structures, which are universal, i.e., easy to model. Thus, the strategy of this technique is to solve the large-scale eddies while modeling the small-scale eddies.

Large-scale eddies in a turbulent flow carry most of the energy, cause most of the transportation, and are highly dependent on the geometry and boundaries. Also, they are anisotropic, inhomogeneous, non-universal, and challenging to model. These characteristics suggest that large-scale structures are the most critical in turbulence, since they are the main actors. Additionally, since the characteristics of the large-scale eddies are dominantly determined by the mean flow characteristics, correctly modeling the large-scale eddies in a single approach is challenging, if not impossible. Because of these reasons, LES attempts to resolve them directly. Moreover, the resolution of the large-scale structures are not very computationally demanding, since mesh detail is not needed to immensely increase to obtain the large-scale eddies.

Small-scale eddies in a turbulent flow act like a sink that takes the energy given by larger structures and loses the given energy to viscosity. The flow geometry and boundaries do not change them. They are isotropic, homogeneous, universal, and easy to model. These traits mean that small-scale structures do not strongly decide the main features of the flow; they merely collect the energy given by larger structures. Furthermore, small-scale eddies are inherently minuscule-sized; thus, a detailed mesh is required if resolved. In order to separate large structures from small structures, governing equations are averaged spatially, or, in other words, filtered. The filtering operation resembles the Reynolds averaging approach, though there are differences. Fundamentally, the small-scale turbulent structures are left as a single variable to model using specific methods after filtering. Similar to the Reynolds decomposition method, it is possible to write any variable as the summation of the filtered and unfiltered counterpart:

$$f = \overline{f} + f''. \tag{4.1}$$

Moreover, a general representation of the filtered variable $\overline{f}$, which is essentially convolution, is shown by Leonard (1975) as:

$$(G * f)(\boldsymbol{x}, t) = \overline{f}(\boldsymbol{x}, t) = \int_{-\infty}^{\infty}\int_{-\infty}^{\infty}\int_{-\infty}^{\infty} G(\boldsymbol{x} - \boldsymbol{\chi}, \Delta) f(\boldsymbol{x}, t) \mathrm{d}^3\boldsymbol{\chi} \tag{4.2}$$

$$= \int_{-\infty}^{\infty}\int_{-\infty}^{\infty}\int_{-\infty}^{\infty} G(\boldsymbol{x}, \Delta) f(\boldsymbol{x} - \boldsymbol{\chi}, t) \mathrm{d}^3\boldsymbol{\chi}, \tag{4.3}$$

where $G(\boldsymbol{x}, \Delta)$ is the filtering function, Δ is the filter width. Additionally, filtering might also be expressed as Equation 4.3 because of the commutativity characteristic of the convolution operation.

There are many functions to select as the filtering function $G(\boldsymbol{x}, \Delta)$. However, most commonly, there are three functions in LES: box or top-hat, sharp spectral, and Gaussian. Nonetheless, the box filter is exclusively used in finite volume discretization-based LES (Davidson, 2023; Versteeg & Malalasekra, 2007). The box filter is shown

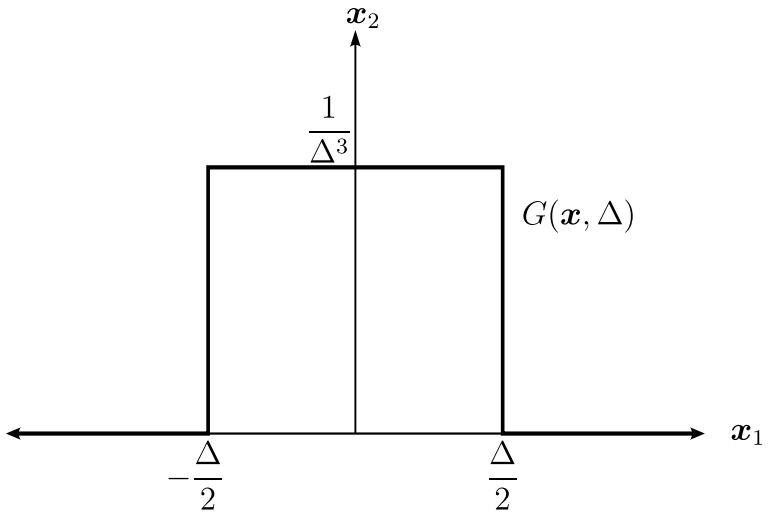

Figure 4.1. Top-Hat or Box Function on a 2D Plane

in Figure 4.1, and given as:

$$G(\boldsymbol{x}, \Delta) = \begin{cases} \frac{1}{\Delta^3}, & |x| < \Delta/2 \\ 0, & |x| > \Delta/2 \end{cases}, \tag{4.4}$$

where filter width Δ could be calculated in various ways, though commonly it is calculated directly as $\Delta = \sqrt[3]{\Delta\boldsymbol{x}_1\Delta\boldsymbol{x}_2\Delta\boldsymbol{x}_3}$.

Since a definition for the separation of large and small scales, filtering, is given now, it is possible to apply this operation to the Navier-Stokes equations. As mentioned earlier, filtering is reasonably similar to Reynolds averaging, except for $\overline{\overline{f}} \neq \overline{f}$ and $\overline{f''} \neq 0$. Even though these exceptions may change based on the used filter function, $G(\boldsymbol{x}, t)$, for the box filter, they stand correct. Noting that, the box filter is selected in this thesis since the software to conduct the simulations, *OpenFOAM*, uses the finite volume method. As a numerical method, the finite volume method introduces filtering by itself, referred to as an implicit filter. The implicit filter arises because the discretized geometry shapes the flow as an averaged form of the flow field over the mesh cells. Therefore, using another filtering kernel would mean that the flow field is filtered twice: first by implicit filtering and then by the selected filtering. Therefore, explicit filtering with another filtering function is unnecessary.

The proper convolution function must satisfy properties to be used as a filtering function, as given below (Sagaut, 2005):

1) $\int_{-\infty}^{\infty}\int_{-\infty}^{\infty}\int_{-\infty}^{\infty} G(\boldsymbol{x}-\boldsymbol{\chi},\Delta)\mathrm{d}^3\boldsymbol{\chi} = 1$, this is demanded by the selected function.

2) For a constant c, $\overline{c} = c$, due to item 1.

3) $\overline{f(\boldsymbol{x},t)+g(\boldsymbol{x},t)} = \overline{f}(\boldsymbol{x},t)+\overline{g}(\boldsymbol{x},t)$, this holds for any convolution, kernel since integral is a linear operator.

4) Commutes with derivation: $\overline{\dfrac{\partial f(\boldsymbol{x},t)}{\partial x}} = \dfrac{\partial \overline{f}(\boldsymbol{x},t)}{\partial x}$. This is true if the limits of filtering is finite and is not a function of derivative's variables. Since such a construction will vanish the extra terms in the Leibniz integral rule (check Subsection A.1.4 for the Leibniz integral rule).

4.1.1 Filtering Incompressible Conservation of Mass Equation

The filtering of the incompressible conservation of mass equation is straightforward, as shown below:

$$\overline{\frac{\partial u_i}{\partial x_j}} = 0 \tag{4.5}$$

$$\frac{\partial \overline{u}_i}{\partial x_j} = 0, \tag{4.6}$$

the second line is obtained using the 4$^{\text{th}}$ property of the filtering operation given earlier.

4.1.2 Filtering Incompressible Navier-Stokes Equations

As expected, filtering the incompressible Navier-Stokes equations involves more than the conservation of mass equation. The non-linear terms in the Navier-Stokes equations

raise problems, like in RANS. The filtered equations may be written as:

$$\overline{\rho\frac{\partial u_i}{\partial t}} + \overline{\rho\frac{\partial u_i u_j}{\partial x_j}} = -\overline{\frac{\partial p}{\partial x_i}} + \overline{\mu\frac{\partial^2 u_i}{\partial x_j \partial x_j}} \tag{4.7}$$

$$\rho\frac{\partial \overline{u}_i}{\partial t} + \rho\frac{\partial \overline{u_i u_j}}{\partial x_j} = -\frac{\partial \overline{p}}{\partial x_i} + \mu\frac{\partial^2 \overline{u}_i}{\partial x_j \partial x_j}, \tag{4.8}$$

since $\overline{u_i u_j}$ is not known, it can not be calculated in terms of filtered variables; however, separately filtered components of velocity, $\overline{u_i}$ and $\overline{u_j}$, are known. Therefore, by adding and subtracting separately filtered components to the left-hand side of the equations, the Navier-Stokes equations may be rewritten as follows:

$$\rho\frac{\partial \overline{u}_i}{\partial t} + \rho\frac{\partial \overline{u_i u_j}}{\partial x_j} - \rho\frac{\partial \overline{u}_i \overline{u}_j}{\partial x_j} + \rho\frac{\partial \overline{u}_i \overline{u}_j}{\partial x_j} = -\frac{\partial \overline{p}}{\partial x_i} + \mu\frac{\partial^2 \overline{u}_i}{\partial x_j \partial x_j} \tag{4.9}$$

$$\rho\frac{\partial \overline{u}_i}{\partial t} + \rho\frac{\partial\Big(\overline{u_i u_j} - \overline{u}_i \overline{u}_j\Big)}{\partial x_j} + \rho\frac{\partial \overline{u}_i \overline{u}_j}{\partial x_j} = -\frac{\partial \overline{p}}{\partial x_i} + \mu\frac{\partial^2 \overline{u}_i}{\partial x_j \partial x_j}, \tag{4.10}$$

defining sub-grid scale tensor as $\tau_{ij} = \rho\overline{u_i u_j} - \overline{u}_i \overline{u}_j$. Now the equations read:

$$\rho\frac{\partial \overline{u}_i}{\partial t} + \frac{\partial \tau_{ij}}{\partial x_j} + \rho\frac{\partial \overline{u}_i \overline{u}_j}{\partial x_j} = -\frac{\partial \overline{p}}{\partial x_i} + \mu\frac{\partial^2 \overline{u}_i}{\partial x_j \partial x_j} \tag{4.11}$$

$$\rho\frac{\partial \overline{u}_i}{\partial t} + +\rho\frac{\partial \overline{u}_i \overline{u}_j}{\partial x_j} = -\frac{\partial \overline{p}}{\partial x_i} + \mu\frac{\partial^2 \overline{u}_i}{\partial x_j \partial x_j} - \frac{\partial \tau_{ij}}{\partial x_j} \tag{4.12}$$

$$\rho\frac{\partial \overline{u}_i}{\partial t} + \rho\frac{\partial \overline{u}_i \overline{u}_j}{\partial x_j} = \frac{\partial}{\partial x_i}\big(-\overline{p} + 2\mu\overline{S}_{ij} - \tau_{ij}\big). \tag{4.13}$$

The filtered Navier-Stokes equations appear almost precisely as the URANS equations found in Equation A.189. The difference is that the newly introduced stress term in LES only covers the small-scale turbulent fluctuations, whereas in URANS, the stress term has to model all the turbulent scales. Moreover, the stress term in LES can be further investigated, unlike its RANS counterpart. Exploring the sub-grid stress term in LES could be done by expanding the non-linear term in the sub-grid stress term. Interestingly, the variables arising from this expansion could be physically interpreted.

The physical interpretation is possible as splitting terms:

$$\tau_{ij} = \rho\overline{u_i u_j} - \rho\overline{u}_i\overline{u}_j \tag{4.14}$$

$$= \rho(\overline{u_i u_j} - \overline{u}_i\overline{u}_j) \tag{4.15}$$

$$= \rho(\overline{(u_i + u_i'')(u_j + u_j'')} - \overline{u}_i\overline{u}_j) \tag{4.16}$$

$$= \rho(\overline{u_i u_j} + \overline{u_i u_j''} + \overline{u_i'' u_j} + \overline{u_i'' u_j''} - \overline{u}_i\overline{u}_j) \tag{4.17}$$

$$= \rho(\overline{u_i u_j} - \overline{u}_i\overline{u}_j + \overline{u_i u_j''} + \overline{u_i'' u_j} + \overline{u_i'' u_j''}), \tag{4.18}$$

Now, the variables in the sub-grid scale stress tensor may be grouped into meaningful terms as:

$$L_{ij} = \rho(\overline{u_i u_j} - \overline{u}_i\overline{u}_j), \tag{4.19}$$

$$C_{ij} = \overline{u_i u_j''} + \overline{u_i'' u_j}, \tag{4.20}$$

$$R_{ij} = \overline{u_i'' u_j''}, \tag{4.21}$$

where this grouping turns the sub-grid scale stress tensor into,

$$\tau_{ij} = L_{ij} + C_{ij} + R_{ij}. \tag{4.22}$$

On this grouped form of sub-grid scale stress tensor, L_{ij} corresponds to Leonard tensor representing the stresses arising due to large-scale structure interactions. C_{ij} corresponds to Clark or cross-stress tensor portraying the stresses appearing by the interactions of large and small scale structures. Lastly R_{ij} corresponds to Reynolds sub-grid stress tensor defining the stresses emerging from the intercourse of small scale structures. All of these terms are unknown and must be modeled to close the filtered Navier-Stokes equations.

4.1.3 Incompressible Smagorinsky Model

Smagorinsky model is the first attempt in LES to model a sub-grid scale stress tensor, τ_{ij}^{SGS}, which was proposed by Smagorinsky (1963). This model uses Boussinesq's eddy viscosity approach to model the sub-grid scale stress tensor, which claims strain rate and stress are related. Moreover, the Smagorinsky model starts from an assumption that sub-grid scale kinetic energy production and dissipation are equal to each other.

Boussinesq's eddy viscosity approach is generalized for Reynolds stress in the earlier Subsection A.4.5, and the generalized incompressible form is given in Equation A.208. If the generalized form is used in filtered sub-grid scale representation, it becomes:

$$\tau_{ij}^{\mathrm{SGS}} = -2\mu^{\mathrm{SGS}}\overline{S}_{ij} + \frac{2}{3}\delta_{ij}\rho k^{\mathrm{SGS}}, \tag{4.23}$$

where μ^{SGS} refers to sub-grid scale viscosity and k^{SGS} is the sub-grid scale kinetic energy. Noting that k^{SGS} can also be expressed as $\frac{1}{2}\tau_{kk}^{\mathrm{SGS}}$.

The eddy viscosity approach does not say anything about sub-grid scale viscosity. However, attacking the sub-grid scale viscosity on dimensional grounds gives a chance to start the exploration. Now, if the kinematic sub-grid scale viscosity, $\nu = \mu/\rho$, is considered, the dimensions are read as L^2/T Accordingly, kinematic viscosity can be written as a multiplication of a length scale, ℓ, and a velocity term, u.

$$\nu^{\mathrm{SGS}} = \ell u = \ell\left(\ell\frac{\Delta u}{\ell}\right). \tag{4.24}$$

In the above dimensional analysis, the length scale, ℓ, should be understood as a variable representing all the sub-grid scale eddies. In the Smagorinsky model, this variable is approximated as a proportion of the filter width, Δ. The proportionality is introduced by a constant called the Smagorinsky constant, C_{S}, and this constant should be between 0 and 1, since sub-grid scale eddy's size can not exceed filter width, i.e., $C_{\mathrm{S}} > 1$ or become negative, i.e., $C_{\mathrm{S}} < 0$.

On the other hand, the velocity, u, represents the speed of all the sub-grid scale eddies as a single value, which is further decomposed as a length scale and a term with a ratio

of velocity to length. Critically, the velocity representation should not be affected by coordinate transformations; moreover, since sub-grid scale eddies essentially arise due to turbulence, this value should be able to mimic how turbulence behaves correctly. The length scale is already an invariant. The invariant value for the acceleration term, $\frac{\Delta u}{\ell}$ is selected to be the magnitude of the second invariant of the shear rate tensor [1].

In light of this discussion, one may define Smagorinsky's representation of sub-grid scale kinematic viscosity as below:

$$\nu^{\mathrm{SGS}} = (C_{\mathrm{S}}\Delta)\left[(C_{\mathrm{S}}\Delta)\,|I_2(D_{ij})|\right] \tag{4.25}$$

$$= (C_{\mathrm{S}}\Delta)^2\,|I_2(2S_{ij})| \tag{4.26}$$

$$= (C_{\mathrm{S}}\Delta)^2\sqrt{\frac{1}{2}\Big[(\mathrm{tr}(2S_{ij}))^2 - tr((2S_{ij})^2)\Big]} \tag{4.27}$$

$$= (C_{\mathrm{S}}\Delta)^2\sqrt{\frac{1}{2}\Big((4S_{ii}^2) - tr(4S_{ij}S_{jk})\Big)} \tag{4.28}$$

$$= (C_{\mathrm{S}}\Delta)^2\sqrt{\frac{1}{2}\Big(0 - 4S_{ij}S_{ji}\Big)} \tag{4.29}$$

$$= (C_{\mathrm{S}}\Delta)^2\sqrt{\frac{1}{2}\Big(4S_{ik}S_{ki}\Big)} \tag{4.30}$$

$$= (C_{\mathrm{S}}\Delta)^2\sqrt{2S_{ik}S_{ik}}, \tag{4.31}$$

here D_{ij} represents shear rate tensor. At Equation 4.29, incompressibility causes $S_{ii} = 0$, and at Equation 4.31, the symmetry property of the strain rate tensor is used, i.e., $S_{ji} = S_{ij}$.

[1] The curious reader may question the reason behind not using the Frobenius norm of velocity to get the invariant magnitudes. The usage of the Frobenius norm is acceptable except for the incorrect results by $\sqrt{2}$ arise since the shear rate is made symmetric by using a summation of two velocity gradients; noting that, usage of the strain rate tensor also causes a similar error. The errors can be seen if the prediction of simple flows such as 2D shear flow, is conducted. While shear rate's second principal invariant yields the correct results, the Frobenius norm of it does not. Interested readers may refer to Bird et al. (1987) for more information, yet they are warned that Bird et al. (1987) represent the magnitude with half of the Frobenius norm; this is what the second invariant boils down to after incorporating the incompressibility.

4.1.4 Alternative Way to Derive Incompressible Smagorinsky Model

At the sub-grid scale levels, Smagorinsky (1963) assumes that turbulence is isotropic and that the sub-grid scale turbulence's kinetic energy remains stationary. This stationary kinetic energy level for the sub-grid scale suggests that the production of sub-grid scale energy is equal to the dissipation of the sub-grid scale kinetic energy.

Expectedly, sub-grid scale kinetic energy production is equal to the dissipation of filtered kinetic energy. Expressing the production of sub-grid scale kinetic energy as the dissipation of filtered kinetic energy:

$$\mathcal{P}^{\mathrm{SGS}} = -\Big(\overline{u_i u_j} - \overline{u}_i \overline{u}_j\Big)\frac{\partial \overline{u}_i}{\partial x_j} \tag{4.32}$$

$$= -\frac{\tau_{ij}^{\mathrm{SGS}}}{\rho}\frac{\partial \overline{u}_i}{\partial x_j} \tag{4.33}$$

$$= \left(2\nu^{\mathrm{SGS}}\overline{S}_{ij} - \frac{2}{3}\delta_{ij}k^{\mathrm{SGS}}\right)\frac{\partial \overline{u}_i}{\partial x_j} \tag{4.34}$$

$$= 2\nu^{\mathrm{SGS}}\overline{S}_{ij}\frac{\partial u_i}{\partial x_j} - \frac{2}{3}\delta_{ij}k^{\mathrm{SGS}}\frac{\partial u_i}{\partial x_j} \tag{4.35}$$

$$= 2\nu^{\mathrm{SGS}}\overline{S}_{ij}\Big(\overline{S}_{ij} + \overline{\Omega}_{ij}\Big) - \frac{2}{3}k^{\mathrm{SGS}}\overbrace{\frac{\partial \overline{u}_i}{\partial x_i}}^{0} \tag{4.36}$$

$$= 2\nu^{\mathrm{SGS}}\overline{S}_{ij}\overline{S}_{ij} + 2\nu^{\mathrm{SGS}}\overbrace{\overline{S}_{ij}\overline{\Omega}_{ij}}^{0} \tag{4.37}$$

$$= 2\nu^{\mathrm{SGS}}\overline{S}_{ij}\overline{S}_{ij}, \tag{4.38}$$

noting that on the 3th line, $\frac{\partial u_k}{\partial x_k} = 0$ due to incompressibility, and on the 4th line, $\overline{S}_{ij}\overline{\Omega}_{ij} = 0$ since multiplication of a symmetric and a skew-symmetric tensor is 0.

The dissipation of the sub-grid scale may be expressed with the help of dimensional analysis. The sub-grid scale kinetic energy dissipation is in the exact dimensions as other terms in the sub-grid scale kinetic energy equation, i.e., the filtered Navier-Stokes equation multiplied by a velocity term. This dimensional equality implies that the

dimensions of any variable in the kinetic energy equation may be found easily. When this is done, dimensions are found as dimensions of $\frac{L^2}{T^3}$, noting that before derivation, the whole equation is divided by the density term.

Since sub-grid scale dissipation is defined in generic terms, the dimensional analysis may be used to define dissipation in terms of known terms. For sub-grid scale kinetic energy, dissipation may be represented as,

$$\epsilon^{\mathrm{SGS}} = C_\epsilon \frac{L^2}{T^3} \tag{4.39}$$

$$= C_\epsilon \left(\frac{L^2}{T}\right)^{\frac{3}{2}} \frac{1}{L} \tag{4.40}$$

$$\epsilon^{\mathrm{SGS}} = C_\epsilon \frac{\left(k^{\mathrm{SGS}}\right)^{\frac{3}{2}}}{\Delta}, \tag{4.41}$$

and in terms of ν^{SGS},

$$\epsilon^{\mathrm{SGS}} = \frac{L^2}{T^3} \tag{4.42}$$

$$= \left(\frac{L^2}{T}\right)^3 \frac{1}{L^4} \tag{4.43}$$

$$= \frac{\left(\nu^{\mathrm{SGS}}\right)^3}{\left(C_{\mathrm{S}}\Delta\right)^4}. \tag{4.44}$$

As indicated earlier, the crux of the matter in the Smagorinsky method is that dissipation

and production should be equal to each other,

$$\epsilon^{\mathrm{SGS}} = \mathcal{P}^{\mathrm{SGS}} \tag{4.45}$$

$$\frac{\left(\nu^{\mathrm{SGS}}\right)^3}{(C_{\mathrm{S}\Delta)^4}} = 2\nu^{\mathrm{SGS}}\overline{S}_{ij}\overline{S}_{ij} \tag{4.46}$$

$$\left(\nu^{\mathrm{SGS}}\right)^2 = (C_{\mathrm{S}}\Delta)^4 2\overline{S}_{ij}\overline{S}_{ij} \tag{4.47}$$

$$\nu^{\mathrm{SGS}} = (C_{\mathrm{S}}\Delta)^2\sqrt{2\overline{S}_{ij}\overline{S}_{ij}}. \tag{4.48}$$

4.1.5 Calculation of Sub-Grid Scale Kinetic Energy

Smagorinsky model is a 0-equation model: There are no additional equations to solve but conservation of mass and momentum equations. However, it is not possible to estimate the sub-grid scale stress

$$\tau_{ij}^{\mathrm{SGS}} = -2\mu^{\mathrm{SGS}}\overline{S}_{ij} + \frac{2}{3}\delta_{ij}\rho k^{\mathrm{SGS}}, \tag{4.49}$$

since k^{SGS} is not expressed in known variables. Note that, the μ^{SGS} can be written in Smagorinsky model as:

$$\nu^{\mathrm{SGS}} = (C_{\mathrm{S}}\Delta)^2\sqrt{2S_{ij}S_{ij}}. \tag{4.50}$$

Surprisingly, just like the derivation of the Smagorinsky model, it is possible to construct an expression expressing k^{SGS} by assuming production of k^{SGS} is equal to dissipation of k^{SGS}. However, this time dimensional analysis should be conducted to express ν^{SGS} in terms of k^{SGS}; when this dimensional analysis is done, ν^{SGS} is found as:

$$\nu^{\mathrm{SGS}} = C_{\mathrm{k}}\sqrt{k^{\mathrm{SGS}}}\Delta, \tag{4.51}$$

where C_k is the proportionality constant.

Now, equating the sub-grid scale kinetic energy dissipation and incompressible sub-grid scale kinetic energy production terms in order to express k^{SGS},

$$\epsilon^{\mathrm{SGS}} = \mathcal{P}^{\mathrm{SGS}} \tag{4.52}$$

$$C_\epsilon \frac{\left(k^{\mathrm{SGS}}\right)^{3/2}}{\Delta} = 2\nu^{\mathrm{SGS}} \overline{S}_{ij} \overline{S}_{ij} \tag{4.53}$$

$$C_\epsilon \frac{\left(k^{\mathrm{SGS}}\right)^{3/2}}{\Delta} = 2C_{\mathrm{k}} \sqrt{k^{\mathrm{SGS}}} \Delta \overline{S}_{ij} \overline{S}_{ij}. \tag{4.54}$$

Finally, simplifying the equation above yields

$$k^{\mathrm{SGS}} = \frac{C_k}{C_\epsilon} \Delta^2 (2\overline{S}_{ij} \overline{S}_{ij}). \tag{4.55}$$

The constant C_k must be stated to complete the discussion. C_k can be found by equating Smagorinsky model's ν^{SGS} definition with current ν^{SGS} definition given in Equation 4.51.

$$\nu^{\mathrm{SGS}} = C_{\mathrm{k}} \sqrt{k^{SGS}} \Delta = (C_{\mathrm{S}} \Delta)^2 \sqrt{2 S_{ij} S_{ij}} \tag{4.56}$$

$$C_{\mathrm{k}} \sqrt{\frac{C_k}{C_\epsilon} \Delta^2 2 \overline{S}_{ij} \overline{S}_{ij}} \Delta = (C_{\mathrm{S}} \Delta)^2 \sqrt{2 S_{ij} S_{ij}} \tag{4.57}$$

$$\frac{C_{\mathrm{k}}^{3/2}}{C_\epsilon} = C_{\mathrm{S}}^2. \tag{4.58}$$

Further simplifying the above expression yields the connection between C_{k} and C_ϵ:

$$C_{\mathrm{S}} = \sqrt{\frac{C_{\mathrm{k}}^{3/2}}{C_\epsilon}}. \tag{4.59}$$

In *OpenFOAM*, the constants are selected as $C_{\mathrm{k}} = 0.094$ and $C_\epsilon = 1.048$ which give

Smagorinsky constant by using the above formula as $C_{\mathrm{S}} \approx 0.166$. On the other hand, Lilly (1966) has estimated these values for homogeneous turbulence to be $C_{\mathrm{k}} = 0.094$ and $C_{\epsilon} = 0.93$; hence $C_{\mathrm{S}} \approx 0.176$.

4.1.6 Shortcomings of Smagorinsky Model

Since the Smagorinsky model is the simplest and the first sub-grid scale modeling attempt, this model has numerous shortcomings. Later, researchers built upon these shortcomings to improve the Smagorinsky model to align with experimental and DNS results, which reflect turbulence better. Nevertheless, below are some noteworthy issues with the Smagorinsky model:

- The sub-grid scale turbulent viscosity, ν^{SGS}, does not vanish in the vicinity of walls where the flow becomes laminar (Kajishima & Taira, 2016; Nicoud & Ducros, 1999; Rodi et al., 2013). The non-zero ν^{SGS} near the walls is a terrible behavior, and in order to salvage the model, dampening functions are often applied.

- Since the sub-grid scale turbulent viscosity, ν^{SGS}, becomes 0 only when there is no strain rate. Therefore, the Smagorinsky model produces turbulence-related stresses even during the laminar flow, suggesting that laminar to turbulent transitions can not be modeled (Rodi et al., 2013).

- Rotation of the fluid elements plays a role in turbulence transportation; their effects are entirely dismissed from the model (Bardina, 1983; Lund & Novikov, 1993; Nicoud & Ducros, 1999).

- Smagorinsky model can only dissipate energy; it can not transfer energy back to the grid scale, referred to as backscatter (Kajishima & Taira, 2016; Rodi et al., 2013). Even though energy transportation happens from larger scales to smaller scales in an average sense, the transfer of energy towards large structures is possible in some random local regions (Kajishima & Taira, 2016). Interestingly, channel flow DNS results of Piomelli et al. (1991) show 50 % of the cells are backscattering, which suggests backscatter is not a rare event. The reason of such a limitation is straightforward: ν^{SGS} value is always positive; thus, production of

sub-grid scale kinetic energy, $\mathcal{P}^{\mathrm{SGS}}$, Equation 4.38, is always positive (Kajishima & Taira, 2016; Rodi et al., 2013).

- Smagorinsky constant, C_{S} has to be calibrated differently based on flow type in order to mimic turbulent behavior correctly. Thus, C_{S} is not a universal constant (Kajishima & Taira, 2016; Rodi et al., 2013). The reason for the requirement for calibration can be attributed to one of the other problems of the model: misbehavior near walls (Sagaut, 2005). In order to remedy the Smagorinsky model's problems, throughout its development, researchers forced the model to function by setting Smagorinsky constants differently based on flow types.

4.1.7 Wall-Adapting Local Eddy-Viscosity Model

The WALE model is another attempt to calculate the sub-grid scale viscosity for LES by Nicoud and Ducros (1999). While WALE avoids the mistakes in the Smagorinsky model, the simplicity is kept. Unlike the Smagorinsky model, the WALE model attempts to model laminar-to-turbulent behavior, provides a universal constant, and considers rotational rate in turbulence generation. Most importantly, WALE imitates the correct turbulence behavior near walls. The model uses a similar structure to the Smagorinsky model, as follows:

$$\nu^{\mathrm{SGS}} = C_{\mathrm{m}}\Delta^2\overline{\mathrm{OP}}(\boldsymbol{x}, t), \tag{4.60}$$

where C_{m} is a constant and $\overline{\mathrm{OP}}(\boldsymbol{x}, t)$ is an operator connecting filtered variables to sub-grid scale viscosity. The WALE model's simple, but effective approach is to pick this operator carefully; thus, there is no need for a complex, computationally demanding algorithm or a challenging implementation requirement. Furthermore, as stated by Nicoud and Ducros (1999), this operator has to satisfy some properties in order to accomplish the behavior of turbulence properly: invariance to coordinate transformations, being easily accessible during CFD simulations, being a function of both strain and rotation rate, and correct asymptotic behavior near the walls, i.e., $\nu^{\mathrm{SGS}} \propto O(y^3)$. In order to provide such an operator, Nicoud and Ducros (1999) started

their approach with a filtered velocity gradient tensor,

$$\overline{g}_{ij} = \frac{\partial \overline{u}_i}{\partial x_j} = \overline{S}_{ij} + \overline{\Omega}_{ij}, \tag{4.61}$$

which is a perfect operator since it depends on both strain-rate and rotation-rate tensors. Unfortunately, this operator also falls into the same pitfall as the Smagorinsky operator: non-physical behavior near the wall, $\overline{OP} \propto O(1)$ when $y \to 0$. In order to remedy this issue, there is a need for a function that at least behaves $\overline{OP} \propto O(y)$ when $y \to 0$. One of the most basic tensors providing this feature is the symmetric part of the square of the velocity gradient tensor, i.e., $\overline{g}^2_{ij} = \overline{g}_{ik}\overline{g}_{kj}$:

$$\overline{\mathcal{S}}_{ij} = \frac{1}{2}\big(\overline{g}_{ik}\overline{g}_{kj} + \overline{g}_{jk}\overline{g}_{ki}\big) = \frac{1}{2}\big(\overline{g}^2_{ij} + \overline{g}^2_{ji}\big). \tag{4.62}$$

Even though the square of the velocity gradient tensor's symmetric part provides $O(y)$ behavior, the authors of WALE prefer to use the deviatoric, or traceless, part of this tensor. The reason for selecting a traceless tensor is not given explicitly; nevertheless, one may speculate that there may be two reasons:

- The traceless tensor separates two phenomena that the symmetric part of the square of the velocity gradient tensor represents: rate of volume change and rate of shear tensor. Volume change is related to the trace of the tensor, and it may be thought not to cause turbulent action; hence, discard the trace.
- Discarding the trace of the tensor since the square of trace in the second invariant does not equal 0 through conservation of mass of incompressible flow, i.e., $[\mathrm{tr}(\mathcal{S}_{ij})]^2 = \mathcal{S}_{ii}\mathcal{S}_{jj} \neq 0$. Even though this is true, the coordinate system's invariant behavior in WALE can be directly determined by using the square of the Frobenius norm, $\mathrm{tr}(\mathcal{S}^2_{ij})$.

However, the reason for using the deviatoric part may be that this usage shockingly provides vanishing turbulent viscosity when the flow is in 2D, pure shear flow, which conforms with the physical behavior. This behavior also allows WALE to predict the laminar-to-turbulent transition, as shown by Nicoud and Ducros (1999).

The deviatoric part is expressed as:

$$\mathrm{dev}(\mathcal{S}_{ij}) = \frac{1}{2}\left(\overline{g}_{ij}^2 + \overline{g}_{ji}^2\right) - \frac{1}{3}\delta_{ij}\overline{g}_{kk}^2 \tag{4.63}$$

$$= \overline{S}_{ik}\overline{S}_{kj} + \overline{\Omega}_{ik}\overline{\Omega}_{kj} - \frac{1}{3}\delta_{ij}(\overline{S}_{mn}\overline{S}_{mn} + \overline{\Omega}_{mn}\overline{\Omega}_{mn}). \tag{4.64}$$

Still, the deviatoric part does not remain invariant under coordinate transformations. To address this problem, the authors of the WALE model utilized the Cayley–Hamilton theorem and assumed incompressibility to derive the second invariant of the deviatoric part as follows:

$$\mathrm{dev}(\mathcal{S}_{ij})\,\mathrm{dev}(\mathcal{S}_{ij}) = \frac{1}{6}\left(S^2S^2 + \Omega^2\Omega^2\right) + \frac{2}{3}S^2\Omega^2 + 2IV_{S\Omega}, \tag{4.65}$$

where the terms on the left-hand side are given as:

$$S^2 = \overline{S}_{ij}\overline{S}_{ij}, \qquad \Omega^2 = \overline{\Omega}_{ij}\overline{\Omega}_{ij}, \qquad IV_{S\Omega} = \overline{S}_{ik}\overline{S}_{kl}\overline{\Omega}_{jl}\overline{\Omega}_{li}.$$

However, the current expression is still incomplete, since it behaves in the order of y^2 near the wall and has dimensions of T^{-2}. This problem is solved by raising this expression to some power while keeping the dimension of the expression the same. In order words, one must get a behavior of $O(y^3)$ while the expression is in the dimensional grounds of T^{-1}. After such a transformation, with consideration of shielding against division by 0 error, the WALE model finally appears as,

$$\nu^{\mathrm{SGS}} = (C_{\mathrm{w}}\Delta)^2\frac{(\mathrm{dev}(\mathcal{S}_{ij})\,\mathrm{dev}(\mathcal{S}_{ij}))^{3/2}}{(\overline{S}_{ij}\overline{S}_{ij})^{5/2} + (\mathrm{dev}(\mathcal{S}_{ij})\,\mathrm{dev}(\mathcal{S}_{ij}))^{5/4}}, \tag{4.66}$$

where C_{w} is obtained by using isotropic turbulence simulations and by considering that the WALE model and Smagorinsky model behave similarly. Nicoud and Ducros (1999) suggested the WALE constant, C_{w}, to be between 0.55 and 0.60 if a similar value to Lilly (1966)'s theoretical calculation on Smagorinsky constant is used. The

Smagorinsky constant is thought to be around 0.185 by Lilly (1966)'s calculations and equal to 0.17 using the later work of Lilly (1967) with the Kolmogorov constant equal to 1.5, $C_{\mathrm{S}} = 0.23 C_{\mathrm{K}}^{-3/4}$.

However, since the Smagorinsky constant is derived under the isotropic turbulence assumption, LES using the Smagorinsky sub-grid scale model predicts too high dissipation of turbulent kinetic energy (Deardorff, 1970). Lower values equal to 0.1 yield satisfactory results; as suggested by Deardorff (1970). Furthermore, if this lower Smagorinsky constant is used to generate WALE's true constant, C_{w}, the result is obtained to be $0.324 \leq C_{\mathrm{w}} \leq 0.336$. Such a lower value of $C_{\mathrm{w}} = 0.325$ is the default value in *OpenFOAM*'s source code for the WALE model. Similarly, the documentation of ANSYS, Inc. (2009) reports the same value for the WALE constant. Nonetheless, no justification is found in either the *OpenFOAM*'s source code or the *Ansys Fluent*'s documentation. Moreover, the WALE constant's range using the lower Smagorinsky constant is just an observation of the current thesis work. Even though usage of a lower Smagorinsky constant for the Smagorinsky model makes sense given the near-wall behavior of the Smagorinsky model, there is no apparent reason to use this value to calculate WALE's constant if, as told by Nicoud and Ducros (1999), WALE model's constant C_{w} is a true constant.

CHAPTER 5

METHODS

This thesis's nasal airflow numerical simulations require surface mesh generation, volume mesh generation, and numerical simulations. In order to have satisfactory results from numerical simulations, all of these steps must be carefully conducted and examined. Therefore, this section is dedicated to these methods, giving a comprehensive overview.

5.1 Surface Mesh Generation From CT Scans

In order to simulate nasal airflow for an individual, the first step is the generation of patient-specific geometries. These geometries are commonly obtained using CT or MRI scans. However, as mentioned in Section 2.5.4, CT scans excel at distinguishing air from any other tissues in the body. This precision enables the extraction of air volume from the CT scans, allowing the generation of surface meshes from CT scans.

Even though air extraction is easily done, the correct radiodensity levels are critical to getting the volume correctly. For this, one must pick lower and upper limits, encompassing all the air-filled spaces. Air is known to have a -1000 HU, which describes the lower limit. However, the upper limit for radiodensity levels to extract air-filled space must be clearly defined. Cherobin et al. (2018) suggest that -800 HU as the upper limit leads to the best correlation, against -550 HU and -300 HU, between rhinomanometry and numerical simulation results. On the other hand, Nakano et al. (2013) reports around -460 HU leads to the lowest error in matching realistic nasal cavity volume.

Commonly, CT scans are taken in one of the anatomical planes: axial, sagittal, or coronal. The other two planes are generated by a process called multiplanar reconstruction. At the end of the whole process of generating of CT scans, only one plane is high in quality, and the other two are represented roughly. Therefore, the resulting 3D pixels, or voxels, are anisotropic, which means the voxels have unequal widths, heights, and depths. The conventional multi-detector CT machines result in non-isotropic scans, whereas newer tomography machines, such as cone-beam CT, can provide isotropic voxels (Velasco & Liang, 2021).

Since there are three different versions of a CT scan of the same individual, selecting the main anatomical plane while generating a surface mesh would result in different outcomes. Nevertheless, the selection of the main plane in order to generate the highest-quality surface mesh is the primary objective. Theoretically, more pixels in the main slices should yield a higher surface mesh quality.

In this work, there are two different CT scans, before and after; therefore, there are six options to pick from. One CT scan is based on the axial plane, and the other is on the sagittal plane. As mentioned earlier, selection is based on the number of pixels around the nasal cavity. Also, generated 3D geometries appeared better in quality. The axial-based CT scan is 512 by 512 pixels and has 213 slices through its axis. The pixels are 0.391 mm by 0.391 mm, and every slice is separated by 0.7 mm. The sagittal-based CT scan is also 512 by 512 pixels, but there are 179 slices. The pixels are 0.38 mm by 0.38 mm, and every slice is separated by 1 mm.

5.1.1 Steps to Create Surface Mesh in *3D Slicer*

To specify the radiodensity levels and generate the surface geometry, a free and open-source medical visualization software called *3D Slicer* is used. *3D Slicer* allows the extraction of surface geometry by using the aforementioned radiodensity thresholds. Moreover, many other capabilities exist, such as smoothing, warping, and cutting the geometry. *3D Slicer* allows the lower threshold value to be set to −1024 HU, most likely due to avoiding errors caused by the generation of CT scans. Therefore, a lower threshold is set to this level while generating surface mesh. For the high threshold level, −400 HU appears to provide the best visually examined result. However, throughout

the whole geometry, manual interventions are applied to correct the possible mistakes and eliminate artifacts. Furthermore, all the sinuses are removed from this surface geometry by using tools available in *3D Slicer*[1]. Removal of sinuses is a vital step since sinuses render the geometry convoluted; the complex geometry leads to a worse quality in the volume mesh and also cripples the solution performance in numerical simulations.

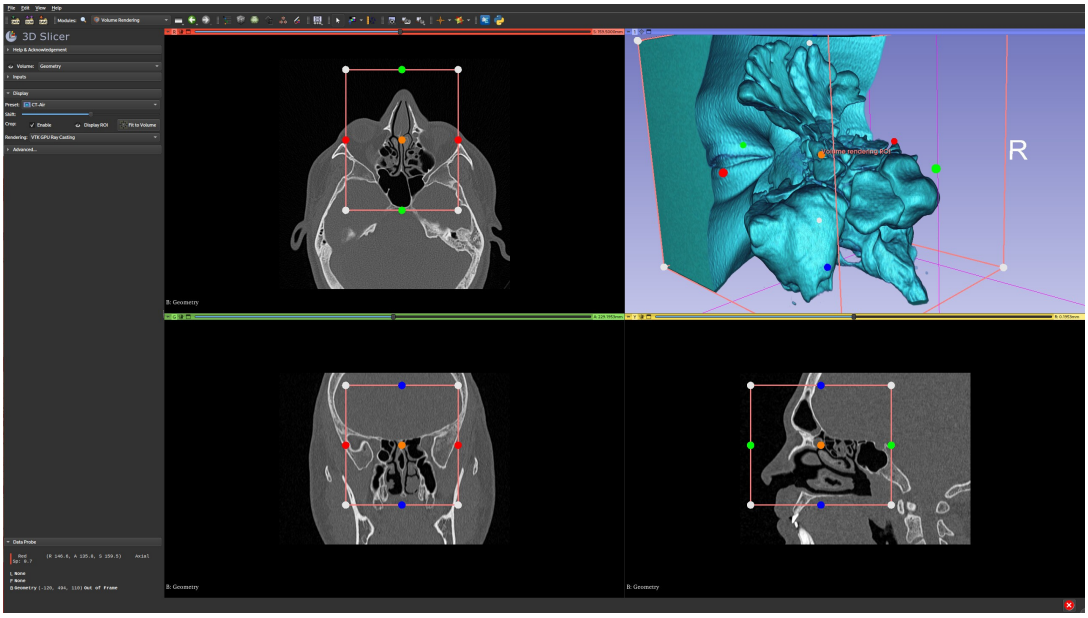

Figure 5.1. Demonstration of *3D Slicer*'s Volume Rendering Module

The reconstruction of the initial surface mesh from the CT scan is done in a few steps:

1) Add the folder containing CT scans to *3D Slicer*.

2) Load the desired CT scan under the *DICOM database*.

3) Simplify the CT scan: Switch to *Volume Rendering* module, set the region of interest limited around the nasal cavity to nasopharynx region as shown in Figure 5.1.

4) Crop the volume using *Crop Volume* module, which can be easily found by searching modules.

[1] Noting that Karbowski et al. (2023) showed that elimination of sinuses causes minuscule differences in numerical simulations.

5) Switch to *Segment Editor*, add a new segment. Set the radiodensity threshold levels by using *Threshold* option.

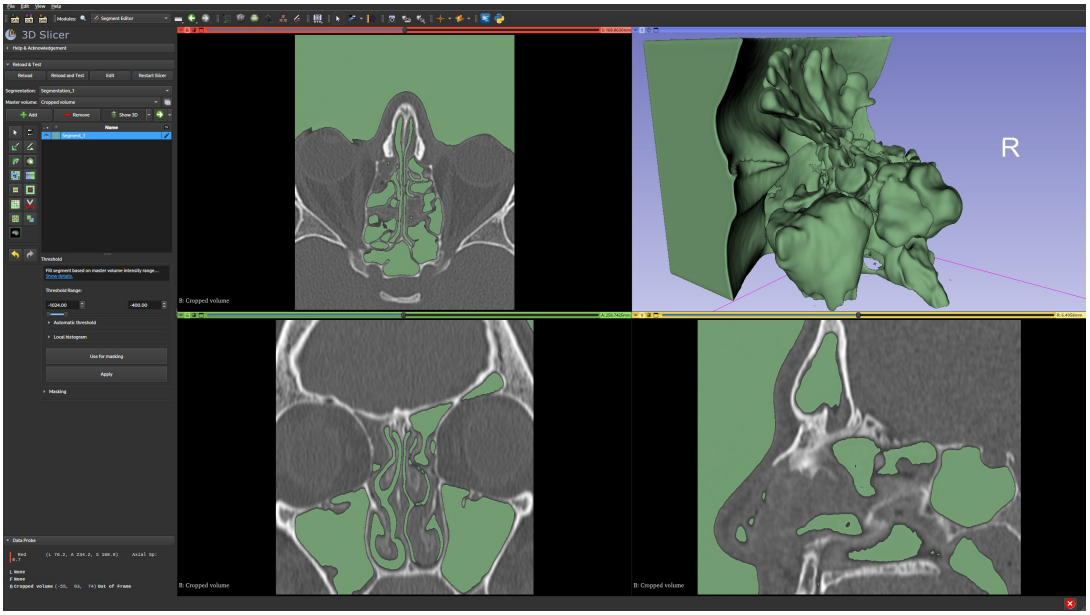

Figure 5.2. Radiodensity Threshold for Air in *3D Slicer*

6) Use *Islands* options to remove floating air volumes disconnected from the nasal cavity.

7) Using *Erase* and *Paint*, remove sinuses or add the misrepresented air in the nasal cavity.

8) Go to the *Segmentations* module and export the surface mesh in *.stl* file format.

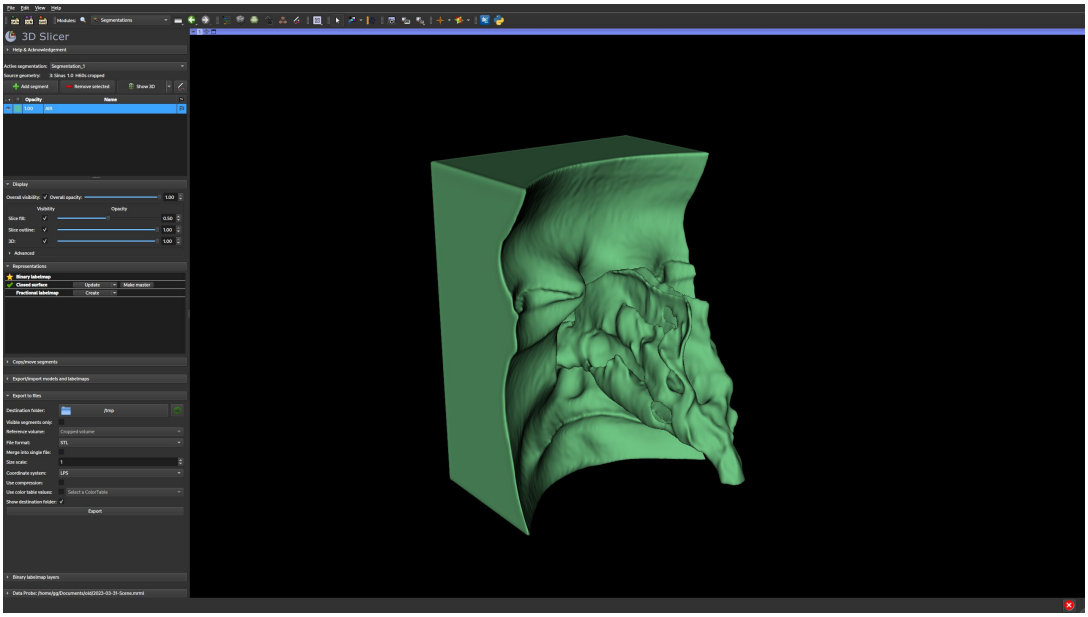

Figure 5.3. *3D Slicer*'s Export Menu After All Steps Completed

5.2 Manual Modifications on the Surface Mesh

The surface mesh generated from *3D Slicer* is unsuitable for numerical simulations. The reason is that this geometry lacks inlet and outlet patches. These patches are used to define boundary conditions, which represent the air's entrance and exit regions. Moreover, the current geometry has a box-like wall around the face, as seen in Figure 5.3. This wall has appeared since CT scans were cut off at some distance. Therefore, the removal of this nonphysical wall is required. Similarly, the nasopharynx region of the surface mesh is closed since *3D Slicer* generates a water-tight surface.

Therefore, both the wall around the face and the closed exit at the nasopharynx should be removed, and two inlet and outlet patches must be created. This task is accomplished by another FOSS called *Blender*. Since *Blender* allows modification of any vertices, edges, and faces, any modification to the surface geometry is technically possible. However, many valuable algorithms, from remeshing to Boolean operators, exist in *Blender*. These algorithms ease and quicken geometry modifications and use.

Moreover, finding topological issues such as intersections and open regions is possible in *Blender*. These issues may arise during surface mesh generation, and

locating the problems is challenging without a proper tool like *Blender*. Also, if the topological issues are left unresolved, they would disallow volumetric mesh generation. Nonetheless, *Blender* is a complicated and hard-to-use program. The explanations and steps discussed are somewhat advanced but crudely explained; thus, one has to be familiar with *Blender* to follow and apply them.

5.2.1 Removal of the Extra Walls

As mentioned earlier, extra patches should be removed before creating inlet and outlet patches. The result is given in Figure 5.4. In this figure, the wall around the face is removed, and the throat is now open.

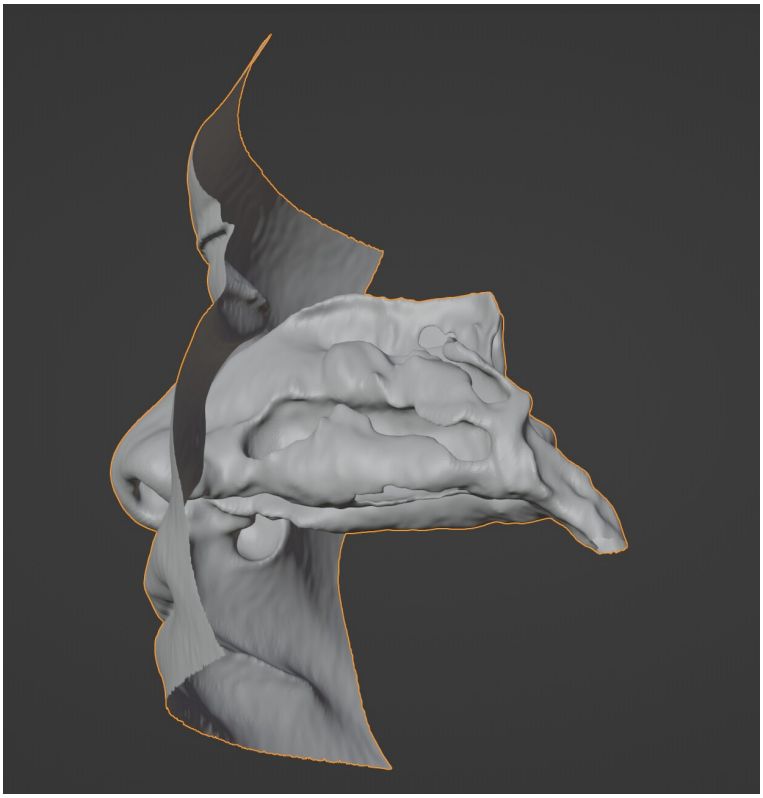

Figure 5.4. The Surface Mesh After Trimming Extra Walls

The removal of these patches is reasonably straightforward, and the steps to follow are given as:

1) Import the geometry to *Blender*.

2) Select the object and switch to the edit mode.

3) Turn on the X-ray mode and use preset viewports to easily select the vertices.

4) Select the vertices and delete all the unnecessary ones.

5.2.2 Removal of the Face Wall

In some cases, the face geometry is avoided in the numerical simulations. There are two strong reasons behind this endeavor: a reduction in the computational costs and an increase in the quality of the volumetric mesh. Including the face requires more points around the face, hence the increase in the computational cost. The second reason is slightly complicated, which stems from having a sharp connection between the face's boundaries and the inlet. Even though these reasons are valid, one has to accept that not including the face in simulations might deteriorate the results.

Steps to remove the face from the other part of the geometry are:

1) Switch to edit mode in *Blender*.

2) Select the vertices around the nostrils, creating a loop around the nostrils.

3) Delete these vertices, creating two unconnected surfaces.

4) Since the surfaces are unconnected, individually selecting unconnected pieces is possible. Select all the separated vertices through the selection of linked vertices.

5) Delete all the selected vertices on the face.

After removing the face, vertices around the nostrils end up in a random pattern. However, these vertices should reside on the same plane or height on the z-axis. The below steps are followed to put the vertices to the same z coordinate:

1) Switch to edit mode in *Blender*.

2) Select all the edges on the nostril.

3) Scale all the selected nodes, leaving x-axis and y-axis as one, while setting the z-axis to zero.

The approach explained above changes all the vertices to the same height; if nostrils are not feasible to warp to the plane parallel to z-axis, the result is unsatisfactory. A more flexible approach to putting all of these vertices to any given plane. This operation can be done by following steps:

1) In object mode, create a plane. Set this plane large enough so that the vertices may be projected onto the plane properly.

2) Select the cavity and switch to the edit mode. Then, select all the edge vertices and group them under a vertex group.

3) In *Modifiers*, tab add a *Shrinkwrap* modifier. Set the target to the plane; also specify the vertex group.

5.2.3 Inlet and Outlet Creation

Since there are two inlets, the left and right nostrils, the declaration of pressure and velocity initial values for them is impossible. Such a declaration would require precursor knowledge on either air fluxes through nostrils or pressure values. Therefore, the current two-inlet approach should be changed. To reduce two inlets into one, the most basic solution is have a rectangular connection representing air around the nostrils. This solution can be obtained by following steps:

1) In object mode, create a cube and make it cover the nostrils.

2) Switch to the *Modifiers* tab, and add a *Boolean* modifier to the nasal cavity. Change the Boolean operator type to *Union*. Set the target as the cube.

3) Separate the cube's faces as a new object.

For outlet creation, the above steps should be followed. However, while creating an outlet, instead of a cube, a plane should intersect with the nasal cavity geometry. Additionally, for the Boolean option, instead of *Union*, *Difference* must be utilized.

After creating the inlet and outlet geometries, the final surface mesh should look like the one in Figure 5.5. Exporting these parts to use them in volumetric mesh generation

is now possible. During this thesis, five files are extracted. Basically, on top of the expected patches, which are named *inlet*, *outlet*, and *body*, there are two extra patches. These patches are named *top* and *bot*, referring to extensions of the inlet and the outlet, respectively.

Lastly, another surface geometry, called *bodyClosed*, is generated by closing all the open areas of the *body* geometry. This surface file is required in later steps to uniformly refine the inside of the main parts of the nasal cavity. Such extra geometry is required due to the lack of setting for the depth of refinements farther from the wall for a single surface in *snappyHexMesh*.

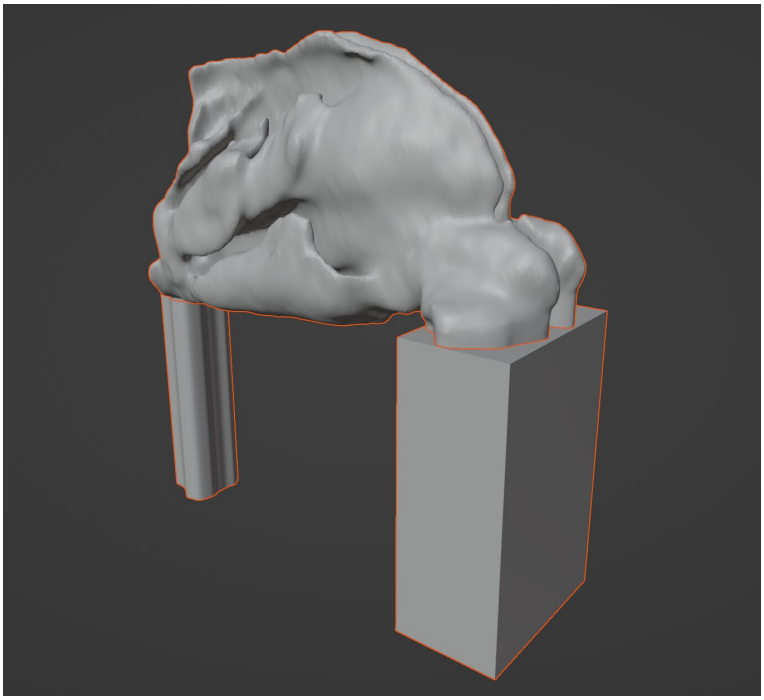

Figure 5.5. The End Result After Adding Inlet and Outlet

5.3 Volumetric Mesh Generation From the Surface Mesh

This section covers the generation of volume mesh using two free and open-source programs: *snappyHexMesh* and *cfMesh*. These software applications are integrated to work with *OpenFOAM*. In this thesis, the overall volumetric mesh is generated by *snappyHexMesh*. This program creates a hexahedral-dominant volume mesh using

a surface mesh. Even though *snappyHexMesh* can do all the work alone, *cfMesh* is used to generate the boundary layer cells. The reason for using *cfMesh* is that when the boundary layer cells are generated by *snappyHexMesh*, the resulting mesh has some bad-quality cells. These cells with low-quality metrics hinder the numerical simulations; thus, simulations must be run without boundary layer cells, or *cfMesh* has to be used to generate boundary layer cells. Initial steps to generate the volumetric mesh are not done by *cfMesh* because it creates bad cells near the surface mesh connections. These cells end up with minimal volume and other poor-quality metrics. If used in a simulation, poor-quality cells cripple the simulation's speed and quality.

Unfortunately, there is no other readily available FOSS to do every required step to generate a volume mesh. However, *snappyHexMesh* is still in active development, and boundary layer cell generation is expected to be further developed, such as generating boundary layer cells at the first step instead of the last.

5.3.1 Background Mesh Generation

Before the generation of the mesh using the surface mesh, a background mesh must be generated. The background mesh is generated with another program integrated into *OpenFOAM* called *blockMesh*. This program is capable of creating detailed geometries using mathematical definitions. However, the usage of mathematical definitions requires a lot of user effort. On the other hand, generating a background mesh with this program is reasonably straightforward.

In order to generate the background mesh, one has to decide two metrics beforehand: the longest hexagonal cell edge length and the background mesh coverage. The most extended hexagonal cell edge lengths are selected arbitrarily, though these edges are commonly selected larger than the targeted cell sizes. The reasoning behind this idea is that the cells near the surface mesh can be refined using *snappyHexMesh*'s options to conform to the surface mesh. The cells away from the walls can be left coarse, since the flow is uniform away from the walls. Moreover, leaving coarse cells reduces the required number of cells substantially, which leads to a faster simulation. On the other hand, the background mesh should shroud the surface mesh to have a conformal volumetric mesh. The free and open-source postprocessing program called *Paraview*

is the easiest way to check the surface mesh's boundaries.

In this thesis, both geometries are created using maximum cell length as $8 \cdot 10^{-4}$ m. This number is selected so that when the cells are refined twice, cell length goes down to $2 \cdot 10^{-4}$ m.

5.3.2 Surface Conforming Volumetric Mesh Generation

This section covers the settings used in *snappyHexMesh* and *cfMesh*. There are three steps to be applied consecutively: castellation, cell snapping, and layer addition. Castellation and snapping cells to surfaces use *snappyHexMesh*. The layer addition step is done by utilizing *cfMesh*.

5.3.2.1 Castellation Step

Since the background mesh has already been generated, the next action is the castellation operation. Castellation operation of *snappyHexMesh* is done by enabling *castellatedMesh*. During this step, the first action is refining the cells around the surface mesh. This refinement is done by dividing every hexahedron cell by eight. Two consecutive refinement processes are demonstrated in the 2D plane with the same edge lengths as this thesis in Figure 5.6.

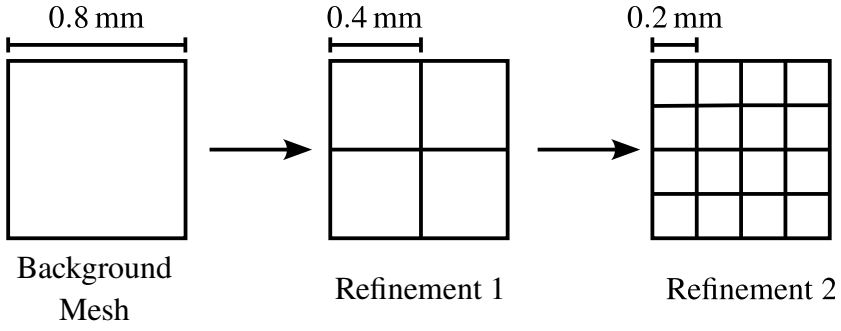

Figure 5.6. Refinement Process for a 2D Mesh

Depending on the options given to *castellatedMeshControls*, *snappyHexMesh*, it decides the amount of refinement and depth of refinement. After the refinement

procedure, the cells mostly standing outside the surface mesh are removed. The whole process is demonstrated in 2D for an arbitrary line and background mesh in Figure 5.7. Also, a part of the midsection of the pre- and post-surgery geometries is given in Figure 5.8 to allow investigation of the current mesh.

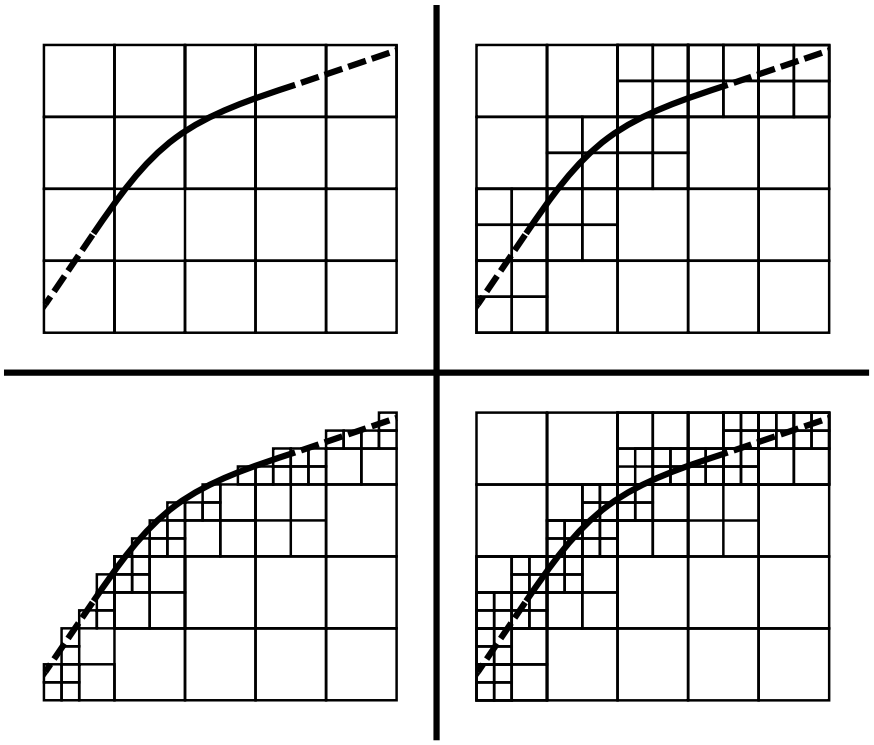

Figure 5.7. Castellation Example for a 2D Mesh

Note. In this figure, the castellation process is given for two refinements. Every step is given clockwise, starting from the left top corner: background mesh and surface mesh, first refinement, second refinement, and removal of extra cells lying outside of geometry.

The refinement settings used in this thesis while the generation of the castellated mesh are highlighted as follows:

- The main surface, *body*, is refined twice by using *bodyClosed*. This refinement reduces the cell edge sizes to $2 \cdot 10^{-4}$ m. Additionally, this surface is set as a *wall.*

- The extended outlet, *bot*, is refined by once near the walls. This refinement is only done for a few cells near the walls. This outlet extension is dedicated as a *wall*.

- The other surfaces, *inlet*, *outlet*, and *top*, are not refined. The surface *top* is set as a *wall*, and the types of the other two surfaces are appointed to be a *patch*.

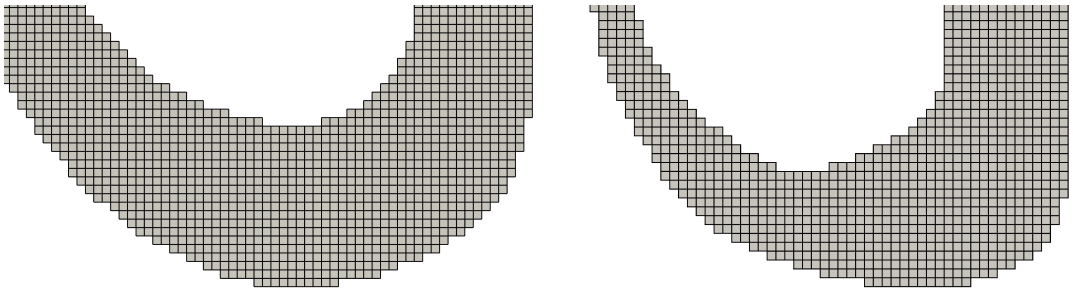

Figure 5.8. Pre- and Post-Surgery Mesh Result After Castellation Step

5.3.2.2 Snapping Step

At this point, the mesh is refined near the surfaces, and the excessive cells are trimmed. It is time to warp the mesh to make it fit the surface. The warpage is done by running *snappyHexMesh*'s *snapping* option. The snapping process introduces mesh quality issues. These mesh quality problems may result in divergence issues and incorrect solutions. The snapped version of the previously shown Figure 5.7 is given without the surface mesh in Figure 5.9. It is possible to speculate from this figure that if refinement near boundaries is lacking, the mesh quality parameters will get higher. Also, the snapped version of Figure 5.8 is demonstrated in Figure 5.10, so the reader can investigate the snapping process.

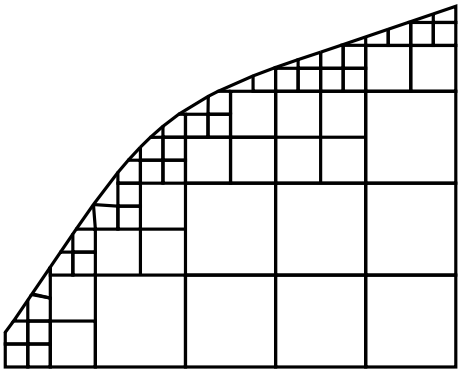

Figure 5.9. Snapping of the Refined Surface in 2D

The most critical mesh quality parameters are maximum non-orthogonality, *maxNon Ortho*, and maximum skewness. The first parameter, *maxNonOrtho*, is suggested to be lower than 65. On the other hand, the upper limit for skewness values is defined differently for internal and external cells, 4 and 20, respectively. The difference between external and internal cells is simply that external cells are located near the surface.

The minimum determinant of the cells is found to be causing problems in the numerical simulations. This parameter is named *minDeterminant* and is set to 0.001 by default. Even though this quality parameter is rarely referenced and mentioned, it may cause critical issues in numerical simulations; specifically, the minimum determinant appears to be connected with divergence in the transient part of this thesis. These limitations appear to be ignored by *snappyHexMesh*; thus, a higher value of 0.01 is set for the snapping phase.

Furthermore, some quality parameters are changed to have better snapping results: *minTetQuality* and *minVol*. The parameter called *minTetQuality*, which describes the tetrahedral cell's quality, is disabled since this parameter appears to be obsolete. Old versions of *OpenFOAM* demand tetrahedral cells to be at high-quality levels to manage particle tracking. In newer versions, *OpenFOAM* uses a better algorithm to handle negative tetrahedral quality values. The second value, *minVol*, describes the minimum volume of the cells. The default value for this parameter is set to $1 \cdot 10^{-13}$ m^3. However, the background mesh starts with a very low volume in the current work: $8 \cdot 10^{-12}$ m^3. Therefore, the *minVol* value was reduced considerably to avoid snapping problems caused by the minimum volume-related limitations. Further examination reveals that

in the end, the minimum volume of a cell has become slightly larger than $1 \cdot 10^{-13}$ m^3. This result suggests that a reduction in the minimum volume is not required but is almost required. Even though the minimum volume is very low, the ratio of neighboring cell volumes is a more informative constraint. This ratio is considerably high; thus, the volume-related mesh quality issues are satisfactory.

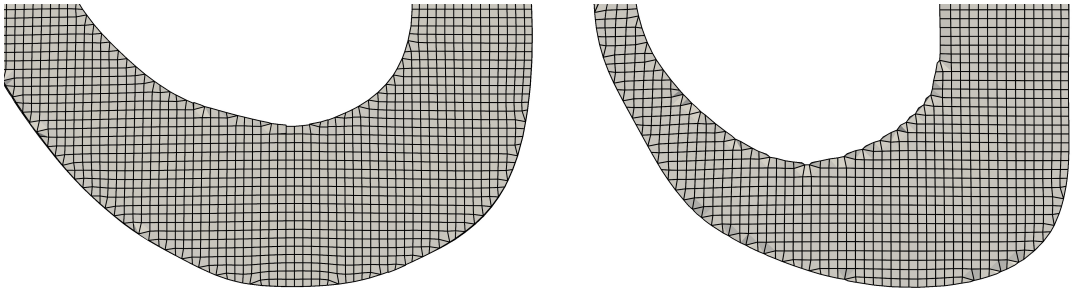

Figure 5.10. Pre- and Post-Surgery Mesh After Snapping Step

5.3.2.3 Boundary Layer Addition Step

Adding boundary layers, also known as prism or inflation layers, is the last step to complete the generation of a volumetric mesh. An example in a 2D plane is given in Figure 5.11, similar to earlier figures in this chapter. Also, layered versions from figures in earlier sections are given in Figure 5.12.

Generally, unlike the first two steps, the layer addition step is optional. If internal cells are fine enough, boundary layer addition may be avoided. However, this step is suggested due to the fluid flow physics behind it. On a wall surface, a fluid element's velocity converges to zero. These very low velocity values near the wall flow create a viscous zone where the flow changes rapidly. Therefore, introducing the boundary layer cells increases the resolution of this rapidly changing zone.

The method of adding boundary cells is critical. These cells are added so that every new layer is slightly thinner than the last layer. This ratio is commonly suggested to be 1.2; this means that the layers get thicker by 20 % compared to the outer one. Such an expansion ratio allows thinner cells to be near the walls, thus capturing the viscous layer with fewer cells.

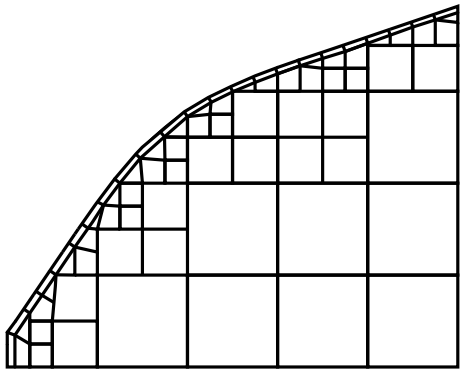

Figure 5.11. Addition of a Single Layer to the Snapped Surface in 2D

The inflation layers, similar to the snapping step, worsen the mesh quality parameters because internal cells get squished in order to create room for boundary layers. Because of the decrease in mesh quality caused by layer addition, the number of layers one may add to the computational mesh is limited. This limitation is especially significant for the programs adding layers at the end of volumetric mesh generation. Both *snappyHexMesh* and *cfMesh* prefer to add the layer cells in this way. Therefore, in this thesis, only three layers are added to the volumetric mesh; however, the internal cells are selected small enough so that three layers are enough to satisfy a good solution for the viscous boundary layers. Also, the layers are added to make every layer smaller than the last one. The expansion ratio is selected to be around 1.2; nonetheless, variations are causing the ratio to fluctuate between 1.3 and 1.1.

The generation of boundary layers using *cfMesh* on a volumetric mesh generated by *snappyHexMesh* appears as a novel approach in the mesh generation literature. Such novelty is expected since both applications are rarely used, while each is a standalone program capable of generating everything independently.

The layer addition process follows the following steps:

1) Move the generated volume mesh to *cfMesh*'s root folder.

2) In *system/controlDict*, the value of *writeFormat* is set to *ascii*. Later, *foamFormat Convert* is run to change the formatting of the text. Change the *writeFormat* back to default *binary*. This step is required since *cfMesh* panics if it faces a mesh generated with *snappyHexMesh* in binary format.

3) Pick the settings in the *system/meshDict* file. The number of layers has been set to two with an expansion ratio of 1.4.

4) Run the *generateBoundaryLayers* command for once.

5) Change the number of boundary layers in *system/meshDict* to one; expansion ratio setting does not matter.

6) Run *generateBoundaryLayers* command again.

The above approach forces *cfMesh* to generate and smooth the internal layers twice to generate boundary layers with good expansion ratios. The sole reason for this unconventional utilization of the *generateBoundaryLayers* command is due to how boundary layers are generated by *cfMesh*. It adds an extra external cell and then divides it into a specified number of layers. This approach causes boundary layer cells to be outrageously smaller than internal cells, causing volume transition between cells to be extraordinarily terrible.

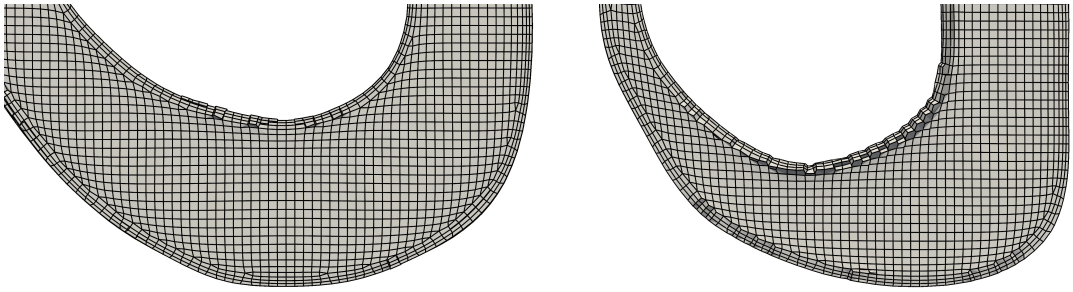

Figure 5.12. Pre- and Post-Surgery Meshes After Adding Boundary Layers

5.3.3 Details of the Generated Mesh

This section reports the details of the generated mesh. These details are quality, number of cells, cell types, and similar. Since two geometries are used throughout this thesis, two different reports are given. Nonetheless, the objective is to generate comparable volumetric meshes. The visual demonstration of the whole mesh is given in Figure 5.13, Figure 5.14, and Figure 5.15 to demonstrate the visual result of the meshing process.

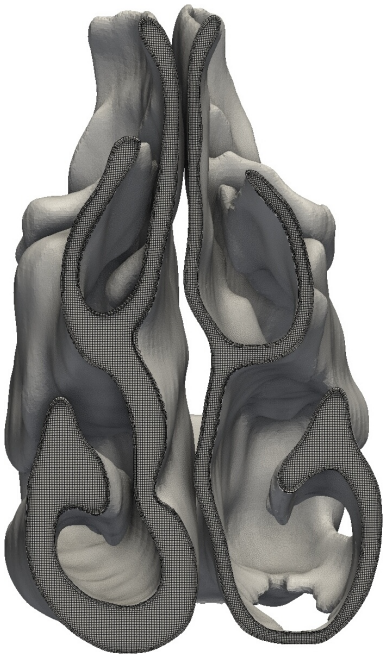

Figure 5.13. Frontal View of Sliced Pre-Surgery Mesh

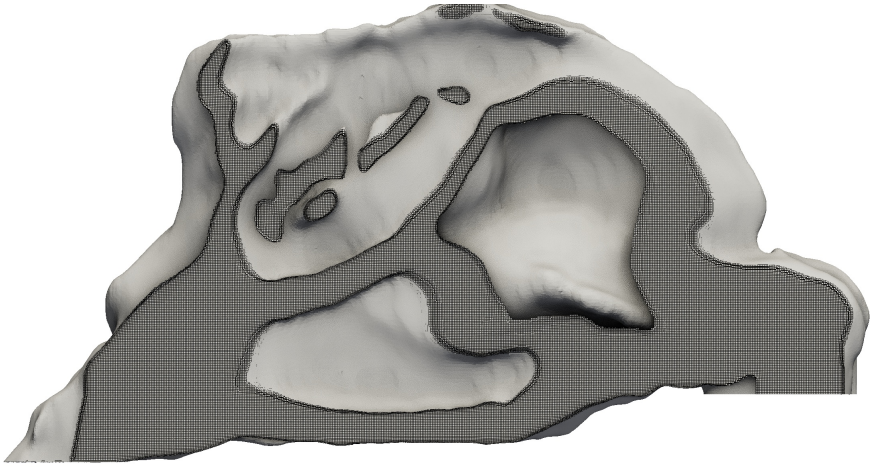

Figure 5.14. Side View of Sliced Pre-Surgery Mesh

5.3.3.1 Pre-Surgery Volumetric Mesh

For the pre-surgery mesh, the number of different types of cells is given in Table 5.1. The details concerning castellated mesh are not provided, as each cell in the volumetric mesh is a perfect hexahedron.

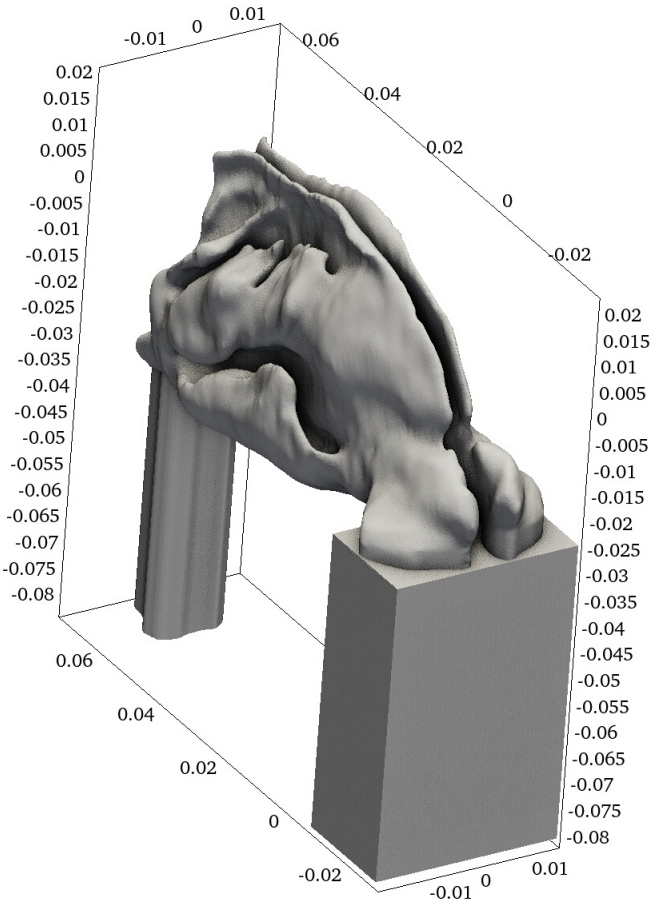

Figure 5.15. View of Complete Pre-Surgery Volumetric Mesh

Table 5.1. Cell Type Distribution in Pre-Surgery Mesh

Cell Type	After Snapping	After Layers
Hexahedra	3800000	5150000
Prism	81400	82100
Tet-wedge	1320	1320
Tetrahedra	17	17
Polyhedra	154000	559000
Total	4040000	5790000

Note. Only up to three significant figures are used in this table.

The mesh quality parameters are given in Table 5.2 for the pre-surgery mesh. The first mesh, the castellated mesh, is solely made of hexahedral cubes without any deformations. Since these kinds of mesh elements are as perfect as possible, their mesh quality parameters are not reported in Table 5.2. Furthermore, in this table, the face flatness values for the snapping state appear problematic since they are lower than the threshold value. Nonetheless, this volumetric mesh is merely a stepping stone to generating a volumetric mesh with boundary layer cells. Therefore, the existence of the bad cells does not matter if they do not persist.

It must be noted that Table 5.2 reports mesh quality parameters by using the *checkMesh* utility of *OpenFOAM*. Therefore, directly comparing other software's quality metrics might not be possible. However, the threshold values provided in the table can serve as a reference point for assessing the validity of the volumetric mesh.

Table 5.2. Pre-Surgery Mesh Quality Parameters

Quality Parameter	After Snapping	After Layers	Threshold
Max. Aspect Ratio	6.3	16	1000
Min. Volume	$7.6 \cdot 10^{-13}$	$9.2 \cdot 10^{-14}$	$1.0 \cdot 10^{-37}$
Max. Non-Orthogonality	40	53	70
Avg. Non-Orthogonality	4.7	9.4	70
Max. Skewness	2.0	2.2	4
Min. Face Flatness	**0.41**	0.80	0.80
Min. Cell Determinant	0.014	0.010	0.001
Min. Face Interpolation	0.08	0.084	0.050
Avg. Face Interpolation	0.49	0.48	0.05
Min. Face Volume Ratio	0.018	0.014	0.01
Avg. Face Volume Ratio	0.94	0.90	0.01

Note. This table reports the results up to two significant figures.

5.3.3.2 Post-Surgery Volumetric Mesh

For the post-surgery mesh, the number of different types of cells is given in Table 5.3. Cell types for the castellated mesh are not reported because cells are solely hexahedra cells. The mesh quality parameters of the volumetric mesh generated using the post-surgery CT scan are given in Table 5.4. The castellated mesh is not reported in this table because it has no meaningful imperfections. This table shows the minimum face flatness below the threshold value after the snapping state. This issue appears because *snappyHexMesh*, for some reason, fails to realize the existence of the problematic cells; thus, it leaves them as they are. However, it is not a critical issue because this mesh is not directly used. It is clear that after boundary layer cell addition, flatness issues vanish. Like pre-surgery mesh quality results, threshold values can not be directly compared because mesh quality parameters are not defined uniformly through various software. Thus, one may compare where the limits reside and estimate the degree of how good the used volumetric mesh is.

Table 5.3. Distribution of the Cell Types in Post-Surgery Mesh

Cell Type	After Snapping	After Layers
Hexahedra	3100000	3960000
Prism	55000	55300
Tet-wedge	874	874
Tetrahedra	1	1
Polyhedra	104000	389000
Total	3260000	4400000

Note. Only three significant figures are used in this table.

Table 5.4. Post-Surgery Mesh Quality Parameters

Quality Parameter	After Snapping	After Layers	Threshold
Max. Aspect Ratio	5.4	15	1000
Min. Volume	$5.7 \cdot 10^{-13}$	$1.0 \cdot 10^{-13}$	$1 \cdot 10^{-37}$
Max. Non-Orthogonality	40	55	70
Avg. Non-Orthogonality	4.3	9.1	70
Max. Skewness	2.0	2.4	4.0
Min. Face Flatness	**0.3**	0.8	0.8
Min. Cell Determinant	$15 \cdot 10^{-3}$	$4.4 \cdot 10^{-3}$	$1 \cdot 10^{-3}$
Min. Face Interpolation	0.13	0.12	0.05
Avg. Face Interpolation	0.49	0.48	0.05
Min. Face Volume Ratio	$3.6 \cdot 10^{-2}$	$3.8 \cdot 10^{-2}$	$1 \cdot 10^{-2}$
Avg. Face Volume Ratio	0.95	0.91	0.01

Note. This table only reports parameters up to two significant figures.

5.4 General Solution Strategy

This thesis's numerical simulations only focus on inhalation at restful and moderate breathing levels. The reason behind not simulating both of the breathing phases is due to time and processing power limitations. Inhalation is selected over exhalation because inhalation is more critical when considering nasal obstruction. Principally, nasal congestion feeling appears due to stimulation levels on the nasal receptors. Unlike exhalation, during inspiration, the stimulation happens for thermo- and mechano-receptors. Also, during inhalation, a lower pressure in the nasal cavity appears. This low pressure leads to shrinkage in the nasal cavity to some degree, thus reducing airflow levels slightly.

What breathing rates should be used for the simulations is still undecided. The most fitting way to choose the breathing rates is to select the same as in the earlier literature.

In this thesis, Hahn et al. (1993)'s distinguished work is selected. This work uses three different flow rates, though the fastest breathing rate is discarded. At the fastest flow rate, the collapse of nasal walls due to low pressure should be so critical that one must represent it. However, the current work does not aim to simulate wall collapses. The selected flow rates are 180 mL/s and 560 mL/s; they correspond to 10.8 L/min and 33.6 L/min. The first breathing rate is called restful, quiet, or normal, whereas the second is called moderate breathing or rapid breathing.

5.5 Turbulence Modeling

Since large eddy resolving is done in this thesis, there is a need for a precursor simulation. This precursor simulation must provide every cell's velocity, pressure, and turbulent kinetic energy values to the secondary pseudo-transient LES. Therefore, the first simulation also has to include a turbulent model. For the first simulation, one of the successful RANS turbulence models is selected, called $k-\omega$ SST. This turbulence model is appropriate for steady-state simulations and fits wall-bounded flows.

5.5.1 Precursor Simulation's Turbulence Model

As mentioned, the precursor turbulence model combines the $k-\omega$ model and Menter's shear stress transform model. This model requires a specification of kinetic energy, k, and specific kinetic energy dissipation rate, ω. These unknowns may be calculated using some correlations, given that one knows the turbulence intensity and geometrical values at the boundaries.

The turbulent kinetic energy may be calculated as,

$$k = 1.5(U_{\text{mean}} I)^2. \tag{5.1}$$

The specific dissipation of kinetic energy can be calculated in two ways. These calculations stem from the connection between the turbulent length scale with the

turbulent kinetic energy and the kinetic energy dissipation rates.

$$\ell = C_{\mu}\frac{k^{1.5}}{\epsilon} \qquad \text{or} \qquad \ell_{\mathrm{m}} = C_{\mu}^{0.75}\frac{k^{1.5}}{\epsilon}, \tag{5.2}$$

where ℓ, ℓ_{m}, C_{μ} and ϵ are turbulent length scale, turbulent length scale based on mixing length, turbulence model constant, kinetic energy dissipation rate, respectively. Moreover, one may directly calculate the specific dissipation rate of kinetic energy using the relationship, $\epsilon = \omega C_{\mu} k$. Accordingly, the specific dissipation of turbulent kinetic energy is found as:

$$\omega = \frac{k^{0.5}}{\ell} \qquad \text{or} \qquad \omega = \frac{k^{0.5}}{C_{\mu}^{0.25}\ell_{\mathrm{m}}}. \tag{5.3}$$

For the turbulent length scales, definitions for fully-developed pipe flow may be used,

$$\ell = 0.038 D_{\mathrm{H}} \qquad \text{or} \qquad \ell_{\mathrm{m}} = 0.07 D_{\mathrm{h}}, \tag{5.4}$$

where D_{H} is the hydraulic diameter. Ultimately, turbulent kinetic energy, ν_{t}, must be calculated to put all of the work above to use. In $k-\omega$ SST model, the calculation is done through:

$$\nu_{\mathrm{t}} = a_1 \frac{k}{\max(a_1\omega,\ |\boldsymbol{S}|F_2)}, \tag{5.5}$$

where a_1 is a constant, F_2 is a model-related variable, and $|\boldsymbol{S}|$ is the magnitude of the strain rate tensor.

Using the same flow rates as Hahn et al. (1993), the reported turbulence intensity values can be used. The vital values for turbulence intensity values are the inlet and outlet values because initial guesses are fixed for these regions. These guesses, along with other variables, the general characteristics of the flow. However, since the turbulence-related profile can not be known for the external cells, turbulence intensity values elsewhere may be used as a compromise. Such a compromise is acceptable during the simulation since the turbulence-related variables should converge toward the correct

values at the internal cells. All the initial guesses for turbulence intensity are given in Table 5.5.

Table 5.5. Turbulence Intensities for Restful Inhalation

Discharge	Nostrils	Nasopharynx
180 mL/s	2.5 %	3.9 %
560 mL/s	2.7 %	4.8 %

Note. Data is obtained from Hahn et al. (1993). The turbulence intensity at the nasopharynx is approximated for the restful state using nearby data and nasopharynx turbulence intensities.

Lastly, in *OpenFOAM*, all the turbulence-related constants are left in their default states. Despite the existence of further intricacies of the $k-\omega$ SST model, further discussion on the model is skipped due to its limited usage as a precursor tool to estimate turbulent viscosities ν_{t}.

5.5.2 Large Eddy Simulation's Turbulence Model

In LES, even though the large eddies do not require modeling, the small eddies must be modeled. Also, resolved eddies' total resolved kinetic energy must dominate the modeled ones. This approach is relatively easily achieved since the smaller the eddies, the less the kinetic energy they carry.

The sub-grid scale turbulence model is selected as WALE. This model is valid for incompressible flows and has several substantial advantages compared to others. The WALE model is computationally cheap, correctly mimics behavior near the walls, and is feasible to simulate transitional turbulence behavior. This model uses Boussinesq's assumption and calculates artificial viscosity and turbulent viscosity.

In *OpenFOAM*, there are a few options related to WALE, and some of these must be set to use WALE as the LES turbulence model. Other options allow modification of

default settings, enabling users to change the values if deemed required. These options are located in *constant/turbulenceProperties*, and described as:

- The variable *simulationType* selects the turbulence model. For LES, it is set to *LES*.
- The parameter called *LESModel* defines which sub-grid scale model is used. For WALE, it is set to *WALE*.
- The property named *delta* describes the method used to estimate filter size. This number is related to cell sizes, and the most straightforward way to find it is to use the cube root of cell volumes. Therefore, this option is selected equal to *cubeRootVol*.
- The sub-grid scale coefficients[2] The values of *Ck* and *Cw* are left as default; the default values are equal to 0.094 and 0.325, respectively.

5.6 Boundary Conditions

Since two different simulations are involved in this thesis, the reader may expect different boundary conditions to be defined for them. However, since pseudo-transient LES is a continuation of the steady-state solution, the boundary conditions in both simulations are the same[3]. However, turbulent kinetic energy and specific dissipation of turbulent kinetic energy boundary conditions are not carried over to LES. The reason is that an LES using WALE as the sub-grid scale turbulence model does not explicitly require or use these values to calculate sub-grid scale turbulent viscosity. Only velocity, pressure, and turbulent viscosity values are carried to the LES as initial guesses in both boundaries and internal cells.

The general overview of the boundary conditions is given in Table 5.6. As hinted earlier, in this table, k and ω are only used in precursor steady-state simulation. More detailed definitions and discussions are given in the upcoming sections.

[2] Note that it is possible to specify *Ce* value for the WALE model as well. However, this value is not used in turbulent viscosity calculations but in the report of dissipation of turbulent kinetic energy during the postprocessing phase.

[3] Having the same boundary conditions is not a strict requirement. For example, a synthetic turbulence generation can be included in the inlet, which requires an update in boundary conditions.

The boundary conditions for the forthcoming sections are straightforwardly defined in *OpenFOAM*. Dirichlet boundary condition is set by using the *fixedValue* along with a value assigned to it. More conveniently, the *noSlip* keyword can be used to set a Dirichlet boundary condition equal to zero. Similarly, the Neumann boundary condition could be set using the *fixedGradient* keyword as the type with a selected value. The Neumann boundary condition equal to zero gradient condition may also be set with *zeroGradient* as the boundary condition type.

Table 5.6. Boundary Conditions For All the Patches

Field Name	p	u	k	ω	ν_{t}
inlet	Neumann $\nabla p = 0$	Dirichlet $U = Q/A$	Dirichlet	Dirichlet	Dirichlet
All Other Patches	Neumann $\nabla p = 0$	Dirichlet $U = 0$	Wall Function	Wall Function	Wall Function
outlet	Dirichlet $p = 0$	Neumann $\nabla U = 0$	Neumann $\nabla k = 0$	Neumann $\nabla \omega = 0$	Neumann $\nabla \nu_{\mathrm{t}} = 0$

5.6.1 Pressure Boundary Conditions

Pressure boundary conditions are set traditionally in this numerical simulation. Since a push flow at the inlet is planned due to better behaviors in convergence and stability, the inlet should be assigned zero gradient pressure boundary conditions by default. The pressure boundary conditions at the inlet and outlet could be set so that there is a flow due to the pressure difference. However, in this case, pressures should be set so that one patch includes a fixed and total pressure since numerical simulations can not solve two fixed pressure boundaries. Flow due to pressure difference is close to reality, given that lungs create pressure differences to push and pull air. Nonetheless, defining a flow caused by velocity is a more common approach in the literature; thus, more results and methods are available to compare and contrast results.

In *OpenFOAM*, the boundary conditions for pressure are set as:

- The boundary condition's type for inlet set to *fixedGradient*. This condition's value is selected to be zero.

- The walls have the same settings as the inlet: a gradient equal to zero.

- Outlet has set to a fixed pressure value equal to zero, e.g., *fixedValue* with the value equal to zero.

5.6.2 Velocity Boundary Conditions

The velocity boundary conditions appear as the reversed version of the pressure boundary conditions. This time, a fixed velocity value is defined at the inlet, and a fixed gradient value is given to the outlet. Expectedly, velocity is set to zero at walls because fluid near the walls should move very slowly, and the velocity should converge to zero towards the walls.

The velocity value is assigned so that it is uniform throughout the inlet. Nevertheless, there are other ways to define the velocity boundary conditions, for example, extrapolation of the profile from neighboring cells. Even though the extrapolated profile may provide a more realistic boundary condition for the inlets, this profile is avoided because it is a point of failure in simulations.

In *OpenFOAM*, these boundary conditions are defined as follows:

- The boundary condition of the inlet is set to *flowRateInletVelocity* with *volumetricFlowRate* equal to the flow rate. Also, the *extrapolateProfile* settings are disabled, representing a uniform profile.

- The boundary condition of all the walls is set to *fixedValue* with a value of zero.

- The outlet's boundary condition is set to *inletOutlet*. This boundary condition is a Neumann boundary condition with a gradient equal to zero if the flow is outwards. However, if the flow turns inwards, it acts like a Dirichlet boundary condition equal to zero. This option suppresses the problematic inwards flow issues at outlets.

5.6.3 Turbulent Kinetic Energy Boundary Conditions

Unlike the velocity and pressure boundary conditions, turbulent kinetic energy requires specific estimations for inlet boundary values. Generally, a Neumann boundary condition with a gradient equal to zero is used for the outlet. Moreover, near the walls, turbulent kinetic energy could be defined using specific functions that help to get physical results. The wall functions are defined in a way that, if required, they reduce down to the most logical state: turbulent energy at the wall should converge to only near zero[4]. Even though this kind of wall functions require extra calculations in all the near-wall cells, the required processing power is minimal given small number of near-wall cells. Moreover, the extra calculations are unimportant because they are only used for the steady-state simulations in this thesis, which are very quickly done compared to unsteady simulations.

Above boundary conditions are defined in *OpenFOAM* as:

- At inlet the boundary condition is set by using keyword *turbulentIntensityKinetic EnergyInlet*. This type requires a definition of turbulence intensity as *intensity* in the vicinity of the inlet. The boundary condition uses similar steps as explained in Section 5.5.

- The boundary condition at all the walls was selected as *kLowReWallFunction*. This wall function combines two wall functions, which makes it possible to model both low- and high-Reynolds number flows using a threshold y^+ value [5]. This flexible wall modeling approach allows correct behavior throughout the wall of the flow. Such an approach is needed because complicated flows may have inconsistent y^+ values on the walls. The volatile behavior would not be feasible to model using a single function; thus, a step-wise wall model is adopted.

- The outlet boundary condition for the turbulent kinetic energy is set to be

[4] The turbulent kinetic energy values should converge towards minimal values, instead of zero, such as $1 \cdot 10^{-16}$ m^2/s^2 in order to avoid division by zero errors.

[5] The interested reader might want to know that here low- and high-Reynolds number refer to the two different approaches. Low-Reynolds number methods aim to resolve the flow near the wall, and the other method skips solving near the wall but models it. The naming does not carry any information on the global Reynolds number of the flow.

fixedGradient with a gradient value of zero.

5.6.4 Boundary Condition for Specific Dissipation of Turbulent Kinetic Energy

Like the turbulent kinetic energy boundary conditions, the dissipation of the turbulent kinetic energy, ω, is defined with built-in functions for the inlet and the walls. At the outlet, a zero gradient boundary condition is applied, assuming the flow is developed in the flow direction.

The boundary conditions are set in *OpenFOAM* as:

- The boundary condition at the inlet is calculated using a function named *turbulentMixingLengthFrequencyInlet*. This function takes the mixing length value to calculate specific dissipation rates. This method uses the same technique given in Equation 5.4 with the mixing length, ℓ_{m}.
- At the walls, *omegaWallFunction* is used as the boundary condition. This boundary condition blends the specific dissipation rates from the viscous and logarithmic ranges together; thus, it is appropriate for both high- and low-Reynolds number simulations.
- The outlet boundary condition is set to a gradient value of zero by using *fixed Gradient* keyword with the gradient value equal to zero.

5.6.5 Boundary Conditions for Turbulent Viscosity

Turbulent viscosity is the most critical boundary condition in this thesis. The importance of this condition is used in both LES and RANS parts. The inlet turbulent viscosity condition is defined straight away using the known values: Calculate the turbulent kinetic energy and dissipation of kinetic energy with Equation 5.5. At the walls, wall functions are used to get better precision. Lastly, at the outlet, a fully-developed flow is assumed; thus, zero gradient boundary conditions are used.

Boundary conditions for turbulent viscosity in *OpenFOAM* are set as:

- At the inlet, using the keyword *calculated*, which directly calculates the turbulent viscosity using Equation 5.4.

- Keyword *nutUSpaldingWallFunction* is used at the walls to calculate turbulent viscosity. This approach introduces a continuous function to calculate turbulent viscosity for the cells on the walls. Moreover, it is valid for both low- and high-Reynolds number approaches. The usage of such wall models is known as wall-modeled large eddy simulation, or WMLES. Using such an approach is essential to getting more physical results if there are non-well-resolved areas in the computational mesh[6].

- The outlet boundary condition for turbulent viscosity is set to the *fixedGradient* keyword, with its value equal to zero.

5.7 Settings of Simulations

In *OpenFOAM*, different settings are required to be specified. These settings are separated into logical files and located in the folder *system* under the root of the project folder. This folder has settings concerning discretization options, matrix solver specifications, time stepping options, algorithms to solve Navier-Stokes equations, residual level controls, and similar.

In the *system* folder, there are three critical files: *controlDict*, *fvSchemes*, *fvSolution*. The first file, *controlDict*, has time-related options, postprocessing function details, and write formats. The second file, *fvSchemes*, has options about discretization schemes for equations related to actively solved equations. The last file, *fvSolution*, has solver settings such as matrix solvers, tolerance limits, relaxation factors, settings of solver algorithms, and similar.

Lastly, due to the requirement of two different simulations, two sets of options are used to generate solutions. These settings are separated into two sections to be able to be individually investigated.

[6] A well-resolved computational mesh is especially costly to solve when the global Reynolds numbers are high. The cost comes from the small size of the viscous sub-layer, which requires many cells due to the need for tiny cells with good volume ratios near the walls.

5.7.1 Settings of Precursor Simulations

Precursor simulations aim to obtain second-order results with absolute errors lower than $1 \cdot 10^{-5}$. In order to do this, a modified version of the SIMPLE algorithm, called SIMPLEC is used. This method allows the usage of lower values for the underrelaxation factors; thus, it has a faster convergence speed. Moreover, in order to decrease the total simulation time, an initial potential flow solution is used. The result of potential flow, initial guesses of the internal pressure, and velocity fields are calculated.

5.7.1.1 Numerical Schemes

The numerical schemes of the steady solution are explained as follows:

- Time-related schemes are ignored with the *steadyState* keyword.
- Gradient schemes are selected as *iterativeGauss* [7] with two iterations enabled. Additionally, a limiter called *cellLimited<Michalak>*[8] is used for the velocity and turbulence-related variables to avoid divergence-related problems. However, the pressure gradients are not limited by any means.
- All divergence schemes are calculated using the Gaussian discretization method. However, the interpolation schemes are calculated differently: second-order upwinding for the velocity term, first-order upwinding for the turbulence-related terms, and a linear method for the deviatoric part of the transpose of the velocity gradient.
- Surface normal gradients are calculated using a corrected scheme[9]. Also, the corrected scheme is used without any limiters[10].

[7] This gradient scheme provides superior results compared to both *leastSquares* and *Gauss-linear* when cells are skew in the mesh. This improvement comes with the cost of increased computation times. About 20-30 % increase in computational time is observed for two iterations compared to the least squares method. However, according to a comparison test given in https://develop.openfoam.com/Development/openfoam/-/merge_requests/500, this method's error rate is 40 % of the least squares method.

[8] This limiter is the bug-fixed version of an already-existent limiter, *cellLimited<cubic>* fixed by Leakey et al. (2022).

[9] This scheme separates orthogonal and non-orthogonal contributions and calculates them individually to add them up. This separation is needed since direct calculation has significantly higher errors than orthogonal calculation methods. Therefore, to get a better approach, non-orthogonal contributions are calculated explicitly. The explicit calculation means that some unknowns in the non-orthogonal part are calculated using the previous iteration's values.

[10] Lastly, the contribution of non-orthogonality may be limited using the *limited* keyword. This approach helps

- Most of the Laplacian schemes are set to *Gauss linear*. Furthermore, the surface normal gradient schemes are required to perform a Gaussian integration. For the surface normal gradients, the corrected approach without limiters is selected, except for a few exceptions. These exceptions are the kinetic energy and specific dissipation of turbulent kinetic energy calculations. These two variables are set to limited[11] so that the non-orthogonal contributions do not exceed orthogonal contributions.

- The schemes concerning interpolation between the face and cell centers are selected to be approximated linearly using the *linear* keyword.

5.7.1.2 Solver Settings

The SIMPLEC algorithm, where C stands for consistency, is used throughout the steady-state simulations. This variant enables the selection of lower relaxation rates compared to SIMPLE. In this context, relaxation means that a blend of old and new results is used to update the results. In *OpenFOAM*, relaxation is given over one and describes the ratio of recently calculated values. For example, if a relaxation factor of 0.3 is used, only 30 % of the recently calculated value is used to update the results.

In this thesis with the SIMPLEC algorithm, the following relaxation values are used: No relaxation for pressure values, and relaxation is set to 0.9 for the velocity and the turbulence-related values[12].

The other details are listed as:

- There are no non-orthogonality correcting loops exists: *nNonOrthogonal Correctors* is set to zero.

- A geometric agglomerated algebraic multi-grid, *GAMG*, solver is used for the pressure solver. Gauss-Seidel method is utilized as the smoother. The tolerance

with extreme non-orthogonal contributions and avoids complications.

[11] The limitation is required to avoid unboundedness issues arising while calculations, i.e., negative or very small k or ω values.

[12] For the SIMPLE algorithm, 0.3 is suggested for the pressure underrelaxation and 0.7 is suggested for the velocity and the turbulent underrelaxation factors.

and relative tolerance are set to $1 \cdot 10^{-6}$, 0.01, respectively[13].

- Identical settings are used for the potential flow solution. Also, since the potential flow calculations are swift, three non-orthogonal correctors are used for the pressure calculations.
- For the velocity and turbulence variables, a preconditioned and stabilized biconjugate gradient method is used by specifying the *PBiCGStab* keyword. The preconditioner is specified as a diagonal-based incomplete lower upper factorization, or *DILU*. The tolerance is set to the same levels as the pressure tolerance levels.
- Caching the first calculations of gradients of velocity, pressure, and turbulence variables are enabled[14].

5.7.1.3 Pre-processing Settings

This section covers the details of the decomposition and renumbering of the volumetric mesh. The decomposition of the mesh is needed in order to solve the governing equations in parallel. Additionally, the volumetric mesh coefficients are renumbered to decrease computational costs.

The parallelization is done by decomposing the volumetric mesh into the desired number of CPU cores. This process may get complicated, given that there are many ways to divide the geometry into smaller geometries. One may think that the best approach is the division of the main mesh into sub-geometries with an equal number of elements. However, this approach would lead to sluggishness because the CPU cores solving the sub-geometries must communicate. This is done using the number of common faces they have with other cores. These commonly shared faces are referred to as processor boundaries, and there are algorithms aiming to reduce the size of these boundaries. One of the algorithms called *scotch* is utilized by *OpenFOAM*. This algorithm tries to minimize processor boundaries while keeping cores with a similar number of cells assigned.

[13] These values mean that iterations stop when the tolerance either drops below 1 % of the initial tolerance or becomes $1 \cdot 10^{-6}$ absolutely.

[14] Caching increases memory transfer requirements but reduces CPU time. Thus, caching may or may not increase simulation speeds depending on the used hardware.

After decomposing the geometry into smaller sub-geometries, a renumbering operation is done to reduce computational cost. This process clusters the non-zero elements near the diagonals, reducing the bandwidth of the matrix. This technique eases the number of future operations needed to solve the governing equations of the flow. In this thesis, the coefficients are reordered by using the reverse Cuthill-McKee algorithm.

The further options concerning the two preprocessing actions are listed as:

- The decomposition is done through *scotch* and baffles[15] are preserved during this decomposition by turning on the *preserveBaffles* option.
- The renumbering is done through the reverse Cuthill-McKee method by specifying the method as *CuthillMchKee* and turning on the setting *reverse*. Also, *sortCoupledFaceCells* is set to true; this option sorts cells at boundaries towards the ends, allowing the use of some solvers that leave the solution of boundaries to last[16].

5.7.2 Settings of the Transient Simulations

In this thesis, the transient simulations aim to obtain second-order results, aiming for a partial convergence between the time steps. To do this, a transient algorithm called PISO is utilized. The PISO algorithm is similar to SIMPLE, though fundamental differences exist. First, this algorithm can generate unsteady behavior of a flow compared to SIMPLE. This is because the time-related terms are not ignored, and the numerical calculations are done with small enough time steps that allow the development of unsteady characteristics. Accordingly, PISO does not require an underrelaxation given that the solved matrices are diagonally dominant due to the small time steps.

Moreover, this algorithm uses a single predictor for the velocity values and two correctors for the pressure values. This process is done a single time for every time step. In SIMPLE, this process is done thousands of times to obtain a steady-state solution.

[15] Baffles refer to the two different faces sharing the same points.

[16] By leaving boundaries to be solved at the end reduces the communication-related wasted time between CPU cores.

The error rate for the PISO algorithm can not be explicitly set, and the residual rates are dependent on the number of correctors and non-orthogonal correctors.

5.7.2.1 Numerical Schemes

For the transient simulations, the numerical schemes are defined as:

- Time-related schemes are solved with the blended version of the Euler and Crank-Nicolson algorithm[17]. In this thesis, a 90 % Crank-Nicolson scheme with a 10 % Euler scheme is preferred. In *OpenFOAM*, the specification is done by setting *ddtSchemes* to *CrankNicolson 0.9*.
- Gradient schemes are set to *iterativeGauss* with two iterations. There are no limiters used. [18]. The avoidance is mainly due to the wish for increased accuracy in large eddy-resolved simulations.
- All divergence values are calculated with the Gaussian discretization scheme with linear interpolation as the interpolation scheme, *Gauss linear*. Since these schemes are central, they have the lowest dissipative-related errors.
- Surface normal gradients are selected the same as the steady-state solution, as *corrected* without any limiters involved.
- Every Laplacian calculation schemes are set to *Gauss linear*. Also, all surface normal gradient calculations are done using the *corrected* scheme.
- Interpolation schemes are set to *linear* interpolation.

5.7.2.2 Solver Settings

Even though the PISO algorithm is used with two correctors, the time step can not be chosen arbitrarily. The time step is selected based on the maximum CFL number. For

[17] This is done to satisfy stability by reducing oscillations with the help of the Euler scheme and high precision using pure Crank-Nicolson. Additionally, this approach provides better boundedness compared to the common second-order method called backward, or implicit, Euler method

[18] Avoiding limiters allows natural development of the flow and prevents errors due to erroneously smoothing the sharpness in the solution.

the restful breathing rate, the time step is set to $4 \cdot 10^{-5}$, and for the moderate breathing level, the time step is set to $1 \cdot 10^{-5}$. This time step results in 0.086 and 0.080 mean CFL numbers for pre-surgery and post-surgery geometries. Additionally, the selected time step results in 0.071 and 0.066 mean CFL numbers for rapid breathing.

Even though the selected time steps generate outstanding CFL numbers, these time steps do not generate maximum CFL numbers that are less than one. However, the maximum CFL numbers are slightly larger than one for a very limited number of cells. For example, the simulation of quick breathing in the post-surgery state only has 30 cells that exceed the CFL number of one in a total of $4.4 \cdot 10^6$ cells; these cells are located near the outlet and appear as polyhedral cells.

The other details about the solver settings may be listed as:

- No non-orthogonality correctors are used.

- Pressure calculations are done by the geometric agglomerated algebraic multi-grid method, *GAMG*. Smoother is selected to be *nonBlockingGaussSeidel*, which allows less communication between CPU cores if decomposed properly. Tolerance is set to absolute tolerance only as $1 \cdot 10^{-6}$.

- Velocity calculations are done by the preconditioned and stabilized biconjugate gradient method, *PBiCGStab*. The preconditioner is selected as the diagonal-based incomplete lower upper factorization, *DILU*. The target tolerance level is selected as $1 \cdot 10^{-6}$ with at least one minimum iterations[19].

- In *OpenFOAM*, it is possible to set different calculation settings for the final iterations. However, nothing special is done for the final iterations of this thesis.

- Caching of gradients for pressure, velocity, and turbulence-related variables is enabled.

[19] The reason for setting the minimum iteration count to one is to avoid having no iterations due to having too low initial tolerances.

5.7.2.3 Pre-processing Settings

The preprocessing settings for the transient large-eddy-resolving simulations are identical to the steady-state solutions specified in Subsubsection 5.7.1.3.

5.7.2.4 Post-processing Settings

This section explains postprocessing settings that are calculated using *OpenFOAM*'s functions. The specific reasons for using these sorts of postprocessing functions are twofold. The first reason is to ease complicated manual calculations in postprocessing. The second reason is to extract simulation-related information at every single time step. Since the traditional postprocessing is done after the simulation, this can not provide any time-related postprocessing information. Therefore, real-time functions are required since collecting results for every time step is unfeasible.

This real-time postprocessing is done through the probes. These probes are inserted to record pressure, velocity, and turbulent viscosity values. The probes are located in various locations of the nasal cavity: entrance, between entrance and middle, middle, back, and at the nasopharynx. Additionally, extra variables are calculated and saved every time other variables are saved on the disk. These variables are y_+ values, LES-quality related variables, wall shear stress, cell CFL numbers, vorticity, Q-criterion, Reynolds stresses, sub-grid scale turbulent kinetic energy, turbulent viscosity, turbulent kinetic energy dissipation, turbulent intensity values, and turbulent length scales.

Furthermore, since LES is transient, the results of a few saved time steps can not be used. During the generation of the steady-state representation, the transient values throughout all the time steps must be averaged. There are no set rules defining this averaging process. However, two vital questions should be answered before deciding on an averaging method:

- When should the averaging process start?
- For how long does the averaging process last?

Before discussing the above questions, one has to define an important variable

commonly referred to in such averaging simulations: flow through time. This variable equals how often the mean flow traveled through the computational geometry, i.e., from inlet to outlet. This variable can be used to give a generalized answer for both questions; hence, it is essential.

The first question should be investigated with the steady-state calculations in mind. Since the initial conditions of the transient simulation are steady-state calculations, one may claim that the averaging process should start immediately. Still, this thought needs to be revised because the steady simulation is just the average solution of many different states of a transient simulation. Therefore, the calculations should be allowed to run for a while to get one of these transient states. All in all, at least half a flow-through time should pass before starting the averaging process. The number of flow-through times for preparation is given for the pre-surgery in Table 5.7 and for the post-surgery in Table 5.8.

The answer to the second question is somewhat arbitrary, given that every flow has unique characteristics. The steady representation of a transient simulation could differ based on many factors, such as boundary conditions, geometry definitions, and physical flow phenomenon. While some flows require a short amount of averaging time, others may need very long time frames to obtain an average solution. Also, while answering this question, one has to consider the feasibility of having longer simulation times. The answer to the second question could be given as follows: The averaging process should last at least a few flow-through times. The number of flow-through times for averaging is given for pre-surgery in Table 5.7 and for post-surgery in Table 5.8.

Table 5.7. Numbers of Flow Through Time for Numerical Simulations of Pre-Surgery State

Breathing Rates	Preparation	Averaging
Restful Breathing	1.4	5
Moderate Breathing	1.5	5.9

Note. These numbers are calculated for the middle of the nasal cavity with an area of 3.78 cm^2; also, the total length of the nasal cavity is measured to be 10 cm.

Table 5.8. Numbers of Flow Through Time for Numerical Simulations of Post-Surgery State

Breathing Rates	Preparation	Averaging
Restful Breathing	1.3	4.5
Moderate Breathing	1.3	5.4

Note. The calculations in this table are done in the middle of the nasal cavity, with an area of 4.16 cm^2. The total length of the nasal cavity is measured at 10 cm.

5.8 Verification of Eddy Resolving Simulations

There are a few requirements for a well-done eddy-resolving simulation. For example, the methods for resolving the governing equations must have low orders of error. These methods must not cause numerical diffusion, and the central schemes should be preferred whenever possible. Moreover, the mesh quality should be in good condition, which is required to have small numerical errors. Most importantly, the computational mesh should be fine enough to resolve more eddies.

Pope (2000) rigorously discusses LES and how much of the eddies should be resolved.

He recommends that the computational mesh should be able to resolve at least 80 % of all the turbulent kinetic energy. The ratio of resolved turbulent kinetic energy to total turbulent kinetic energy should be greater than 0.8, i.e.,

$$\Gamma_{\mathrm{k}} = \frac{k_{\mathrm{res}}}{k_{\mathrm{tot}}} \geq 0.8, \tag{5.6}$$

where Γ_{k}, k_{res}, k_{tot} represents the Pope index, resolved turbulent kinetic energy, and total turbulent kinetic energy, respectively.

Moreover, Celik et al. (2005) suggested two different quality indices to estimate how well a LES is resolved. One of these indices is based on the Kolmogorov length scale, and the other one is based on viscosity. According to Celik et al. (2005), indices between 75 % to 85 % are found satisfactory, the values more than 80 % represents a good LES, and the values greater than 95 % are considered a DNS.

Kolmogorov length-based index may be estimated using the following expression:

$$\Gamma_{\eta} = \frac{1}{1 + \alpha_{\eta}\left(\dfrac{h}{\eta}\right)^{m}}, \tag{5.7}$$

where Γ_{η}, α_{η}, m, h, η respectively: Celik index based on Kolmogorov length, an empirical constant, another empirical constant, grid size, Kolmogorov length scale.

Viscosity-based index may be calculated with:

$$\Gamma_{\nu} = \frac{1}{1 + \alpha_{\nu}\left(\dfrac{\nu_{\mathrm{eff}}}{\nu}\right)^{n}}, \tag{5.8}$$

where Γ_{ν}, α_{ν}, n, ν_{eff}, ν respectively: Celik index using viscosity, an empirical constant, another empirical constant, effective viscosity, and molecular viscosity.

CHAPTER 6

RESULTS AND DISCUSSIONS

This chapter is dedicated to reporting the data obtained from the nasal breathing simulations and the overall nasal geometry. The reported findings are inspired by those in other nasal breathing CFD simulations; however, as many as different reports are provided in this thesis. The main reason for providing different reports is to enlighten all the possible reasons behind nasal obstruction. Conducting an LES implies high-quality results, offering exceptional insights into pre- and post-surgery nasal airflow simulations.

The results are given when the nasal cavities are sliced into 15 different parts that are normal to the nasal airflow, i.e., slices that are perpendicular to streamlines. The visual representation of all of these 15 slices is given in Figure 6.1.

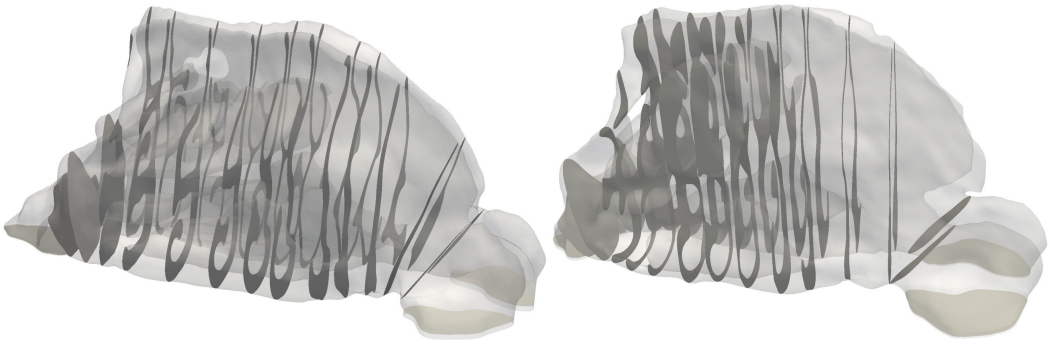

Figure 6.1. 15 Slices Used Throughout the Results for Pre-Surgery (Left) and Post-Surgery (Right)

In Figure 6.1, the most critical slices are listed as follows:

- The 1st slice is the nostrils.

- The 2nd slice corresponds to the nasal valve area.
- The 5th slice represents the tip of the lower conchae.
- The 7th slice is the tip of the middle conchae.
- In the 11th slice, all three conchae are visible.
- In the 13th slice, left and right passageways start to unite.
- The 15th slice is the throat.

However, in some parts of the text, the 15th slice, which represents the throat, is ignored due to the atypical results caused by its inclusion. This is wholly justified, since either the nasopharynx or its vicinity are not altered via the surgery.

In the simulations, a computer with an AMD Ryzen 3950x processor with 16 cores are used. All the cores were used throughout the simulations though the computer was also actively used during the simulations. Using this processor, precursor simulations took from 5 to 8 hours in wall-clock time depending on the iterations. Transient simulations took 4 to 5 days in walltime, where quick simulations end up near 5 days.

6.1 Results Obtained From Nasal Geometry

This section reports the geometrical characteristics of before and after the surgery. As mentioned in the literature review, Chapter 3, most of the other research found nasal geometry is commonly thought irrelevant to nasal obstruction. Yet, understanding the changes in nasal geometry is beneficial to understanding the result of the surgical approach.

6.1.1 Surface Area Through the Nasal Geometry

Since the mechano- and thermo-receptors are distributed throughout the nasal cavity and are the critical factor in obstruction, the surface area through the nasal cavity appears to be a decent parameter to investigate.

Expectedly, after surgery, the surface area of the nasal geometry is changed, given the alterations done to the tissue in the cavity. However, it is not known if the total surface area is increased or decreased, and if so, where the changes are developed.

The total surface areas before and after surgery of the nasal geometry are given in Figure 6.2. This figure shows that the total surface area shrank after the surgical operation. This change indicates that the total area available for receptors to interact gets smaller. However, this result can not be directly connected to a worse feeling of nasal obstruction because the flow around the tissues is not known. For example, a nasal cavity could be so clogged that airflow is so low that the surface area is irrelevant. Furthermore, since there is ambiguity about where the surface areas increased and decreased, this requires a local investigation of the nasal cavity.

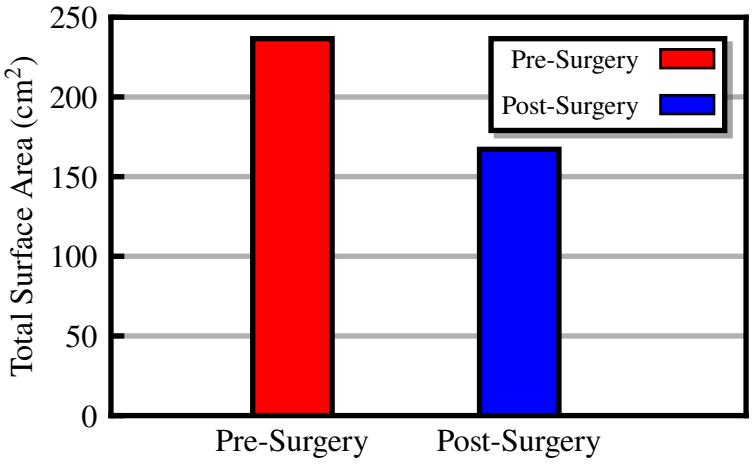

Figure 6.2. Total Surface Area Through the Cavities

A similar trend is seen in the surface area through the nasal cavity can be seen in Figure 6.3. This graph clearly shows that the total surface area through slices decreases; however, the surface areas appear especially smaller in the second half of the nasal passageways. This result could be caused by the endoscopic sinus surgery; however, pinpointing the cause is not very easy. For example, one may argue that some change in the surface area is not necessarily caused by the surgical operation but by the nasal cycle.

When left and right passageways are investigated separately for surface areas per slice, similar results appear in the summed surface area profile. Initial surface areas are

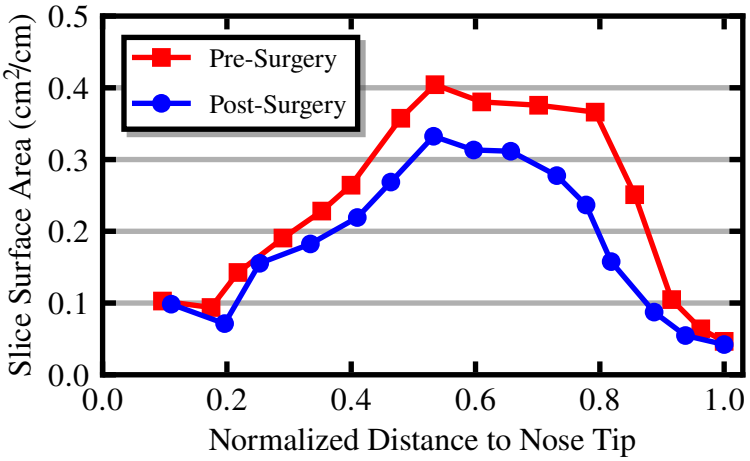

Figure 6.3. Total Surface Area Profile of Both Cavities

similar in pre- and post-surgery geometries, while surface areas are highly different in the second section. These profiles are given for left and right passageways in Figure 6.4 and Figure 6.5, respectively.

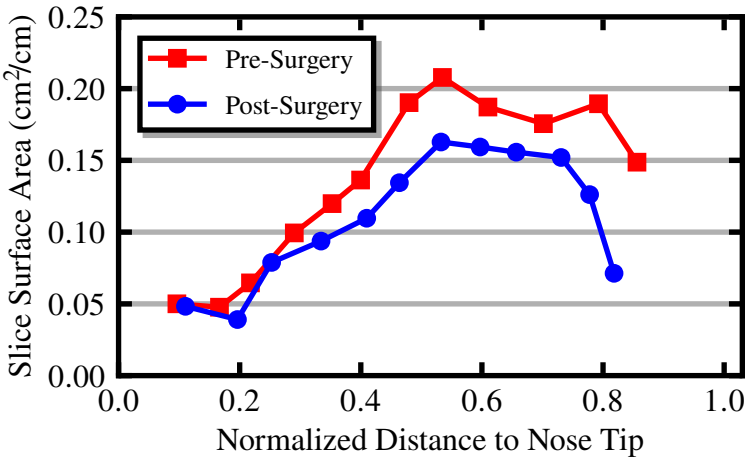

Figure 6.4. Left Passageway's Surface Area Profiles

6.1.2 Cross-Sectional Area Through the Nasal Geometry

Even though the previously mentioned literature claims that cross-sectional area is not directly connected to nasal obstruction feeling, cross-sectional change is the main change surgeries generate. The earlier academic work claims that the relationship between healthy airflow and cross-sectional area is associated with the process of

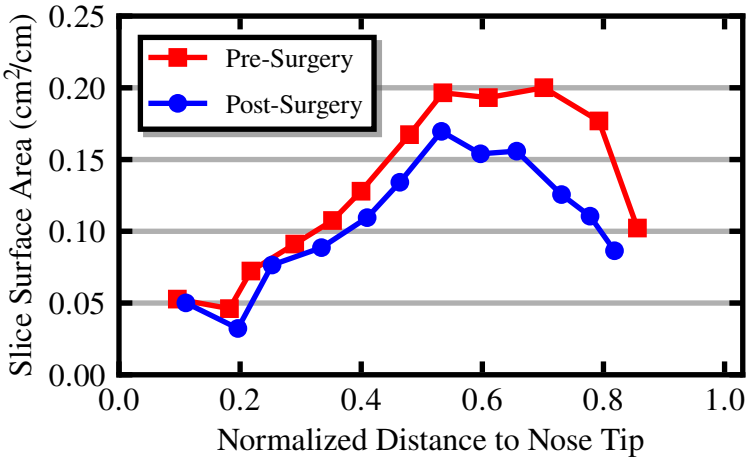

Figure 6.5. Right Passageway's Surface Area Profiles

increasing cross-sectional area, which means more flow in that part.

Eventually, most nasal surgeries change the cross-sectional area of the nasal cavity. The change appears either as a value or as a change in balance between passageways. The ones that increase the total value of cross-sectional area also reduce the forces and heat exchange on the nasal walls, thus reducing the stimulation of the nasal receptors. However, this intervention is necessary since the airflow must either be redirected or increased.

On the other hand, the surgeries aim to balance left and right passageway areas to fix airflow patterns, and total cross-sectional area changes are less susceptible to stimulation decrease issues. Nonetheless, it is rare to see such surgeries being applied alone in the practice since practitioners routinely incorporate nasal area-increasing techniques into nasal area-balancing surgeries.

In this thesis, both nasal areas are balanced and changed through septoplasty, turbinoplasty, and endoscopic sinus surgery. Especially, turbinoplasty greatly increases the cross-sectional area, while septoplasty balances the left and right passageways. The total change is given in Figure 6.6. According to this figure, one may observe that post-surgery areas around the middle of the nasal cavity appear much higher. This condition changes towards the back of the nasal cavity, and here, pre-surgery areas are considerably bigger than their counterparts. The reason for higher pre-surgery areas may be attributed to possible variations during the geometry generation and to the

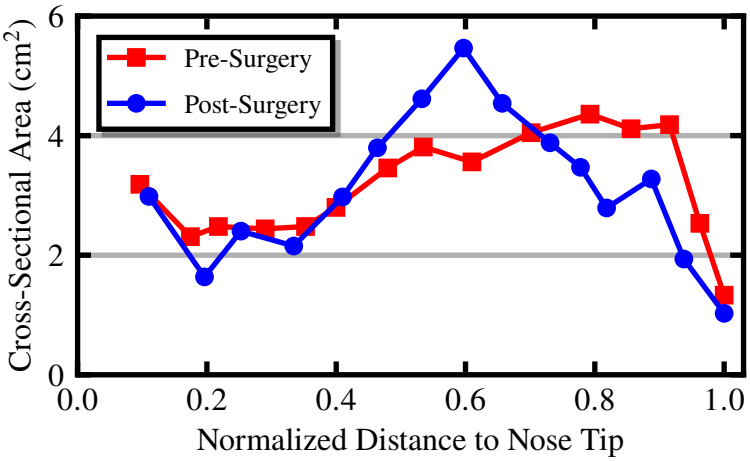

Figure 6.6. Cross-Sectional Area Profiles of Nasal Geometries

effects of the nasal cycle.

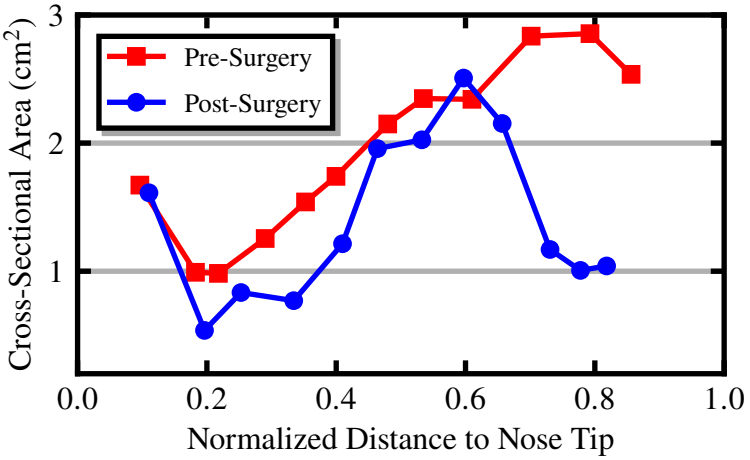

Figure 6.7. Cross-Sectional Area Profiles of Right Passageway Geometries

The right nasal passageway's cross-sectional area profile is given in Figure 6.7. This figure shows that the pre-surgery geometries are larger than the post-surgery ones, almost exclusively throughout the whole system. This indicates that such a change could be due to varying shrinkage and enlargement in the turbinates due to the nasal cycle. Therefore, this profile indicates that CT scans were taken while the dominant nasal passageways were different. Despite the nasal cycle, surgery undeniably brings the areas to parity between congested and obstructed conditions.

The left nasal cavity's cross-sectional area is demonstrated in Figure 6.8. In contrast

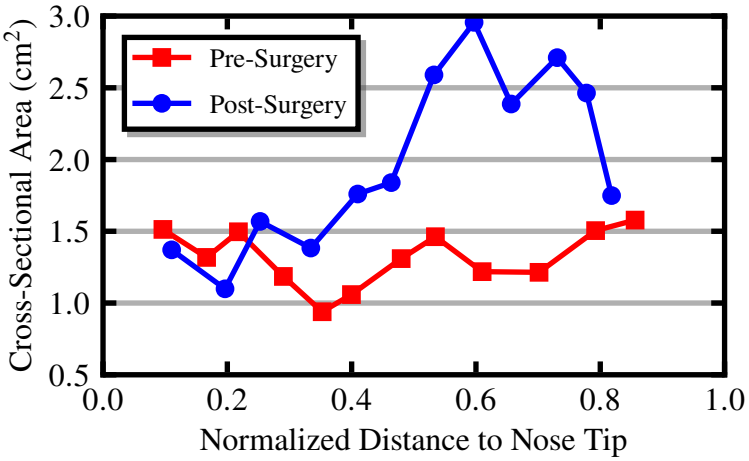

Figure 6.8. Cross-Sectional Area Profiles of Left Passageway Geometries

to the right cavity, post-surgery cross-sectional areas are significantly larger than pre-surgery areas. This dominance is almost persistent throughout the system, except for the initial part where turbinates are missing. Furthermore, the difference between the cross-sectional areas is excruciatingly distinguishable compared to the right nasal airway. This establishes the results of both the cycle and the surgery.

6.1.3 Volume of The Nasal Geometry

The total volume of the nasal geometry is a quick way to determine total area changes throughout the nasal cavity, as given in Figure 6.6. The total cross-sectional area change is unclear, since the post-surgery area appears larger around the mid-section but smaller towards the end. However, this vagueness could be revealed by comparing the total volumes before and after the surgical procedure.

6.2 Results Obtained From Numerical Simulations

This section focuses on the fluid-mechanics-related outcomes obtained from CFD simulations. To avoid confusion, two inhalation discharges are investigated separately. Some results presented here, such as nasal resistance and turbulent kinetic energies, are not commonly agreed as a signal of better nasal airflow in the literature. The reason behind the controversy is not definite. One may speculate that nasal surgeries are so

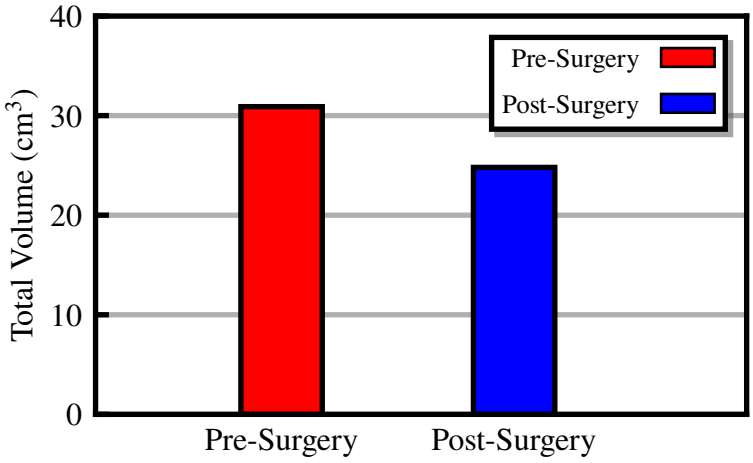

Figure 6.9. Total Volume of Nasal Cavity

effective in improving some parameters that even the poorly done surgeries increase them. Therefore, some improvement in such parameters can not be considered as a valid indicator of better nasal flow.

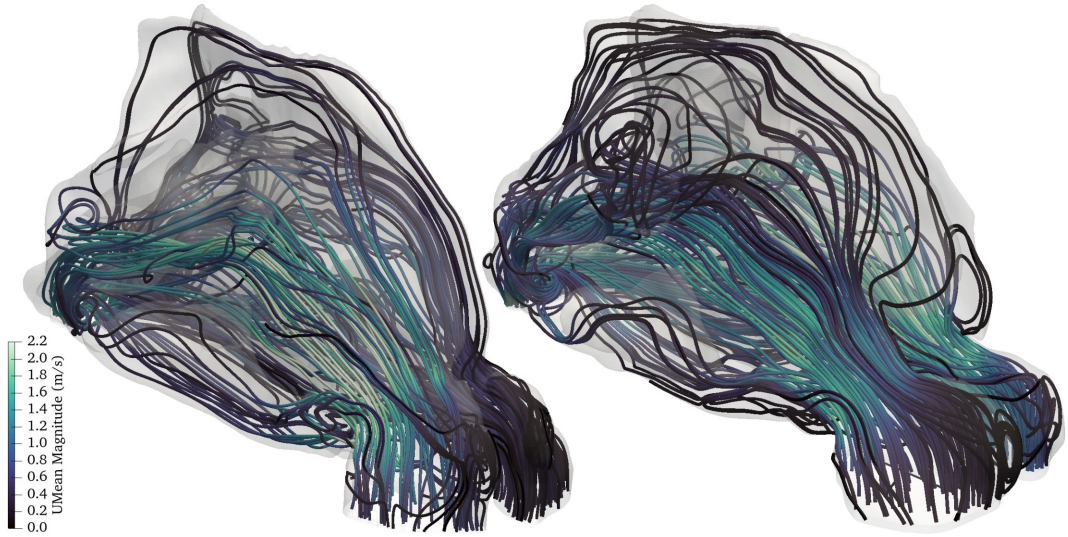

Figure 6.10. Streamlines for Pre-Surgery (Left) and Post-Surgery (Right): Slow Inhalation

The visualizations of airflow are given as streamlines in Figure 6.10 and Figure 6.11 for the slow and quick inhalation states. These images are given for mean flow state, and one may realize that there are many vortices appearing in the mean flow. Vortices appears to be more common in the post-surgery state of the nasal cavity. Additionally,

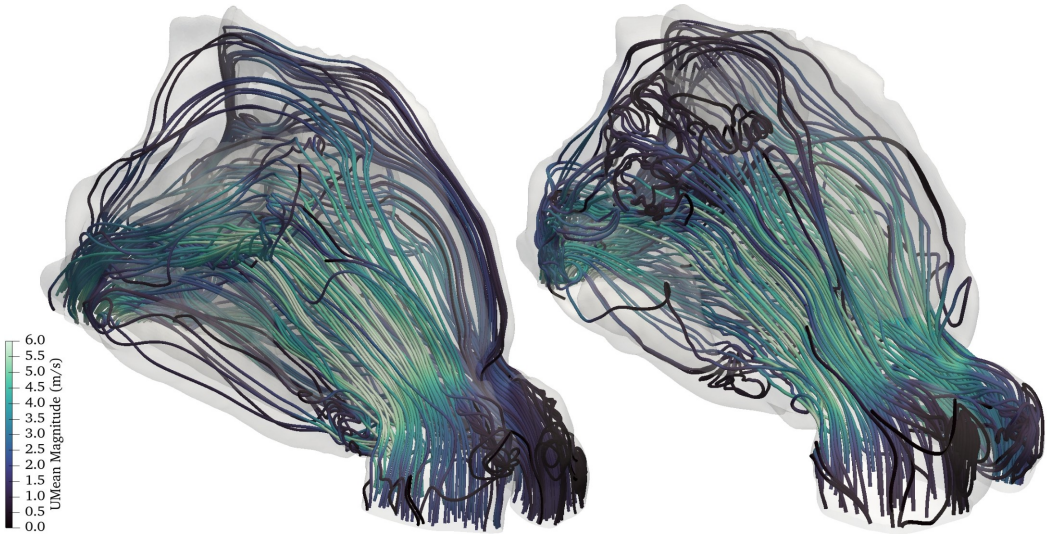

Figure 6.11. Streamlines for Pre-Surgery (Left) and Post-Surgery (Right): Quick Inhalation

vortices get more chaotic in the quick inhalation state. Lastly, it is possible to observe that there are more streamlines passing through the roof of the nasal cavity. For this result, one should investigate discharge rates separately, as given in Table 6.8 and Table 6.9. These tables also suggest a higher flow ratio in the superior areas of the nasal cavity in the quick state.

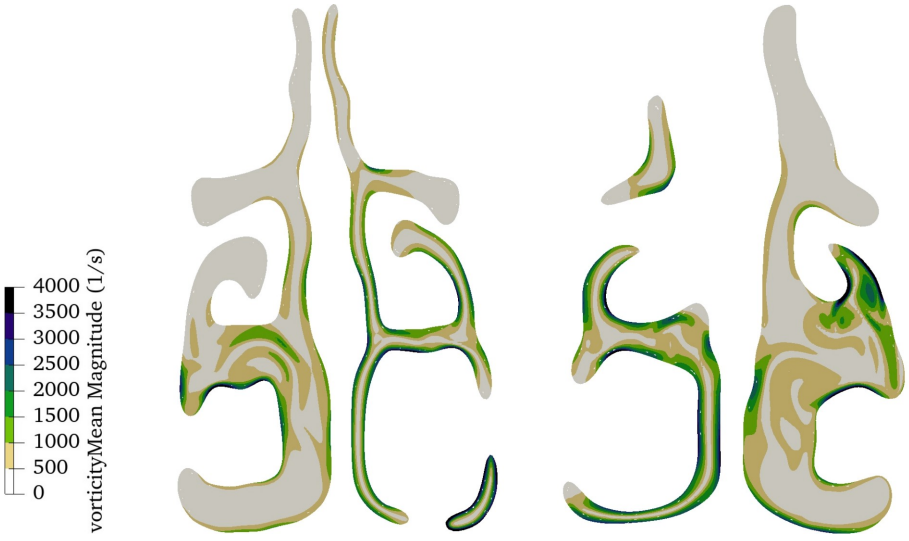

Figure 6.12. Vorticity of the 11^{th} Slice for Pre-Surgery (Left) and Post-Surgery (Right): Restful State

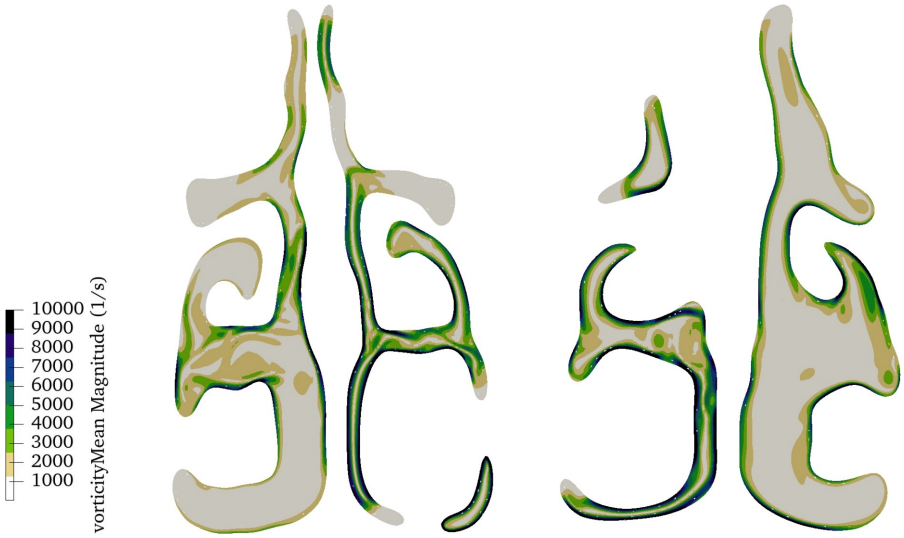

Figure 6.13. Vorticity of the 11th Slice for Pre-Surgery (Left) and Post-Surgery (Right): Quick State

The vorticity is further studied for the 11th slice for deeper understanding in terms of vorticity magnitudes. The results are given in Figure 6.12 and Figure 6.13 for the slow and quick inhalation states. These figures help understanding rotation in the fluid, and they possibly signify areas with high turbulence levels. On both discharge levels, vorticity magnitudes appears to be higher on the clogged sides. Also, the highest intensity of vorticity magnitude appears to be in the middle parts of the nasal cavity.

6.2.1 Pressure Results

Pressure drop is one of the traditional parameters, because it can be measured in vivo by a rhinomanometer. However, a rhinomanometer can only measure total pressure drop values at the nasal system's start and end. Since a numerical simulation is conducted, this subsection focuses on the total pressure changes and the pressure profiles.

6.2.1.1 Restful Inhalation's Pressure Results

Pressure development profiles obtained before and after the surgeries are given in this subsection for the restful inhalation discharge of 10.8 L/min.

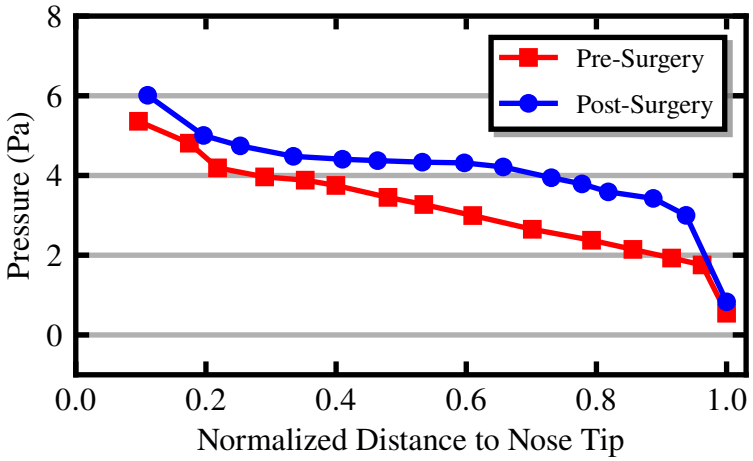

Figure 6.14. Restful Inhalation's Pressure Drop Profile Nostril to Throat: Both Cavities Averaged

In Figure 6.14, the pressure drop profile is given for the pre-surgery using a red line with squares as the data points. Here, it is possible to observe in the before-the-surgery state that pressure drops are remarkable near the nasal cavity's start and end. Such significant changes are expected because of the small cross-sectional areas near the nasal valve and the nasopharynx. Moreover, pressure steadily declines in the middle part of the nasal cavity, i.e., from the start of the turbinates to the end of them.

The post-surgical pressure development is given in Figure 6.14 in a blue line with circles indicating the data points. Like pre-surgery, the high pressure drops near the entrance and exit are visible. However, these pressure values drop more violently in this post-surgery state. In contrast to the pre-surgery pressure profile, post-surgery pressure values stays steady near the middle part of the system. This behavior signals that surgery allows a uniform flow behavior and possibly reduces energy losses in the system. However, velocities should be investigated to strengthen these arguments.

Paradoxically, when Figure 6.14 is observed as a whole, the total pressure drop required to move the air increases after the surgical operation. Especially since the surgical operations included turbinoplasty, which shaves some turbinates, the increased pressure drop requirement is puzzling. The confusion could be solved if the pressure drop is considered from the nostrils to the start of the nasopharynx. This means that the last point should be discarded in the system. Such an investigation is justifiable because

nasal surgeries do not alter any part of the proximity of the nasopharynx.

Moreover, the pressure drop in this area appears unusually high compared to other work in the literature. Similarly, the geometry used by Strien et al. (2021) also had such an extraordinary nasal geometry. They also discarded the nasopharynx while investigating the numerical simulation results.

From Figure 6.14, one may determine the required pressure drop between the 1^{st} and 14^{th} decreases after the post-surgery results. However, the result is not evident or precise in the figure. Therefore, after the elimination of the slice representing the throat, the total pressure drop in the nasal cavity is given in Table 6.1. Unambiguously, this table shows that the surgery helps reduce the required pressure to carry the same flowrate. Note that similar results are obtained if the comparison is made for the 13^{th} or 12^{th} slices rather than the 14^{th} slice.

Table 6.1. Pressure Values: Both Cavity Averaged

State	Nostrils (Pa)	Before Nasopharynx (Pa)	Difference (Pa)
Before Surgery	6.6	2.2	4.4
After Surgery	7.4	3.7	3.7

After understanding that the surgery helps to reduce the required pressure drop for a given flow rate, another issue emerges: The cross-sectional area profile of the nasal cavity, Figure 6.6, disagrees with the pressure drop rate. Similarly, the reduced nasal cavity total volume predicts that the pressure drop should increase. The most straightforward explanation for this unexpected result is that airflow in the nasal cavity is not uniform but localized. This means that air flows at some specific locations, and the flow area around them is enlarged. Indeed, air flows mainly in the nasal cavity's middle and inferior meatus areas, which surround the turbinates. Turbinoplasty directly increases these areas and causes lower pressure requirements for airflow.

When the left and right nostrils are investigated separately, pressure profiles appear similar to the averaged version. Also, total pressure drops for singular inspection are given in Table 6.2. These values are given for the nostrils and, just before the

passageways merge: the 1st and 13th slices.

Table 6.2. Pressures for Singular Cavities

State	Nostril (Pa)	Before Merge (Pa)	Difference
Left Cavity			
Before Surgery	6.8	2.6	4.2
After Surgery	7.7	4.1	3.6
Right Cavity			
Before Surgery	6.3	2.6	3.7
After Surgery	7.0	4.7	2.4

Lastly, pressure profiles in a slice that covers all three conchae, superior, middle, and inferior, are given in Figure 6.15. This profile is unsatisfactory for comparing before and after results because the pressure values are relative pressures. Earlier comparisons should be preferred over this visual comparison. However, this figure allows visualization of the pressure variation near the known structures of the nasal cavity. In this figure, the left side represents the pre-surgery geometry, and the right side represents the post-surgery geometry. In Figure 6.15, one may observe that pressures are low near the septum wall but increasing away from the septum. Similarly, superior areas of the cavity exhibit higher pressure, possibly due to low velocity values. Moreover, the magnitude of pressure appears to be highest on the clogged side of the nasal cavity, between the inferior concha and septum.

6.2.1.2 Quick Inhalation's Pressure Results

Pressure profiles are also obtained for quick inhalation to compare how they change before and after the nasal surgery. The information given here is similar to restful inhalation data. The last slice representing the nasopharynx is excluded from the numerical data given in Table 6.3. Also, the pressure development profile is given in Figure 6.16 to show changes in pressure values.

Figure 6.15. Pressures of the 11th Slice for Pre-Surgery (Left) and Post-Surgery (Right): Restful State

Table 6.3. Pressures for Quick Inhalation

State	Nostril (Pa)	Ending Plane (Pa)	Difference
Both Cavities			
Before Surgery	42.6	16.0	26.7
After Surgery	54.7	26.8	27.9
Left Cavity			
Before Surgery	44.2	20.5	23.8
After Surgery	52.0	36.1	15.9
Right Cavity			
Before Surgery	41.0	20.0	21.0
After Surgery	57.4	31.4	25.9

According to Figure 6.16, high-pressure drops are observed in the nasal pressure profiles similar to restful inhalation. This phenomenon is due to air acceleration in the nasal valve and nasopharynx regions, causing lower pressure zones. Nevertheless,

the pressure drops appear larger at the nasal valve and nasopharynx regions; the increment appears more pronounced in the post-surgical geometry. This behavior could be explained by the lower pressure drop rates near the middle parts of the nasal cavity in after-surgery geometry.

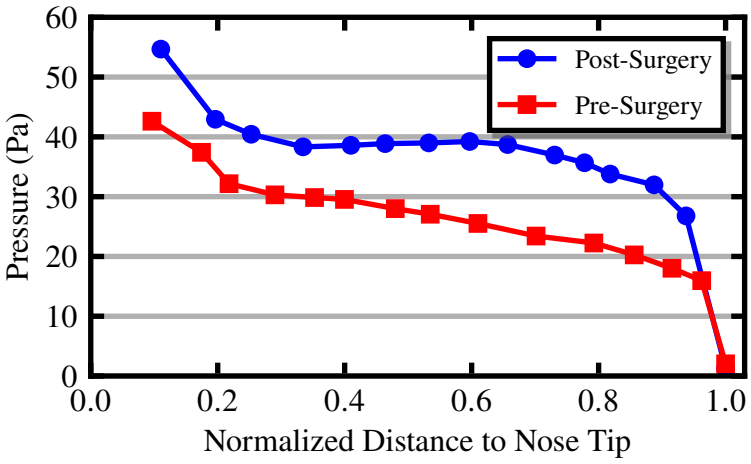

Figure 6.16. Quick Inhalation's Pressure Drop Profile Nostril to Throat: Both Cavities Averaged

The pressure profiles in the 11^{th} slice, which covers all three conchae, are given in Figure 6.17. As mentioned in the restful breathing subsubsection, Subsubsection 6.2.1.1 can not be compared with before and after results because pressures are relative pressures. The results concerning the pressure-related profile in the 11^{th} slice of quick inhalation resemble the restful pressure results. The only exception is that the magnitude of pressure values reaches higher values given the high discharge rate.

6.2.2 Discharge Rates

Even though total discharge is given as an input to the numerical system, since nasal flow is divided into two pipe-like cavities, separate discharges can not be known as a priori. Therefore, the discharges for individual passageways are reported in this subsection's subsubsections.

Before proceeding further, the general outlook on velocity magnitudes could be given. Pre-surgery regular and quick breathing rates are given in Figure 6.18. Similarly, Figure 6.19 represents the post-surgery velocity magnitudes. The comparison and

Figure 6.17. Pressures of the 11th Slice for Pre-Surgery (Left) and Post-Surgery (Right): Quick State

comments on these images are unnecessary. The only reason for including them in this part is to show the reader the resulting profiles while avoiding cluttering with individual figures. The reader should be able to understand better the general picture of the airflow in the nasal cavity with these figures.

Figure 6.18. Restful Inhalation's Velocity Magnitudes in All Slices for Pre-Surgery (Left) and Post-Surgery (Right)

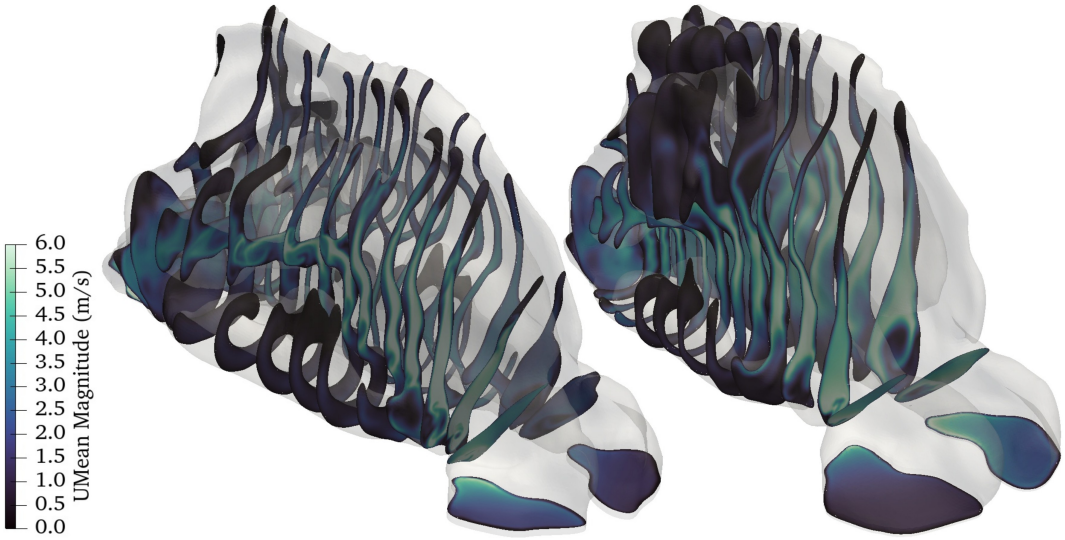

Figure 6.19. Quick Inhalation's Velocity Magnitudes in All Slices for Pre-Surgery (Left) and Post-Surgery (Right)

6.2.2.1 Restful Inhalation's Discharge Results

The discharges per passageway for restful inhalation, 10.8 L/min, are given in Table 6.4. According to this table, flow mainly passes through the right passageway during restful inhalation. 70 % of the air passes through the right nasal cavity. However, after the surgery, this dominance shifts to the other passageway. This shift is probably due to the effects of the nasal cycle rather than surgery.

Table 6.4. Discharge Values in Nasal Passageways: Restful Breathing

State	Left (L/min)	Right (L/min)
Before Surgery	3.2	7.6
After Surgery	7.3	3.5

Slow inhalation's velocity profiles for pre- and post-surgery geometries are given in Figure 6.20 for the 11^{th} slice. It is seen that velocity magnitudes reach up to 1.8 m/s in this slice. This figure shows that flow clearly peaks in some areas, then sharply reduces to near-zero values. Such a behavior suggests a laminar-like flow appearing in the cavity. The behavior can be clearly understood when compared to the quick inhalation velocity profile shown in Figure 6.21: On main passageways, velocities do not peak,

but a general high velocity appears all around the slice.

Figure 6.20. Velocity Magnitudes of the 11th Slice for Pre-Surgery (Left) and Post-Surgery (Right): Restful State

6.2.2.2 Quick Inhalation's Discharge Results

The discharge values per passageways for the quick inhalation, 33.6 L/min, are given in Table 6.5. Similar to the restful inhalation results, before the surgery, the right nostril is the dominant side of the nasal airflow, and the left side is the dominant side after the surgery. However, the dominant airflow behavior gets milder compared to the restful inhalation state.

Table 6.5. Discharge Values in Nasal Passageways: Quick Breathing

State	Left (L/min)	Right (L/min)
Before Surgery	12.4	21.2
After Surgery	21.0	12.6

Quick inhalation's velocity profiles for pre- and post-surgery geometries are given in Figure 6.21 for the 11th slice. It is seen that velocity magnitudes reach up to 5.5 m/s in this area. In pre-surgery geometry, flow in the right nasal cavity is mainly around

the middle part of the geometry. Also, the flow on the right appears more uniform throughout the section. On the other hand, the post-surgery geometry shows signs of more uniform flow in both cavities.

Figure 6.21. Velocity Magnitudes of the 11th Slice for Pre-Surgery (Left) and Post-Surgery (Right): Quick State

6.2.3 Wall Shear Stresses

As explained in detail in the literature review chapter, Chapter 3, the wall shear stress values represent mechanical stimulation. Also, wall shear stress values are parallel to the heat convection rates (Elad et al., 2006; Zhao et al., 2011). Therefore, the stimulation on both the mechanical and the cold receptors could be explained by wall shear stresses. Therefore, wall shear stress values are the key factor in determining nasal obstruction. A considerable reduction in wall shear stresses signals that a person could feel an obstructed breathing even though there is airflow. This subsection compares and discusses wall shear stresses and total forces appearing on the 15 slices selected through the nasal cavities.

6.2.3.1 Restful Inhalation's Wall Shear Stresses

This subsubsection focuses on the wall shear stress and wall shear force profiles of the restful inhalation. The wall shear stresses are reported in average terms. Force-related profiles are reported per meter due to slices being in 2D structures. Figure 6.22 depicts and compares the wall shear stress profiles of the pre- and post-surgery geometries.

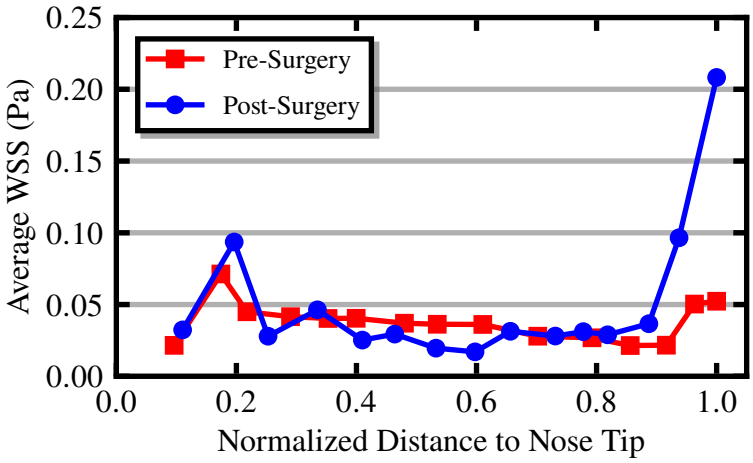

Figure 6.22. Wall Shear Stress Profiles: Restful Inhalation

According to the wall shear stress profile, after the surgery, the average wall shear stress values for restful inhalation do not decrease by a large margin. Still, there is a slight decrease in the average values. However, these results cannot be attributed to a feeling of nasal obstruction without a visual examination of the slices. This is because pre-surgery values might appear high due to some local shear stress peak, while post-surgery results are uniform. Such a result would indicate that more nasal receptors get stimulated due to uniform shear stresses.

Furthermore, unlike the wall shear stress profile, the force profile in Figure 6.23 shows a considerable change. The total force exerted on the nasal cavity decreases by a significant amount after the surgery. Such a change is expected given that the wall shear stresses do not change while the surface areas decrease after the surgery. This result possibly indicates that total stimulation in the nasal cavity is decreased at the end. Nonetheless, this outcome is challenging to justify as the stimulation is viewed as a ratio, thereby rendering the forces depicted in Figure 6.23 meaningless. This is because the ratio of stimulated receptors to not-stimulated receptors during the airflow

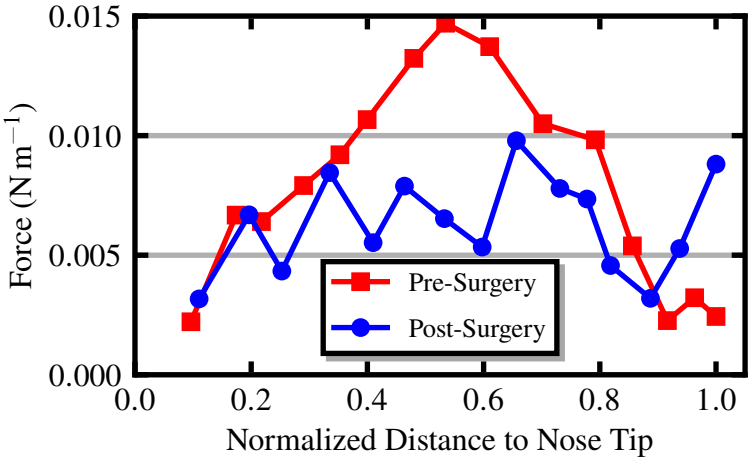

Figure 6.23. Wall Shear Force Profiles: Restful Inhalation

does not change based on wall shear stresses. In contrast, it is possible to claim that, despite the reduced surface area, an increase in the density of receptors would lead to better nasal patency. Such a hypothesis requires research on the change in number of nasal receptors after the surgery; thus, drawing a conclusion from this result is not possible.

6.2.3.2 Quick Inhalation's Wall Shear Stresses

This subsubsection focuses on the wall shear stresses and the wall shear forces in the quick inhalation state. Similar unit conversations that are explained in the restful inhalation state can be applied in this section as well. Figure 6.24 draws the wall shear stress profiles, and Figure 6.25 shows the wall shear force profiles.

The results for both wall shear stresses and forces are similar to those for the restful inhalation state. Expectedly, the results are magnified, and the magnification is about four times the restful inhalation state. However, a discernible difference is visible when comparing Figure 6.24 and Figure 6.25 with the outcomes of relaxed inhalation. In post-surgery geometry, the wall shear and force values increase more than they do in pre-surgery geometry. Turbulence and eddy formations in the mean flow are possible suspects for this intensified increase.

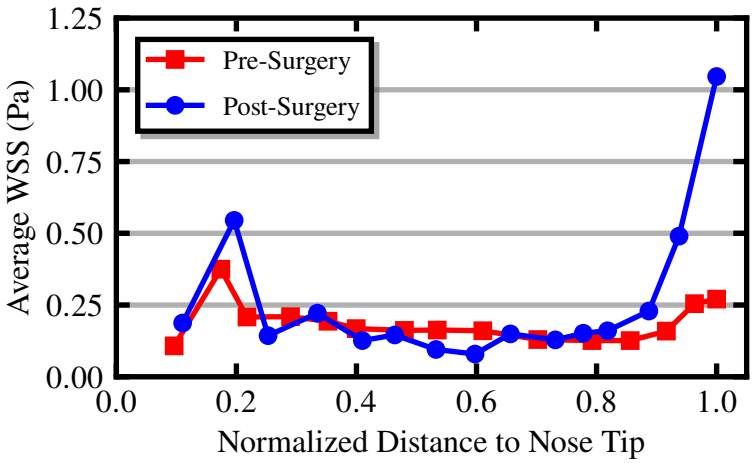

Figure 6.24. Wall Shear Stress Profiles: Quick Inhalation

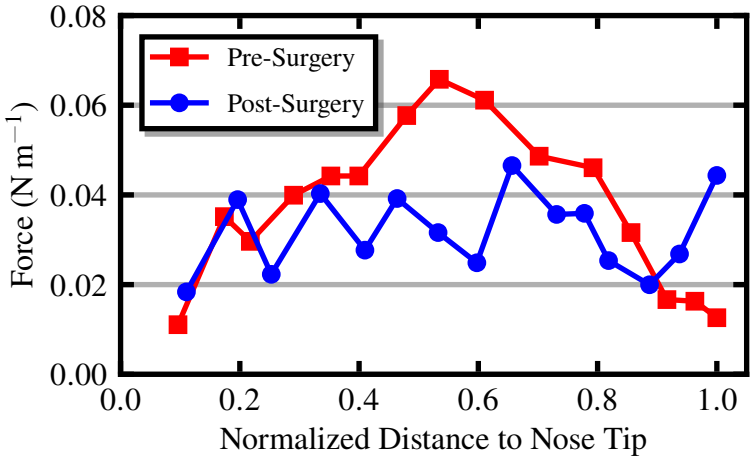

Figure 6.25. Wall Shear Force Profiles: Quick Inhalation

6.2.4 Nasal Resistances

Nasal airway resistance is a common metric reported in the literature. This metric is defined as the pressure drop through the nasal cavity to volumetric flow, as follows:

$$R = \frac{\Delta p}{Q}. \tag{6.1}$$

Since the nasal airway resistance metric is commonly used, comparing this parameter with others in the literature is possible. The comparison is generally done so that pressure drops and volumetric flow rates are drawn on a graph. This comparison could

be accepted as a semi-validation of the numerical simulation. It is not a full validation because the two nasal geometries are different. All in all, nasal resistance provides partial validation by enabling the comparison of upper and lower boundaries in earlier academic work.

6.2.4.1 Restful Inhalation's Nasal Resistance Results

The nasal resistance values for restful inhalation could be directly calculated using the pressure drop values and discharges in earlier sections. Therefore, Table 6.6 shows nasal resistances for pre- and post-surgery numerical simulations of restful inhalation.

Table 6.6. Nasal Resistance Values of Restful Inhalation

State	Resistance (Pa s/m^3)
Both Cavities	
Before Surgery	0.34
After Surgery	0.41
Left Cavity	
Before Surgery	1.31
After Surgery	0.49
Right Cavity	
Before Surgery	0.49
After Surgery	0.69

6.2.4.2 Quick Inhalation's Nasal Resistance Results

Similar to restful inhalation, the nasal resistance values are calculated using the earlier pressure and discharges given in earlier sections. The results are given in Table 6.7, which shows nasal resistances for pre- and post-surgery numerical simulations of quick inhalation.

Table 6.7. Nasal Resistance Values of Quick Inhalation

State	Resistance (Pa s/m^3)
Both Cavities	
Before Surgery	0.79
After Surgery	0.83
Left Cavity	
Before Surgery	1.92
After Surgery	0.76
Right Cavity	
Before Surgery	0.99
After Surgery	2.06

6.2.5 Turbulent Kinetic Energy

Turbulent kinetic energy is the summation of the energies carried by the eddies in the turbulent flow. The total turbulent kinetic energy represents the amount of turbulence in the flow. Moreover, an argument that claims the total kinetic energies may be able to predict nasal obstruction is possible. The argument appears in line with pressure drop and nasal resistance, since turbulence causes an increase in total energy loss.

6.2.5.1 Restful Inhalation's Turbulent Kinetic Energy Results

The total turbulent kinetic energy results from the numerical simulation of slow inhalation state are given in Figure 6.26. In this figure, the red line with square data points represents the pre-surgery total turbulent kinetic energies, and the blue line with circular data points shows the post-surgery turbulence energy. Both before and after the surgery, the total kinetic energy in the airflow is considerably low.

The low energies are no surprise since the flow is very slow. However, pre-surgery geometry can produce higher turbulence values compared to its counterpart. This result suggests that the geometry is able to produce a more turbulent airflow. Therefore,

before the surgery, the total heat exchange and diffusion of molecules appear higher in the nasal flow. These phenomena are related to the mixing of the liquid; thus, turbulence intrinsically enhances them. Furthermore, heat exchange and diffusion are crucial in the nasal cavity because they provide better nasal patency and smelling ability. Therefore, it is possible that surgery disrupts the characteristics of slow inhalation and may exacerbate the ongoing issues.

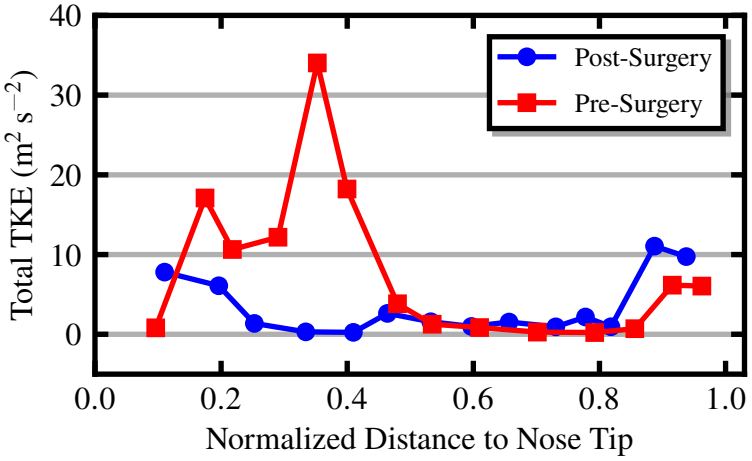

Figure 6.26. Turbulent Kinetic Energy Profile: Restful Inhalation

The reason behind the higher kinetic energy results in pre-surgery geometry is paradoxical. This is because, in a wall-bounded flow, the surface area of the flow is connected to the degree of turbulence. This relationship is derived from the Reynolds number, which is calculated as:

$$\mathrm{Re} = \frac{U D_{\mathrm{H}}}{\nu} = 4\frac{Q}{P\nu}, \tag{6.2}$$

where U, D_{H}, ν, Q, and P are velocity, hydraulic diameter, kinematic viscosity, discharge and wetted perimeter, respectively.

The mere difference in pre- and post-surgery geometries in the Reynolds number is the wetted perimeter of the flow. Accordingly, given the same fluid and flow rate, a smaller wetted perimeter should increase the turbulence levels in the flow. In a nasal airflow, the wetted perimeter is equal to the surface area, since the liquid is a gas. In Figure 6.3, it is shown that surgery leads to a shrinkage in the surface area. If the surface area is

smaller after surgery, one may expect the Reynolds number to go up.

However, the increase in turbulent kinetic energy signals that another variable plays a role in the generation of turbulence. A straightforward reason does not easily justify this surprising result, though some theories could be made. The simplest explanation is probably connected to the fact that nasal airflow happens locally through the nasal geometry. This localized airflow renders those approaches concerning the whole area invalid. In other words, due to the localized airflow, the wetted perimeter also gets localized; therefore, the localized wetted perimeter disallows the use of the above Reynolds number approach.

6.2.5.2 Quick Inhalation's Turbulent Kinetic Energy Results

Figure 6.27 represents the turbulent kinetic energy profile for the quick inhalation with a volumetric flow rate of 33.6 L/min. Similar to other figures, the red line with circles represents the pre-surgery, and the blue line with squares represents the post-surgery results.

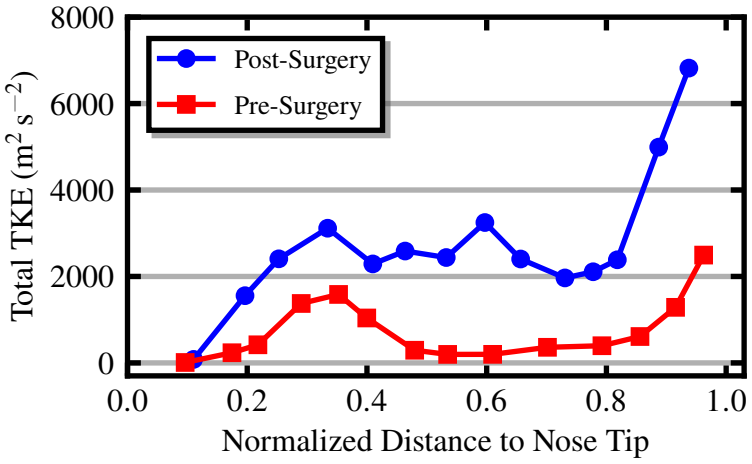

Figure 6.27. Turbulent Kinetic Energy Profile: Quick Inhalation

Compared to restful inhalation, the total energies are multiple orders of magnitude higher, especially for the post-surgery results. Contrary to restful inhalation results, the total turbulent energy is now more prominent in the post-surgery geometry. Similar arguments for restful turbulent kinetic energy could be given: Post-surgery geometry appears to have better diffusive and heat exchange due to higher turbulence values.

Moreover, the increase in turbulent kinetic energy conforms more to the Reynolds number approach explained earlier in the restful inhalation part of turbulent kinetic energy. Total turbulent kinetic energy increases since surface area decreases with the same volumetric airflow rate in the nasal cavity. The shift in turbulent energy behavior is probably due to the flow turning more uniform in the flow area, thus making more of the wetted perimeter relevant.

6.2.6 Localized Discharge Rates

As earlier sections mentioned, the global investigation of nasal geometry leads to unpredicted results. It is shown that, especially during restful inhalation, the localized flow pattern in nasal airflow leads to a higher pressure drop through higher cross-sectional areas and increased turbulent behavior. Therefore, investigating nasal airflow part by part should yield better results, at least for restful inhalation. Indeed, similar investigations are seen in the literature by Keyhani et al. (1995), Li, Farag, et al. (2017), Malik et al. (2019), and Subramaniam et al. (1998).

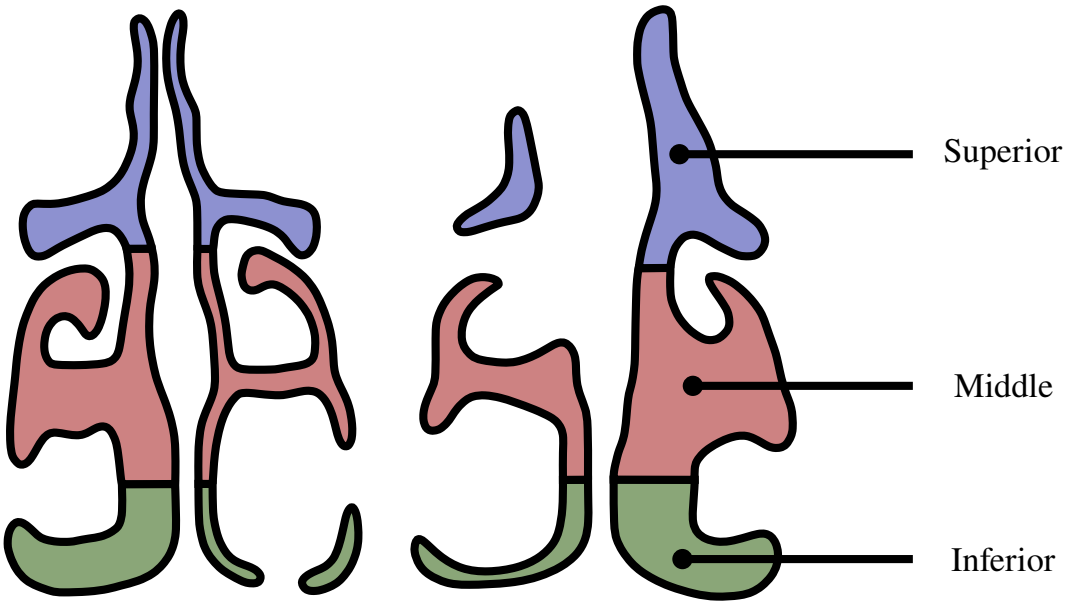

Figure 6.28. Sectioned Pre- and Post-Surgery Shape of the 11th Slice

The localized discharges are investigated in a slice encompassing all three turbinates: inferior, middle, and superior. This plane is divided into three pieces to cover these conchae: the inferior, middle, and superior parts. The sectioned plane is shown for

before and after geometry in Figure 6.28. This plane is the 11^{th} plane for both of the geometries located at points 0.79 and 0.78 normalized lengths between the tip of the nostril and the end of the nasal cavity, respectively. In the before surgery state, geometry's left passageway has a clogged point in the inferior section. Similarly, the after geometry in the figure has a clogged part in the superior and middle sections of the right passageway. Even though these clogged parts do not exist throughout the nasal geometry, they alter the total flow rate of the whole geometry.

6.2.6.1 Restful Inhalation's Localized Discharge Results

The flow rates are localized according to the cross-sectional areas shown in Figure 6.28. Also, the localized results are given in Table 6.8. As mentioned earlier, investigations based on localized flow rates excel at predicting nasal obstruction because of the high variations in the flow plane.

Table 6.8. Normal Inhalation's Localized Flow Parameters in the 11^{th} Slice

	Before		After	
	Discharge	Velocity	Discharge	Velocity
Superior	0.65	0.10	0.43	0.080
Middle	7.1	0.52	6.8	0.65
Inferior	3.1	0.52	3.5	0.70

Note. Discharge values are given in L/min, and velocity values are given in m/s. Two significant figures are used to report values.

Table 6.8 indicates that the flow rates and velocities are considerably changed throughout the section. The flow rates in the superior and middle regions shifted towards the inferior regions. Given the turbinoplasty surgery in the inferior turbinates, this change is expected.

Moreover, after the surgery, flow around the turbinates does not get heavily disrupted, unlike in other academic works such as Li, Farag, et al. (2017). The work of Li, Farag,

et al. (2017) shows that some surgeries lead to very low inferior flow rates, which cause almost no stimulation on the inferior turbinates. On the other hand, current surgery is able to increase flow around the inferior turbinate. Therefore, flow is not disrupted to the degree that it is focused only on a single localized area.

On another note, the low flow rates in the superior region are reported in the work on healthy individuals by Malik et al. (2019). Furthermore, Malik et al. (2019) showed that the peak flow appears on either the middle or inferior turbinate; however, higher volumetric flow rates through the cavity's middle part correlate to better nasal patency ratings. Since the currently investigated nasal cavity is not healthy, it is unknown if such a correlation could be applied to current results.

6.2.6.2 Quick Inhalation's Localized Discharge Results

The flow rates are locally investigated in the cross-sectional areas shown in Figure 6.28. These localized flow rates for quick inhalation are given in Table 6.9. Even though the uniform comparison appears viable for this flow rate, one may see that flow rates and velocities are highly non-uniform in the quick inhalation results.

Table 6.9. Quick Inhalation's Localized Flow Parameters in the 11^{th} Slice

	Before		After	
	Discharge	Velocity	Discharge	Velocity
Superior	2.8	0.42	2.2	0.41
Middle	23	1.7	21	2.0
Inferior	7.6	1.3	11	2.1

Note. Discharge values are given in L/min, and velocity values are given in m/s. Two significant figures are used to report values.

In quick inhalation, Table 6.9 shows that the inferior region flow rate gets noticeably higher than before the surgery. Again, this result could be interpreted as satisfactory or unsatisfactory based on viewpoint. This surgery is satisfactory because there

are examples of surgeries that lead to erratic middle airway dominant flow. This singular-area dominant flow causes extreme wearing and drying in the middle section while generating insignificant stimulation in other parts of the nasal cavity. These characteristic airflow patterns cause nasal obstruction, crusting, and a dry-feeling symptoms.

On the other hand, as shown by Malik et al. (2019), an increase in inferior volumetric flow could be related to nasal obstruction feelings. However, the airflow did not evolve into inferior airflow dominated but got a slight increase. Therefore, it is hard to claim that the feeling of nasal obstruction is stronger now.

6.2.7 Investigation of Localized Wall Shear Stresses

In this section, wall shear stresses are examined regionally by using local data and as a whole plane by using the cross-sectional view of the walls. Similar to localized investigation of the discharge rates, investigation of wall shear stress in three areas is preferred, given the highly localized behavior of nasal airflow. Therefore, unlike Subsection 6.2.3 a plane that covers all three turbinates, the 11^{th} slice, is sectioned into superior, middle, and inferior parts. These parts cover their respective turbinates, which represent the stimulation on them.

6.2.7.1 Restful Inhalation's Local Shear Stresses

This subsubsection explores wall shear stress-related values for the restful inhalation state. Figure 6.29 shows wall shear stresses for pre- and post-surgery geometries. 11^{th} slice's total surface area per length, total wall shear stresses, average wall shear stress values, and wall shear force per length are given in Table 6.10. Note that wall shear stresses are given in m^2/s^2. Thus, one may convert the results into Pa by multiplying the given values by the density of air, ρ, which could be taken as $1.225\,\text{kg/m}^3$.

In Figure 6.29, one may observe that wall shear stresses are reaching up to $0.14\,\text{m}^2/\text{s}^2$, which is equal to 0.17 Pa. The shear stresses appear more uniform and high on the clogged side in pre- and post-surgery geometries. Also, stresses near the superior

parts are considerably lower than the slice's inferior and middle parts. Lastly, even though turbinates are reduced through turbinoplasty, wall shear rates do not appear significantly reduced in the nasal cavity.

Figure 6.29. Wall Shear Stress Values for Pre-Surgery (Left) and Post-Surgery (Right): Restful Inhalation

Note. Wall shear stress values are given per density of air.

Even though it is possible to visually examine wall shear stresses as planes, perhaps the better way is to separate walls into the already-mentioned sections. In Table 6.10, it is possible to observe that total force appears to be lower in every region, though not by a considerable margin. Given a turbinoplasty, a significant change is expected since the surface area gets smaller, also an increase in cross-sectional area. However, slight changes show that stimulation on the nasal receptors did not decrease enough to cause complications such as empty nose syndrome. Furthermore, it is possible to see that average wall shear stresses are almost the same as their pre-surgery counterparts. These values are important because receptors require a threshold stress value to get aroused; therefore, one may say that the surgery is very well done. Lastly, the post-surgery wall shear stresses in Table 6.10 are not high due to some peaks in the geometry. Figure 6.29 shows the average wall shear stresses distributed uniformly throughout

the cross-section. Such uniform stresses are vital because if the stresses were focused on some local zone, this would lead to symptoms similar to those seen in empty nose syndrome.

Table 6.10. Restful Inhalation's Localized Wall Shear Stress Values

	Before			After		
	SA	WSS	Force	SA	WSS	Force
Superior	0.12	$8.8 \cdot 10^{-3}$	$1.0 \cdot 10^{-3}$	0.070	$1.0 \cdot 10^{-2}$	$7.2 \cdot 10^{-4}$
Middle	0.17	$2.6 \cdot 10^{-2}$	$4.4 \cdot 10^{-3}$	0.10	$3.2 \cdot 10^{-2}$	$3.2 \cdot 10^{-3}$
Inferior	0.078	$3.3 \cdot 10^{-2}$	$2.6 \cdot 10^{-3}$	0.065	$3.2 \cdot 10^{-2}$	$2.1 \cdot 10^{-3}$

Note. The surface areas and the forces are given per length in this table. The surface areas are in m^2/m, the wall shear stresses are in m^2/s^2, the wall shear forces are in $m^3/(s^2\,m)$. Two significant figures are used to report values in this table.

6.2.7.2 Quick Inhalation's Local Wall Shear Stresses

This subsubsection is dedicated to investigating the quick inhalation results in terms of wall shear stresses and shear forces. Figure 6.30 represents the wall shear stresses for pre- and post-surgery geometries for the 11^{th} slice. Also, total surface area per length, total wall shear stresses, average wall shear stress values, and wall shear force per length are given in Table 6.11. The wall shear stresses are given in m^2/s^2, which could be converted into Pa by multiplying given values by the density of air, ρ, which could be taken as $1.225\,kg/m^3$.

The wall shear stresses appear similar to the restful inhalation state, except for some local differences and magnitudes. As shown in Figure 6.30, wall shear values reach up to $0.7\,m^2/s^2$. This peak value is five times higher than restful inhalation peak values. This means that peak wall shear values increase more than the increase seen in discharge rates, 10.8 L/min to 33.6 L/min: around three times the discharge rate.

Moreover, when Figure 6.30 is compared with Figure 6.29, one may realize that the

Figure 6.30. Wall Shear Stress Values for Pre-Surgery (Left) and Post-Surgery (Right): Quick Inhalation

Note. Wall shear stress values are given per density of air.

intensity of wall shear stresses changes in some parts of the geometry. During quick inhalation, shear stresses near the middle turbinate get more noticeable in intensity. These pronounced stress levels could be observed around the middle part of the right cavities. On the other hand, near the inferior turbinates, shear stresses get weaker compared to restful inhalation.

Table 6.11 reports the mean localized wall shear forces, stresses, and surface areas. Similar to peak shear stress and the increased magnitudes shown in Figure 6.30, localized shear values are increased by a very good margin. The wall shear stresses and forces are magnified by four, five, and five times in the pre-surgery state in superior, middle, and inferior areas, respectively. When the post-surgery magnification is compared, shear stresses and forces increase by seven, five, and four times compared to restful inhalation in a quick inhalation state. These values are given for the nasal geometry's superior, middle, and inferior parts.

These results show that the stresses can get enhanced to higher values in post-surgery

Table 6.11. Quick Inhalation's Localized Wall Shear Stress Values

	Before			After		
	SA	WSS	Force	SA	WSS	Force
Superior	0.12	$3.7 \cdot 10^{-2}$	$4.2 \cdot 10^{-3}$	0.070	$8.2 \cdot 10^{-2}$	$5.8 \cdot 10^{-3}$
Middle	0.17	$1.4 \cdot 10^{-1}$	$2.4 \cdot 10^{-2}$	0.10	$1.5 \cdot 10^{-1}$	$1.5 \cdot 10^{-2}$
Inferior	0.078	$1.3 \cdot 10^{-1}$	$9.8 \cdot 10^{-3}$	0.065	$1.3 \cdot 10^{-1}$	$8.6 \cdot 10^{-3}$

Note. The surface areas and the forces are given per length in this table. The surface areas are in m^2/m, the wall shear stresses are in m^2/s^2, the wall shear forces are in $m^3/(s^2\ m)$. Two significant figures are used to report values in this table.

geometry compared to pre-surgery geometry. This example shows that shear stresses develop to higher values in post-surgery airflow, causing more stimulation on nasal receptors. Conclusively, the surgery aids the magnification of the local wall shear stresses in the quick inhalation state.

6.2.8 Energy Spectral of Numerical Simulations

Energy spectra distribution is a representation of the energy of the velocity fluctuations against their frequencies. Such plots represent the turbulent kinetic energy transfer and dissipation throughout the domain of interest. Moreover, it has been shown that the inertial sub-range could be represented as a function of kinetic energy with a power of -5/3. This representation is called the -5/3 law and is derived for the flows with isotropic turbulence.

Chiefly in LES, the spectral energy density profiles could be used for two unknowns:

1) If the flow exhibits turbulence, turbulent fluctuations caused by eddies should generate a turbulent energy spectra profile, which exhibits high-frequency fluctuations. On the other hand, if laminar flow is observed, this profile could exhibit fluctuations generated by mean flow characteristics, i.e., mean flow

eddies.

2) In a good LES, a high amount of turbulent kinetic energy should be resolved. If so, the inertial sub-range should appear on the ESD profile. Even though the -5/3 law is derived for an isotropic turbulent flow, a similar dissipation profile could be expected.

In order to generate ESD profiles, one may get the fluctuations of all the points in a domain, possibly a set of uniform points, and print the fluctuations. However, it is also possible to use Taylor's frozen turbulence hypothesis to generate such a profile without the need to record a set of points. This hypothesis claims that during the advection of turbulent eddies by mean flow, properties of these eddies do not change. Therefore, a single point is enough to catch all the eddies if tracked for a long enough time. In light of Taylor's hypothesis, current work tracked two points in the nasal cavity and generated ESD profiles from them. These two points are selected to be the lower part of the right cavities and the middle part of the left cavities. In Figure 6.31 the two points where fluctuations are tracked are given; the small filled circle corresponds to the right bottom point, and the big empty circle points to the middle left point.

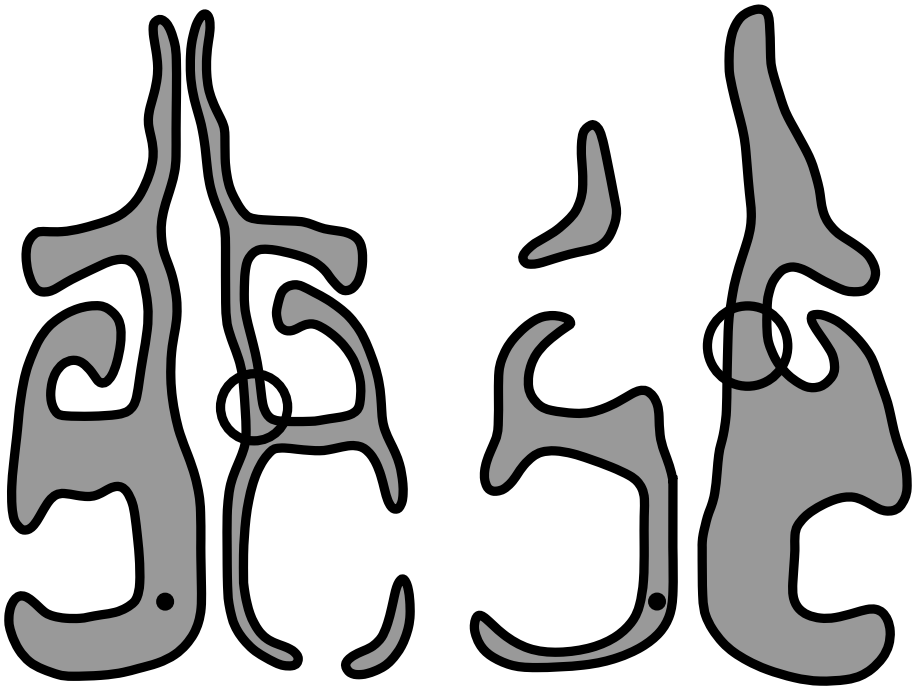

Figure 6.31. Locations of the Tracked Fluctuations in the 11^{th} Slice

6.2.8.1 Restful Inhalation's Energy Spectral Density

Restful inhalation's pre- and post-surgery ESD profiles are given in Figure 6.32 and Figure 6.33 for the left passageway's middle area and the right passageway's bottom point. These profiles are generated from a single point's velocity fluctuations throughout the simulation. In these figures, energy profiles tend to decrease with a constant slope. The decrease is logarithmic, though shown linearly, since the graphs are logarithmic.

One may speculate that neither of the profiles in the figure fits the expected spectral density; rather, the kinetic energy decreases logarithmically compared to turbulent fluctuations. Therefore, it is possible to claim that restful inhalation does not appear to have turbulent behavior. This conclusion is also commonly supported by literature claiming that flow is laminar during slow breathing rates.

Furthermore, for restful inhalation, the current mesh can not be judged by the results obtained in this subsubsection by Figure 6.32 and Figure 6.33 because the flow is not turbulent.

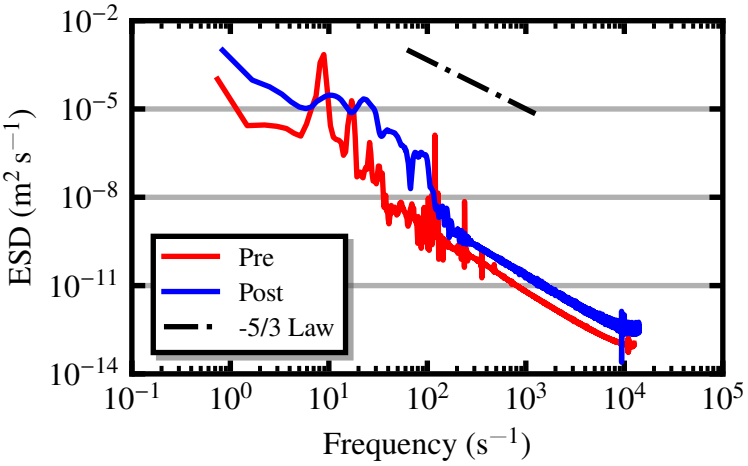

Figure 6.32. ESD Profile of the 11th Slice's Left Middle: Restful State

6.2.8.2 Quick Inhalation's Energy Spectral Density

Pre- and post-surgery ESD profiles for the quick inhalation state are given in Figure 6.32 and Figure 6.33 for the left passageway's middle point and the right

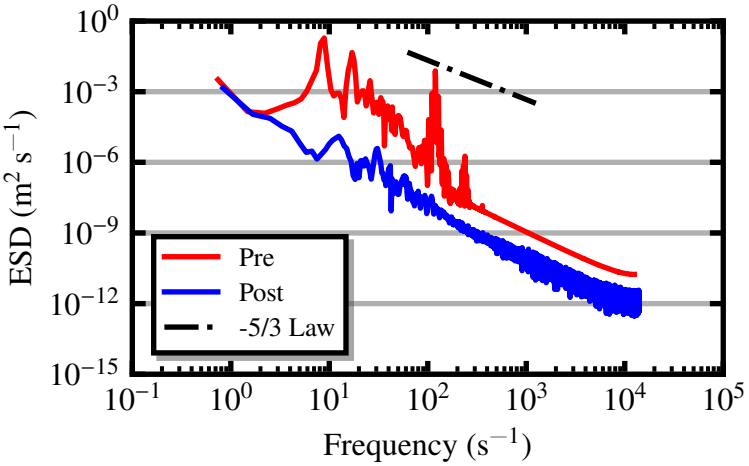

Figure 6.33. ESD Profile of the 11th Slice's Right Bottom: Restful State

passageway's bottom point. These profiles are generated from a single point's velocity fluctuations throughout the whole simulation.

Unlike restful inhalation, these figures appear more like the ESD profiles of other turbulent flows. The left part of the profiles is flat, representing the initial range; this part represents the biggest scales of turbulence. Then, one may see a scale representing the so-called inertial sub-range, which, for isotropic turbulence, is found to scale with -5/3 of turbulent kinetic energy. At the inertial sub-range, turbulent kinetic energy flows without the hindrance of viscosity's effects. At the right-most part, the viscous sub-range starts, where the turbulent kinetic energy gets dissipated by viscosity into thermal energy. Even though such a turbulent structure is apparent on Figure 6.32 and Figure 6.33, the behavior after the discontinuous point, which is on the highest frequency range, appears to be an unorthodox one. One may speculate that this unknown behavior could be caused by LES's inability to model these high-frequency eddies.

Lastly, it is possible to claim that the grid is good enough to resolve at least the inertial sub-range. Even though the inertial sub-range is visible in these profiles, this result is not satisfactory since the results are valid for only two points, and it is impossible to know how much of the total energy is resolved.

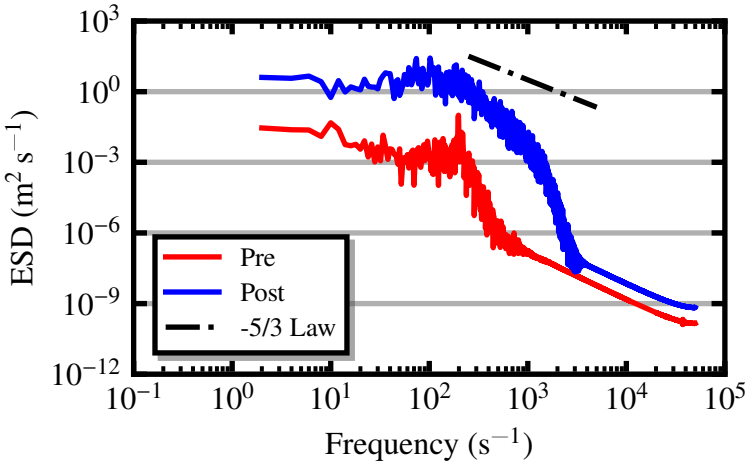

Figure 6.34. ESD Profile of the 11$^{\text{th}}$ Slice's Left Middle: Quick State

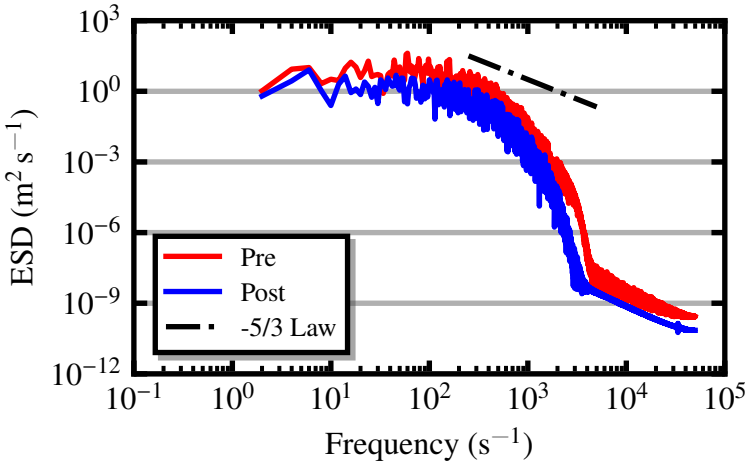

Figure 6.35. ESD Profile of the 11$^{\text{th}}$ Slice's Right Bottom: Quick State

6.3 Verification of Numerical Simulations

This section establishes some proof that the eddy-resolving simulation is a high quality LES. Two critical factors are discussed that quantify the quality of the eddy-resolving simulation grid and time resolutions.

The grid quality is measured by using Celik et al. (2005)'s Γ_η and Γ_ν indices. Regarding time resolution, the time step is initially limited only by a CFL number since some unknowns must be known for turbulence-related time step limitations. Then, the

resulting Kolmogorov time scale is calculated using:

$$\tau_\eta = \sqrt{\frac{\nu}{\epsilon}}, \tag{6.3}$$

where ν is the kinematic viscosity of the fluid, and ϵ is the turbulent kinetic energy dissipation. The Kolmogorov time scale is calculated separately for every cell in the flow geometry.

6.3.1 Verification of Grid Resolution

For the verification of grid resolution, Kolmogorov length-based Celik index, Γ_η, is given as images in the below subsubsections. The other Celik index, which is based on viscosity, Γ_ν, is only reported in the upper and lower limit values. The reasoning behind this choice is to reduce clutter while providing the visualization of the better-detailed results between Celik indices. More details about grid verification are given Section 5.8.

6.3.1.1 Restful Inhalation's Grid Resolution

For the restful inhalation state, the Celik indices using the Kolmogorov length, η, is given Figure 6.36. For this figure, it is clear that the grid is not only adequate but superb given that the minimum Γ_η reaches barely 0.91 at some locations. Furthermore, the pre-surgery geometry appears to have even higher values for the Γ_η.

However, the given figure is only a single slice of the whole geometry. As expected, this figure can not represent the total picture, and it is given here to demonstrate how the index appears. Therefore, it is better to report worse conditions for Celik indices: lower limits. In the whole pre-surgery geometry, the minimum indices are: $\min(\Gamma_\eta) = 0.82$ and $\min(\Gamma_\nu) = 0.89$. In the post-surgery geometry, the minimum indices are: $\min(\Gamma_\eta) = 0.8$ and $\min(\Gamma_\nu) = 0.87$.

The minimum values above only appear at certain places in the whole geometry. Therefore, arbitrarily, one may check how many of the cells are below certain threshold

values. The threshold values are chosen without any reason but to show that the minimum values are nothing but some exceptions. Only 0.04 % of pre-surgery cells and 0.05 % of post-surgery cells are below $\Gamma_\eta = 0.9$. Moreover, only 0.06 % of pre-surgery cells and 0.08 % of post-surgery cells are below $\Gamma_\nu = 0.94$.

The above results show that most of the cells are very well refined, though some low-refinement zones exist. According to Celik et al. (2005), when these indices are above 75 %, LES is accepted as satisfactory.

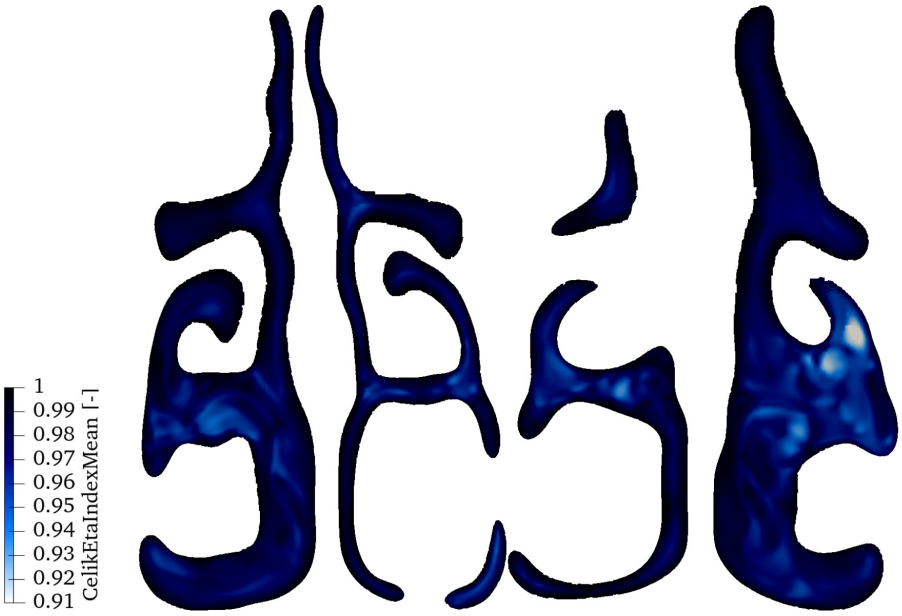

Figure 6.36. Kolmogorov Length Based Celik Index of the 11$^{\text{th}}$ Slice for Pre-Surgery (Left) and Post-Surgery (Right): Restful State

6.3.1.2 Quick Inhalation's Grid Resolution

For the quick inhalation state, the Celik indices using the Kolmogorov length, η, are given in Figure 6.37. Similar to the restful inhalation figure, this appears exceptional. However, it is possible to observe that Γ_η values are lower than the restful state. This is expected since the higher flow rates increase turbulence, which requires a better-refined surface.

Again, the given figure is merely a single slice in the total geometry; thus, it is better to mention the total geometry's Celik indices. Pre-surgery geometry has $\min(\Gamma_\eta) = 0.78$

and $\min(\Gamma_\nu) = 0.84$, and post-surgery geometry has $\min(\Gamma_\eta) = 0.76$ and $\min(\Gamma_\nu) = 0.82$.

Importantly, only 0.4 % of pre-surgery cells and 0.6 % of post-surgery cells cells are below $\Gamma_\eta = 0.9$. Moreover, only 1 % of pre-surgery cells 0.9 % of post-surgery cells are below $\Gamma_\nu = 0.94$. The pre-surgery geometry has $\min(\Gamma_\eta) = 0.76$ and $\min(\Gamma_\nu) = 0.82$. Importantly, only 0.4 % of pre-surgery cells are below $\Gamma_\eta = 0.9$, and only 1 % of pre-surgery cells are below $\Gamma_\nu = 0.94$.

Figure 6.37. Kolmogorov Length Based Celik Index of the 11$^{\text{th}}$ Slice for Pre-Surgery (Left) and Post-Surgery (Right): Quick State

6.3.2 Verification of Time Resolution

6.3.2.1 Restful Inhalation's Time Resolution

In restful inhalation, a time step of $\Delta t = 4 \cdot 10^{-5}\,\mathrm{s}$ is used. This time step should be lower than the Kolmogorov time scale if all the frequencies of turbulence can be simulated. One may claim that the Kolmogorov time scale is too refined for a LES because it is not able to simulate the smallest scale eddies. Nonetheless, this length scale is a promising point to start the checks.

The geometry representing before the surgery of the nasal cavity resulted in minimum Kolmogorov time scales of $\tau_\nu = 8.5 \cdot 10^{-5}\,\mathrm{s}$. On the other hand, post-surgery geometry had Kolmogorov time scales of $\tau_\nu = 6.3 \cdot 10^{-5}\,\mathrm{s}$. These values show that the selected time step, $\Delta t = 4 \cdot 10^{-5}\,\mathrm{s}$, can be used without any concerns. Furthermore, the time step could be increased if other factors, such as CFL number, allow.

6.3.2.2 Quick Inhalation's Time Resolution

In restful inhalation, a time step of $\Delta t = 1 \cdot 10^{-5}\,\mathrm{s}$ is selected. Again, this time step must be lower than the Kolmogorov time scale if all the frequencies are required to be resolved, for example, during a DNS. However, resolving large structures in the turbulence frequencies is possible with a larger time step. Additionally, it is possible to resolve all the turbulent frequencies, except for some cells. These conditions are heavily affected by geometry; thus, a calculation of the Kolmogorov time scale is required.

Pre-surgery simulation had the minimum Kolmogorov time scale $\tau_\nu = 1.02 \cdot 10^{-5}\,\mathrm{s}$. Post-surgery numerical simulation's minimum Kolmogorov timescale is found to be $1.16 \cdot 10^{-5}\,\mathrm{s}$. These results clearly show that the current time step value of $\Delta t = 1 \cdot 10^{-5}\,\mathrm{s}$ is perfectly resolving all turbulent frequencies in every cell of the geometry.

Interestingly, there were around 300 cells in both of the geometries requiring $\tau_\nu = 3 \cdot 10^{-5}\,\mathrm{s}$. Therefore, it is possible to use a higher time step considering that only a large-eddy resolving is simulated, not a DNS. However, these time steps create numerical instability; hence, they are avoided.

6.4 Validation of Numerical Simulations

The validation of the numerical simulations is supposed to be done using an experimental setup with the same geometry as the current nasal cavity. Since such an experimental setup is not within the bounds of this thesis, a other way to validate the simulations is done: by using data of other work in the literature. Such a partial validation is done by comparing nasal resistances with Wen et al. (2008) and Strien

et al. (2021)'s data. Also, Inthavong et al. (2014)'s nasal resistance regression line, $\Delta p = 0.059Q^2$, is used in the validation process. These pressure drop versus discharge levels are given in Table 6.12. This table represents the pressure drops for 10.8 L/min and 33.6 L/min.

Table 6.12. Pressure Values for Averaged Cavities Against Literature

Name	Δp for 10.8 L/min	Δp for 33.6 L/min
Wen et al. (2008)'s CFD data	6.26 Pa	41.1 Pa
Strien et al. (2021)'s CFD data	6.9 Pa	45.9 Pa
Strien et al. (2021)'s experimental data	5.0 Pa	52.6 Pa
Inthavong et al. (2014)'s regression line	6.88 Pa	66.6 Pa
Current pre-surgery data	5.90 Pa	40.6 Pa
Current post-surgery data	6.35 Pa	53.4 Pa

Note. In the original texts of Wen et al. (2008) and Strien et al. (2021), the data is given for 10 L/min and 30 L/min. These values are linearly interpolated in this table.

A comparison using Table 6.12 reveals that pressure drop values for discharge rates are within logical grounds for both pre-surgery and post-surgery states. Both low discharge level values appear to be within other research's upper and lower bounds. On the other hand, the pre-surgery pressure drop is lower than all other pressure drop values; nonetheless, it is not exceedingly low but almost equal to Wen et al. (2008)'s results. The post-surgery quick inhalation pressure drop is very close to Strien et al. (2021)'s experimental results.

The validation using Table 6.12 shows that current numerical simulations agree with the data in other literature. Nonetheless, this validation is not the ultimate validation but more of a sanitary check for the results of this thesis. Experimental work is needed

to compare current numerical simulation results as a total validation.

CHAPTER 7

CONCLUSIONS

Large eddy simulations of the same patient's before and after surgery states of the nasal cavities are simulated in this thesis. The results show that surgery can increase cross-sectional area values while maintaining high and well-distributed wall shear stresses, and it does not direct flow to a single part of the nasal cavity. These results promise that if the nasal surgery is done properly, post-surgery syndromes that result in a decrease in quality of life can be avoided.

Even though there is no direct questionnaire collected from the patient, there is no revision surgery requirement reported for this individual. Such a result suggests that the surgery ended up relieving the patient; thus, the current conclusions and results reported in this dissertation are in line with reality.

In this work, the consideration of nasal geometry as a singular element to predict the results of nasal surgeries is shown to be fallacious. For example, even though the nasal perimeter decreases with the same flow rate, nasal turbulent kinetic energy does not increase but reduces in the post-surgery state. Another example is the nasal resistance values in the post-surgery state. Paradoxically, nasal resistance increases at both discharge levels, suggesting that the individual feels more obstruction after the surgery. Nonetheless, the results differ when the nasal geometry is separated into a few parts. Traditionally, this is done by splitting nasal geometry into three parts: superior, middle, and inferior. When discharge rates and wall shear stresses are compared in these three regions near three turbinates, results suggest that wall shear stresses and volumetric flow rates do not diverge from the initial results.

Investigation of local airflow characteristics is important because the nasal obstruction

does not stem from high nasal resistance or clogged nasal passageways. The main reason for such a feeling is due to the flowing air's low stimulation of nasal receptors. Surgeries tend to alter the nasal geometry so that the area of the airflow plane increases. This change naturally causes a drop in the wall shear stresses, resulting in lower stimulation on the receptors.

The results obtained in this thesis may not be directly comparable with other numerical results in the literature or future work. However, given that the results are considered within limits, they can be used to compare them to other nasal airflow simulations. Also, current work should be used as a guide to understand how nasal surgery affects nasal airflow, what kinds of changes are expected, and similar. The indirect comparison is needed because nasal geometry is delicate and dynamic; however, the approaches and information presented in this study could be applied to other nasal geometries to predict the wellness of the nasal airflow.

This work is one of the limited examples of a simulation of the nasal cavity using nothing but open-source software. Also, it is one of the handful works that is an LES with settings given explicitly. To accomplish the nasal simulation, Slicer 3D is used to generate surface geometry from a CT scan. *Blender* is used to generate inlet and outlet sections for the surface geometry. *OpenFOAM*'s *snappyHexMesh* and *cfMesh* are used for volumetric geometry creation. Ultimately, simulations are done by using *OpenFOAM*, and postprocessing is done on *Paraview*. The support and documentation for these programs can be unclear at times. Nonetheless, the numerical investigation is successfully carried out through trial and error and occasionally examining the source code.

Moreover, this thesis can potentially be regarded as one of the most elaborate pieces of work on nasal simulation in the literature. This is because all the nasal airflow-related topics, from biological to engineering perspectives, are investigated and explained as deeply as possible in this dissertation. The tedious investigation is summarized in three parts: biological, fluid, mechanical, and their combinations. The explanation of medical topics related to nasal health is given as healthy airflow in the upper respiratory system, biological mechanisms of nasal obstruction, and nasal illnesses that cause low nasal patency. In this master's thesis, a comprehensive

work on topics related to fluid mechanics is done: tensor mathematics-related operations, conservation of mass equations, Newton's second law of motion, Cauchy momentum equations, generalization of Newtonian law of viscosity, Navier-Stokes equations' derivation for incompressible and compressible flows, derivation of RANS equations for incompressible and compressible flows, generalization of eddy viscosity approximation of Boussinesq, filtering of incompressible NS equations, Smagorinsky model, sub-grid scale kinetic energy for 0-equation models, WALE model. Furthermore, a detailed discussion on the medical and numerical investigation of nasal airflow is given about the steadiness of nasal airflow: how to determine steady or unsteady behavior, the creation of nasal geometry from CT scans, the conduction of numerical nasal airflow simulations, and the proper interpretation of nasal airflow results.

7.1 Future Work

The first aim of future work should be the production of an experimental work validating current numerical simulation results. Even though some characteristics are compared with other nasal simulations in the literature, this validation can not be accepted as a sufficient validation because of the high variations in nasal geometries. Hence, valid experimental work must be done to support the usage of the results given in this thesis.

On the other hand, current nasal simulations are done using a workstation, which substantially limits the total number of cells in nasal airflow simulations. Even though this limitation does not have a high impact on the simulation, it is still possible to increase resolved turbulent kinetic energy and reduce dependence on sub-grid scale models. This would increase the accuracy of the current simulations.

Moreover, current simulations are done using volumetric meshes with very weak points. In these weak points, the velocities appear very high and cells have very small volumes; this causes very high CFL numbers and limits the total simulation in terms of the total required time to conduct the numerical simulation. These cells appear near the connection points of different surface meshes and are not easily avoidable with current tools. This problem may hinder future work focusing on more intricate simulations,

such as transient simulations or simulations with more refined cells.

Current simulations are done so that flow level to be at the same discharge level throughout the time, i.e., flow is like a quasi-steady flow. This approach can be changed into a fully unsteady simulation of multiple whole breathing cycles. This kind of simulation can be effortlessly obtained by changing a few settings used in the current simulations. Nonetheless, the cost of such a numerical simulation is much higher than the current simulations, given that one needs to simulate breathing patterns in a few cycles, while a single cycle takes more computational time than a whole quasi-steady simulation.

The other possible issue with the current work is the usage of a rectangular inlet to combine the nostrils, due to the inability to specify discharge rates precisely. In other academic work, this has been done by defining an atmosphere around the face as a half-sphere. This approach represents realistic conditions much better than the current approach. Moreover, such an approach includes possible disturbances caused by the face structure in the simulation. However, this approach increases computational costs and may generate numerical instabilities due to the requirement of complex boundary conditions, such as extrapolated velocity profiles.

Lastly, in this thesis, the two CT scans with different dominant airflow channels are used. This limitation is caused by the effects of the nasal cycle. Even though there are numerous issues have the potential to corrupt the results, avoiding this complexity is simple; thus, should be sought after in future work.

BIBLIOGRAPHY

Akryl, L., & Jmarchn. (2010). *Conducting passages of the human respiratory system*. Retrieved March 22, 2023, from https://en.wikipedia.org/wiki/File:Illu_conducting_passages.svg

ANSYS, Inc. (2009). *Ansys fluent 12.0 theory guide*. Version 12.0. https://www.afs.enea.it/project/neptunius/docs/fluent/html/th/main_pre.htm

Aris, R. (1989). *Vectors, tensors, and the basic equations of fluid mechanics*. Dover Publications.

Avrunin, O. G., Nosova, Y. V., Abdelhamid, I. Y., Pavlov, S. V., Shushliapina, N. O., Bouhlal, N. A., Ormanbekova, A., Iskakova, A., & Harasim, D. (2021). Research active posterior rhinomanometry tomography method for nasal breathing determining violations. *Sensors*, *21*(24), 8508. https://doi.org/10.3390/s21248508

Aydın, İ. (2021). Lecture notes of CE 539 advanced mechanics of fluids I. https://catalog.metu.edu.tr/course.php?prog=562&course_code=5620539

Balatinec, L., Uroić, T., & Jasak, H. (2021). Open-source CFD analysis of nasal flows. *OpenFOAM® Journal*, *1*, 2–26. https://doi.org/10.51560/ofj.v1.38

Bardina, J. (1983). *Improved turbulence models based on large eddy simulation of homogeneous, incompressible, turbulent flows* [Doctoral dissertation, Stanford University]. https://ntrs.nasa.gov/api/citations/19840009460/downloads/19840009460.pdf

Belli, S., Yildirim, M., Eroglu, S., & Emre, F. K. (2018). Single-sided sinonasal mass: a retrospective study. *Northern Clinics of Istanbul*, *5*(2), 139–143. https://doi.org/10.14744/nci.2017.57984

Benchetrit, G., Shea, S., Dinh, T., Bodocco, S., Baconnier, P., & Guz, A. (1989). Individuality of breathing patterns in adults assessed over time. *Respiration Physiology*, *75*(2), 199–209. https://doi.org/10.1016/0034-5687(89)90064-9

Berger, M., Giotakis, A. I., Pillei, M., Mehrle, A., Kraxner, M., Kral, F., Recheis, W., Riechelmann, H., & Freysinger, W. (2021). Agreement between rhinomanometry and computed tomography-based computational fluid dynamics. *International Journal of Computer Assisted Radiology and Surgery*, *16*(4), 629–638. https://doi.org/10.1007/s11548-021-02332-1

Berger, M., Pillei, M., Mehrle, A. H., Recheis, W., Kral, F., Kraxner, M., Bárdosi, Z. R., & Freysinger, W. (2020). Nasal cavity airflow: comparing laser doppler anemometry and computational fluid dynamic simulations. *Respiratory Physiology & Neurobiology*, *283*, 103533. https://doi.org/10.1016/j.resp.2020.103533

Bhattacharyya, N. (2003). The economic burden and symptom manifestations of chronic rhinosinusitis. *American Journal of Rhinology*, *17*(1), 27–32. https://doi.org/10.1177/194589240301700106

Bird, R. B., Armstrong, R. C., & Hassager, O. (1987). *Dynamics of polymeric liquids: fluid mechanics* (2nd ed.). Wiley-Interscience.

Borojeni, A. A. T., Garcia, G. J. M., Moghaddam, M. G., Frank-Ito, D. O., Kimbell, J. S., Laud, P. W., Koenig, L. J., & Rhee, J. S. (2020). Normative ranges of nasal airflow variables in healthy adults. *International Journal of Computer Assisted Radiology and Surgery*, *15*(1), 87–98. https://doi.org/10.1007/s11548-019-02023-y

Branstetter, B. F., & Weissman, J. L. (2005). Role of MR and CT in the paranasal sinuses. *Otolaryngologic Clinics of North America*, *38*(6), 1279–1299. https://doi.org/10.1016/j.otc.2005.08.013

Brüning, J., Hildebrandt, T., Heppt, W., Schmidt, N., Lamecker, H., Szengel, A., Amiridze, N., Ramm, H., Bindernagel, M., Zachow, S., & Goubergrits, L. (2020). Characterization of the airflow within an average geometry of the healthy human nasal cavity. *Scientific Reports*, *10*(1), 3755. https://doi.org/10.1038/s41598-020-60755-3

Bugten, V., Nilsen, A. H., Thorstensen, W. M., Moxness, M. H. S., Amundsen, M. F., & Nordgård, S. (2016). Quality of life and symptoms before and after nasal septoplasty compared with healthy individuals. *BMC Ear, Nose and Throat Disorders*, *16*(13). https://doi.org/10.1186/s12901-016-0031-7

Bundersamt für Strahlenschutz. (2022, October 13). *Limit values for occupationally exposed persons*. https://www.bfs.de/EN/topics/ion/radiation-protection/occupation/limitvalues/limit-values_node.html

Burrow, A., Eccles, R., & Jones, A. S. (1983). The effects of camphor, eucalyptus and menthol vapour on nasal resistance to airflow and nasal sensation. *Acta Oto-Laryngologica*, *96*(1-2), 157–161. https://doi.org/10.3109/00016488309132886

Cakmak, O., Tarhan, E., Coskun, M., Cankurtaran, M., & Çelik, H. (2005). Acoustic rhinometry: accuracy and ability to detect changes in passage area at different locations in the nasal cavity. *Annals of Otology, Rhinology & Laryngology*, *114*(12), 949–957. https://doi.org/10.1177/000348940511401211

Calmet, H., Inthavong, K., Owen, H., Dosimont, D., Lehmkuhl, O., Houzeaux, G., & Vázquez, M. (2021). Computational modelling of nasal respiratory flow. *Computer Methods in Biomechanics and Biomedical Engineering*, *24*(4), 440–458. https://doi.org/10.1080/10255842.2020.1833865

Calmet, H., Gambaruto, A. M., Bates, A. J., Vázquez, M., Houzeaux, G., & Doorly, D. J. (2016). Large-scale CFD simulations of the transitional and turbulent regime for the large human airways during rapid inhalation. *Computers in Biology and Medicine*, *69*, 166–180. https://doi.org/10.1016/j.compbiomed.2015.12.003

Casey, K. P., Borojeni, A. A. T., Koenig, L. J., Rhee, J. S., & Garcia, G. J. M. (2017). Correlation between subjective nasal patency and intranasal airflow distribution. *Otolaryngology–Head and Neck Surgery*, *156*(4), 741–750. https://doi.org/10.1177/0194599816687751

Celik, I. B., Cehreli, Z. N., & Yavuz, I. (2005). Index of resolution quality for large eddy simulations. *Journal of Fluids Engineering*, *127*(5), 949–958. https://doi.org/10.1115/1.1990201

Chang, H., & Masry, O. A. E. (1982). A model study of flow dynamics in human central airways. part i: axial velocity profiles. *Respiration Physiology*, *49*(1), 75–95. https://doi.org/10.1016/0034-5687(82)90104-9

Chen, X. B., Lee, H. P., Hin Chong, V. F., & Wang, D. Y. (2009). Assessment of septal deviation effects on nasal air flow: a computational fluid dynamics model. *The Laryngoscope*, *119*(9), 1730–1736. https://doi.org/10.1002/lary.20585

Chen, Y., Feng, X., Shi, X., Cai, W., Li, B., & Zhao, Y. (2023). Evaluation of computational fluid dynamics models for predicting pediatric upper airway airflow characteristics. *Medical & Biological Engineering & Computing*, *61*(1), 259–270. https://doi.org/10.1007/s11517-022-02715-9

Cherobin, G. B., Voegels, R. L., Gebrim, E. M. M. S., & Garcia, G. J. M. (2018). Sensitivity of nasal airflow variables computed via computational fluid dynamics to the computed tomography segmentation threshold (D. Tang, Ed.). *PLOS ONE*, *13*(11), e0207178. https://doi.org/10.1371/journal.pone.0207178

Cherobin, G. B., Voegels, R. L., Pinna, F. R., Gebrim, E. M. M. S., Bailey, R. S., & Garcia, G. J. M. (2021). Rhinomanometry versus computational fluid dynamics: correlated, but different techniques. *American Journal of Rhinology & Allergy*, *35*(2), 245–255. https://doi.org/10.1177/1945892420950157

Chhabra, N., & Houser, S. M. (2011). The surgical management of allergic rhinitis. *Otolaryngologic clinics of North America*, *44*(3), 779–795. https://doi.org/10.1016/j.otc.2011.03.007

Cleveland Clinic. (2021, February 5). *Nasal polyps*. https://my.clevelandclinic.org/health/diseases/15250-nasal-polyps

Corda, J. V., Shenoy, B. S., Lewis, L., K., P., Khader, S. M. A., Ahmad, K. A., & Zuber, M. (2022). Nasal airflow patterns in a patient with septal deviation and comparison with a healthy nasal cavity using computational fluid dynamics. *Frontiers in Mechanical Engineering*, *8*, 1009640. https://doi.org/10.3389/fmech.2022.1009640

Corey, J. P., Gungor, A., Nelson, R., Fredberg, J., & Lai, V. (1997). A comparison of the nasal cross-sectional areas and volumes obtained with acoustic rhinometry

and magnetic resonance imaging. *Otolaryngology–Head and Neck Surgery*, *117*(4), 349–354. https://doi.org/10.1016/s0194-5998(97)70125-6

Currie, I. G. (2002). *Fundamental mechanics of fluids* (3rd ed.). Marcel Dekker.

D'Amato, M., Molino, A., Calabrese, G., Cecchi, L., Annesi-Maesano, I., & D'Amato, G. (2018). The impact of cold on the respiratory tract and its consequences to respiratory health. *Clinical and Translational Allergy*, *8*(20), 1–8. https://doi.org/10.1186/s13601-018-0208-9

Darquenne, C., & Prisk, G. K. (2004). Aerosol deposition in the human respiratory tract breathing air and 80:20 heliox. *Journal of Aerosol Medicine*, *17*(3), 278–285. https://doi.org/10.1089/jam.2004.17.278

Datta, R. K., Ramya, B., & Vinay, S. R. (2018). Comparative study between partial inferior turbinectomy and submucosal diathermy for treatment of inferior turbinate hypertrophy due to allergic rhinitis. *International Journal of Otorhinolaryngology and Head and Neck Surgery*, *4*, 362–367. https://doi.org/10.18203/issn.2454-5929.ijohns20180425

Davidson, L. (2023). Fluid mechanics, turbulent flow and turbulence modeling. https://www.tfd.chalmers.se/~lada/postscript_files/solids-and-fluids_turbulent-flow_turbulence-modelling.pdf

Dayal, A., Rhee, J. S., & Garcia, G. J. M. (2016). Impact of middle versus inferior total turbinectomy on nasal aerodynamics. *Otolaryngology–Head and Neck Surgery*, *155*(3), 518–525. https://doi.org/10.1177/0194599816644915

Deardorff, J. W. (1970). A numerical study of three-dimensional turbulent channel flow at large reynolds numbers. *Journal of Fluid Mechanics*, *41*(2), 453–480. https://doi.org/10.1017/s0022112070000691

DeConde, A. S., Mace, J. C., Bodner, T., Hwang, P. H., Rudmik, L., Soler, Z. M., & Smith, T. L. (2014). SNOT-22 quality of life domains differentially predict treatment modality selection in chronic rhinosinusitis. *International Forum of Allergy and Rhinology*, *4*(12), 972–979. https://doi.org/10.1002/alr.21408

Di, M.-Y., Jiang, Z., Gao, Z.-Q., Li, Z., An, Y.-R., & Lv, W. (2013). Numerical simulation of airflow fields in two typical nasal structures of empty nose syndrome: a computational fluid dynamics study (T. W. Secomb, Ed.). *PLOS ONE*, *8*(12), e84243. https://doi.org/10.1371/journal.pone.0084243

Doorly, D., Taylor, D., & Schroter, R. (2008). Mechanics of airflow in the human nasal airways. *Respiratory Physiology & Neurobiology*, *163*(1), 100–110. https://doi.org/10.1016/j.resp.2008.07.027

Eccles, R. (2003). Menthol: effects on nasal sensation of airflow and the drive to breathe. *Current Allergy and Asthma Reports*, *3*(3), 210–214. https://doi.org/10.1007/s11882-003-0041-6

Elad, D., Liebenthal, R., Wenig, B. L., & Einav, S. (1993). Analysis of air flow patterns in the human nose. *Medical & Biological Engineering & Computing*, *31*(6), 585–592. https://doi.org/10.1007/BF02441806

Elad, D., Naftali, S., Rosenfeld, M., & Wolf, M. (2006). Physical stresses at the air-wall interface of the human nasal cavity during breathing. *Journal of Applied Physiology*, *100*(3), 1003–1010. https://doi.org/10.1152/japplphysiol.01049.2005

Ferziger, J. H., Perić, M., & Street, R. L. (2020). *Computational methods for fluid dynamics*. Springer International Publishing. https://doi.org/10.1007/978-3-319-99693-6

Fisher, E. W., Lund, V. J., & Scadding, G. K. (1994). Acoustic rhinometry in rhinological practice: discussion paper. *Journal of the Royal Society of Medicine*, *87*(7), 411–413. https://doi.org/10.1177/014107689408700713

Friedman, M., & Schalch, P. (2009). Chapter 19 - effects of nasal surgery on snoring and sleep apnea. In *Sleep apnea and snoring* (pp. 124–128). Elsevier. https://doi.org/10.1016/b978-1-4160-3112-3.00019-x

Gambaruto, A. M., Taylor, D. J., & Doorly, D. J. (2012). Decomposition and description of the nasal cavity form. *Annals of Biomedical Engineering*, *40*(5), 1142–1159. https://doi.org/10.1007/s10439-011-0485-0

Gänger, S., & Schindowski, K. (2018). Tailoring formulations for intranasal nose-to-brain delivery: a review on architecture, physico-chemical characteristics and mucociliary clearance of the nasal olfactory mucosa. *Pharmaceutics*, *10*(3), 116. https://doi.org/10.3390/pharmaceutics10030116

Garcia, G. J., Hariri, B. M., Patel, R. G., & Rhee, J. S. (2016). The relationship between nasal resistance to airflow and the airspace minimal cross-sectional area. *Journal of Biomechanics*, *49*(9), 1670–1678. https://doi.org/10.1016/j.jbiomech.2016.03.051

Garcia, G. J., Tewksbury, E. W., Wong, B. A., & Kimbell, J. S. (2009). Interindividual variability in nasal filtration as a function of nasal cavity geometry. *Journal of Aerosol Medicine and Pulmonary Drug Delivery*, *22*(2), 139–156. https://doi.org/10.1089/jamp.2008.0713

Ge, W., Wang, D., Chuang, C.-C., Li, Y., Rout, R., Siddiqui, S., & Kamat, S. (2022). Real-world cost of nasal polyps surgery and risk of major complications in the united states: a descriptive retrospective database analysis. *ClinicoEconomics and Outcomes Research*, *14*, 691–697. https://doi.org/10.2147/ceor.s380411

Göktepe, S. (2021). CE 7026 continuum mechanics lecture notes. https://catalog.metu.edu.tr/course.php?prog=562&course_code=5627026

Gray, L. (1965). The deviated nasal septum—II— prevention and treatment. *The Journal of Laryngology & Otology*, *79*(9), 806–816. https://doi.org/10.1017/s0022215100064392

Gray, L. P. (1978). Deviated nasal septum incidence and etiology. *Annals of Otology, Rhinology & Laryngology*, *87*(3), 3–20. https://doi.org/10.1177/00034894780873s201

Gray, L. P. (1980). Relationship of septal deformity to snuffly noses, poor feeding, sticky eyes and blocked naso-lacrimal ducts. *International Journal of Pediatric Otorhinolaryngology*, *2*(3), 201–215. https://doi.org/10.1016/0165-5876(80)90046-4

Hahn, I., Scherer, P. W., & Mozell, M. M. (1993). Velocity profiles measured for airflow through a large-scale model of the human nasal cavity. *Journal of Applied Physiology*, *75*(5), 2273–2287. https://doi.org/10.1152/jappl.1993.75.5.2273

Harugop, A. S., Mudhol, R. S., Hajare, P. S., Nargund, A. I., Metgudmath, V. V., & Chakrabarti, S. (2012). Prevalence of nasal septal deviation in new-borns and its precipitating factors: a cross-sectional study. *Indian Journal of Otolaryngology and Head & Neck Surgery*, *64*(3), 248–251. https://doi.org/10.1007/s12070-011-0247-1

Hazeri, M., Farshidfar, Z., Faramarzi, M., Sadrizadeh, S., & Abouali, O. (2020). Details of the physiology of the aerodynamic and heat and moisture transfer in the normal nasal cavity. *Respiratory Physiology & Neurobiology*, *280*, 103480. https://doi.org/10.1016/j.resp.2020.103480

Hebbink, R. H., Wessels, B. J., Hagmeijer, R., & Jain, K. (2023). Computational analysis of human upper airway aerodynamics. *Medical & Biological Engineering & Computing*, *61*(2), 541–553. https://doi.org/10.1007/s11517-022-02716-8

Hörschler, I., Schröder, W., & Meinke, M. (2010). On the assumption of steadiness of nasal cavity flow. *Journal of Biomechanics*, *43*(6), 1081–1085. https://doi.org/10.1016/j.jbiomech.2009.12.008

Inthavong, K., Chetty, A., Shang, Y., & Tu, J. (2018). Examining mesh independence for flow dynamics in the human nasal cavity. *Computers in Biology and Medicine*, *102*, 40–50. https://doi.org/10.1016/j.compbiomed.2018.09.010

Inthavong, K., Ma, J., Shang, Y., Dong, J., Chetty, A. S. R., Tu, J., & Frank-Ito, D. (2017). Geometry and airflow dynamics analysis in the nasal cavity during inhalation. *Clinical Biomechanics*, *66*, 97–106. https://doi.org/10.1016/j.clinbiomech.2017.10.006

Inthavong, K., Shang, Y., & Tu, J. (2014). Surface mapping for visualization of wall stresses during inhalation in a human nasal cavity. *Respiratory Physiology & Neurobiology*, *190*, 54–61. https://doi.org/10.1016/j.resp.2013.09.004

Isabey, D., & Chang, H. K. (1981). Steady and unsteady pressure-flow relationships in central airways. *Journal of Applied Physiology*, *51*(5), 1338–1348. https://doi.org/10.1152/jappl.1981.51.5.1338

Isabey, D., Chang, H. K., Delpuech, C., Harf, A., & Hatzfeld, C. (1986). Dependence of central airway resistance on frequency and tidal volume: a model study.

Journal of Applied Physiology, *61*(1), 113–126. https://doi.org/10.1152/jappl.1986.61.1.113

Jessen, M., Ivarsson, A., & Malm, L. (1989). Nasal airway resistance and symptoms after functional septoplasty: comparison of findings at 9 months and 9 years. *Clinical Otolaryngology*, *14*(3), 231–234. https://doi.org/10.1111/j.1365-2273.1989.tb00366.x

Jiang, J., & Zhao, K. (2010). Airflow and nanoparticle deposition in rat nose under various breathing and sniffing conditions—a computational evaluation of the unsteady and turbulent effect. *Journal of Aerosol Science*, *41*(11), 1030–1043. https://doi.org/10.1016/j.jaerosci.2010.06.005

Jones, A. S., Crosher, R., Wight, R. G., Lancer, J. M., & Beckingham, E. (1987). The effect of local anaesthesia of the nasal vestibule on nasal sensation of airflow and nasal resistance. *Clinical Otolaryngology*, *12*(6), 461–464. https://doi.org/10.1111/j.1365-2273.1987.tb00233.x

Jones, A. S., Willatt, D. J., & Durham, L. M. (1989). Nasal airflow: resistance and sensation. *The Journal of Laryngology & Otology*, *103*(10), 909–911. https://doi.org/10.1017/s0022215100110485

Juliá, J., Burchés, M. E., & Martorell, A. (2011). Active anterior rhinomanometry in paediatrics. normality criteria. *Allergologia et Immunopathologia*, *39*(6), 342–346. https://doi.org/10.1016/j.aller.2010.10.004

Jung, H. (2021). Basic physical principles and clinical applications of computed tomography. *Progress in Medical Physics*, *32*(1), 1–17. https://doi.org/10.14316/pmp.2021.32.1.1

Kajishima, T., & Taira, K. (2016). *Computational fluid dynamics* (1st ed.). Springer International Publishing. https://doi.org/10.1007/978-3-319-45304-0

Karbowski, K., Kopiczak, B., Chrzan, R., Gawlik, J., & Szaleniec, J. (2023). Accuracy of virtual rhinomanometry. *Polish Journal of Medical Physics and Engineering*, *29*(1), 59–72. https://doi.org/10.2478/pjmpe-2023-0008

Keyhani, K., Scherer, P. W., & Mozell, M. M. (1995). Numerical simulation of airflow in the human nasal cavity. *Journal of Biomechanical Engineering*, *117*(4), 429–441. https://doi.org/10.1115/1.2794204

Kiechle, B. (2007). *MRI*. https://www.flickr.com/photos/geneticmemories/565630192

Kimbell, J., Gross, E., Joyner, D., Godo, M., & Morgan, K. (1993). Application of computational fluid dynamics to regional dosimetry of inhaled chemicals in the upper respiratory tract of the rat. *Toxicology and Applied Pharmacology*, *121*(2), 253–263. https://doi.org/10.1006/taap.1993.1152

Leakey, S., Glenis, V., & Hewett, C. (2022). Artificial compressibility with riemann solvers: convergence of limiters on unstructured meshes. *OpenFOAM® Journal*, *2*, 31–47. https://doi.org/10.51560/ofj.v2.49

Lee, K. B., Jeon, Y. S., Chung, S.-K., & Kim, S. K. (2016). Effects of partial middle turbinectomy with varying resection volume and location on nasal functions and airflow characteristics by CFD. *Computers in Biology and Medicine*, *77*, 214–221. https://doi.org/10.1016/j.compbiomed.2016.08.014

Lee, T.-J., Fu, C.-H., Wu, C.-L., Tam, Y.-Y., Huang, C.-C., Chang, P.-H., Chen, Y.-W., & Wu, M.-H. (2016). Evaluation of depression and anxiety in empty nose syndrome after surgical treatment. *The Laryngoscope*, *126*(6), 1284–1289. https://doi.org/10.1002/lary.25814

Leonard, A. (1975). Energy cascade in large-eddy simulations of turbulent fluid flows. In F. Frenkiel & R. Munn (Eds.), *Turbulent diffusion in environmental pollution* (pp. 237–248, Vol. 18). Elsevier. https://doi.org/10.1016/S0065-2687(08)60464-1

Li, C., Farag, A. A., Leach, J., Deshpande, B., Jacobowitz, A., Kim, K., Otto, B. A., & Zhao, K. (2017). Computational fluid dynamics and trigeminal sensory examinations of empty nose syndrome patients. *The Laryngoscope*, *127*(6), E176–E184. https://doi.org/10.1002/lary.26530

Li, C., Farag, A. A., Maza, G., McGhee, S., Ciccone, M. A., Deshpande, B., Pribitkin, E. A., Otto, B. A., & Zhao, K. (2018). Investigation of the abnormal nasal aerodynamics and trigeminal functions among empty nose syndrome patients.

International Forum of Allergy & Rhinology, *8*(3), 444–452. https://doi.org/10.1002/alr.22045

Li, C., Jiang, J., Dong, H., & Zhao, K. (2017). Computational modeling and validation of human nasal airflow under various breathing conditions. *Journal of Biomechanics*, *64*, 59–68. https://doi.org/10.1016/j.jbiomech.2017.08.031

Lilly, D. K. (1966). On the application of the eddy viscosity concept in the inertial sub-range of turbulence. *NCAR manuscript*, *123*. https://doi.org/10.5065/D67H1GGQ

Lilly, D. K. (1967). The representation of small-scale turbulence in numerical simulation experiments. *Proceedings of the IBM Scientific Computational Symposium on Environmental Sciences*, 195–210. https://cir.nii.ac.jp/crid/1570854174114088448

Liu, T., Han, D., Wang, J., Tan, J., Zang, H., Wang, T., Li, Y., & Cui, S. (2011). Effects of septal deviation on the airflow characteristics: using computational fluid dynamics models. *Acta Oto-Laryngologica*, *132*(3), 290–298. https://doi.org/10.3109/00016489.2011.637233

Lund, T. S., & Novikov, E. A. (1993). Parameterization of subgrid-scale stress by the velocity gradient tensor. *Annual Research Briefs, 1992*, 27–43.

Malik, J., Li, C., Maza, G., Farag, A. A., Krebs, J. P., McGhee, S., Zappitelli, G., Deshpande, B., Otto, B. A., & Zhao, K. (2019). Computational fluid dynamic analysis of aggressive turbinate reductions: is it a culprit of empty nose syndrome? *International Forum of Allergy & Rhinology*, *9*(8), 891–899. https://doi.org/10.1002/alr.22350

Malik, J., Spector, B. M., Wu, Z., Markley, J., Zhao, S., Otto, B. A., Farag, A. A., & Zhao, K. (2022). Evidence of nasal cooling and sensory impairments driving patient symptoms with septal deviation. *The Laryngoscope*, *132*(3), 509–517. https://doi.org/10.1002/lary.29673

Mathai, J. (2004). Inferior turbinectomy for nasal obstruction review of 75 cases. *Indian Journal of Otolaryngology and Head and Neck Surgery*, *56*, 23–26. https://doi.org/10.1007/BF02968766

Mayo Clinic. (2021). *Deviated septum*. https://www.mayoclinic.org/diseases-conditions/deviated-septum/symptoms-causes/syc-20351710

Mayo Clinic. (2022). *CT scan*. https://www.mayoclinic.org/tests-procedures/ct-scan/about/pac-20393675

Mayo Clinic. (2023). *Nasal polyps*. https://www.mayoclinic.org/diseases-conditions/nasal-polyps/symptoms-causes/syc-20351888

McKemy, D. D., Neuhausser, W. M., & Julius, D. (2002). Identification of a cold receptor reveals a general role for TRP channels in thermosensation. *Nature*, *416*(6876), 52–58. https://doi.org/10.1038/nature719

Metson, R. B. (2005). *The harvard medical school guide to healing your sinuses*. McGraw-Hill.

Meusel, T., Negoias, S., Scheibe, M., & Hummel, T. (2010). Topographical differences in distribution and responsiveness of trigeminal sensitivity within the human nasal mucosa. *PAIN®*, *151*(2), 516–521. https://doi.org/10.1016/j.pain.2010.08.013

Mondina, M., Marro, M., Maurice, S., Stoll, D., & de Gabory, L. (2012). Assessment of nasal septoplasty using nose and rhinoqol questionnaires. *European Archives of Oto-Rhino-Laryngology*, *269*, 2189–2195. https://doi.org/10.1007/s00405-011-1916-0

Naclerio, R. M., Bachert, C., & Baraniuk, J. N. (2010). Pathophysiology of nasal congestion. *International Journal of General Medicine*, *3*, 47–57. https://doi.org/10.2147/ijgm.s8088

Naito, K., Horibe, S., Tanabe, Y., Kato, H., Yoshioka, S., & Tateya, I. (2023). Objective assessment of nasal obstruction. *Fujita Medical Journal*, *9*(2), 53–64. https://doi.org/10.20407/fmj.2021-029

Nakano, H., Mishima, K., Ueda, Y., Matsushita, A., Suga, H., Miyawaki, Y., Mano, T., Mori, Y., & Ueyama, Y. (2013). A new method for determining the optimal CT threshold for extracting the upper airway. *Dentomaxillofacial Radiology*, *42*(3), 26397438. https://doi.org/10.1259/dmfr/26397438

Nathan, R. A., Eccles, R., Howarth, P. H., Steinsvåg, S. K., & Togias, A. (2005). Objective monitoring of nasal patency and nasal physiology in rhinitis. *Journal of Allergy and Clinical Immunology*, *115*(3), S442–S459. https://doi.org/10.1016/j.jaci.2004.12.015

National Center for Health Statistics. (2015–2018). *Crude percentages of sinusitis for adults aged 18 and over, United States* (Data set). Data set. National Center for Health Statistics. Retrieved June 16, 2023, from https://www.cdc.gov/nchs/nhis/ADULTS/www/index.htm

National Institute of Biomedical Imaging and Bioengineering. (2022, April 1). *Magnetic resonance imaging (mri)*. https://www.nibib.nih.gov/science-education/science-topics/magnetic-resonance-imaging-mri

Nicoud, F., & Ducros, F. (1999). Subgrid-scale stress modelling based on the square of the velocity gradient tensor. *Flow, Turbulence and Combustion*, *62*(3), 183–200. https://doi.org/10.1023/a:1009995426001

Nilsen, A. H., Helvik, A.-S., Thorstensen, W. M., & Bugten, V. (2018). A comparison of symptoms and quality of life before and after nasal septoplasty and radiofrequency therapy of the inferior turbinate. *BMC Ear, Nose and Throat Disorders*, *18*(1). https://doi.org/10.1186/s12901-017-0050-z

Pawade, A. R. (2021). *Computational modeling of airflow in a human nasal cavity* [Master's thesis, Chalmers University Of Technology].

Pedersen, L., Schiöler, L., Finjan, S., Davidsson, Å., Sunnergren, O., Holmberg, K., Emanuelsson, C. A., & Hellgren, J. (2019). Prognostic factors for outcome after septoplasty in 888 patients from the swedish national septoplasty register. *European Archives of Oto-Rhino-Laryngology*, *276*(8), 2223–2228. https://doi.org/10.1007/s00405-019-05440-6

Pedersen, L. A., Dölvik, S., Holmberg, K., Emanuelsson, C. A., Johansson, H., Schiöler, L., Hellgren, J., & Steinsvåg, S. (2021). Surgery to relieve nasal obstruction: outcome for 366 patients operated on by one senior surgeon. *European Archives of Oto-Rhino-Laryngology*, *278*(10), 3867–3875. https://doi.org/10.1007/s00405-021-06696-7

Pedley, T. J. (1976). Viscous boundary layers in reversing flow. *Journal of Fluid Mechanics*, *74*(1), 59–79. https://doi.org/10.1017/s0022112076001687

Pedley, T. J. (1977). Pulmonary fluid dynamics. *Annual Review of Fluid Mechanics*, *9*(1), 229–274. https://doi.org/10.1146/annurev.fl.09.010177.001305

Pedley, T. J., Schroter, R. C., & Sudlow, M. F. (1977). Gas flow and mixing in the airways. In B. A. of the Lung (Ed.), *Bioengineering aspects of the lung*. Marcel Dekker Inc.

Piomelli, U., Cabot, W. H., Moin, P., & Lee, S. (1991). Subgrid-scale backscatter in turbulent and transitional flows. *Physics of Fluids A: Fluid Dynamics*, *3*(7), 1766–1771. https://doi.org/10.1063/1.857956

Pope, S. B. (2000). *Turbulent flows*. Cambridge University Press.

Pynnonen, M. A., & Davis, M. M. (2014). Extent of sinus surgery, 2000 to 2009: a population-based study. *The Laryngoscope*, *124*(4), 820–825. https://doi.org/10.1002/lary.24335

Quadrio, M., Pipolo, C., Stefano Corti, F. M., Pesci, C., Saibene, A. M., Zampini, S., & Felisati, G. (2016). Effects of ct resolution and radiodensity threshold on the cfd evaluation of nasal airflow. *Medical & Biological Engineering & Computing*, *54*(2), 411–419. https://doi.org/10.1007/s11517-015-1325-4

Radulesco, T., Meister, L., Bouchet, G., Giordano, J., Dessi, P., Perrier, P., & Michel, J. (2019). Functional relevance of computational fluid dynamics in the field of nasal obstruction: a literature review. *Clinical Otolaryngology*, *44*(5), 801–809. https://doi.org/10.1111/coa.13396

Radulesco, T., Meister, L., Bouchet, G., Varoquaux, A., Giordano, J., Mancini, J., Dessi, P., Perrier, P., & Michel, J. (2019). Correlations between computational fluid dynamics and clinical evaluation of nasal airway obstruction due to septal deviation: an observational study. *Clinical Otolaryngology*, *44*(4), 603–611. https://doi.org/10.1111/coa.13344

Rodi, W., Constantinescu, G., & Stoesser, T. (2013). *Large-eddy simulation in hydraulics* (1st ed.). CRC Press.

Sagaut, P. (2005). *Large eddy simulation for incompressible flows* (3rd ed.). Springer Berlin, Heidelberg. https://doi.org/10.1007/b137536

Sanmiguel-Rojas, E., Burgos, M. A., del Pino, C., Sevilla-García, M. A., & Esteban-Ortega, F. (2018). Robust nondimensional estimators to assess the nasal airflow in health and disease. *International Journal for Numerical Methods in Biomedical Engineering*, *34*(1), e2906. https://doi.org/10.1002/cnm.2906

Santosh, U. P. R., & Rao, S. V. M. (2013). Inferior turbinectomy for nasal obstruction-study of 219 cases. *Journal of Evolution of Medical and Dental Sciences*, *2*, 1371–1376. https://doi.org/10.14260/jemds/394

Schillaci, A., & Quadrio, M. (2022). Importance of the numerical schemes in the CFD of the human nose. *Journal of Biomechanics*, *138*, 111100. https://doi.org/10.1016/j.jbiomech.2022.111100

Schroter, R. C., & Sudlow, M. F. (1969). Flow patterns in models of the human bronchial airways. *Respiration Physiology*, *7*(3), 341–355. https://doi.org/10.1016/0034-5687(69)90018-8

Shi, H., Kleinstreuer, C., & Zhang, Z. (2006). Laminar airflow and nanoparticle or vapor deposition in a human nasal cavity model. *Journal of Biomechanical Engineering*, *128*(5), 697–706. https://doi.org/10.1115/1.2244574

Singh, N. P., & Inthavong, K. (2021). Can computational fluid dynamic models help us in the treatment of chronic rhinosinusitis. *Current Opinion in Otolaryngology & Head & Neck Surgery*, *29*(1), 21–26. https://doi.org/10.1097/moo.0000000000000682

Smagorinsky, J. (1963). General circulation experiments with the primitive equations: i. the basic experiment. *Monthly weather review*, *91*(3), 99–164. https://doi.org/10.1175/1520-0493(1963)091%3C0099:GCEWTP%3E2.3.CO;2

Song, O. K., Chung, Y. E., Seo, N., Baek, S.-E., Choi, J.-Y., Park, M.-S., & Kim, M.-J. (2019). Metal implants influence CT scan parameters leading to increased local radiation exposure: a proposal for correction techniques (G. E. Woloschak, Ed.). *PLOS ONE*, *14*(8), e0221692. https://doi.org/10.1371/journal.pone.0221692

Sooknundun, M., Kacker, S. K., Bhatia, R., & Deka, R. (1986). Nasal septal deviation: effective intervention and long term follow-up. *International Journal of Pediatric Otorhinolaryngology*, *12*(1), 65–72. https://doi.org/10.1016/s0165-5876(86)80059-3

Stewart, M. G., Smith, T. L., Weaver, E. M., Witsell, D. L., Yueh, B., Hannley, M. T., & and, J. T. J. (2004). Outcomes after nasal septoplasty: results from the nasal obstruction septoplasty effectiveness (NOSE) study. *Otolaryngology–Head and Neck Surgery*, *130*(3), 283–290. https://doi.org/10.1016/j.otohns.2003.12.004

Strien, J. V., Shrestha, K., Gabriel, S., Lappas, P., Fletcher, D. F., Singh, N., & Inthavong, K. (2021). Pressure distribution and flow dynamics in a nasal airway using a scale resolving simulation. *Physics of Fluids*, *33*(1), 011907. https://doi.org/10.1063/5.0036095

Subramaniam, R. P., Richardson, R. B., Morgan, K. T., Kimbell, J. S., & Guilmette, R. A. (1998). Computational fluid dynamics simulations of inspiratory airflow in the human nose and nasopharynx. *Inhalation Toxicology*, *10*(2), 91–120. https://doi.org/10.1080/089583798197772

Sullivan, C. D., Garcia, G. J. M., Frank-Ito, D. O., Kimbell, J. S., & Rhee, J. S. (2014). Perception of better nasal patency correlates with increased mucosal cooling after surgery for nasal obstruction. *Otolaryngology–Head and Neck Surgery*, *150*(1), 139–147. https://doi.org/10.1177/0194599813509776

Tarabichi, M., & Fanous, N. (1993). Finite element analysis of airflow in the nasal valve. *Archives of Otolaryngology - Head and Neck Surgery*, *119*(6), 638–642. https://doi.org/10.1001/archotol.1993.01880180054010

Tennekes, H., & Lumley, J. L. (1972). *A first course in turbulence*. MIT press.

Tomkinson, A., & Eccles, R. (1995). Errors arising in cross-sectional area estimation by acoustic rhinometry produced by breathing during measurement. *Rhinology*, *33*, 138–40.

Tsega, E. G., Katiyar, V., & Gupta, P. (2019). Breathing patterns of healthy human response to different levels of physical activity. *Journal of Biomedical Engineering and Technology*, *7*(1), 1–4. https://doi.org/10.12691/jbet-7-1-1

United Nations Scientific Committee on the Effects of Atomic Radiation. (2022). *Sources, effects and risks of ionizing radiation, united nations scientific committee on the effects of atomic radiation (unscear) 2020/2021 report, volume i* (2021st ed.). United Nations. https://www.un-ilibrary.org/content/books/9789210010030

van den Bosch, F. C. (2023). Summary sheets of astronomy 320: physical processes in astronomy. http://www.astro.yale.edu/vdbosch/astro320.html

Vecchietti, L. (2021). *A direct numerical simulation code for the flow in the human nose* [Master's thesis, Polytechnic University of Milan].

Velasco, R. C. R., & Liang, H. (2021). Cone-beam computed tomography (cbct) applications in dentistry. https://www.dentalcare.com/en-us/ce-courses/ce531/introduction

Versteeg, H., & Malalasekra, W. (2007). *An introduction to computational fluid dynamics: The finite volume method (2nd edition)*. Prentice Hall.

Wen, J., Inthavong, K., Tu, J., & Wang, S. (2008). Numerical simulations for detailed airflow dynamics in a human nasal cavity. *Respiratory Physiology & Neurobiology*, *161*(2), 125–135. https://doi.org/10.1016/j.resp.2008.01.012

Wiesmiller, K., Keck, T., Rettinger, G., Leiacker, R., Dzida, R., & Lindemann, J. (2006). Nasal air conditioning in patients before and after septoplasty with bilateral turbinoplasty. *The Laryngoscope*, *116*, 890–894. https://doi.org/10.1097/01.mlg.0000201995.02171.ea

Wilcox, D. C. (2006). *Turbulence modeling for cfd* (3rd ed.). D C W Industries.

Womersley, J. R. (1955). Method for the calculation of velocity, rate of flow and viscous drag in arteries when the pressure gradient is known. *The Journal of Physiology*, *127*(3), 553–563. https://doi.org/10.1113/jphysiol.1955.sp005276

Zhao, K., Blacker, K., Luo, Y., Bryant, B., & Jiang, J. (2011). Perceiving nasal patency through mucosal cooling rather than air temperature or nasal resistance (N. A. Cohen, Ed.). *PLOS ONE*, *6*(10), e24618. https://doi.org/10.1371/journal.pone.0024618

Zhao, K., & Jiang, J. (2014). What is normal nasal airflow? a computational study of 22 healthy adults. *International Forum of Allergy & Rhinology*, *4*(6), 435–446. https://doi.org/10.1002/alr.21319

Zhao, K., Jiang, J., Blacker, K., Lyman, B., Dalton, P., Cowart, B. J., & Pribitkin, E. A. (2014). Regional peak mucosal cooling predicts the perception of nasal patency. *The Laryngoscope*, *124*(3), 589–595. https://doi.org/10.1002/lary.24265

Zubair, M., Abdullah, M. Z., Ismail, R., Shuaib, I. L., Hamid, S. A., & Ahmad, K. A. (2012). Review: a critical overview of limitations of CFD modeling in nasal airflow. *Journal of Medical and Biological Engineering*, *32*(2), 77. https://doi.org/10.5405/jmbe.948

APPENDIX A

MISCELLANEOUS FLUID MECHANICS BACKGROUND

A.1 Fluid Mechanics Preliminaries

A.1.1 Descriptions of Motion

In continuum mechanics, the motion of any substance is represented either in Lagrangian configuration or in Eulerian configuration; Lagrangian and Eulerian configurations are also named referential and spatial configurations, respectively. Lagrangian way of describing motion is done by following an element throughout its movements. On the contrary, the Eulerian way of motion description inspects a fixed point and defines motion with respect to fixed locations.

A.1.2 Mappings Between Lagrangian and Eulerian Settings

The descriptions of motion can be mapped to each other with geometric mappings. The transformations used in the chapters below are the mappings between surfaces and volumetric elements. The derivation given in this subsection is given in parallel to Göktepe (2021).

The mapping of tangential surfaces is done through tangential vectors. This mapping, also known as the deformation gradient, is used to translate deformations between Lagrangian and Eulerian settings. Avoiding the underlying definitions and derivations for brevity, directly write down the relationship as:

$$\mathrm{d}\boldsymbol{x}_i = \boldsymbol{F}\mathrm{d}\boldsymbol{X}_i \tag{A.1}$$

where $\mathrm{d}\boldsymbol{x}_i$ and $\mathrm{d}\boldsymbol{X}_i$ denote the differential tangent vectors in Eulerian and Lagrangian definitions, and $\boldsymbol{F}$ is the deformation gradient.

Secondly, volumetric mapping, or Jacobi mapping, can be done using tangential mapping. For this, one should construct differential volume elements using differential tangent vectors $\mathrm{d}\boldsymbol{x}_i$ and $\mathrm{d}\boldsymbol{X}_i$ for both referential and spatial settings. Lagrangian infinitesimal volume element is expressed as,

$$\mathrm{d}V = \mathrm{d}\boldsymbol{X}_1 \cdot (\mathrm{d}\boldsymbol{X}_2 \times \mathrm{d}\boldsymbol{X}_3). \tag{A.2}$$

For the Eulerian counterpart, the volume element is

$$\mathrm{d}v = \mathrm{d}\boldsymbol{x}_1 \cdot (\mathrm{d}\boldsymbol{x}_2 \times \mathrm{d}\boldsymbol{x}_3). \tag{A.3}$$

Now, plugging in the tangential mapping given in Equation A.1 to the right-hand side of the description of the Eulerian infinitesimal volume element as given in Equation A.3,

$$\begin{aligned}
\mathrm{d}v &= \mathrm{d}\boldsymbol{x}_1 \cdot (\mathrm{d}\boldsymbol{x}_2 \times \mathrm{d}\boldsymbol{x}_3) && \text{(A.4)}\\
&= (\boldsymbol{F}\mathrm{d}\boldsymbol{X}_1) \cdot [\boldsymbol{F}\mathrm{d}\boldsymbol{X}_2 \times (\boldsymbol{F}\mathrm{d}\boldsymbol{X}_3)] && \text{(A.5)}\\
&= \det(\boldsymbol{F})\mathrm{d}\boldsymbol{X}_1 \cdot [\mathrm{d}\boldsymbol{X}_2 \times (\mathrm{d}\boldsymbol{X}_3)] && \text{(A.6)}\\
&= J\overbrace{\mathrm{d}\boldsymbol{X}_1 \cdot [\mathrm{d}\boldsymbol{X}_2 \times (\mathrm{d}\boldsymbol{X}_3)]}^{\mathrm{d}V} && \text{(A.7)}\\
&= J\mathrm{d}V, && \text{(A.8)}
\end{aligned}$$

noting that the equality of $\boldsymbol{\mathcal{A}a} \cdot (\boldsymbol{\mathcal{A}b} \times \boldsymbol{\mathcal{A}c}) = \det(\boldsymbol{\mathcal{A}})\boldsymbol{a} \cdot (\boldsymbol{b} \times \boldsymbol{c})$ is used in this derivation.

In short, the volumetric mapping is the Jacobian of the deformation gradient,

$$\mathrm{d}v = J\mathrm{d}V. \tag{A.9}$$

A.1.3 Derivative of the Determinant of a Second Order Tensor by Itself

In this section, proof of the expression

$$\frac{\partial[\det(\boldsymbol{\mathcal{A}})]}{\partial \boldsymbol{\mathcal{A}}} = \det(\boldsymbol{\mathcal{A}})\boldsymbol{\mathcal{A}}^{-T} \tag{A.10}$$

is given. This expression is used to derive the material derivative of the deformation gradient. The material derivative of the deformation gradient is used to come up with a simplified expression for the conservation of mass equation; hence, it is a critical piece to collect. Even though derivation is not necessary, it should be given for the sake of completeness. The proof, however, incorporates the Gateaux derivative and employs the characteristic equation of a tensor, resulting in a degree of difficulty when compared to the rest of this thesis.

Gateaux derivative of a second-order tensor $\boldsymbol{\mathcal{A}}$ with respect to itself is

$$\frac{\partial[\det(\boldsymbol{\mathcal{A}})]}{\partial \boldsymbol{\mathcal{A}}}\Delta\boldsymbol{\mathcal{A}} = \frac{\mathrm{d}}{\mathrm{d}\epsilon}\big[\det(\boldsymbol{\mathcal{A}}) + \det(\epsilon\Delta\boldsymbol{\mathcal{A}})\big]_{\epsilon=0} \tag{A.11}$$

$$= \frac{\mathrm{d}}{\mathrm{d}\epsilon}\big[\det(\boldsymbol{\mathcal{A}} + \epsilon\Delta\boldsymbol{\mathcal{A}})\big]_{\epsilon=0} \tag{A.12}$$

$$= \frac{\mathrm{d}}{\mathrm{d}\epsilon}\left[\det\left(\epsilon\boldsymbol{\mathcal{A}}\left(\frac{1}{\epsilon} + \boldsymbol{\mathcal{A}}^{-1}\Delta\boldsymbol{\mathcal{A}}\right)\right)\right]_{\epsilon=0} \tag{A.13}$$

$$= \frac{\mathrm{d}}{\mathrm{d}\epsilon}\left[\epsilon^3\det(\boldsymbol{\mathcal{A}})\det\left(\frac{\boldsymbol{I}}{\epsilon} + \boldsymbol{\mathcal{A}}^{-1}\Delta\boldsymbol{\mathcal{A}}\right)\right]_{\epsilon=0} \tag{A.14}$$

$$= \det(\boldsymbol{\mathcal{A}})\frac{\mathrm{d}}{\mathrm{d}\epsilon}\left[\epsilon^3\det\left(\frac{\boldsymbol{I}}{\epsilon} + \boldsymbol{\mathcal{A}}^{-1}\Delta\boldsymbol{\mathcal{A}}\right)\right]_{\epsilon=0}, \tag{A.15}$$

where $\boldsymbol{I}$ refers to identity matrix.

Furthermore, one may express the characteristic equation of a tensor with principal invariants as:

$$\det(\boldsymbol{\mathcal{M}} + \lambda\boldsymbol{I}) = \lambda^3 + I_1(\boldsymbol{\mathcal{M}})\lambda^2 + I_2(\boldsymbol{\mathcal{M}})\lambda + I_3(\boldsymbol{\mathcal{M}}), \tag{A.16}$$

where $I_1(\boldsymbol{\mathcal{M}}),\ I_2(\boldsymbol{\mathcal{M}}),\ I_3(\boldsymbol{\mathcal{M}})$ refer to principal invariants. They are defined as,

$$I_1(\boldsymbol{\mathcal{M}}) = \mathrm{tr}(\boldsymbol{\mathcal{M}}), \tag{A.17}$$

$$I_2(\boldsymbol{\mathcal{M}}) = 0.5\big\{[\mathrm{tr}(\boldsymbol{\mathcal{M}})]^2 - \mathrm{tr}(\boldsymbol{\mathcal{M}^2})]\big\}, \tag{A.18}$$

$$I_3(\boldsymbol{\mathcal{M}}) = \det(\boldsymbol{\mathcal{M}}). \tag{A.19}$$

Equation A.16 is plugged in to Equation A.15, considering $\lambda = \dfrac{1}{\epsilon}$ and $\boldsymbol{\mathcal{M}} = \boldsymbol{\mathcal{A}}^{-1}\Delta\boldsymbol{\mathcal{A}}$,

$$\frac{\partial[\det(\boldsymbol{\mathcal{A}})]}{\partial\boldsymbol{\mathcal{A}}} : \Delta\boldsymbol{\mathcal{A}} = \det(\boldsymbol{\mathcal{A}})\frac{\mathrm{d}}{\mathrm{d}\epsilon}\left[\epsilon^3\left(\frac{1}{\epsilon^3} + \frac{1}{\epsilon^2}I_1 + \frac{1}{\epsilon}I_2 + I_3\right)\right]_{\epsilon=0} \tag{A.20}$$

$$= \det(\boldsymbol{\mathcal{A}})\frac{\mathrm{d}}{\mathrm{d}\epsilon}\left[1 + \epsilon I_1 + \epsilon^2 I_2 + \epsilon^3 I_3\right]_{\epsilon=0} \tag{A.21}$$

$$= \det(\boldsymbol{\mathcal{A}})\Big[(I_1 + 2\epsilon I_2 + 3\epsilon^2 I_3)\Big]_{\epsilon=0} \tag{A.22}$$

$$= \det(\boldsymbol{\mathcal{A}})I_1. \tag{A.23}$$

Now, the first invariant could be expressed as the trace operator. Next, the trace is converted to a double contraction, i.e., a tensor contraction, as shown below.

$$\frac{\partial[\det(\boldsymbol{\mathcal{A}})]}{\partial\boldsymbol{\mathcal{A}}} : \Delta\boldsymbol{\mathcal{A}} = \det(\boldsymbol{\mathcal{A}})\mathrm{tr}(\boldsymbol{\mathcal{A}}^{-1}\Delta\boldsymbol{\mathcal{A}}) \tag{A.24}$$

$$= \det(\boldsymbol{\mathcal{A}})[(\boldsymbol{\mathcal{A}}^{-1})^T : \Delta\boldsymbol{\mathcal{A}}] \tag{A.25}$$

$$= \det(\boldsymbol{\mathcal{A}})[\boldsymbol{\mathcal{A}}^{-T} : \Delta\boldsymbol{\mathcal{A}}]. \tag{A.26}$$

In the above derivation, $tr(\boldsymbol{AB}) = A^T : B$ is invoked. Then, the derivation is concluded as:

$$\frac{\partial[\det(\boldsymbol{\mathcal{A}})]}{\partial\boldsymbol{\mathcal{A}}} = \det(\boldsymbol{\mathcal{A}})\boldsymbol{\mathcal{A}}^{-T}. \tag{A.27}$$

A.1.4 Leibniz Integral Rule

While deriving balance laws, such as conservation of mass, a material derivative of the interested property is integrated throughout a volume element. During this process, the material derivative is commonly moved into the integration using the Leibniz integral rule. The rule is expressed for the arbitrary variables x and y as:

$$\frac{\mathrm{D}}{\mathrm{D}t}\int_{g(t)}^{h(t)} f(x,t)\mathrm{d}x = \int_{g(t)}^{h(t)} \frac{\mathrm{D}f(x,t)}{\mathrm{D}t}\mathrm{d}x + f(x,h(t))\frac{\mathrm{D}h(t)}{\mathrm{D}t} - f(x,g(t))\frac{\mathrm{D}f(t)}{\mathrm{D}t}. \quad \text{(A.28)}$$

If the integral limits do not depend on the derivative, the derivatives appearing on the second and third terms on the right-hand side would drop. This is shown as,

$$\frac{\mathrm{D}}{\mathrm{D}t}\int_{a}^{b} f(x,t)\mathrm{d}x = \int_{a}^{b} \frac{\mathrm{D}f(x,t)}{\mathrm{D}t}\mathrm{d}x, \quad \text{(A.29)}$$

where a and b are some scalars or functions that do not depend on temporal and spatial variables.

A.1.5 Material Derivative of Determinant of the Deformation Gradient Tensor

During the derivation of the balance laws, the conversion of Eulerian volume description to Lagrangian volume description is occasionally done by using $\mathrm{d}v = J\mathrm{d}V$. Following this conversation, the material derivative is applied to this expression. Therefore, one has to take the material derivative of the Jacobian of the gradient tensor. The current derivative in question is expressed mathematically as:

$$\frac{\mathrm{D}(\det(\boldsymbol{F}))}{\mathrm{D}t} = \frac{\mathrm{D}J}{\mathrm{D}t} = \dot{J}, \quad \text{(A.30)}$$

and this expression can be reduced to simpler terms. In this section, the simplification is shown for the material derivative of the Jacobian gradient tensor.

The chain rule is used to make the derivative in a more comprehensible form:

$$\dot{J} = \frac{\partial(\det(\boldsymbol{F}))}{\partial \boldsymbol{F}} : \frac{\mathrm{D}(\det(\boldsymbol{F}))}{\mathrm{D}t} \tag{A.31}$$

$$= \frac{\partial(\det(\boldsymbol{F}))}{\partial \boldsymbol{F}} : \dot{\boldsymbol{F}}. \tag{A.32}$$

In Subsection A.1.3, the determinant of a matrix's proof and expression are given. Using the expression Equation A.10 for the derivative, and continuing:

$$\frac{\partial(\det(\boldsymbol{F}))}{\partial \boldsymbol{F}} : \dot{\boldsymbol{F}} = \det(\boldsymbol{F})\boldsymbol{F}^{-T} : \dot{\boldsymbol{F}} \tag{A.33}$$

$$= \det(\boldsymbol{F})\boldsymbol{I} : \dot{\boldsymbol{F}}\boldsymbol{F}^{-1}. \tag{A.34}$$

In order to continue with the derivation, the right side of the double contraction may be stripped down as,

$$\dot{\boldsymbol{F}}\boldsymbol{F}^{-1} = \dot{\overline{\left(\frac{\partial \boldsymbol{x}}{\partial \boldsymbol{X}}\right)}}\frac{\partial \boldsymbol{X}}{\partial \boldsymbol{x}} \tag{A.35}$$

$$= \frac{\partial \dot{\boldsymbol{x}}}{\partial \boldsymbol{X}}\frac{\partial \boldsymbol{X}}{\partial \boldsymbol{x}} \tag{A.36}$$

$$= \frac{\partial \dot{\boldsymbol{x}}}{\partial \boldsymbol{x}} \tag{A.37}$$

$$= \frac{\partial \boldsymbol{u}}{\partial \boldsymbol{x}} \tag{A.38}$$

$$= \boldsymbol{\nabla}\boldsymbol{u}. \tag{A.39}$$

Furthermore, it is possible to simplify the derivation as:

$$\frac{\partial(\det(\boldsymbol{F}))}{\partial \boldsymbol{F}} : \dot{\boldsymbol{F}} = \det(\boldsymbol{F})\, \boldsymbol{I} : \boldsymbol{\nabla}(\boldsymbol{u}) \tag{A.40}$$

$$= \det(\boldsymbol{F})\, (\boldsymbol{I} : \boldsymbol{\nabla}(\boldsymbol{u})) \tag{A.41}$$

$$= \det(\boldsymbol{F})\, \mathrm{tr}(\boldsymbol{\nabla}(\boldsymbol{u})) \tag{A.42}$$

$$= \det(\boldsymbol{F})\, \boldsymbol{\nabla} \cdot (\boldsymbol{u}) \tag{A.43}$$

$$= \det(\boldsymbol{F})\, \mathrm{div}(\boldsymbol{u}). \tag{A.44}$$

In short, the derivation ends up as:

$$\frac{\mathrm{D}(\det(\boldsymbol{F}))}{\mathrm{D}t} = \frac{\mathrm{D}J}{\mathrm{D}t} = \dot{J} = \det(\boldsymbol{F})\, \mathrm{div}(\boldsymbol{u}) = J\, \mathrm{div}(\boldsymbol{u}). \tag{A.45}$$

A.2 Fundamental Principles and Governing Equations for Fluid Mechanics

A.2.1 Conservation of Mass

Conservation of mass, also called the balance of mass or continuity equation, dictates that the mass of any part of the material remains constant throughout time. This assumption considers the flow as a closed system that does not lose any part of itself during a specific time frame. This subsection follows Göktepe (2021)'s approach closely, except that the derivation is simplified and Leibniz integration rule usage is explicitly stated.

For the whole body of material with mass m, one may express the conservation of mass as,

$$\frac{\mathrm{D}m}{\mathrm{D}t} = 0. \tag{A.46}$$

Similarly, a conservation of mass equation may be written for a cut from this material

body. This cut is named Ω_0 in the Lagrangian frame and Ω in the Eulerian frame. Expressing this mathematically in the Eulerian frame,

$$\frac{\mathrm{D}}{\mathrm{D}t}\Big(\int_{\Omega} \mathrm{d}m\Big) = \frac{\mathrm{D}}{\mathrm{D}t}\Big(\int_{\Omega} \rho \mathrm{d}v\Big) = 0. \tag{A.47}$$

Here, one may translate $\mathrm{d}v$ to $\mathrm{d}V$ with the already derived mapping as shown in Equation A.9 as,

$$\frac{\mathrm{D}}{\mathrm{D}t}\Big(\int_{\Omega_0} \rho J \mathrm{d}V\Big) = 0. \tag{A.48}$$

Applying the Leibniz integration rule to represent the material time derivative in Newton's notation, then expanding the derivative with the multiplication rule:

$$0 = \int_{\Omega_0} \frac{\mathrm{D}}{\mathrm{D}t}\big(\rho J\big)\mathrm{d}V \tag{A.49}$$

$$= \int_{\Omega_0} \overline{\dot{\big(\rho J\big)}}\mathrm{d}V \tag{A.50}$$

$$= \int_{\Omega_0} \big(\dot{\rho} J + \rho \dot{J}\big)\mathrm{d}V. \tag{A.51}$$

Expanding the material derivative of the Jacobian with Equation A.45,

$$0 = \int_{\Omega_0} \big(\dot{\rho} J + \rho J \mathrm{div}(\boldsymbol{u})\big)\mathrm{d}V \tag{A.52}$$

$$= \int_{\Omega_0} J\big(\dot{\rho} + \rho \mathrm{div}(\boldsymbol{u})\big)\mathrm{d}V \tag{A.53}$$

$$= J\big(\dot{\rho} + \rho \mathrm{div}(\boldsymbol{u})\big) \tag{A.54}$$

$$= \dot{\rho} + \rho \mathrm{div}(\boldsymbol{u}). \tag{A.55}$$

Finally, the balance of mass equation is found as,

$$\dot{\rho} + \rho \operatorname{div}(\boldsymbol{u}) = 0, \tag{A.56}$$

or alternatively,

$$\frac{\mathrm{D}\rho}{\mathrm{D}t} + \rho \frac{\partial u_i}{\partial x_i} = 0, \tag{A.57}$$

$$\frac{\mathrm{D}\rho}{\mathrm{D}t} + \rho \boldsymbol{\nabla} \cdot \boldsymbol{u} = 0, \tag{A.58}$$

$$\frac{\partial \rho}{\partial t} + \boldsymbol{\nabla} \cdot (\rho \boldsymbol{u}) = 0. \tag{A.59}$$

A.2.2 Incompressible Conservation of Mass Equation

In this part, the continuity equation is investigated for incompressible fluid flows. The continuity equation for compressible fluids in differential form is already derived as,

$$\frac{\partial \rho}{\partial t} + \boldsymbol{\nabla} \cdot (\rho \boldsymbol{u}) = 0. \tag{A.60}$$

The differential form can be written in Einstein notation as:

$$\frac{\partial \rho}{\partial t} + \frac{\partial (\rho u_i)}{\partial x_i} = 0. \tag{A.61}$$

The next step is the separation of density and velocity in the second term. In this manner, it is vital to point out that both velocity and density could be and are characterized by both temporal and spatial variables. Therefore, using the product rule to separate the density and velocity,

$$\frac{\partial \rho}{\partial t} + u_i \frac{\partial \rho}{\partial x_i} + \rho \frac{\partial u_i}{\partial x_i} = 0. \tag{A.62}$$

At this point, there is no further expansion that can be done for compressible flows; thus, the continuity equation for compressible flows is Equation A.62. On the other hand, for incompressible flows, the material time derivative of density is equal to zero, i.e.,

$$\frac{\mathrm{D}\rho}{\mathrm{D}t} = \frac{\partial \rho}{\partial t} + u_i \frac{\partial \rho}{\partial x_i} = 0. \tag{A.63}$$

One may find this expression in the incompressible continuity equation, Equation A.62,

$$\overbrace{\frac{\partial \rho}{\partial t} + u_i \frac{\partial \rho}{\partial x_i}}^{0} + \rho \frac{\partial u_i}{\partial x_i} = 0 \tag{A.64}$$

$$\rho \frac{\partial u_i}{\partial x_i} = 0 \tag{A.65}$$

$$\boxed{\frac{\partial u_i}{\partial x_j} = 0}. \tag{A.66}$$

Also, this equation is commonly referred to as,

$$\boldsymbol{\nabla} \cdot \boldsymbol{u} = 0. \tag{A.67}$$

A.2.3 Newton's Second Law of Motion

Newton's second law of motion is widely known and considered groundbreaking. The second law of motion describes how forces affect objects in terms of their motion. Even though this subject is widely known and deeply explored, external force is often thought to merely equal mass and acceleration. However, this equality has to be proven equal to the momentum change, as Newton stated. Moreover, the second law is generally described in terms of only ordinary derivatives; this requires a conversation on Newton's second law of motion on partial derivatives. Therefore, there is a need for an in-depth discussion of the second law of motion.

Newton's second law of motion is defined as applied force is equal to change in

momentum, i.e.,

$$\boldsymbol{F} = \frac{\mathrm{d}\boldsymbol{P}}{\mathrm{d}t} = \frac{\mathrm{d}(m\boldsymbol{u})}{\mathrm{d}t}. \tag{A.68}$$

In this equation, one may warp the total derivatives to partial derivatives. This expansion for a function $f = f(\boldsymbol{x}, t)$,

$$\frac{\mathrm{d}f}{\mathrm{d}t} = \frac{\partial f}{\partial t} + \frac{\partial f}{\partial x_1}\frac{\mathrm{d}x_1}{\mathrm{d}t} + \frac{\partial f}{\partial x_2}\frac{\mathrm{d}x_2}{\mathrm{d}t} + \frac{\partial f}{\partial x_3}\frac{\mathrm{d}x_3}{\mathrm{d}t} \tag{A.69}$$

$$= \frac{\partial f}{\partial t} + \frac{\partial f}{\partial x_1}u_1 + \frac{\partial f}{\partial x_2}u_2 + \frac{\partial f}{\partial x_3}u_3 \tag{A.70}$$

$$= \frac{\partial f}{\partial t} + u_j\frac{\partial f}{\partial x_j}. \tag{A.71}$$

The above expression may be called a material derivative or a material time derivative. It is shown as,

$$\frac{\mathrm{d}f}{\mathrm{d}t} = \frac{\partial f}{\partial t} + \boldsymbol{u}\cdot\boldsymbol{\nabla} f \tag{A.72}$$

$$= \frac{\partial f}{\partial t} + u_j\frac{\partial f}{\partial x_j}. \tag{A.73}$$

Since the spatial variables $x,\ y,\ z$ in the second law of motion may change with respect to time, the time derivative should be expressed in its partial differential form, i.e., it is actually a material derivative. Rewriting the second law of motion in partial derivative form,

$$\boldsymbol{F} = \frac{\mathrm{d}(m\boldsymbol{u})}{\mathrm{d}t} = \frac{\mathrm{D}(m\boldsymbol{u})}{\mathrm{D}t}. \tag{A.74}$$

Use chain rule and separate m and $\boldsymbol{u}$ from each other:

$$\boldsymbol{F} = u\frac{\mathrm{D}m}{\mathrm{D}t} + m\frac{\mathrm{D}\boldsymbol{u}}{\mathrm{D}t}. \tag{A.75}$$

From the law of conservation of mass, Equation A.46, one knows that mass does not change with respect to time. Using this information to simplify the second law.

$$\boldsymbol{F} = u\overbrace{\frac{\mathrm{D}m}{\mathrm{D}t}}^{0} + m\frac{\mathrm{D}\boldsymbol{u}}{\mathrm{D}t} \tag{A.76}$$

$$= m\frac{\mathrm{D}\boldsymbol{u}}{\mathrm{D}t} \tag{A.77}$$

$$= \rho V\frac{\mathrm{D}\boldsymbol{u}}{\mathrm{D}t}, \tag{A.78}$$

alternatively, in Einstein notation,

$$F_i = \rho V\left(\frac{\partial u_j}{\partial t} + u_j\frac{\partial u_i}{\partial x_j}\right). \tag{A.79}$$

In the long run, one concludes that the second law of motion can be translated into its most known forms,

$$\boldsymbol{F} = m\frac{\mathrm{D}\boldsymbol{u}}{\mathrm{D}t}, \tag{A.80}$$

and,

$$\boldsymbol{F} = m\boldsymbol{a}. \tag{A.81}$$

To conclude this section, proof is given for the equality of the momentum change and the product of mass and acceleration. This equality is almost always taken for granted; furthermore, the second law is thought to be the product of mass and acceleration rather than a change of momentum with respect to time.

A.2.4 Cauchy Momentum Equations

This section discusses the mathematical expression of the momentum transportation process on some continuum elements. These expressions are known as the Cauchy momentum equation and are a generalized form of the Navier-Stokes equations. These expressions are commonly expressed in either differential or integral forms. Only the differential form is derived and explained here, hence the brevity.

Firstly, forces on a differential body should be defined. Also, what stresses and forces this body experiences should be shown. The forces that are in question are not the fundamental forces that describe the most basic interactions between materials. Conversely, they are the forces that can change the momentum of objects. These forces may be expressed as the Newtonian description of forces.

The forces affecting bodies could be divided into two categories: body forces and surface forces (Aydın, 2021). Body forces are the kind of forces that act on the whole volume of the fluid without any physical contact (Aydın, 2021). Some examples of these forces are gravitational forces, magnetic forces, and electrical forces. On the other hand, surface forces directly appear due to the physical interaction between two bodies. Since electrons, or in general, fermions, can not coexist at the exact location due to the Pauli exclusion principle, they repel each other due to electromagnetic forces. Surface forces are often expressed in normal and tangential components, such as pressure forces and friction forces (Aydın, 2021).

$$\boldsymbol{F}^{\text{body}} = m\boldsymbol{B} = mB_i = m(B_{\text{x}}\boldsymbol{e}_1 + B_{\text{y}}\boldsymbol{e}_2 + B_{\text{z}}\boldsymbol{e}_3). \tag{A.82}$$

The forces acting on a body cause deformation in the same body. Stresses cause these deformations. Stress is the ratio of force to the area this force acts on. For a differential element, the stress vector becomes:

$$\boldsymbol{t} = \lim_{\Delta A \to 0} \frac{\boldsymbol{\Delta F}}{\Delta A}. \tag{A.83}$$

Stresses acting on a differential element are expressed as a second-order stress tensor,

also known as the Cauchy stress tensor,

$$\boldsymbol{t} = \boldsymbol{\sigma}\boldsymbol{n}. \tag{A.84}$$

The Cauchy stress tensor is further expressed in its orthogonal and parallel components:

$$\boldsymbol{\sigma} = \sigma_{ij}(\boldsymbol{e}_i \otimes \boldsymbol{e}_i) = \begin{bmatrix} \sigma_{11} & \sigma_{12} & \sigma_{13} \\ & \sigma_{22} & \sigma_{23} \\ \text{sym.} & & \sigma_{33} \end{bmatrix}. \tag{A.85}$$

This tensor is symmetric due to the conservation of angular momentum, which states that total angular momentum on a closed system is preserved if there is no external force application. Also, this tensor's diagonal elements are referred to as normal stresses, and the non-diagonal elements are known as shear stresses. An illustration of the Cauchy stress tensor on a differential element is given in Figure A.1. If the differential element is in equilibrium, one may expect stresses to point in reverse directions with equal magnitudes.

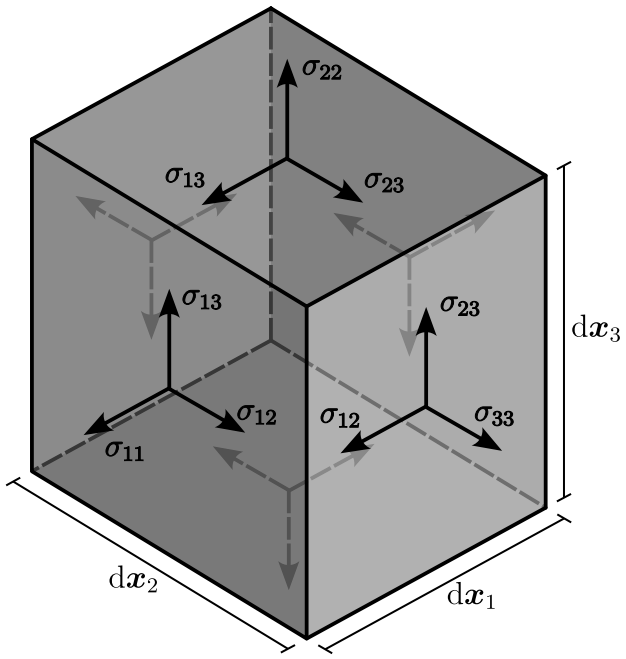

Figure A.1. Cauchy Stress Tensor on a Differential Element

After the introduction of the Cauchy stress tensor, one may write down Cauchy momentum equations that describe the transportation of momentum throughout the materials. Cauchy momentum equations only describe momentum transportation for materials that can be modeled as a continuum.

The first step to derive the equation is to consider a change in stresses in a differential continuum element. For this, one has to consider stress as a field changing over a particular direction. Since the considered element is differential, one may claim that the change is constant and can be approximated by multiplying it by the distance $\mathrm{d}x_i$. Figure A.2 shows this behavior for stress vectors parallel to the z-axis.

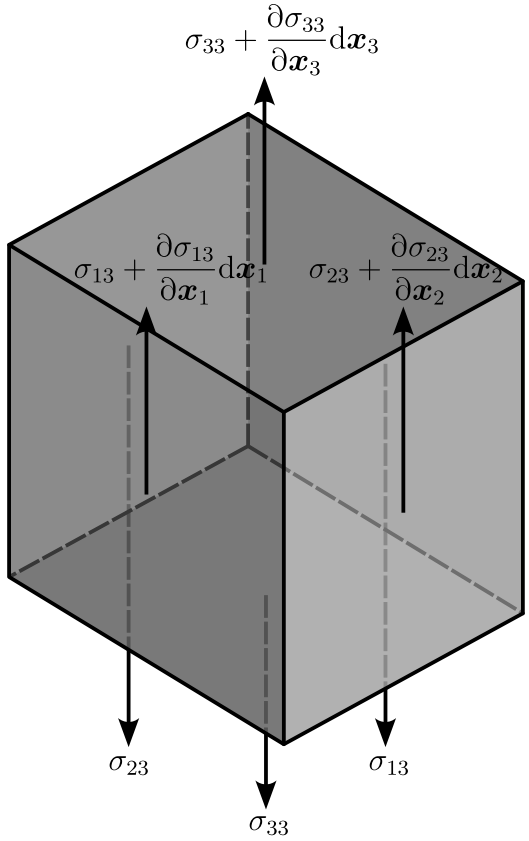

Figure A.2. Cauchy Stress Tensor on a Differential Element

Here, one may find the surface forces on the differential element. This is done by multiplying stresses with the corresponding areas and summing them up for each axis.

For the $\boldsymbol{x}_3$ direction, the equation of forces is:

$$(\mathrm{d}F_3)^{\text{surface}} = \left(\frac{\partial \sigma_{13}}{\partial x_1}\mathrm{d}\boldsymbol{x_1}\right)\cdot(\mathrm{d}\boldsymbol{x_2}\times\mathrm{d}\boldsymbol{x_3}) + \left(\frac{\partial \sigma_{23}}{\partial x_2}\mathrm{d}\boldsymbol{x_2}\right)\cdot(\mathrm{d}\boldsymbol{x_1}\times\mathrm{d}\boldsymbol{x_3}) \tag{A.86}$$

$$+\left(\frac{\partial \sigma_{33}}{\partial x_3}\mathrm{d}\boldsymbol{x_3}\right)\cdot(\mathrm{d}\boldsymbol{x_1}\times\mathrm{d}\boldsymbol{x_2})$$

$$= \left(\frac{\partial \sigma_{13}}{\partial x_1} + \frac{\partial \sigma_{23}}{\partial x_2} + \frac{\partial \sigma_{33}}{\partial x_3}\right)[\mathrm{d}\boldsymbol{x_1}\cdot(\mathrm{d}\boldsymbol{x_2}\times\mathrm{d}\boldsymbol{x_3})]. \tag{A.87}$$

Or above equation may be generalized for any axis, x_i, as may be shown in Einstein notation,

$$(\mathrm{d}F_i)^{\text{surface}} = \left(\frac{\partial \sigma_{ji}}{\partial x_j}\right)\mathrm{d}V. \tag{A.88}$$

Additionally, the body forces must be considered in this equation; for that, the mass of a differential element, $\mathrm{d}m$, could be described as follows:

$$\mathrm{d}m = \rho \mathrm{d}V. \tag{A.89}$$

Now, the body force $\boldsymbol{F}^{\text{body}}$ given in Equation A.82 can be reshaped to,

$$\mathrm{d}\boldsymbol{F}^{\text{body}} = \mathrm{d}m\boldsymbol{B} = \rho \mathrm{d}V\boldsymbol{B} \tag{A.90}$$

$$\mathrm{d}F_i^{\text{body}} = \rho \mathrm{d}V B_i. \tag{A.91}$$

Introducing these body forces into this force equilibrium equation:

$$\mathrm{d}F_i = \left(\frac{\partial \sigma_{ji}}{\partial x_j} + \rho B_i\right)\mathrm{d}V. \tag{A.92}$$

Finally, Equation A.92 is placed into Newton's second law of motion, Equation A.79, as the force term, $\boldsymbol{F}$. However, one has to consider rewriting the second law of motion

for a differential element. Newton's second law of motion is

$$F_i = \rho V \left(\frac{\partial u_i}{\partial t} + u_j \frac{\partial u_i}{\partial x_j} \right). \tag{A.93}$$

Rewriting this equation for a differential element,

$$\mathrm{d}F_i = \rho \mathrm{d}V \left(\frac{\partial u_i}{\partial t} + u_i \frac{\partial u_j}{\partial x_i} \right). \tag{A.94}$$

Finally, equating the second law with forces on the differential element to find the Cauchy momentum equation.

$$\rho \mathrm{d}V \left(\frac{\partial u_i}{\partial t} + u_j \frac{\partial u_i}{\partial x_j} \right) = \left(\frac{\partial \sigma_{ji}}{\partial x_j} + \rho B_i \right) \mathrm{d}V \tag{A.95}$$

$$\rho \left(\frac{\partial u_i}{\partial t} + u_j \frac{\partial u_i}{\partial x_j} \right) = \frac{\partial \sigma_{ji}}{\partial x_j} + \rho B_i \tag{A.96}$$

$$\rho \left(\frac{\mathrm{D}\boldsymbol{u}}{\mathrm{D}t} \right) = \boldsymbol{\nabla} \cdot \boldsymbol{\sigma} + \rho \boldsymbol{B}. \tag{A.97}$$

In the end, the Cauchy momentum equation can be rewritten in a more common form,

$$\frac{\mathrm{D}\boldsymbol{u}}{\mathrm{D}t} = \frac{1}{\rho} \boldsymbol{\nabla} \cdot \boldsymbol{\sigma} + \boldsymbol{B}. \tag{A.98}$$

A.3 Generalization of Newtonian Law of Viscosity

Newtonian law of viscosity aims to model viscous stresses during fluid flow. For a 1D flow, this law predicts that stresses emerge with respect to strain rates linearly,

$$\tau = \mu \frac{\mathrm{d}u_1}{\mathrm{d}x_2}, \tag{A.99}$$

where τ is the stress, μ is a constant named viscosity, and $\frac{\mathrm{d}u_1}{\mathrm{d}x_2}$ is the strain rate.

For the 1D case, this model claims that there is a single unknown, namely μ. However, when the law is generalized for 3D cases, the model evolves into a complicated state due to an enormous amount of unknowns. This generalization may be shown in mathematical notation as,

$$\boldsymbol{\tau} = \boldsymbol{\mu} : \frac{\partial \boldsymbol{u}}{\partial \boldsymbol{x}} \tag{A.100}$$

$$\tau_{ij} = \mu_{ijkl} \frac{\partial u_k}{\partial x_l}. \tag{A.101}$$

Since stress and velocity gradient are both second-order tensors, the viscous stress tensor should be a fourth-order tensor in order to represent the most general form. This is due to the requirement of mapping every single element between these two second-order tensors. More concretely, if the second-order tensors have nine elements, in order to map nine elements to another nine elements, one would require 81 different constants. Fortunately, these 81 different viscosity constants or variables might be reduced by making assumptions about the fluid's behavior and characteristics. Therefore, one should define the fluid's characteristics and how these characteristics shape the viscous stress tensor, μ.

This talk is limited to a Newtonian fluid. Newtonian fluids are Stokesian fluids with an extra assumption of linearity; they are non-elastic viscous fluids (Aris, 1989). According to Aris (1989) and van den Bosch (2023), these assumptions for a Newtonian fluid are:

- Locality: Stress tensor is a function of strain and thermodynamic variables, e.g., pressure and temperature. This means that motions that do not cause strain, such as rotation, would not cause any stress in the fluid element.
- Homogeneity: Stress tensor does not directly depend on spatial variables, $\boldsymbol{x}$. In other words, stress tensors may only depend on spatial variables either due to their thermodynamic part or due to the strain rate's dependence on spatial variables.
- Isotropy: Fluid behaves the same in every direction, which means it has no directional preference.

- Linearity: Stress tensor and strain tensor are related linearly.

With the above assumptions in mind, one may begin investigating the viscous stress tensor. The aim is to reduce 81 unknowns, and the first step in this direction is to separate the viscous stress tensor from the Cauchy stress tensor. The reasoning for this separation is straightforward: the thermodynamic pressure does not appear due to viscous action. This reasoning makes sense since viscous stress is caused by strain rate, and there is stress on a fluid even if there is not a strain rate on the fluid.

Separating thermodynamic pressure from the Cauchy stress tensor to get the viscous stress, $\boldsymbol{\tau}$:

$$\boldsymbol{\sigma} = -p\boldsymbol{I} + \boldsymbol{\tau} \tag{A.102}$$

$$\sigma_{ij} = -p\delta_{ij} + \tau_{ij}. \tag{A.103}$$

The second step is to write the strain rate tensor as a combination of symmetric and skew-symmetric tensors. This is possible for any second-order tensor, and for an arbitrary tensor $\boldsymbol{A}$, this can be shown as,

$$\boldsymbol{A} = \overbrace{\frac{1}{2}\left(\boldsymbol{A} + \boldsymbol{A}^T\right)}^{\text{Symmetric}} + \overbrace{\frac{1}{2}\left(\boldsymbol{A} - \boldsymbol{A}^T\right)}^{\text{Skew-symmetric}}. \tag{A.104}$$

Writing the velocity gradient tensor as its combination of symmetric and skew-symmetric forms,

$$\frac{\partial u_k}{\partial x_l} = \frac{1}{2}\left(\frac{\partial u_k}{\partial x_l} + \frac{\partial u_l}{\partial x_k}\right) + \frac{1}{2}\left(\frac{\partial u_k}{\partial x_l} - \frac{\partial u_l}{\partial x_k}\right) \tag{A.105}$$

$$\frac{\partial u_k}{\partial x_l} = S_{kl} + \Omega_{kl}. \tag{A.106}$$

The skew-symmetric part of the velocity gradient, Ω_{kl}, appears as the vorticity, which is also described in vector calculus as $\boldsymbol{\nabla} \times \boldsymbol{u}$. Since the vorticity contributes only to the

rotation of a fluid element, it does not cause any strain. Therefore, the skew-symmetric part does not cause any shear, i.e., shear only appears due to the symmetric part,

$$S_{kl} = \frac{1}{2}\left(\frac{\partial u_k}{\partial x_l} + \frac{\partial u_l}{\partial x_k}\right), \tag{A.107}$$

which is also named the strain rate tensor.

Rewriting the general form of Newton's viscosity law,

$$\tau_{ij} = \mu_{ijkl} S_{kl} \tag{A.108}$$

$$\tau_{ij} = \mu_{ijkl} \frac{1}{2}\left(\frac{\partial u_k}{\partial x_l} + \frac{\partial u_l}{\partial x_k}\right). \tag{A.109}$$

At this point, the rank-4 viscous stress tensor should be simplified by some assumptions and considerations. Here, one may rewrite a generalized fourth-order tensor using an isotropic assumption. According to Aris (1989), an isotropic fourth-order tensor $\mathbb{A}$ may be written in its most general form as,

$$A_{ijkl} = \lambda\delta_{ij}\delta_{kl} + \mu(\delta_{ik}\delta_{jl} + \delta_{il}\delta_{jk}) + \nu(\delta_{ik}\delta_{jl} - \delta_{il}\delta_{jk}). \tag{A.110}$$

Applying this general isotropic form for the viscous stress tensor, $\mathbb{\mu}$, and plugging it into the generalized viscosity law, Equation A.108,

$$\tau_{ij} = [\lambda\delta_{ij}\delta_{kl} + \mu(\delta_{ik}\delta_{jl} + \delta_{il}\delta_{jk}) + \nu(\delta_{ik}\delta_{jl} - \delta_{il}\delta_{jk})]S_{kl} \tag{A.111}$$

$$\tau_{ij} = \lambda\delta_{ij}S_{kk} + \mu(S_{ij} + S_{ji}) + \nu(S_{ij} - S_{ji}). \tag{A.112}$$

Simplifying the equation by using $S_{ij} = S_{ji}$ since $\boldsymbol{S}$ is a symmetric tensor,

$$\tau_{ij} = \lambda\delta_{ij}S_{kk} + \mu(S_{ij} + S_{ij}) + \nu(S_{ij} - S_{ij}) \tag{A.113}$$

$$\tau_{ij} = \lambda\delta_{ij}S_{kk} + 2\mu S_{ij} \tag{A.114}$$

$$\tau_{ij} = \lambda\delta_{ij}\left[\frac{1}{2}\left(\frac{\partial u_k}{\partial x_k} + \frac{\partial u_k}{\partial x_k}\right)\right] + 2\mu\left[\frac{1}{2}\left(\frac{\partial u_i}{\partial x_j} + \frac{\partial u_j}{\partial x_i}\right)\right] \tag{A.115}$$

$$\tau_{ij} = \lambda\delta_{ij}\frac{\partial u_k}{\partial x_k} + \mu\left(\frac{\partial u_i}{\partial x_j} + \frac{\partial u_j}{\partial x_i}\right). \tag{A.116}$$

Now, one may write the Cauchy stress tensor, Equation A.103, using Equation A.116,

$$\sigma_{ij} = -p\delta_{ij} + \lambda\delta_{ij}\frac{\partial u_k}{\partial x_k} + \mu\left(\frac{\partial u_i}{\partial x_j} + \frac{\partial u_j}{\partial x_i}\right). \tag{A.117}$$

A.3.1 Incompressible Generalized Law of Viscosity

For an incompressible flow, conservation of mass reduces to $\frac{\partial u_k}{\partial x_k} = 0$; this leaves Cauchy stress tensor to:

$$\sigma_{ij} = -p\delta_{ij} + \mu\left(\frac{\partial u_i}{\partial x_j} + \frac{\partial u_j}{\partial x_i}\right), \tag{A.118}$$

where the only unknowns are the pressure and shear viscosity, μ. The shear viscosity is considered a function of material, temperature, pressure, and shear rate; however, for a Newtonian fluid, the main factors defining the shear viscosity are temperature and material. Note that shear viscosity μ's value can be easily obtained experimentally.

A.3.2 Compressible Generalized Law of Viscosity

For compressible flows, it is possible to introduce new variables in such a way that allows $\frac{\partial u_i}{\partial x_j}$ part of the generalized viscosity law to vanish. This maneuver allows the usage of conservation of mass equation, since $\frac{\partial u_k}{\partial x_k}$ already exists in the conservation of

mass equation. Therefore, one may better speculate about the generalized law.

In order to get rid of the $\frac{\partial u_i}{\partial x_j}$ introduce mean pressure,

$$\overline{p} = -\frac{1}{3}\sigma_{ii}. \tag{A.119}$$

Expanding the above equation's right-hand side with already generalized Cauchy stress, Equation A.117, now yields:

$$\overline{p} = -\frac{1}{3}\Bigg[- p\delta_{ii} + \lambda\delta_{ii}\frac{\partial u_k}{\partial x_k} + \mu\left(\frac{\partial u_i}{\partial x_i} + \frac{\partial u_i}{\partial x_i}\right)\Bigg] \tag{A.120}$$

$$= -\frac{1}{3}\Bigg[- p\delta_{ii} + \lambda\delta_{ii}\frac{\partial u_k}{\partial x_k} + 2\mu\frac{\partial u_i}{\partial x_i}\Bigg] \tag{A.121}$$

$$= -\frac{1}{3}\Bigg[- 3p + 3\lambda\frac{\partial u_i}{\partial x_i} + 2\mu\frac{\partial u_i}{\partial x_i}\Bigg] \tag{A.122}$$

$$= -\frac{1}{3}\Bigg[- 3p + (3\lambda + 2\mu)\frac{\partial u_i}{\partial x_i}\Bigg] \tag{A.123}$$

$$= p - \left(\lambda + \frac{2}{3}\mu\right)\frac{\partial u_i}{\partial x_i}. \tag{A.124}$$

This derivation now evolves into an equation that shows the difference between mean pressure and thermodynamic pressure,

$$\overline{p} - p = -\left(\lambda + \frac{2}{3}\mu\right)\frac{\partial u_i}{\partial x_i} \tag{A.125}$$

$$\overline{p} - p = -\eta\frac{\partial u_i}{\partial x_i}, \tag{A.126}$$

where η is called bulk viscosity.

Rewriting the conservation of mass equation, Equation A.57, in order to incorporate it

into the mean pressure equation:

$$\frac{\mathrm{D}\rho}{\mathrm{D}t} + \rho\frac{\partial u_i}{\partial x_i} = 0 \tag{A.127}$$

$$\frac{\partial u_i}{\partial x_i} = -\frac{1}{\rho}\frac{\mathrm{D}\rho}{\mathrm{D}t}. \tag{A.128}$$

Plug $\frac{\partial u_i}{\partial x_i}$ into the mean pressure,

$$\overline{p} - p = -\eta\left(- \frac{1}{\rho}\frac{\mathrm{D}\rho}{\mathrm{D}t}\right) \tag{A.129}$$

$$\overline{p} - p = \eta\frac{1}{\rho}\frac{\mathrm{D}\rho}{\mathrm{D}t}. \tag{A.130}$$

Bulk viscosity is taken equal to zero by Stokes, which is commonly known as Stokes's hypothesis, i.e.,

$$\eta = 0 \tag{A.131}$$

$$\lambda = -\frac{2}{3}\mu. \tag{A.132}$$

As told by van den Bosch (2023), Stokes's hypothesis certainly holds for monatomic fluids where atoms do not have any rotational or vibrational degrees of freedom. However, since other molecules, such as polyatomic fluids, may have rotational and vibrational degrees of freedom, Stokes's hypothesis is incorrect. This condition gets more severe if there is a high volumetric change (van den Bosch, 2023). The reasoning behind such phenomenon is that high values of $\frac{\mathrm{D}\rho}{\mathrm{D}t}$ exacerbate the magnitude η. On the other hand, according to Currie (2002), η commonly does not deviate from zero; thus, Stokes's hypothesis is considered acceptable.

By using Stokes's hypothesis, the generalized law of viscosity for Newtonian fluids

may be rewritten as:

$$\tau_{ij} = -\frac{2}{3}\mu\delta_{ij}\frac{\partial u_k}{\partial x_k} + \mu\left(\frac{\partial u_i}{\partial x_j} + \frac{\partial u_j}{\partial x_i}\right). \tag{A.133}$$

Additionally, the Cauchy stress tensor becomes,

$$\sigma_{ij} = -p\delta_{ij} - \frac{2}{3}\mu\delta_{ij}\frac{\partial u_k}{\partial x_k} + \mu\left(\frac{\partial u_i}{\partial x_j} + \frac{\partial u_j}{\partial x_i}\right). \tag{A.134}$$

A.3.3 Navier-Stokes Equations

The Navier-Stokes equations, which are derived from the Cauchy momentum equations, are found as,

$$\rho\left(\frac{\mathrm{D}\boldsymbol{u}}{\mathrm{D}t}\right) = \boldsymbol{\nabla}\cdot\boldsymbol{\sigma} + \rho\boldsymbol{B}. \tag{A.135}$$

Currently, these equations, together with the conservation of mass equation, are able to model the flow of a fluid, yet there exists a problem: there are more unknowns than equations. Currently, there are four equations, and they have nine unknowns within them: six unknowns arising from the Cauchy stress tensor and another three unknowns from the velocity. The inequality means that, even though this system of partial differential equations is able to model fluid flow, they can not be solved. In order to get a solution, there is a need to get equation numbers and unknown numbers equal. The possible approaches for this may be listed as follows:

- Express some unknowns in terms of other unknowns.
- Use empirical knowledge to estimate unknowns.
- Generate more equations describing the system.

The first approach appears to be less challenging and more comprehensive compared to other approaches; thus, it is preferred over others. However, expressing some unknowns

as other unknowns is still a tough job to do. In order to accomplish this, one may use the stress-strain relationship for shear stresses in the Cauchy stress tensor, as explained in Section A.3.

A.3.4 Incompressible Navier-Stokes Equations

For an incompressible flow condition, Cauchy momentum equations might be rewritten using an incompressible kind of generalized Newtonian law of viscosity, as explained in Subsection A.3.1. Rewriting the Cauchy momentum equations in Einstein notation then, plugging the generalized viscosity law for incompressible flows, Equation A.118, into the momentum equations:

$$\rho\frac{\partial u_i}{\partial t}+\rho u_j\frac{\partial u_i}{\partial x_j}=\frac{\partial \sigma_{ji}}{\partial x_j}+\rho B_i \tag{A.136}$$

$$\rho\frac{\partial u_i}{\partial t}+\rho u_j\frac{\partial u_i}{\partial x_j}=\frac{\partial}{\partial x_j}\Bigg[-p\delta_{ij}+\mu\bigg(\frac{\partial u_i}{\partial x_j}+\frac{\partial u_j}{\partial x_i}\bigg)\Bigg]+\rho B_i. \tag{A.137}$$

Assuming dynamic viscosity, μ, does not change spatially,

$$\rho\frac{\partial u_i}{\partial t}+\rho u_j\frac{\partial u_i}{\partial x_j}=-\frac{\partial p}{\partial x_i}+\mu\Bigg[\frac{\partial^2 u_i}{\partial x_j\partial x_j}+\frac{\partial^2 u_j}{\partial x_j\partial x_i}\Bigg]+\rho B_i, \tag{A.138}$$

Use the conservation of mass equation for incompressible flows, $\frac{\partial u_j}{\partial x_j}=0$,

$$\rho\frac{\partial u_i}{\partial t}+\rho u_j\frac{\partial u_i}{\partial x_j}=-\frac{\partial p}{\partial x_i}+\mu\Bigg[\frac{\partial^2 u_i}{\partial x_j\partial x_j}+\frac{\partial}{\partial x_i}\overbrace{\frac{\partial u_j}{\partial x_j}}^{0}\Bigg]+\rho B_i \tag{A.139}$$

$$\rho\frac{\partial u_i}{\partial t}+\rho u_j\frac{\partial u_i}{\partial x_j}=-\frac{\partial p}{\partial x_i}+\mu\frac{\partial^2 u_i}{\partial x_j\partial x_j}+\rho B_i, \tag{A.140}$$

or in vector notation,

$$\rho\frac{\mathrm{D}\boldsymbol{u}}{\mathrm{D}t}=-\boldsymbol{\nabla}p+\mu\boldsymbol{\nabla}^2\boldsymbol{u}+\rho\boldsymbol{B}. \tag{A.141}$$

There are four equations and four unknowns, which are obtainable since the number of equations and unknowns is equal. This concludes the derivation of the Navier-Stokes equations for incompressible flow conditions.

A.3.5 Compressible Navier-Stokes Equations

Like the incompressible counterpart, the compressible Navier-Stokes equations can be written using Cauchy momentum equations and Stokes's hypothesis, as explained in Subsection A.3.2.

Rewriting the Cauchy momentum equations in Einstein notation, then plugging the compressible version of the generalized law of viscosity, Equation A.134, into it:

$$\rho\frac{\partial u_i}{\partial t} + \rho u_j\frac{\partial u_i}{\partial x_j} = \frac{\partial \sigma_{ji}}{\partial x_j} + \rho B_i \tag{A.142}$$

$$\rho\frac{\partial u_i}{\partial t} + \rho u_j\frac{\partial u_i}{\partial x_j} = \frac{\partial}{\partial x_j}\bigg[- p\delta_{ij} + \mu\bigg(- \frac{2}{3}\delta_{ij}\frac{\partial u_k}{\partial x_k} + \frac{\partial u_i}{\partial x_j} + \frac{\partial u_j}{\partial x_i}\bigg)\bigg] + \rho B_i. \tag{A.143}$$

Simplifying further by assuming dynamic viscosity, μ, does not change spatially:

$$\rho\frac{\partial u_i}{\partial t} + \rho u_j\frac{\partial u_i}{\partial x_j} = -\frac{\partial p}{\partial x_i} + \mu\bigg(- \frac{2}{3}\frac{\partial}{\partial x_i}\frac{\partial u_k}{\partial x_k} + \frac{\partial^2 u_j}{\partial x_j \partial x_j} + \frac{\partial}{\partial x_j}\frac{\partial u_j}{\partial x_i}\bigg) + \rho B_i \tag{A.144}$$

$$\rho\frac{\partial u_i}{\partial t} + \rho u_j\frac{\partial u_i}{\partial x_j} = -\frac{\partial p}{\partial x_i} + \mu\bigg(- \frac{2}{3}\frac{\partial}{\partial x_i}\frac{\partial u_j}{\partial x_j} + \frac{\partial^2 u_j}{\partial x_j \partial x_j} + \frac{\partial}{\partial x_i}\frac{\partial u_j}{\partial x_j}\bigg) + \rho B_i \tag{A.145}$$

$$\rho\frac{\partial u_i}{\partial t} + \rho u_j\frac{\partial u_i}{\partial x_j} = -\frac{\partial p}{\partial x_i} + \mu\bigg(\frac{1}{3}\frac{\partial}{\partial x_i}\frac{\partial u_j}{\partial x_j} + \frac{\partial^2 u_j}{\partial x_j \partial x_j}\bigg) + \rho B_i, \tag{A.146}$$

or in vector notation,

$$\rho\frac{\mathrm{D}\boldsymbol{u}}{\mathrm{D}t} = -\boldsymbol{\nabla} p + \mu\bigg(\frac{1}{3}\boldsymbol{\nabla}(\boldsymbol{\nabla}\cdot\boldsymbol{u}) + \boldsymbol{\nabla}^2\boldsymbol{u}\bigg) + \rho\boldsymbol{B}. \tag{A.147}$$

The unknowns are obtainable since the number of equations and unknowns are equal. Derivation of the Navier-Stokes equation for incompressible flow conditions is

concluded here.

A.4 Turbulence Modeling

Turbulence is seemingly random, chaotic changes in pressure, velocity, and other properties of a fluid flow. It is well-known yet not well-established, and it is described as the most important unsolved classical physics problem by the famous physicist Richard Feynman. There is no exact solution or method to solve turbulence, i.e., the Navier-Stokes equations. Strangely, there is also no well-agreed description of the turbulence. Generally, turbulence is described by characteristics of the phenomenon: randomness, high diffusivity (mixing), high Reynolds number, 3D vorticity fluctuations, dissipation or energy loss, and dependence on flow rather than fluid (Tennekes & Lumley, 1972). Even though there is no perfect explanation and solution for turbulence, there are many models and methods exist. These models and methods enable simulation of the turbulent flow's behavior; thus, numerical techniques can solve fluid flow.

Turbulence in the Navier-Stokes equations appears from the so-called non-linear term, $\big(\boldsymbol{u} \cdot \boldsymbol{\nabla}\big)\boldsymbol{u}$, existing in the Navier-Stokes equations. Even though the non-linearity exists, since the non-linearity is not on the highest order term, this non-linearity is called quasi-linear, which behaves somewhat better than fully non-linear PDEs.

The differential form of the Navier-Stokes equations may be decomposed into mean and fluctuating parts with the use of the Reynolds decomposition method. Then the decomposed form can be averaged over time. In the end, one would get the averaged Navier-Stokes equations. The average results are of the main interest for the most, rather than random fluctuations.

A.4.1 Reynolds Decomposition and Reynolds Averaging

Most engineering problems depend on the knowledge of mean flow variables because the fluctuations caused by turbulence are minuscule compared to the magnitude of the mean flow's values. This is true only if the instantaneous velocity fluctuations caused by the turbulence are lower than the mean flow, i.e., $|u'| \ll |U|$. This kind of

relationship is commonly described by defining turbulence intensity, which describes the root-mean-square of the fluctuating part of the velocity to mean flow velocity. It is calculated as the percentage as shown in Equation A.148. Turbulence intensity is divided into three categories: low, medium, and high. These classifications correspond to lower than 1 %, between 1 % and 5 %, higher than 5 % turbulence intensity levels.

$$I = 100\frac{\sqrt{u_i' u_i'}}{\sqrt{U_j U_j}}\% \tag{A.148}$$

Since the mean flow variables are the point of interest, the equations describing the instantaneous flow variables may be decomposed into mean and fluctuating parts. This decomposition may provide a superior understanding and description of the chaotic nature of the Navier-Stokes equations. These mean values could be assumed time-wise means; however, if found necessary, the techniques can be altered to be applied on average to multiple identical systems. Moreover, in order to keep the discussion simple and bounded, only the time average is demonstrated here. Also, the stationary processes are discussed in this section. An example of the stationary process in terms of velocities is given in Figure A.3. Subsection A.4.2 discusses the non-stationary applications.

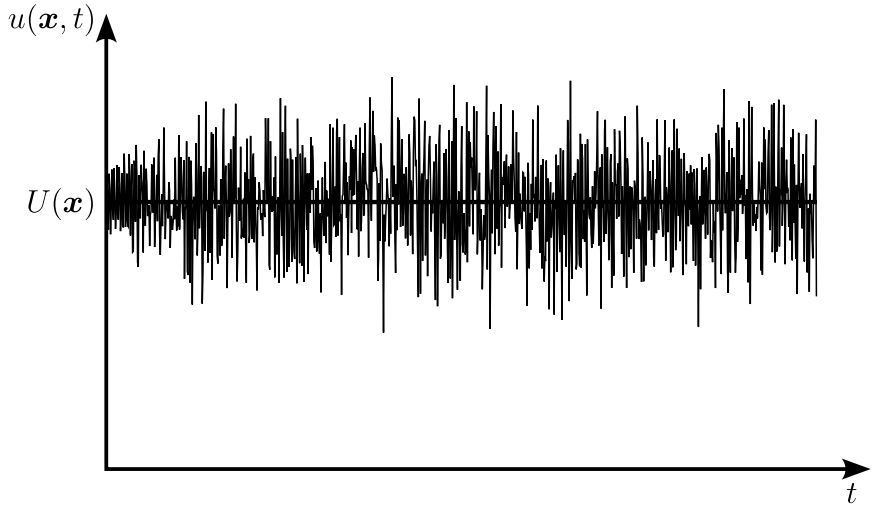

Figure A.3. A Stationary Time Series of Velocity Evolution

In order to decompose instantaneous fields such as $u_i(\boldsymbol{x},t),\ p(\boldsymbol{x},t),\ \tau_{ij}(\boldsymbol{x},t)$ to the

mean and instantaneous parts Reynolds decomposition are used as shown:

$$\begin{aligned} u_i(\boldsymbol{x},t) &= U_i(\boldsymbol{x}) + u_i(\boldsymbol{x},t)' & u_i &= U_i + u_i' \\ p(\boldsymbol{x},t) &= P(\boldsymbol{x}) + p(\boldsymbol{x},t)' & p &= P + P' \\ & \text{or in short} & & \\ \tau_{ij}(\boldsymbol{x},t) &= T_{ij}(\boldsymbol{x}) + \tau_{ij}(\boldsymbol{x},t)' & \tau_{ij} &= \overline{T_{ij}} + \tau_{ij}' \\ s_{ij}(\boldsymbol{x},t) &= S_{ij}(\boldsymbol{x}) + s_{ij}(\boldsymbol{x},t)' & s_{ij} &= S_{ij} + s_{ij}' \end{aligned} \tag{A.149}$$

The average of the instantaneous velocity field is

$$\frac{1}{\mathcal{T}} \lim_{\mathcal{T}\to\infty} \int_t^{t+\mathcal{T}} u_i(\boldsymbol{x},t) = \overline{u_i(\boldsymbol{x},t)} = U_i(\boldsymbol{x}). \tag{A.150}$$

Similarly, the time average of the mean velocity is itself, i.e.,

$$\frac{1}{\mathcal{T}} \lim_{\mathcal{T}\to\infty} \int_t^{t+\mathcal{T}} U_i(\boldsymbol{x}) = \overline{U_i(\boldsymbol{x})} = U_i(\boldsymbol{x}). \tag{A.151}$$

In addition, it is possible to show that the time average of the fluctuating part is equal to zero:

$$\overline{u_i(\boldsymbol{x},t)} = \overline{U_i(\boldsymbol{x})} + \overline{u_i(\boldsymbol{x},t)'} \tag{A.152}$$

$$U_i(\boldsymbol{x}) = U_i(\boldsymbol{x}) + \overline{u_i(\boldsymbol{x},t)'} \tag{A.153}$$

$$\overline{u_i(\boldsymbol{x},t)'} = 0. \tag{A.154}$$

Moreover, decomposition and averaging rely on other rules. Some rules are collected under Equation A.155. Generally, these rules appear due to the linearity of the time-averaging operator, which is a definite integral. The further explanations and derivations

of these equations are skipped for brevity.

$$\begin{aligned}
\overline{Au_i} &= A\overline{u_i} = AU_i \\
\overline{u_i + u_j} &= \overline{u_i} + \overline{u_j} = U_i + U_j \\
\overline{U_i u_j} &= U_i\overline{u_j} = U_i U_j \\
\overline{\frac{\partial u_i}{\partial x_j}} &= \frac{\partial \overline{u_i}}{\partial x_j} = \frac{\partial U_i}{\partial x_j} \\
\overline{u_i' u_j'} &\neq \overline{u_i'} \cdot \overline{u_j'}
\end{aligned} \tag{A.155}$$

Lastly, it is important to stress that the Reynolds averaging is just time-averaging. The mean flow variables must not be dependent on time as a variable, i.e., $U_i \neq U_i(t)$. If the mean flow variables vary in time, which is not the case, one has to use other averaging techniques, such as ensemble averaging. In other words, flow characteristics must not be functions of time in order to exploit Reynolds-averaging; if not, multiple experimental data may be used for averaging. Furthermore, hinging upon this fact, one can say

$$\frac{\partial U_i}{\partial t} = 0, \tag{A.156}$$

since U_i is not a function of t.

A.4.2 Reynolds Averaged Incompressible Conservation of Mass Equation

The incompressible continuity equation is explained in Subsection A.2.2. In this subsection, decomposition and averaging processes for continuity equations are developed. The breathing process in the nasal cavity is considered incompressible because it moves at a fraction of the speed of pressure wave propagation in air. Therefore, the current investigation's focus is only on the incompressible continuity equation.

Rewriting the incompressible continuity equation as given in Equation A.66:

$$\frac{\partial u_i}{\partial x_j} = 0. \tag{A.157}$$

Decomposing velocity into the mean and fluctuating terms,

$$\frac{\partial\big(U_i + u_i'\big)}{\partial x_j} = 0 \tag{A.158}$$

$$\frac{\partial U_i}{\partial x_j} + \frac{\partial u_i'}{\partial x_j} = 0. \tag{A.159}$$

There is no further simplifications exist; hence, take the time average,

$$\overline{\frac{\partial U_i}{\partial x_j}} + \overline{\frac{\partial u_i'}{\partial x_j}} = 0. \tag{A.160}$$

Simplifying the equation by using definitions given in Equation A.155,

$$\frac{\partial \overline{U_i}}{\partial x_j} + \frac{\partial \overline{u_i'}}{\partial x_j} = 0 \tag{A.161}$$

$$\frac{\partial U_i}{\partial x_j} + \frac{\partial \overline{u_i'}}{\partial x_j} = 0 \tag{A.162}$$

$$\boxed{\frac{\partial U_i}{\partial x_j} = 0}. \tag{A.163}$$

Surprisingly, the mean-flow continuity equation is analogous to the instantaneous continuity equation. This equation may also be written as,

$$\boldsymbol{\nabla U} = 0. \tag{A.164}$$

A.4.3 Incompressible Reynolds Averaged Navier-Stokes Equations

In this subsection, Reynolds decomposition and averaging for the incompressible Navier-Stokes equations are discussed. This discussion demonstrates the non-linearity effect, which is the turbulence, on the averaged Navier-Stokes differential equations. The end result should indicate that fluctuations in the instantaneous flow fields also characterize the mean fields.

The incompressible Navier-Stokes equations in vector notation is

$$\rho\frac{\partial \boldsymbol{u}}{\partial t} + \rho\big(\boldsymbol{u}\cdot\boldsymbol{\nabla}\big)\boldsymbol{u} = -\boldsymbol{\nabla}p + \mu\nabla^2\boldsymbol{u}. \tag{A.165}$$

In order to bring ease of writing and understanding, instead of writing all three equations separately, it is better to write them in Einstein's notation,

$$\rho\frac{\partial u_i}{\partial t} + \rho u_j\frac{\partial u_i}{\partial x_j} = -\frac{\partial p}{\partial x_i} + \mu\frac{\partial^2 u_i}{\partial x_j \partial x_j}. \tag{A.166}$$

Moreover, since incompressible Navier-Stokes equations are discussed, one may express convective terms as below,

$$u_j\frac{\partial u_i}{\partial x_j} = \frac{\partial u_i u_j}{\partial x_j}. \tag{A.167}$$

The above convective representation is only be written if $\boldsymbol{\nabla}\cdot\boldsymbol{u} = \frac{\partial u_i}{\partial x_i} = 0$ holds due to the incompressibility. Expanding the right-hand side of the above equation by using the product rule:

$$\frac{\partial u_i u_j}{\partial x_j} = u_i\overbrace{\frac{\partial u_j}{\partial x_j}}^{0} + u_j\frac{\partial u_i}{\partial x_j} \tag{A.168}$$

$$= u_j\frac{\partial u_i}{\partial x_j}. \tag{A.169}$$

Now the incompressible equations are ready and stand as,

$$\rho\frac{\partial u_i}{\partial t}+\rho\frac{\partial u_i u_j}{\partial x_j}=-\frac{\partial p}{\partial x_i}+\mu\frac{\partial^2 u_i}{\partial x_j \partial x_j}. \tag{A.170}$$

Velocity and pressure terms can be separated into time-averaged and time-wise fluctuating parts. Applying this to Navier-Stokes equations:

$$\rho\frac{\partial\big(U_i+u_i'\big)}{\partial t}+\rho\frac{\partial\big[\big(U_i+u_i'\big)\big(U_j+u_j'\big)\big]}{\partial x_j}=-\frac{\partial\big(P+p'\big)}{\partial x_i}+\mu\frac{\partial^2\big(U_i+u_i'\big)}{\partial x_j \partial x_j}. \tag{A.171}$$

Furthermore, expanding the multiplications and separating the summations inside the partial derivatives,

$$\rho\frac{\partial\big(U_i+u_i'\big)}{\partial t}+\rho\frac{\partial\big[U_iU_j+U_iu_j'+u_i'U_j+u_i'u_j'\big]}{\partial x_j}=-\frac{\partial\big(P+p'\big)}{\partial x_i}+\mu\frac{\partial^2\big(U_i+u_i'\big)}{\partial x_j \partial x_j}. \tag{A.172}$$

After the above steps, the equations become ready for Reynolds averaging. The initial form of the averaged Navier-Stokes equations is obtained, though without averaging simplifications, is

$$\rho\overline{\frac{\partial\big(U_i+u_i'\big)}{\partial t}}+\rho\overline{\frac{\partial\big[U_iU_j+U_iu_j'+u_i'U_j+u_i'u_j'\big]}{\partial x_j}}=-\overline{\frac{\partial\big(P+p'\big)}{\partial x_i}}+\mu\overline{\frac{\partial^2\big(U_i+u_i'\big)}{\partial x_j \partial x_j}}. \tag{A.173}$$

Simplifying the equation by using definitions given in Equation A.155,

$$\rho\frac{\partial\left(\overline{U_i+u_i'}\right)}{\partial t}+\rho\frac{\partial\left[\overline{U_iU_j+U_iu_j'+u_i'U_j+u_i'u_j'}\right]}{\partial x_j}=-\frac{\partial\left(\overline{P+p'}\right)}{\partial x_i}+\mu\frac{\partial^2\left(\overline{U_i+u_i'}\right)}{\partial x_j\partial x_j} \tag{A.174}$$

$$\rho\frac{\partial\left(\overline{U_i}+\overline{u_i'}\right)}{\partial t}+\rho\frac{\partial\left[\overline{U_iU_j}+\overline{U_iu_j'}+\overline{u_i'U_j}+\overline{u_i'u_j'}\right]}{\partial x_j}=-\frac{\partial\left(\overline{P}+\overline{p'}\right)}{\partial x_i}+\mu\frac{\partial^2\left(\overline{U_i}+\overline{u_i'}\right)}{\partial x_j\partial x_j} \tag{A.175}$$

$$\rho\frac{\partial\left(U_i+0\right)}{\partial t}+\rho\frac{\partial\left[U_iU_j+U_i\overline{u_j'}+\overline{u_i'}U_j+\overline{u_i'u_j'}\right]}{\partial x_j}=-\frac{\partial\left(P+0\right)}{\partial x_i}+\mu\frac{\partial^2\left(U_i+0\right)}{\partial x_j\partial x_j} \tag{A.176}$$

$$\rho\frac{\partial U_i}{\partial t}+\rho\frac{\partial\left[U_iU_j+U_i\cdot 0+0\cdot U_j+\overline{u_i'u_j'}\right]}{\partial x_j}=-\frac{\partial P}{\partial x_i}+\mu\frac{\partial^2U_i}{\partial x_j\partial x_j} \tag{A.177}$$

$$\rho\cdot 0+\rho\frac{\partial U_iU_j}{\partial x_j}+\frac{\partial\overline{u_i'u_j'}}{\partial x_j}=-\frac{\partial P}{\partial x_i}+\mu\frac{\partial^2U_i}{\partial x_j\partial x_j} \tag{A.178}$$

$$\boxed{\rho\frac{\partial U_iU_j}{\partial x_j}+\rho\frac{\partial\overline{u_i'u_j'}}{\partial x_j}=-\frac{\partial P}{\partial x_i}+\mu\frac{\partial^2U_i}{\partial x_j\partial x_j}}. \tag{A.179}$$

In the literature, the Reynolds-averaged Navier-Stokes equations are further compacted by introducing the Reynolds stress tensor and mean strain rate tensor. These two tensors are rank-2 tensors, and they are symmetric except for some anisotropic liquids (Wilcox, 2006). They can be written as,

$$\tau_{ij}=\begin{bmatrix}\tau_{11} & \tau_{12} & \tau_{13}\\ & \tau_{22} & \tau_{23}\\ \text{sym.} & & \tau_{33}\end{bmatrix},\qquad \overline{S}_{ij}=\begin{bmatrix}\overline{S}_{11} & \overline{S}_{12} & \overline{S}_{13}\\ & \overline{S}_{22} & \overline{S}_{23}\\ \text{sym.} & & \overline{S}_{33}\end{bmatrix}. \tag{A.180}$$

Reynolds stress tensor is

$$\tau_{ij}=\rho\overline{u_i'u_j'}. \tag{A.181}$$

The mean strain rate tensor may be found by taking the time average of the strain rate tensor. In short, the mean strain rate tensor is

$$\overline{S}_{ij} = \frac{1}{2}\Big[\boldsymbol{\nabla} U + (\boldsymbol{\nabla} U)^{\mathrm{T}}\Big] = \frac{1}{2}\left(\frac{\partial U_i}{\partial x_j} + \frac{\partial U_j}{\partial x_i}\right). \tag{A.182}$$

Taking the derivative of viscous stress tensor with respect to j index and multiplying it with 2μ. Then, in order to obtain a viscous term in the averaged equation, one has to cancel the divergence of the velocity since it is 0 due to incompressibility.

$$2\mu\frac{\partial \overline{S}_{ij}}{\partial x_j} = 2\mu\frac{\partial}{\partial x_j}\left[\frac{1}{2}\left(\frac{\partial U_i}{\partial x_j} + \frac{\partial U_j}{\partial x_i}\right)\right] \tag{A.183}$$

$$= \mu\left[\frac{\partial^2 U_i}{\partial x_j \partial x_j} + \frac{\partial^2 U_i}{\partial x_j \partial x_i}\right] \tag{A.184}$$

$$= \mu\left[\frac{\partial^2 U_i}{\partial x_j \partial x_j} + \frac{\partial}{\partial x_j}\left(\overbrace{\frac{\partial U_i}{\partial x_i}}^{0}\right)\right] \tag{A.185}$$

$$= \mu\frac{\partial^2 U_i}{\partial x_j \partial x_j} \tag{A.186}$$

Finally, the averaged differential equation takes a somewhat recognizable form

$$\rho\frac{\partial U_i U_j}{\partial x_j} = \frac{\partial}{\partial x_j}\big(-p\delta_{ij} + 2\mu\overline{S}_{ij} - \tau_{ij}\big). \tag{A.187}$$

Surprisingly, averaged equations appear almost like the original Navier-Stokes equations. This appearance is only disturbed by the Reynolds stress tensor, which is the multiplication of the fluctuations. Ultimately, the whole problem also lies in this fluctuating term: There is no equation describing its behavior, but it is needed to calculate the mean flow variables. Depending on the perspective, there are either six unknowns or three unknowns. If one considers Reynolds stress tensor as an unknown which is a symmetric tensor, there are six unknowns as: $\tau_{11},\ \tau_{12},\ \tau_{13},\ \tau_{22},\ \tau_{23},\ \tau_{33}$. On the other hand, if another considers unknowns as the velocity fluctuations, there are only three unknowns as $u_1',\ u_2',\ u_3'$. Considering both perspectives, it is clear that there

are more unknowns than equations. This is known as the turbulent closure problem. All in all, there is no way to calculate the mean flow without solving instantaneous flow equations, except if one comes up with a way to calculate the recently incorporated unknowns.

A.4.4 Incompressible Unsteady Reynolds Averaged Navier-Stokes Equations

Sometimes, in literature, it is possible to see unsteady terms in the Navier-Stokes equations are left as they are. These formulations are commonly called URANS equations. The unsteady term occurs due to a non-stationary process of unsteady flow, as an example demonstrated in Figure A.4. However, the reasoning behind this approach is seldom explained. Since time-averaged velocities do not have a gradient, in the above subsection, $\frac{\partial U_i}{\partial t} = 0$ is assumed. Therefore, the reason why this gradient in URANS formulation is not equal to zero should be clarified.

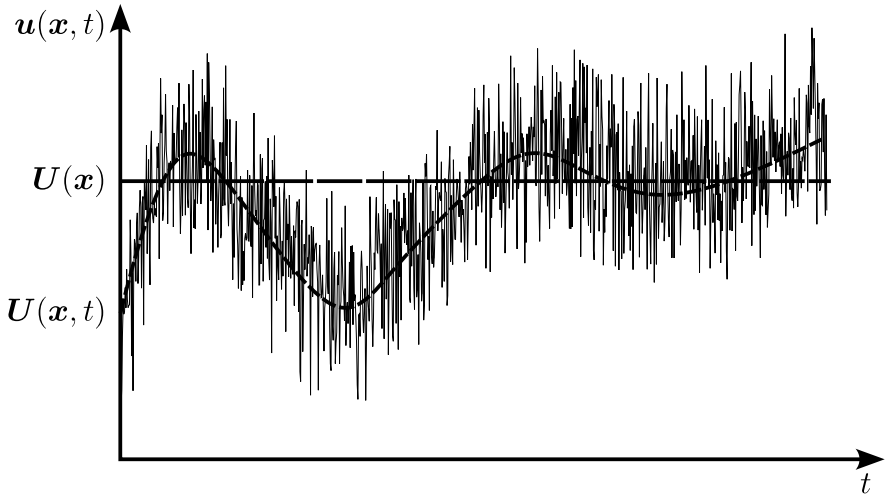

Figure A.4. A Non-Stationary Time Series of Velocity Evolution

Note. This image has two means: $\boldsymbol{U}(\boldsymbol{x})$ could be understood as a time-wise mean, i.e., steady flow rate, and $\boldsymbol{U}(\boldsymbol{x},t)$ may be thought as a mean appearing from the ensemble averaging.

According to Ferziger et al. (2020) and Wilcox (2006), non-stationary turbulence might be time-averaged if there is very slow unsteadiness that is not due to turbulence; in other words, time-averaging is only possible if the time scales of unsteady fluctuations are much bigger than turbulent fluctuations' time scales. The other reasoning given by Ferziger et al. (2020) is the usage of averaging over ensembles; ensemble averaging also removes random fluctuations since there are so many processes and every single one of them has a random phase; therefore, their average removes the turbulent fluctuations to leave the averaged representation of the flow.

URANS is similar to RANS and may be given similar to Equation A.179 as:

$$\rho\frac{\partial U_i}{\partial t}+\rho\frac{\partial U_iU_j}{\partial x_j}+\frac{\partial\overline{u_i'u_j'}}{\partial x_j}=-\frac{\partial p}{\partial x_i}+\mu\frac{\partial^2U_i}{\partial x_j\partial x_j}, \tag{A.188}$$

or similar to Equation A.187 as:

$$\rho\frac{\partial U_i}{\partial t}+\rho\frac{\partial U_iU_j}{\partial x_j}=\frac{\partial}{\partial x_j}\big(-p\delta_{ij}+2\mu\overline{S}_{ij}-\tau_{ij}\big). \tag{A.189}$$

A.4.5 Generalization of Eddy Viscosity Approximation

As demonstrated, Reynolds stress tensor, $\rho\overline{u_i'u_j'}=\tau_{ij}$ is the reason of the turbulent closure problem. This symmetric tensor introduces six unknowns that must be modeled in order to solve RANS, URANS, or filtered Navier-Stokes equations. The turbulent closure problem is most commonly solved by assuming the stresses may be approximated as an extra viscosity called eddy viscosity or sometimes turbulent viscosity, μ_t. Boussinesq first proposed this approximation; therefore, it is commonly referred to as Boussinesq's hypothesis or Boussinesq's approximation.

Naively, one may approximate eddy viscosity similar to the relationship between velocity gradient (shear rate) and shear stress as:

$$\rho\overline{u_i'u_j'}=\tau_{ij}=-\mu_\mathrm{t}\dot{\gamma}=-\mu_\mathrm{t}\left(\frac{\partial U_i}{\partial x_j}+\frac{\partial U_j}{\partial x_j}\right). \tag{A.190}$$

Since the relationship between shear stresses and strain rates is written solely for shear stresses, the current model fails to predict normal stresses, i.e., when $i = j$. In order to see this issue, one should set $i = j$:

$$\tau_{ij} = -\mu_{\mathrm{t}} \left(\frac{\partial U_i}{\partial x_i} + \frac{\partial U_i}{\partial x_i} \right) \tag{A.191}$$

$$= -2\mu_{\mathrm{t}} \frac{\partial U_i}{\partial x_i}, \tag{A.192}$$

if the flow is incompressible, $\frac{\partial U_i}{\partial x_i} = 0$:

$$\tau_{ij} = -2\mu_{\mathrm{t}} \overbrace{\frac{\partial U_i}{\partial x_i}}^{0} = 0, \tag{A.193}$$

which suggests that when the flow is incompressible, the summation of normal stresses is strangely equal to zero. This is clearly incorrect, and even the summation is defined as turbulent kinetic energy, $k = \frac{1}{2}\overline{u_i' u_i'}$. In order to compensate for this problem, introduce the missing term to the right-hand side of Equation A.192.

$$\tau_{ij} = -\mu_{\mathrm{t}} \left(\frac{\partial U_i}{\partial x_j} + \frac{\partial U_j}{\partial x_i} \right) + \frac{1}{3} \delta_{ij} \rho \overline{u_k' u_k'} \tag{A.194}$$

$$= -\mu_{\mathrm{t}} \left(\frac{\partial U_i}{\partial x_j} + \frac{\partial U_j}{\partial x_i} \right) - \frac{2}{3} \delta_{ij} \rho k, \tag{A.195}$$

where δ_{ij} ensures this term appears only when $i = j$, and $\frac{1}{3}$ exists since $\delta_{ii} = 3$.

The above-generalized form of the eddy viscosity approximation is complete for incompressible flows. For incompressible flows, the current model is faulty; in order

to see the problem, one should set $i = j$ in Equation A.195:

$$\tau_{ii} = -\mu_{\mathrm{t}}\left(\frac{\partial U_i}{\partial x_i} + \frac{\partial U_i}{\partial x_i}\right) + \frac{1}{3}\delta_{ii}\rho k \tag{A.196}$$

$$\rho k = -2\mu_{\mathrm{t}}\left(\frac{\partial U_i}{\partial x_i}\right) + \frac{1}{3}3\rho k \tag{A.197}$$

$$0 = -2\mu_{\mathrm{t}}\left(\frac{\partial U_i}{\partial x_i}\right), \tag{A.198}$$

the result suggests $\frac{\partial U_i}{\partial x_i} = 0$ for incompressible flows, which is not true for incompressible flows. In order to correct this error, one may introduce another term to Equation A.195 that makes this term vanish when $i = j$ as follows:

$$\tau_{ij} = -\mu_{\mathrm{t}}\left(\frac{\partial U_i}{\partial x_j} + \frac{\partial U_j}{\partial x_i}\right) + \frac{1}{3}\delta_{ij}\rho k + \frac{1}{3}\mu_{\mathrm{t}}\delta_{ij}\frac{\partial U_k}{\partial x_k} \tag{A.199}$$

$$= -\mu_{\mathrm{t}}\left(\frac{\partial U_i}{\partial x_j} + \frac{\partial U_j}{\partial x_i} + \frac{2}{3}\mu_{\mathrm{t}}\delta_{ij}\frac{\partial U_k}{\partial u_k}\right) - \frac{1}{3}\delta_{ij}\rho k, \tag{A.200}$$

where δ_{ij} ensures the term appears only when $i = j$, and $\frac{1}{3}$ exists since $\delta_{ii} = 3$.

Lastly, one may use the definition of strain rate tensor to shorten the equation. In order to accomplish this task, the strain rate tensor S_{ij} should be separated into deviatoric

(traceless) and hydrostatic parts. The deviatoric part of the strain rate tensor is

$$\mathrm{dev}(S_{ij}) = S_{ij} - \mathrm{hyd}(S_{ij}) \tag{A.201}$$

$$= S_{ij} - \frac{1}{3}\delta_{ij}\mathrm{tr}(S_{ij}) \tag{A.202}$$

$$= S_{ij} - \frac{1}{3}\delta_{ij}S_{ii} \tag{A.203}$$

$$= \frac{1}{2}\left(\frac{\partial U_i}{\partial x_j} + \frac{\partial U_j}{\partial x_i}\right) - \frac{1}{3}\delta_{ij}\frac{1}{2}\left(\frac{\partial U_i}{\partial x_j} + \frac{\partial U_i}{\partial x_i}\right) \tag{A.204}$$

$$= \frac{1}{2}\left(\frac{\partial U_i}{\partial x_j} + \frac{\partial U_j}{\partial x_i}\right) - \frac{1}{3}\delta_{ij}\frac{\partial U_i}{\partial x_i} \tag{A.205}$$

$$= \frac{1}{2}\left(\frac{\partial U_i}{\partial x_j} + \frac{\partial U_j}{\partial x_i} - \frac{2}{3}\delta_{ij}\frac{\partial U_i}{\partial x_i}\right). \tag{A.206}$$

The deviatoric part of the strain rate tensor is double the first term in the right-hand side of Equation A.200; this realization finishes the derivation and reduces Equation A.200 to:

$$\tau_{ij} = -2\mu_\mathrm{t}\,\mathrm{dev}(S_{ij}) + \frac{2}{3}\delta_{ij}\rho k. \tag{A.207}$$

For incompressible flows, the generalized eddy viscosity approximation is ultimately

$$\tau_{ij} = -2\mu_\mathrm{t}S_{ij} + \frac{2}{3}\delta_{ij}\rho k. \tag{A.208}$$

All in all, the Reynolds stress tensor is now expressed in milder terms. However, this expression does not provide any way to calculate eddy viscosity, μ_t, and k; it solely allows approximation of Reynolds stress tensor if these two terms are known. Therefore, modeling is required to solve RANS equations, such as algebraic equations or two-equation turbulence models.